High-Quality Microcrystalline Silicon for Efficient Thin-Film Solar Cells: Insights into Plasma and Material Properties

THÈSE N° 5991 (2013)

PRÉSENTÉE LE 29 NOVEMBRE 2013

À LA FACULTÉ DES SCIENCES ET TECHNIQUES DE L'INGÉNIEUR LABORATOIRE DE PHOTOVOLTAÏQUE ET COUCHES MINCES ÉLECTRONIQUES PROGRAMME DOCTORAL EN SCIENCE ET GÉNIE DES MATÉRIAUX

ÉCOLE POLYTECHNIQUE FÉDÉRALE DE LAUSANNE

POUR L'OBTENTION DU GRADE DE DOCTEUR ÈS SCIENCES

PAR

Grégory BUGNON

acceptée sur proposition du jury:

Prof. P. Muralt, président du jury Prof. C. Ballif, Dr F. Sculati-Meillaud, directeurs de thèse Dr J. Cashmore, rapporteur Dr I. Furno, rapporteur Dr T. Matsui, rapporteur



Résumé

Cette thèse étudie le lien entre la qualité du silicium microcristallin (μc -Si:H) et ses conditions de dépôt par plasma dans la fabrication de cellules solaires en couches minces de silicium. Le rôle des interfaces et de la qualité du μc -Si:H sur les performances du dispositif est analysé en détail.

Du fait de la faible absorption du μc -Si:H aux grandes longueurs d'onde, son utilisation dans des cellules solaires nécessite le dépôt de couches photo-actives avec des épaisseurs typiques de quelques micromètres. La croissance a généralement lieu sur des surfaces très texturées, qui permettent d'augmenter le piégeage de lumière—et donc son absorption—, mais qui peuvent potentiellement induire des défauts structurels dans le film lors de sa croissance. Par conséquent, l'un des principaux défis de cette technologie est l'identification des paramètres de dépôt de plasma permettant la croissance d'un film de μc -Si:H de très haute qualité à une vitesse de dépôt élevée et ce, sur des substrats texturés qui garantissent une bonne efficacité de piégeage de la lumière.

Dans une première approche, les rôles de la fraction de dissociation du silane et de la pression du dépôt sont étudiés. Avec une pression et une dissociation de silane croissantes, la densité de défauts du μc -Si:H est considérablement réduite conduisant à l'amélioration des performances des cellules solaires. Une estimation de l'énergie moyenne avec laquelle les ions bombardent le substrat soutient l'hypothèse que le bombardement ionique est le principal responsable des différences observées.

Un aspect fondamental du dépôt du μc -Si:H sur des substrats hautement texturés est mis en évidence : deux phases distinctes du μc -Si:H contribuent à l'efficacité globale de la cellule solaire, et peuvent toutes deux contrôler les performances des cellules. La première phase concerne le corps du matériau, et domine les performances sur substrats plats. Sur morphologies rugueuses cependant, des zones nanoporeuses défectueuses induites par le substrat—la deuxième phase—se développent et se révèlent beaucoup plus sensibles aux conditions du dépôt par plasma et à la morphologie du substrat. L'importance relative de cette phase défectueuse secondaire est mise en évidence au travers de nouvelles expériences d'exposition à l'humidité. L'utilisation de couches dopées d'oxyde de silicium permet d'atténuer l'influence de ces régions nanoporeuses sur le rendement des cellules solaires.

Une étude comparative des fréquences d'excitation du plasma de 13,56 MHz (RF) et 40,68 MHz (VHF) montre que, même si les deux permettent la croissance du corps du matériau de très bonne qualité, le rendement des cellules préparées en VHF est toujours en retrait pour des vitesses de croissance inférieures à $5\,\text{Å}\,\text{s}^{-1}$. Cette différence est reliée à une densité plus

élevée de régions nanoporeuses défectueuses dans les cellules préparées en VHF comme en témoignent les expériences d'exposition à l'humidité, conduisant à de fortes instabilités de la tension en circuit ouvert de ces cellules solaires. Cependant, l'utilisation du VHF s'avère bénéfique à plus haute vitesse de dépôt, grâce notamment à un bombardement ionique moindre et au maintien d'une qualité du corps du matériau plus élevée par rapport au RF. L'interaction cruciale entre la vitesse de croissance du μc -Si:H et la morphologie du substrat à l'égard de la formation des régions nanoporeuses est examinée plus en détail. Il est démontré que les régimes à haute dissociation de silane (avec un flux d'hydrogène réduit) ou une pression accrue conduisent au développement d'un μc -Si:H plus dense bien qu'ils soient associés à une augmentation des réactions secondaires en phase gazeuse et à la formation de poudre. L'utilisation d'une distance interélectrode réduite permet d'atteindre une vitesse de croissance du μc -Si:H plus élevée en maintenant une qualité du corps du matériau plus grande. Des simulations de plasma, effectuées dans le cadre d'une collaboration avec l'Université de Patras, suggèrent que les améliorations observées sont principalement liées à une contribution relative accrue de monoradicaux de silane moins réactifs, tels SiH₃ ou Si₂H₅.

Ensuite, dans le but de mieux comprendre la formation de ces deux phases distinctes du silicium microcristallin, les contraintes intrinsèques du matériau sont étudiées et corrélées à la densité de défauts dans le corps du matériau.

Enfin, les performances des cellules en couches minces de silicium sont améliorées grâce à l'utilisation d'une nouvelle couche tampon d'oxyde de silicium à l'interface p-i. Pour les cellules μc -Si:H, tous les paramètres électriques peuvent être améliorés. En ce qui concerne les cellules en silicium amorphe, la dégradation induite par la lumière est réduite permettant ainsi d'atteindre des rendements stabilisés plus élevés. En outre, cette couche tampon agit comme une barrière efficace à la contamination au bore.

Globalement, ce travail a contribué à mieux comprendre les exigences du μc -Si:H pour les applications photovoltaïques et de quelle manière ses propriétés sont liées aux conditions de dépôt par plasma. Grâce aux développements mentionnés ci-dessus, des progrès significatifs ont été accomplis à la fois dans la compréhension et dans la réalisation de cellules solaires. Une cellule solaire simple-jonction microcristalline avec une remarquable efficacité de 10.9% a ainsi pu être obtenue ; ce qui à notre connaissance est la valeur la plus haute jamais rapportée dans la littérature. Ce travail a également participé au développement de cellules solaires tandem et triple-jonction de très haute efficacité au PV-Lab.

Mots clés:

Photovoltaïque, silicium, cellule solaire à haut rendement, couche mince, silicium amorphe, silicium microcristallin, multi-jonction, simple-jonction, micromorphe, triple-jonction, plasma, déposition, PECVD, fréquence d'excitation, RF, VHF, piégeage de la lumière, morphologie de surface, régions nanoporeuses, cracks, interface p-i, contamination au bore, contamination, dopage, compensation, nucléation, oxyde de zinc, oxyde de silicium, couches optiques, anti-reflet, conductivité transverse, matériau à phase mixte, nanostructure, rugosité, chaleur humide, stabilité électrique, contrainte intrinsèque, contrainte en compression.

Abstract

This thesis investigates the link between the plasma deposition conditions and microcrystalline silicon (μc -Si:H) material quality for thin-film silicon photovoltaic applications. The role of interfaces and the μc -Si:H material quality on the device performance are analyzed in detail.

The low absorption of μc -Si:H at long wavelengths requires the deposition of absorber layers with thicknesses of typically a few micrometers for use in multi-junction TF Si solar cells. The growth typically takes place on highly textured surfaces, which provide increased light absorption—often called light trapping—but which potentially induce structural defects in the film during its growth. Therefore, to further improve the TF Si technology, one of the main challenges is the identification of the determinant plasma deposition parameters that result in the growth of very high-quality μc -Si:H at an increased deposition rate on textured substrates that guarantee efficient light trapping.

As a first approach to better understand the plasma conditions necessary for the growth of high-quality μc -Si:H, the roles of both the silane depletion fraction and the deposition pressure are studied in an industrial-type large-area KAI reactor. With increasing pressure and silane depletion, the μc -Si:H defect density is significantly lowered leading to improved solar cell performance. An estimation of the average energy with which ions impinge on the substrate supports the hypothesis that ion bombardment is mainly responsible for the observed differences.

Then, a fundamental aspect of μc -Si:H deposition on highly textured substrates is highlighted: two different phases of μc -Si:H material contribute to the overall solar cell efficiency, both of which can drive cell performance. The first phase relates to the bulk material and dominates the performance of cells on flat substrates. However, on rough morphologies, substrate-induced defective localized nanoporous regions—the second phase—develop and are found to be significantly more sensitive to the plasma process conditions and substrate morphology than the bulk phase. The relative importance of this secondary defective phase is shown through the use of new damp-heat experiments. Silicon oxide doped layers are demonstrated to mitigate the influence of these nanoporous regions on the solar cell performance.

Next, a comparative study of the plasma excitation frequencies of 13.56 MHz (RF) and 40.68 MHz (VHF) shows that, while both allow for the growth of very good-quality bulk material, the efficiency of VHF-prepared cells is always poorer compared to that of RF-prepared cells within the range of our study for growth rates below $5\,\text{Å}\,\text{s}^{-1}$. This decrease in solar cell performance is related to a higher density of nanoporous regions in the VHF-prepared cells as

evidenced by damp-heat experiments, leading to strong open-circuit voltage instabilities. Still, the use of VHF is shown to be beneficial at increased deposition rates, thanks to reduced ion bombardment and improved bulk material quality.

The crucial interplay between μc -Si:H growth rate and substrate morphology with regard to the formation of nanoporous regions is further discussed for regimes with high deposition rates of around $10~{\rm \AA\,s^{-1}}$. It is shown that high-silane-depletion regimes with significantly reduced ${\rm H_2}$ flow rate or increased pressure lead to a denser μc -Si:H material but are associated with increased secondary gas-phase reactions and powder formation. The use of a reduced interelectrode distance is demonstrated to allow for the growth of μc -Si:H with significantly improved bulk material quality at higher growth rates. Plasma simulations performed in collaboration with the University of Patras are presented and suggest that improvements observed in the μc -Si:H material quality are related mainly to an increased contribution of less reactive silane monoradicals, such as ${\rm SiH_3}$ and ${\rm Si_2H_5}$, to the growing film, as compared to highly reactive ones such as ${\rm SiH_2}$ and ${\rm SiH}$.

Then, in an effort to better understand the formation of these two distinct μc -Si:H phases, the intrinsic stress within μc -Si:H i-layers is studied and correlated with the bulk defect density. Further improvements to both μc -Si:H and a-Si:H solar cells are obtained by introducing a novel intrinsic silicon oxide buffer layer at the p-i interface. For μc -Si:H solar cells, all electrical parameters are improved unless the i-layer is significantly more amorphous-rich and high quality, in which case an improvement only in carrier collection in the blue region is observed. In a-Si:H solar cells the silicon oxide buffer is shown to lower light-induced degradation, which is one of the weak points of TF Si technology. Furthermore, for both a-Si:H and μc -Si:H solar cells, the buffer can also act as an efficient barrier to boron cross-contamination, eliminating the need for additional time-consuming processing steps such as a water flush for single-chamber processes.

Overall, this work contributes to a better understanding of the μc -Si:H material requirements for PV applications and how they relate to the plasma deposition conditions. Based on all the aforementioned developments, significant progress has been made in the understanding and the fabrication of thin-film silicon solar cells based on μc -Si:H. An outstanding single-junction μc -Si:H solar cell of 10.9% was attained; to our knowledge this is the highest reported in the literature. This work also contributed to the development of very high-efficiency tandem and triple-junction thin-film silicon solar cells at PV-Lab.

Keywords:

Photovoltaics, silicon, solar cells, high-efficiency, thin films, amorphous silicon, microcrystalline silicon, multi-junction, single-junction, micromorph, triple-junction, plasma, deposition, PECVD, excitation frequency, RF, VHF, light trapping, surface morphology, nanoporous regions, cracks, p-i interface, boron cross-contamination, contamination, doping, compensation, nucleation, zinc oxide, silicon oxide, optical layers, anti-reflection, shunt quenching, transverse conductivity, mixed-phase material, nanostructure, roughness, damp-heat, electrical stability, intrinsic stress, compressive stress.

Contents

Ał	ostra	ct (Français/English)	V
1	Intr	roduction	1
	1.1	General context	1
	1.2	Photovoltaic energy	2
	1.3	Thin-film silicon photovoltaics	3
	1.4	Current status of research on μc -Si:H	4
	1.5	The goals and structure of this thesis	11
	1.6	Contribution of this thesis to the research field	13
2	Exp	perimental details	15
	2.1	Solar cell preparation overview	15
	2.2	Plasma conditions analysis	19
	2.3	Solar cell measurement and material characterization	22
3	Infl	uence of the deposition pressure and silane depletion on μc -Si:H quality and so-	-
	lar (cell performance	25
	3.1	Introduction	25
	3.2	Study of μc -Si:H deposition conditions in a CCP-VHF discharge	26
		3.2.1 Influence of the deposition pressure	26
		3.2.2 Influence of the hydrogen flow rate and silane depletion	29
	3.3	Material characterization	31
		3.3.1 Defect density of the μc -Si:H intrinsic layer	31
		3.3.2 Amorphous to microcrystalline transitions	33
	3.4	Simple model for ion bombardment energy	34
	3.5	Conclusion	37
4	_	hlighting the contributions of two different phases of μc -Si:H material to overall	l
	sola	ar cell performances	39
	4.1	Introduction	39
	4.2	Role of plasma process conditions on material porosity	40
		4.2.1 SiO _x doped layers in μc -Si:H solar cells deposited at a high-deposition rate	40
		4.2.2 In depth μc -Si:H material characterization	43
	4.3	Interplay between substrate roughness and PECVD process	47

Contents

	4.4	Material stability and evidence of the nanoporous phase	48
	4.5	On the role of the SiO_x doped layers	50
	4.6	Conclusion	51
5	Con	nparison of plasma excitation frequencies for the growth of high-quality μc -Si:H	[
		yers	53
	5.1	On the use of very-high frequency in capacitively coupled plasmas	53
	5.2	22-mm-gap reactor configuration	56
		5.2.1 Standard-gap deposition regimes	57
		5.2.2 Analysis of solar cell performance	58
		5.2.3 Conclusion	63
	5.3	12-mm-gap reactor configuration	64
		5.3.1 13.56 MHz excitation frequency	64
		5.3.2 40.68 MHz excitation frequency	71
		5.3.3 Conclusion	75
	5.4	Material analysis and stability study	75
		5.4.1 FTPS comparison of cells prepared using RF and VHF	76
		5.4.2 Stability study of μc -Si:H-based solar cells	77
		5.4.3 Conclusion and current view	80
	5.5	Conclusions	81
6	Hig	h deposition rate of device-grade μc -Si:H	83
	6.1	Introduction	83
	6.2	PEPPER project	84
	6.3	Influence of pressure and hydrogen flow	85
	6.4	Impact of the substrate morphology	89
		6.4.1 On the sharpness of the LPCVD ZnO front contacts	89
		6.4.2 Single-junction μc -Si:H solar cells	90
		6.4.3 Filtered μc -Si:H solar cells	93
		6.4.4 Conclusion	96
	6.5	Influence of the interelectrode gap	96
	6.6	RF vs. VHF with reduced interelectrode distance	98
	6.7	Modeling of gas-phase and μc -Si:H film growth mechanisms	99
			100
			101
		·	104
	6.8	• •	105
7	Intr	rinsic stress in μc -Si:H	107
-	7.1	·	107
	7.2		108
	7.3	First observations at low deposition rates	
		7.3.1 Plasma deposition conditions	

		7.3.2 Material characterization	110
		7.3.3 Solar cell performance	113
		7.3.4 Conclusion	114
	7.4	Relationship to μc -Si:H bulk defect density	114
	7.5	Intrinsic stress and μc -Si:H porosity in complete solar cells	116
	7.6	Conclusion	118
8	Silic	con oxide buffer layer at the $p ext{-}i$ interface in $\mu c ext{-Si:H}$ and $a ext{-Si:H}$ solar cells	119
	8.1	Introduction	119
	8.2	SiO_x buffer layer in single-junction μc -Si:H solar cells	120
		8.2.1 Role of the i -layer crystalline fraction	121
		8.2.2 Extremely fast and efficient single-chamber deposition process	124
		8.2.3 Gains as a function of substrate morphology for cells deposited at a high	
		rate	127
		8.2.4 Gains with improved i -layer material quality and lower ϕ_c	128
	8.3	SiO_x buffer layer in single-junction a -Si:H solar cells	132
		8.3.1 Improved a -Si:H stability	133
		8.3.2 Boron cross-contamination analysis	135
	8.4	Conclusions	136
9	Nota	able solar cell results	137
	9.1	Single-junction μc -Si:H	137
	9.2	Micromorph solar cells	139
	9.3	Triple-junction solar cells	140
10		clusion and perspectives	143
	10.1	General conclusions	143
	10.2	Perspectives	146
A	Deta	ailed solar cells performances of the comparative study of RF and VHF	149
В	On	the use of the differential pumping for high pressure plasmas	151
C	LPC	VD ZnO-based intermediate reflector for Micromorph tandem solar cells	155
Bi	bliog	raphy	168
Cı	ırricı	ulum Vitae	197
Re	mer	ciements	199

1 Introduction

1.1 General context

The explosive growth of energy consumption observed today is sustained by the strong economic and industrial expansion of developing countries along with the steadily increasing demand of highly developed countries. According to a recent report from the International Energy Agency (IEA) [IEA 12], more than 81% of the energy consumed every day comes from non-renewable sources such as fossil fuels (oil, coal and natural gas). However, the increasing exploitation of these limited resources presents risks for the environment, including pollution and greenhouse gas emissions. Although there are significant uncertainties in the known fossil fuel reserves, the supply may become exhausted in just a few generations with the current global demand.

While nuclear energy alone currently accounts for almost 6% of the world energy supply, its inherent massive threats to the environment and humankind cannot be disregarded. Long-lasting damage is associated with (i) the extraction of raw uranium ore (e.g. leaks and spills of contaminated water affecting the life in the surrounding regions), (ii) high-level radioactive hazardous wastes (e.g. long-term management, illegal dumping, accidents, etc.) and (iii) the inevitable and seemingly unending list of radioactive incidents and potential major nuclear disasters. Hence the benefits and risks posed by nuclear energy production suggest that it is not the complete answer and that sustainable alternatives have to be found and efficiently implemented to replace it.

Furthermore, the geographic concentration, as well as uneven distribution, of fossil fuels and uranium reserves poses additional problems of security of supply and energy independence for countries. As a direct consequence, land conflicts threaten peace even more and regional or international crises are inevitable in this context.

In view of these facts, the deployment of renewable energies (*e.g.* wind, solar, tidal, geothermal, etc.) has a considerable potential to ensure both a secure and sustainable development. Although considered optimistic, the current Greenpeace EU Energy [R] evolution sce-

nario [Greenpeace 12] gives an in-depth review and analysis of the actual requirements needed to phase out fossil fuels and cut CO_2 emissions. More importantly it provides clear pathways for how to accomplish the shift from our current energy system towards a global integration of renewable sources. In addition to renewable energy generation, a necessary step is the development of grid energy storage solutions and a lot of research has to be done in that direction as well, *e.g.* in batteries, hydrogen storage, flywheels, electric vehicles, compressed-air power plants, seasonal hydro pump storage, etc. This vision of global renewable energy integration is not purely fictional, but efficient incentives are required for its effective development and implementation in our current energy infrastructure.

1.2 Photovoltaic energy

Photovoltaic (PV) solar energy in particular is expected to grow dramatically in the coming years. Many institutions have developed possible growth scenarios for PV electricity generation capacity over the next decades, and these are compared in the Renewable Energy Snapshots 2012 [Jaeger-Waldau 13]. According to the IEA's latest PV technology roadmap [IEA 10], solar power could reach retail grid parity in many regions by 2020, provide around 11% (3100 GW capacity) of global electricity production by 2050 and avoid 2.3 gigatonnes of CO₂ emissions per year. Due to the rapid price drop of PV these last years, grid parity is is in fact already attained in many countries, *e.g.* Germany, Spain, Italy, Mexico, Australia, etc. Of course, such figures suppose the adoption by governments of a framework with efficient policies and sustained effort in PV research and development. The flexibility of PV technology in terms of its implementation is one of its main advantages: it can be used either in centralized large industrial power plants of several hundreds of kilowatts to gigawatts, or in distributed smaller-scale commercial and residential systems that are grid-connected or stand-alone installations.

Figure 1.1 gives an overview of the whereabouts of recent PV production and installation.

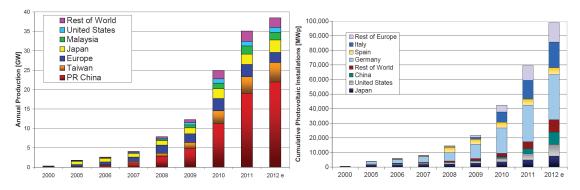


Figure 1.1: Left: World PV production from 2000 to 2012. Right: Cumulative PV installations from 2000 to 2012. (Source: EU Renewable Energy Snapshots 2012 [Jaeger-Waldau 13]).

We see that China and Taiwan now account for more than 65% of the global production, and most of these modules are installed in Europe.

Even though the PV market is currently dominated by crystalline silicon (c-Si) technologies with around 85–90% market share [IEA 10], thin-film technologies which currently account for 10–15% of the market, are an attractive alternative. Thin-film solar cells are currently based on four types of materials: silicon (Si), cadmium telluride (CdTe), copper indium gallium selenide (CIS or CIGS), and organic molecules. Although thin-film solar cells can potentially be produced at a lower cost than typical c-Si solar cells, a lot of pressure has been put on thin-film manufacturers these last 4–5 years. Aggressive development of the already mature c-Si technology has favored the further ramping up and allowed for economies of scale. Additionally, the Chinese government has offered significant indirect subsidies to domestic PV companies. As a result of this, the production costs of c-Si PV systems plummeted, the market ended up being in overcapacity and companies flooded the global market with PV modules, distorting the real production prices. This has been followed by a strong industry consolidation, so that only a few thin-film PV manufacturers remain.

However, thin-film manufacturers can still reduce production costs, increase efficiency, benefit from economies of scale, and have significant other advantages. First of all, thin-film modules can be made much lighter and more flexible than c-Si PV modules, reducing installation costs and also enabling new applications. They also perform much better under high temperatures and are more shade tolerant; hence they sustain a higher relative power output. Their relative lower efficiency is easily compensated by these advantages in a large-scale industrial PV power plant of several hundreds of kW or more, for which the space needed is less important than, e.g. on a rooftop. Last but not least, their homogenous appearance favors their integration into buildings (with possible variations in color and transparency) and overall acceptance by society which is a very important factor for widespread integration of PV. All of these features may justify the continued existence of the thin-film manufacturers who survive the current crisis.

1.3 Thin-film silicon photovoltaics

TF Si solar cell technology in particular is recognized having a tremendous potential for low-cost mass production of PV electricity worldwide in the coming years [IEA 10, Jacobson 11]. Its main advantages are the large availability and non-toxicity of the raw materials used, providing excellent scale-up capability to terawatt levels [Feltrin 08]. Another advantage lies in its compatibility with mass-production and low-temperature processes for both superstrate and low-cost flexible substrate configurations. TF Si solar cells are likely to play a major role in the upcoming years in meeting the massive demand for PV energy. However, the technology must overcome two main challenges to remain competitive: significantly improving efficiency and to further reducing production costs.

Originally based on the use of hydrogenated amorphous silicon material (a-Si:H) as sole

absorber material, TF Si solar cells have since combined a-Si:H with hydrogenated microcrystalline silicon (μc -Si:H) in tandem or triple junctions. This multi-junction approach was proven to be the key for achieving higher conversion efficiencies [Shah 04, Saito 05, Yunaz 07b, Matsui 10, Konagai 11, Yan 11]. Indeed, such configurations allow for a better use of the solar spectrum energy since μc -Si:H has a lower bandgap of 1.1 eV, compared to 1.7 eV for a-Si:H, and can thus absorb the infrared (IR) light that passes through a-Si:H. Moreover, μc -Si:H material is considered to be stable with regard to light-induced degradation (LID) unlike a-Si:H [Staebler 77]. As of yet, the micromorph tandem cell configuration [Meier 96]—based on the monolithic interconnection of an a-Si:H top cell and a μc -Si:H bottom cell—represents one of the most effective approaches for the fabrication of relatively thin (1–3 μ m) yet highly efficient TF Si solar cell devices, that are approaching for 14% stable efficiency in the short term [Meillaud 06] and possibly going over 16–18% with triple-junction. The micromorph concept is illustrated in Figure 1.2.

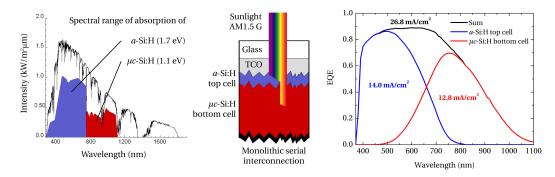


Figure 1.2: Micromorph tandem cell concept based on the monolithic interconnection of an a-Si:H top cell and μ c-Si:H bottom cell with different spectral ranges of absorption. Right: External quantum efficiency of a micromorph cell.

Based on this tandem configuration, record-low production costs of 0.5 dollars per watt-peak were announced to be within reach even at modest production volumes of around 150 MW [Oerlikon Solar 12]. Triple-junction a-Si:H/ μc -Si:H/ μc -Si:H solar cell devices further push stabilized efficiencies even further thanks to the use of a thinner a-Si:H top cell leading to reduced LID. However, in this case, much thicker μc -Si:H active layers are required to ensure sufficiently high currents in all of the subcells, significantly increasing the cost of this solution. Extensive information and references on TF Si solar cells can be found in a recently released reference book [Shah 10].

1.4 Current status of research on μc -Si:H

Intrinsic μc -Si:H growth

First developments of radio-frequency (rf) glow discharge deposition of a-Si:H layers started in the late 1960s with the experiments of Sterling and Chittick [Sterling 65, Chittick 69]. At

that time, the first tests were done simply with pure silane (SiH₄) in a quartz reaction tube surrounded by a high-impedance coil operated with a 500 W 1 MHz oscillator. Plasma-enhanced chemical vapor deposition (PECVD) and the analysis of the silicon-based material deposited has come a long way since then. While at first μc -Si:H could be prepared only by chemical transport in a low-pressure hydrogen (H₂) plasma [Veprek 68], Japanese groups later demonstrated that μc -Si:H could be obtained as well directly from SiH₄ rf glow discharges [Usui 79, Matsuda 80]. μc -Si:H is a complex mixed-phase material, consisting of small crystalline grains (typically in the range of 3–30 nm) embedded in an amorphous matrix and arranged in large conglomerates (with a typical size of hundreds of nm), together with disordered regions and voids. It was established that the microstructure of the material can be varied from a completely amorphous phase to a microcrystalline phase in the same reactor simply by adjusting the deposition conditions.

A breakthrough happened in 1994 at IMT Neuchâtel when Meier et al. showed for the first time a μc -Si:H intrinsic layer (i-layer) that could effectively be used as an absorber layer of a p-i-n solar cell with an efficiency of 4.6% [Meier 94b]. This was realized thanks to slight boron-compensation of the i-layer through micro-doping. Since then, development has been ongoing with regard to device-grade μc -Si:H for absorber layers in p-i-n or n-i-p single- and multi-junction solar cells. In particular, better control of oxygen contamination was found to be key for obtaining a high-quality μc -Si:H with improved transport properties [Torres 96].

Multiple deposition plasma techniques were developed to deposit μc -Si:H, including the layer-by-layer technique at first (which alternates a thin a-Si:H layer and a H $_2$ plasma treatment to induce crystallization). However, since then, the standard SiH $_4$ /H $_2$ dilution technique using a capacitively coupled plasma with excitation frequencies of 13.56 MHz or above remains one of the best way to obtain high-quality μc -Si:H [Rath 03].

The use of diluent gases other than hydrogen, such as argon or helium, can induce significant modifications of the plasma conditions (electron temperature, ion bombardment, powder formation) and layer properties (nucleation conditions, grain sizes); however, no significant advantage has ever been observed compared to the standard H_2 dilution for the μc -Si:H i-layer quality. The use of fluoride gases is known to be advantageous for a-Si:H [Ovshinsky 78, Bruno 09] and its alloys [Perrin 90, Cicala 98] (improved mobility, reduced defect density, denser microstructure), and can control hydrogen content of silicon films. Interesting observations were made lately showing that fluorine can, under specific deposition conditions, favor the growth of larger crystallites in μc -Si:H [Djeridane 08].

Further comprehension of the underlying physics of the deposition mechanisms remains a critical barrier to reaching higher efficiencies at higher growth rates. For example deposition of a 1- μ m-thick μ c-Si:H layer for a typical bottom cell takes one hour at 3 Å s⁻¹. Considering the cost of hardware and deposition time, fast deposition of high-quality μ c-Si:H is a key issue that remains to be solved, particularly on textured substrates that guarantee efficient light trapping.

Crystallinity and control of the microstructure of μc -Si:H

Three major models have been proposed to explain μc -Si:H growth and formation as a function of plasma species—with a particular focus on hydrogen—and deposition conditions. These models are [Matsuda 04]:

- The surface diffusion model, in which extensive hydrogen at the surface induces local heating (chemical reactions). This leads to increased diffusion of radicals on the growth surface and, thus, a larger probability for them to find energetically favorable sites. As a result, a more ordered structure is obtained.
- The selective etching model, in which incoming atomic hydrogen breaks the weak Si-Si bonds from the defective a-Si:H lattice network (a factor of 10 has been observed for the etch rate compared to μc -Si:H [van Oort 87]). Sylil (SiH₃) radical precursors can then replace weakly bound Si atoms and form stronger Si-Si bonds.
- The chemical-annealing model, in which the subsurface becomes hydrogen rich through permeation. Exothermic reactions can take place (H_2 molecule + dangling bond formed), and energy dissipated in the network induces bulk structural rearrangement, leading to a more "flexible" network, *i.e.* to conditions favorable to the formation of a μc -Si:H network.

A critical parameter of the μc -Si:H microstructure is the Raman crystallinity factor. For integration in a p-i-n single-junction or tandem solar cell, the best Raman crystallinity factor for the μc -Si:H absorber layer was observed to be around 60% [Vetterl 00]. This requirement

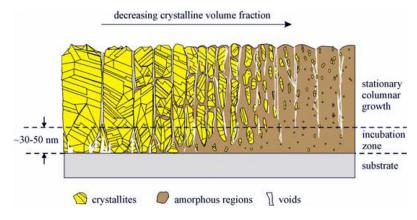


Figure 1.3: Schematic diagram of the transition from μ c-Si:H on the left to a-Si:H on the right [van den Donker 06].

also defines a limited window of operation when tuning the process parameters. A schematic diagram of the transition from amorphous to fully crystalline material is shown in Figure 1.3.

Although a Raman crystallinity factor of approximately 60% gives the "best" material for a given deposition regime, it is not sufficient to ensure that the material is device grade. For

instance, poor material quality, linked with post-deposition oxidation, has been attributed to the presence of poorly passivated crystalline surfaces by hydrogen (mono-, di- or trihydride) [Smets 08], observable by Fourier transform infrared spectroscopy (FTIR). The absence of this hydrogen FTIR signature is required for device-grade μc -Si:H, with well-passivated crystalline grain boundaries by a-Si:H, but this does not strictly ensure the highest performance in solar cells (as will be discussed in Chapter 4).

The preponderant role of the ratio of the atomic hydrogen to silicon radicals fluxes toward the growth surface, $\kappa = \Gamma_{\rm H}/\Gamma_{\rm Si}$ was recognized early as a key aspect for determining the transition from a-Si:H to μc -Si:H. The reason is that a high hydrogen dilution (*i.e.* low silane concentration $c = {\rm SiH_4/(SiH_4 + H_2)}$) was typically required to obtain a more crystalline material. Only recently, however, has κ been quantified using different methods [Klein 05, Dingemans 08, Nunomura 09]. κ can vary depending on the growth surface effective temperature and additional effects from the ion energy bombardment contribution. Lately, a simple, yet elegant, model, established a direct link between κ and the actual silane concentration in the plasma c_p [Strahm 07c, Howling 10], making the latter a determining factor in the a-Si:H/ μc -Si:H transition. As shown in Figure 1.4 μc -Si:H can be obtained within the transition region for any c, provided the silane depletion fraction D ($c_p = c(1 - D)$) is sufficiently high to reach the threshold ratio κ .

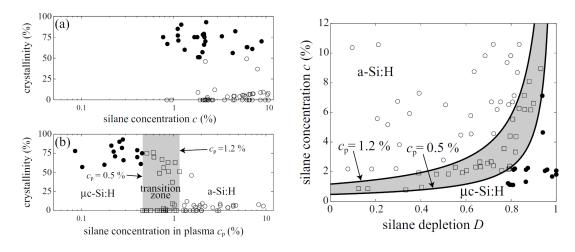


Figure 1.4: Left: Raman crystallinity factor of samples deposited with various parameters as a function of (a) the silane input concentration, and (b) the silane concentration in the plasma. Right: Plot of the transition zone (shaded) defined by iso- c_p curves, and experimental data as a function of the silane depletion fraction and the silane input concentration c [Strahm 07c] (right image was corrected for the silane depletion units, and the inverted iso- c_p values).

This threshold can be reached, for example, either through enhanced residence time (through increased pressure or lower total input flow rates), or simply by an increase of rf power density, which explains why material in the transition can also be obtained by using pure SiH₄

only [van den Donker 05]. However, this model does not take into account polysilane and powder formation, nor ion bombardment, which can affect the plasma conditions, dominate the final microstructure of the deposited material, and eventually affect the μc -Si:H material quality as we will see in this thesis.

High-pressure depletion regimes

High-pressure depletion (HPD) deposition regimes were first used by Guo et~al.~ [Guo 98] and allowed for higher growth rates of device-quality μc -Si:H. Before that, μc -Si:H was typically grown at pressures below 1 mbar. The HPD technique is thought to be favorable for high deposition rates because of the reduction of the ion bombardment energy towards the growth surface thanks to increased ion collisions in the sheath. Multiple studies have been done to analyze the best HPD conditions to increase solar cell efficiencies. Matsui et~al. [Matsui 03b] showed that higher deposition pressure results in denser grain columns along with improved IR spectral response. p-i-n solar cells with high stable efficiencies of 10.0% were be prepared [Gordijn 06a] and the cells' performances with respect to defect densities were observed [Gordijn 06b]. Also, the negative impact of plasma-induced substrate heating during high-power deposition, which can become especially important for high-deposition-rate regimes, was demonstrated [van den Donker 06].

The exact effect of ion bombardment on solar cell performance is difficult to assess because of the difficulty in measuring the ion energy in actual plasma deposition conditions. For instance, retarded field energy analyzers—typically used to analyze the distribution of ion energies—cannot operate above 1 mbar, as the ions' mean free path becomes smaller than the actual length they have to cross within the tool.

It is generally assumed that high ion energy is detrimental for the growth of the film because of the defect creation, sputtering or even amorphization of the network. However moderate energy directed toward the growth surface can also promote surface diffusion or desorption of growth species, leading to a denser material. Furthermore ion bombardment has been proven to be favorable for the nucleation as it favors the formation of a porous and hydrogen-rich material [Kalache 03], with increasing compressive stress [Fujiwara 02], which in turn allows effective nucleation. It was shown as well that moderate bias conditions led to an improved grain boundary passivation and densification of the a-Si:H tissue [Bronneberg 12a]. One has to remember that the mean ion energy on its own does not have a lot of significance, as the actual energy distribution functions of all the specific ions impinging the growth surface should be considered instead. Recently, the chemical nature of the positive ion population of SiH₄/H₂ discharges was measured by energy-filtered quadrupole mass spectrometry [Nunomura 08]. The species were measured thanks to a differentially pumped stage between the sampling orifice and the analyzer, so that the study could be performed at high deposition pressures of 0.1–10 Torr, which are relevant to the actual HPD conditions for μc -Si:H growth. Interestingly, we see in Figure 1.5b the significant contribution of higher polysilicon hydride ion groups

with increasing pressure. The peak energy of the ion distribution function is also plotted in Figure 1.5b(c). However, the orifice was located near the plasma edge (1 cm) and not directly at the substrate position where plasma conditions can be different.

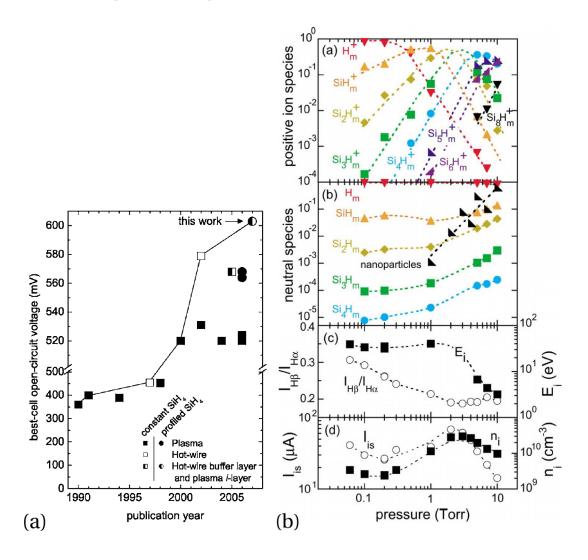


Figure 1.5: (a) Evolution of the best V_{oc} of μc -Si:H solar cells [van den Donker 07]. (b) Relative ion flux concentrations (a), relative neutral flux concentrations and nanoparticle abundance (b), plasma parameters (c), ion density (n_i) and ion saturation current I_{is} (d) as a function of pressure [Nunomura 08].

As shown in Figure 1.5a, a very high open-circuit voltage ($V_{\rm oc}$) of 603 mV was be obtained thanks to the combined use of SiH₄ flow profiling, to control the microstructure over the growth direction, with a p-i interface deposited by hot-wire chemical vapor deposition (HWCVD) [van den Donker 07]. Although the exact origins of the $V_{\rm oc}$ gains with HWCVD are not yet clear, the study highlights the crucial role of the p-i interface in the overall μc -Si:H

solar cell performance.

To conclude, dedicated plasma conditions are necessary to obtain high-quality μc -Si:H bulk material (*i.e.* well-passivated crystalline grains with few dangling bonds and a dense structure within the large conglomerates), but substrate morphology can have a crucial impact on the material density and solar cell performance as we will see.

Alternative methods of μc -Si:H deposition

Many other alternative plasma deposition methods have been evaluated for μc -Si:H growth, e.g. microwave plasmas [Soppe 03, Jia 07], inductively coupled plasmas (ICPs) [Takahashi 07], atmospheric PECVD [Kakiuchi 06, Kakiuchi 09], modified-cyclotron-resonance (ECR) plasmas [Dao 07, Kroely 10], expanding thermal (ETPs) plasmas [Bronneberg 12b], etc. However, capacitively coupled PECVD, alone or with HWCVD [van den Donker 05], has been the only one that allows the fabrication of very high-quality μc -Si:H for PV applications since then.

Other promising approaches, compatible with large-area processing, such as ladder-shaped electrode [Takeuchi 01], multi-hollow cathode [Niikura 04, Smets 08], or CCP discharges using the electrical asymmetry effect technique [Hrunski 13] are interesting and under development as well. In particular, the modified hollow cathode from Sanyo [Terakawa 13] is interesting as it provides a localized pumping along with a very high-density plasma localized at the tips of the protruding cathode. In this configuration, and depending on the process conditions, the electrodes effective surfaces seen by the plasma may be such that a strong self-bias could in fact develop on the $\it rf$ electrode, due to the apparent asymmetry, and reduce the ion bombardment on the substrate.

Development of nanoporous regions in thin-film silicon solar cells

The μc -Si:H material can also have a less dense microstructure, being considered more "porous" *within* the large conglomerates, *i.e.* what we usually refer to as the μc -Si:H bulk material. Typically this can be observed by FTIR, with a poor passivation of the crystallites, and leads to poor solar cell performances associated with post-oxidation and electrical instabilities of the μc -Si:H films over time [Matsui 03b, Finger 03, Smets 08, Bronneberg 11] (*e.g.* reduced EQE in the infrared similar to n-type contamination).

In the case of TF Si solar cell applications, μc -Si:H growth typically takes place on highly textured surfaces that provide high light-trapping potential and increased short-circuit current. However, such textures tend to promote the development of nanoporous regions (sometimes refereed to as "cracks") specifically where one growth front encounters another. This was already noticed for a-Si:H growth on rough substrates [Sakai 90, Knoesen 95] but is even worse for μc -Si:H [Nasuno 01]. The influence of the substrate's geometrical parameters on these regions in the case of μc -Si:H growth has been studied in greater detail [Python 08, Python 09, Li 09, Naruse 12]. Deposition temperature may help alleviate this problem but it remains to

be evaluated more precisely [Python 10]. The influence of the substrate morphology on the formation of these nanoporous regions can be seen in Figure 1.6.

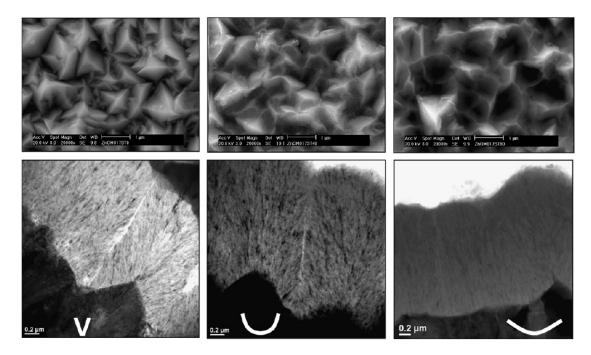


Figure 1.6: Up: SEM micrographs of ZnO surface treated with increasing time to go from a V-to U-shape morphology. Down: corresponding bright field TEM cross-section micrographs of μ c-Si:H p-i-n cell on these ZnO substrates. Taken from [Python 08] (IMT PV-Lab).

This *substrate-induced* nanoporous zone development also affects the performance stability of cells over time. It was shown to occur more easily on rougher substrates [Boccard 11], but is also very dependent on the deposition conditions [Frammelsberger 10]. The nanoporous regions act like bad diodes and generate shunting issues in the solar cells. An equivalent circuit model consisting of parallel connected diodes with different electronic quality showed that variations of the local saturation current density result in a degradation of the overall $V_{\rm oc}$ and fill factor [Grabitz 05]. Hence, the deposition requirements for homogeneously *dense* μc -Si:H remain to be understood. This would also permit the use of highly textured substrates with greater light-trapping potential in the future.

1.5 The goals and structure of this thesis

The objectives of this thesis are to

• Identify the determinant plasma deposition parameters that affect the quality of μc -Si:H material deposited in the transition zone from the a-Si:H to μc -Si:H phases using PECVD for TF Si PV applications.

- Analyze in detail both the defect density of the bulk μc -Si:H material and the formation of substrate-induced nanoporous regions during the growth and link them to solar cell performance.
- Evaluate the use of an industrial-type large-area reactor specifically for the growth of high-quality μc -Si:H.
- Increase the growth rate of μc -Si:H significantly while keeping reasonable material quality.
- Find solutions to improve the material quality and the overall TF Si solar cell performance through improved cell design.

The structure of this thesis is as follows: Chapter 2 first details the basics of TF Si solar cell fabrication and measurement, together with plasma and material characterization. However, each subsequent chapter still contains sufficient information regarding the relevant experimental details to ensure comprehension independent of the reading of previous chapters.

In Chapter 3, the roles of both the deposition pressure and silane depletion fraction on the μc -Si:H material quality are evaluated with an emphasis on very high depletion regimes. Benefits from the use of higher deposition pressure and depletion regimes are linked to a significant reduction of the bulk defect density in μc -Si:H i-layers. An amorphization process is observed and attributed to high ion bombardment conditions. A simple evaluation of the mean ion energy is proposed which underlines the importance of controlling ion energies to improve μc -Si:H quality.

Chapter 4 highlights the contribution of two different phases of μc -Si:H to the overall solar cell performance. The first phase relates to the bulk material and dominates cell performance on flat substrates. However, TF Si solar cells are typically grown on rough substrates to increase light trapping, in which case defective localized nanoporous regions appear and dominate cell performance. It is observed that material characterization alone cannot discriminate between the deposition regimes leading to this secondary phase; only the actual solar cell performance and its stability with regard to a new damp-heat test can assess the relative importance of the secondary phase. We demonstrate that the influence of these defective zones can be mitigated by suitable plasma processes and silicon oxide doped layers to reach high-efficiency, stable, TF Si solar cells.

A comparative study of the 13.56 MHz and 40.68 MHz rf plasma excitation frequencies for the growth of very high-quality μc -Si:H is presented in Chapter 5 for two interelectrode distances. Transport properties are evaluated directly within μc -Si:H single-junction solar cells by thickening the i-layer and observing the associated performance losses due to recombination in the bulk. A systematic defect density evaluation demonstrates that comparable high-quality bulk material can be obtained using both frequencies. However, the μc -Si:H material grown on rough substrates using the lower frequency is more dense and leads to better performance

overall. Still, the use of the higher frequency is shown to be beneficial for increased deposition rate, limiting the power density requirements compared to 13.56 MHz and resulting in reduced ion bombardment and improved bulk material quality.

After these detailed investigations into the material properties of μc -Si:H deposited with the most favorable conditions, we study in Chapter 6 the very high-rate deposition of μc -Si:H solar cells. It is shown that high depletion regimes with significantly reduced H₂ flow or increased pressure are associated with significantly more secondary gas-phase reactions and powder formation. The crucial interplay between μc -Si:H growth rate and substrate morphology with regard to the formation of nanoporous regions is then further discussed. The use of a reduced interelectrode distance is shown to allow for the growth of μc -Si:H material with improved bulk material quality at higher rates. Results from a collaboration with the University of Patras to perform plasma simulations of known conditions are then presented and discussed.

In Chapter 7, intrinsic compressive stress within μc -Si:H i-layers is studied. Low-stress μc -Si:H material seems to correspond to improved solar cell performance. Further experiments demonstrate a clear correlation of intrinsic stress with the bulk defect density of μc -Si:H i-layers, both being symptomatic of a change in the ion bombardment energy conditions during deposition. It was however not possible to correlate intrinsic stress of the i-layer with the disappearance of nanoporous regions once the μc -Si:H material is integrated in actual solar cells, on rough substrates.

The use of a novel intrinsic silicon oxide buffer layer at the p-i interface of TF Si solar cells is presented in Chapter 8. Significant improvements are observed for both μc -Si:H and a-Si:H solar cells. For μc -Si:H solar cells, all electrical parameters are improved unless the i-layer is significantly amorphous-rich and of improved quality, in which case only an improvement in carrier collection in the blue region is observed. Still, μc -Si:H i-layer nucleation is favored on top of such a buffer layer. In a-Si:H solar cells, the silicon oxide buffer layer acts as an efficient barrier to boron cross-contamination, eliminating the need for additional time-consuming processing steps such as water flush.

The last chapter briefly summarizes the best TF Si solar cell efficiencies obtained in the laboratory as a result of the μc -Si:H development presented in this thesis. Results include single-junction and multi-junction cells in both the p-i-n and n-i-p configurations.

The general conclusions of this thesis are then drawn and perspectives are discussed. The use of differential pumping for high-pressure regimes is discussed in Appendix B while detailed solar cell results from Section 5.2.1 are presented in Appendix A.

1.6 Contribution of this thesis to the research field

This thesis contributes many different results—given below—to the field of TF Si solar cells.

- The specific roles of the silane depletion fraction and deposition pressure for depositing high-quality μc -Si:H were examined. A simple mean ion bombardment energy model shows that increased pressure is favorable for better-performing solar cells.
- The contribution of two distinct μc -Si:H material phases on solar cell performance on textured substrates was demonstrated. Assessing the material quality only by evaluating the bulk phase is not sufficient. The formation of a secondary phase, which consists of nanoporous regions, was shown to be highly sensitive to the deposition conditions and substrate geometry, especially at high deposition rates. The porosity of the material was demonstrated through new damp-heat experiments done directly on solar cells deposited on rough substrates.
- The use of silicon oxide doped layers was shown to mitigate the negative impact that the nanoporous regions have on the overall cell performance, while the implementation of an undoped silicon oxide layer at the p-i interface results in superior performances for both a-Si:H and μc -Si:H solar cells. An enhanced anti-reflective effect and improved nucleation conditions of the μc -Si:H i-layer were observed. For a-Si:H, stabilized efficiency is improved and the buffer layer also effectively reduces boron cross-contamination in a single-chamber process.
- The use of a lower plasma excitation frequency for the growth of high-quality μc -Si:H was demonstrated to lead to a denser material and better-performing solar cells. Still, above a certain growth rate, the use of higher excitation frequencies becomes favorable again, as the bulk phase quality dominates cell performance.
- Plasma conditions at the onset of powder formation (reached by either by increasing the pressure or reducing the H_2 flow) during growth of the i-layer were shown to lead to better-performing solar cells at a higher growth rate thanks to denser μc -Si:H material.
- A reduction of the interelectrode gap distance was shown to be very beneficial for the bulk material quality of μc -Si:H deposited at high rates, and is associated with improved solar cell performance.
- A correlation between reduced intrinsic stress of μc -Si:H material, improved bulk material quality, and solar cell performance was highlighted.

Based on all of these developments, significant progress has been made in the understanding and the fabrication of TF Si solar cells based on μc -Si:H material. Furthermore, an outstanding single-junction μc -Si:H solar cell efficiency of 10.9% was attained, the highest reported in the literature according to our knowledge. Several articles were published in peer-reviewed journals as a first-author [Bugnon 09, Bugnon 10, Bugnon 11a, Bugnon 12, Bugnon 13]. A dedicated study on LPCVD ZnO-based intermediate reflector in micromorph tandem solar cells was also published [Bugnon 11b], and is simply reported in the Appendix C. As part of this ongoing effort, three patents were filled.

2 Experimental details

This chapter details the main experimental methods used thorough this thesis work. First, Section 2.1 gives some insights into solar cell realization and details the deposition reactors. Section 2.2 describes some of the tools used to analyze the plasma conditions and Section 2.3 presents the techniques used to characterize the solar cells and the deposited material.

2.1 Solar cell preparation overview

The preparation of a TF Si solar cell involves the deposition of many different layers which will be detailed in this section. All the cells presented in this thesis are in the superstrate configuration, also called p-i-n configuration, as the p-layer is deposited first on glass covered with front electrode. This means that the glass, used as a supporting structure during the manufacturing of all the layers, will eventually be facing upward and act as a window layer to couple sunlight into the solar cell device behind it. A scanning electron microscopy (SEM) image of such a ssuperstrate configuration is shown for a micromorph tandem cell in Figure 2.1.

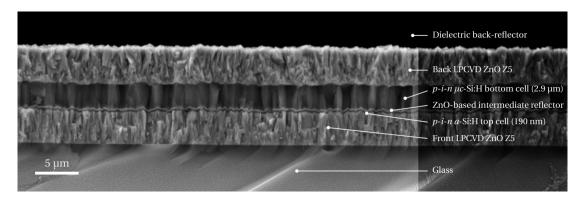
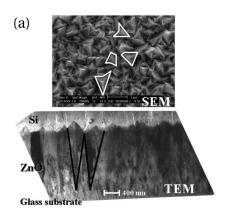


Figure 2.1: Cross section SEM image of a thick micromorph tandem cell incorporating a ZnO-based intermediate reflector, where all the main layers are indicated. The solar cell and SEM imaging were done by Dr. Didier Dominé (IMT-PV-Lab).

Single-junction and multi-junction p-i-n are typically prepared according to the following sequences: first, a 0.5 mm-thick alumino-borosilicate glass (Schott AF45) is cleaned. It is then coated with a transparent conductive oxide (TCO) layer that will act as front contact. At IMT, we typically use zinc-oxide (ZnO) obtained by low-pressure chemical vapor deposition (LPCVD). Next, the single-junction or multi-junction p-i-n cell is deposited on top of it using a PECVD reactor (in the case of tandem or triple junction, the p-i-n subcells are simply stacked on top of each other). After that, the cells are patterned to 0.25 cm 2 or 1.0 cm 2 before being covered by a LPCVD ZnO layer again, which will be used as the back electrode. Structuration of cells may also be made by use of laser scribing (P3 step) with the removal of silicon and back TCO around the cell. Single-junction μc -Si:H solar cells are typically patterned to a 0.25 cm 2 , so that 16 cells can be obtained on a 4 × 4 cm 2 substrate. For multi-junction solar cells, they are patterned to 1.0 cm 2 leading to 6 cells per substrate.

LPCVD ZnO:B contact layers

As just mentioned, both the front- and back-contact typically consist in LPCVD ZnO thinfilms. Under our deposition conditions, ZnO layers naturally evolve as randomly distributed pyramidal-shaped structures as shown in Figure 2.2a [Fa \ddot{y} 10, Nicolay 09]. Such textured surfaces are important in the case of TF Si solar cells, as they induce an efficient light scattering within the solar cell (see Figure 2.2b), increasing light absorption and photo-generated current. ZnO layers also need to be highly transparent and sufficiently conductive: for this purpose diborane (B₂H₆) is used as a dopant gas, while diethylzinc (DEZ) and water vapor are used as precursors gas. The doping can then be controlled by adjusting the B₂H₆/DEZ ratio.



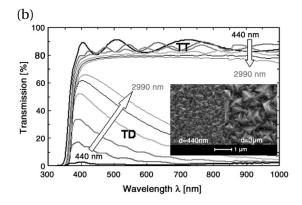


Figure 2.2: (a) SEM (top) and TEM (bottom) micrographs of a $2 \, \mu m$ -thick LPCVD ZnO:B layer. (b) Total (TT) and diffuse (TD) transmittance of LPCVD ZnO with various thicknesses. The inset picture consists of two micrographs of a thin (440 nm) and a thick (3 μm) ZnO layers. Taken from [Fa \ddot{y} 10] (IMT PV-Lab).

For μc -Si:H single-junction solar cells, we typically use a lowly doped 4.5- μ m-thick (Z5) ZnO front-contact layer with large pyramids. These large structures can then be smoothed through the use of an argon-based plasma [Bailat 06, Boccard 12a] and referred to as Z5 followed by the Ar treatment time (in minutes). A Z5 treated for 45 minutes, which is our standard for the development of μc -Si:H solar cells, will then simply be referred to as a Z5 45'. Please note that the original plasma treatment was transferred to a new plasma etching system during this study. Unless specified, the treatment was then always done in the new (Oxford) system with a slightly faster process than in the previous (IPL) system. As a result the Z5 60' done in IPL is equivalent to the standard Z5 45' done in the Oxford. In some cases we also completely flattened the surface of our reference substrate, through a mechanical polishing step (Z5 P) [Cuony 11]. Thinner ZnO layers of 1.5 μ m (Z1) and 2 μ m (Z2) with a higher doping concentration, along with Asahi U, were used as front electrodes as well. Table 2.1 summarizes important morphology and electrical parameters of the ZnO layers used in this thesis.

Table 2.1: Details of the ZnO substrates used for the present study and the main parameters describing their surface morphology.

Substrate	Z1	Z2	Z5/2	Z5	Z5 20'	Z5 45'
Thickness (µm)	1.3	2.0	2.4	5.0	< 5.0	< 5.0
$\sigma_{\rm RMS}$ (nm)	49	79	100	184	168	106
Pyramid size (nm)	160	250	270	600	600	600
Average facet inclination (°)	30	40	-	45	-	18
Ironed surface (μm²)	142	155	138	167	137	115
Haze at 600 nm	12	37	55	96	87	68
Sheet Resistance ($\Omega \square^{-1}$)	18	9	9	25	-	-
Mobility (cm 2 V $^{-1}$ s $^{-1}$)	24	37	41	48	-	-
Electron density ($10^{19} \mathrm{cm}^{-3}$)	9.2	9.2	3.5	3.5	-	-
Resistivity ($10^{-3} \Omega \text{ cm}$)	2.8	1.8	3.7	4.4	-	-

Silicon layers deposition

In superstrate configuration, the p-layer is the first silicon layer deposited on the front contact. It has to ensure a good ohmic contact with the front ZnO layer and induce a high built-in voltage in the device. The p-layer is then followed by the deposition of the i- and n-layers. All silicon layers were prepared in large-area PECVD systems, called KAI reactors, composed of a PlasmaBox installed within a large vacuum chamber (see simple schematic in Figure 2.3). The PlasmaBox chambers were developed by Unaxis Displays (which became part of Oerlikon Solar and now TEL Solar), and are smaller versions of the large area industrial KAI[™]systems [Schmitt 89, Bubenzer 90, Perrin 00].

These plasma chambers consist of a closed aluminum plasma reactor with a showerhead electrode at 24.5 mm from the grounded bottom electrode. This configuration offers the possibility of a directed pumping from one of the plasma reactor's wall, which allows rapid plasma equilibration time [Howling 07] and uniform deposition [Sansonnens 00]. The presence of a differential pumping between the outer chamber and the PlasmaBox limits cross contamination in the deposition chamber during the process. We will see however that this differential pumping can lead to some issues when working at high deposition pressures (cf. discussions in Appendix B). Isothermal heating is obtained in the deposition chamber thanks to a resistive heating wire placed on both sides of the reactor.

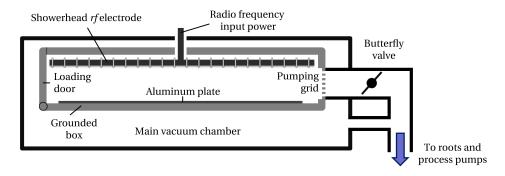


Figure 2.3: Lateral view of a KAI PlasmaBox installed in a large vacuum deposition chamber with a basic differential pumping implementation.

Radio-frequency power is supplied either via a 13.56 MHz (RF) or a 40.68 MHz (VHF) generator, feeding the power through an automatic matching-box, directly connected to the center of the cathode. Such industrial-type PECVD chamber is very close to a symmetric system, and the measured self-bias voltage $V_{\rm dc}$ is usually smaller compared to to a typical laboratory system. The peak-to-peak voltage $V_{\rm pp}$ is also routinely measured in the KAI-S with a calibrated high impedance capacitive gauge on the cathode.

Two KAI reactors were used for all the experiments presented in this thesis: a single-PlasmaBox chamber KAI-S system and a dual-PlasmaBox chamber KAI-M reactor, with electrode areas of $46 \times 56 \text{ cm}^2$ and $49 \times 60 \text{ cm}^2$, respectively. The dual-PlasmaBox reactor is composed of two chambers connected through a vacuum transfer chamber. The main advantage such dual chamber system is the possibility to have a dedicated intrinsic chamber, hence limiting the risks of dopant cross-contamination.

All μc -Si:H depositions performed in the KAI-S or the KAI-M were done at a temperature T=180 °C unless stated otherwise. The a-Si:H layers and corresponding p-i-n solar cells, employed as top cell in micromorphs, were deposited in the KAI-S system, with a T set at 200 °C. Mixtures of SiH₄ and H₂ were used to prepare intrinsic silicon layers, while carbon dioxide (CO₂) was added to obtain SiO_x layers. Trimethylboron (TMB) and phosphine (PH₃) gases were used for p-type and n-type doping, respectively. After each cell deposition the

systems were systematically cleaned by plasma using either SF₆+O₂, or later on, NF₃+Ar mixtures.

2.2 Plasma conditions analysis

Average residence time

In order to correlate plasma conditions and material quality or solar cell performances, typical plasma parameters such as gas residence time and silane depletion had to be monitored as described in this section. The residence time τ , defined as the average amount of time that a particle spends the system, is evaluated here for a PlasmaBox chamber that we consider perfectly tight and leak-free as a first approximation. This closed-reactor configuration allows very rapid equilibration times compared to a typical laboratory open reactor [van den Donker 06, Howling 07]. The calculation assumes steady-state conditions, a single source gas with an input volumetric flow rate Q—as defined under standard conditions for temperature and pressure (STP)—with constant gas density n and pressure p in the entire reactor volume V. It follows that

 $\tau = \frac{\text{Number of gas molecules in the reactor volume}}{\text{Source gas input rate}}$

$$= \frac{N \text{ [part.]}}{S \text{ [part. s}^{-1]}} = \frac{V \text{ [m}^3]}{S \text{ [part. s}^{-1]}} \times n \text{ [part. m}^{-3}]$$

which, assuming STP conditions for the volumetric flow rate Q, leads to

$$\tau = \left(\frac{V \text{ [m^3]}}{Q \text{ [m^3 s^{-1}]}} \times \frac{T_{273\text{K}}}{p_{\text{atm.}}} \times k_B\right) \times \frac{p}{k_B T}$$

$$= \left(\frac{V \text{ [cm}^3]}{Q \text{ [cm}^3 \text{ min}^{-1}]/60} \times \frac{273.15}{1013.25}\right) \times \frac{p \text{ [mbar]}}{T \text{ [K]}}$$

with Φ [sccm] $\equiv Q$ [cm³ min⁻¹], so that we get the residence time value simply through

$$\tau = 16.2 \times \frac{V \text{ [cm}^3] p \text{ [mbar]}}{\Phi \text{ [sccm]} T \text{ [K]}}.$$
(2.1)

Silane depletion fraction

The silane depletion fraction *D*, defined as a measure of the reduction of silane partial pressure due to dissociation by the plasma, was measured in the exhaust line of the KAI-M reactor thanks to a tunable quantum cascade laser (QCL)-based absorption spectrometer. The setup was developed and installed on our KAI-M system by Dr. Richard Bartlome. More details of this installation can be found in [Bartlome 09]. This IR laser-based diagnostic technique is non-

intrusive and very sensitive. Its very high resolution permits to resolve Doppler-broadened rotovibrational absorption lines of silane in a single-pass in the evacuation line of the PECVD system with excellent signal-to-noise ratio. Figure 2.4 presents a simple sketch of the setup used for this measurement, as published in [Bartlome 09].

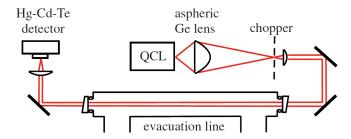


Figure 2.4: Optical setup of the quantum cascade laser based IR spectrometer for silane depletion measurement in the exhaust line of the KAI-M reactor [Bartlome 09].

The Peltier-cooled IR QCL used for that purpose emits around 4.6 μ m. Then, by varying the current supplied to the QCL, the wavenumber can be tuned between 2241 and 2245 cm⁻¹. This range allows for a clean observation of the intense roto-vibrational absorption lines of the v_3 band of SiH₄, as it is free from any other absorbing species signature. The beam is first collimated by a set of two lenses and chopped at a frequency of 1 kHz before entering the 3.7 m evacuation line of the reactor. The QCL beam at the exit is then focused on a thermoelectric-cooled Hg–Cd–Te photovoltaic detector and a lock-in amplifier is used to detect and measure the signal.

Examples of silane absorption spectra acquired by this setup are shown in Figure 2.5. Silane depletion fraction can then for example be obtained by comparing the peak center at 2243.827 cm⁻¹ under steady-state conditions before and after ignition of the plasma. The time resolution is also very good, being lower than 40 ms, allowing the acquisition of very fast transient phenomena. When the setup was not available, the silane depletion fraction was simply derived from the actual growth rate (method described in Chapter 3). When this technique is used instead, it will be specified in the text.

Powder detection technique

Under particular conditions, powder formation can occur in silane-based plasmas [Dorier 92, Takai 00]. A powder detection system was also developed by Dr. Richard Bartlome on the same deposition system. Only the basics are presented here, more being available in his review of laser-based applications for thin-film photovoltaics [Bartlome 10]. The technique relies on laser light scattering (LLS) of the particles detected in the exhaust line, just behind the pumping grid, thanks to a vacuum cross-piece.

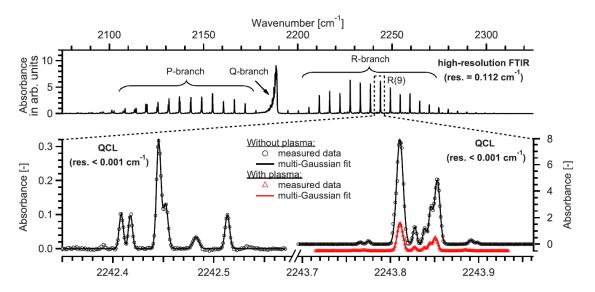


Figure 2.5: The v_3 band of SiH₄ acquired by a high-resolution FTIR (upper part of the figure), the Doppler-resolved R(9) multiplet of SiH₄ acquired by the QCL before and after igniting the plasma in the high-deposition-rate regime (right hand side of the inset), and weak unassigned absorption lines of SiH₄ that only appear in the spectrum acquired by the QCL (left hand side of the inset). For illustrative purposes, the spectrum of SiH₄ acquired after igniting the plasma is slightly shifted in the vertical axis. Figure and caption are taken from [Bartlome 09].

The light source consists in a low-cost high-power (500 mW) compact Nd:YAG laser emitting at 532 nm. The beam is directed towards the center of the vacuum cross-piece, where it can interact with large particles that scatter the light. A fast silicon-based photodetector then retrieves the scattered light after it passed through a polarizer and an interference filter to remove parasitic light emission. The time resolution is below 40 ms and the detectable particle size estimated at around 50 nm. A simple schematic of the LLS setup is shown in Figure 2.6.

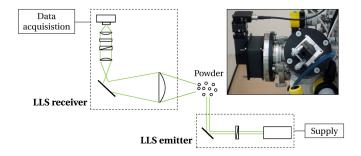


Figure 2.6: Principle of the LLS measurement done at the exhaust of the PlasmaBox, just behind the pumping grid.

Optical emission spectroscopy

Optical emission spectroscopy (OES) is a powerful, non-intrusive, diagnostic tool that permits to retrieve important information about the plasma chemistry, as described in [Fantz 98, Howling 07]. An Ocean Optics 2000+ OES on the viewport located on the side of the reactor, was used in our work.

The set-up was used to integrate emission intensities from the H_2 Fulcher (600–630 nm) and G_0B_0 (461–464 nm) were integrated. Both originate from electron-impact excitation of the H_2 ground state but with a different emission rate coefficient as a function of the electron temperature T_e (the ratio H_α/H_β originating from atomic hydrogen was also used sometimes for the same purpose). Hence the ratio $I_{G_0B_0}/I_{Ful}$ allows to check T_e variation over time, and in particular from ignition to steady-state equilibrium. SiH* emission (409–423 nm), originating from electron impact SiH₄ excitation, along with proper H_2^* background subtraction (obtained using similar plasma conditions with pure H_2), was used to get silane density information in the plasma [Strahm 09].

The set-up also permitted to confirm powder formation through the use of time-resolved OES by observing the integrated intensity of H_2 Fulcher lines, as this latter is proportional to the plasma electron density [Strahm 09]. The oscillations observed on this quantity represent the cycle of particle growth and ejection out of the plasma region, see Section 6.3.

2.3 Solar cell measurement and material characterization

Solar cell current-voltage and external quantum efficiency measurements

After structuration to 0.25 cm^2 or 1 cm^2 areas, solar cell performances are evaluated by means of current-voltage (I-V) and external quantum efficiency (EQE) to calculate their conversion efficiency.

The I-V characteristics of the solar cells are obtained with a class AAA dual lamp Wacom solar simulator (WXS-220S-L2) in standard test conditions (25 °C, AM1.5 global reference spectrum, 100 mW cm $^{-2}$). The open-circuit voltage ($V_{\rm oc}$) and fill factor (FF) are derived from a four probe voltage sweep measurement using a Keithley sourcemeter. The short-circuit current density ($J_{\rm sc}$) of the cells are based on EQE measurement. A typical I-V is shown in Figure 2.7.

EQE measures the probability an incident photon of a given energy can generate an electronpair that will eventually contribute to the external current density of the solar cell. J_{sc} is then obtained by the convolution of the EQE with the incoming photon flux of the AM1.5 global reference spectrum. For single-junction, the application of a reverse dc bias voltage (typically -1 or -2 V) during the EQE measurement, super-imposes an electric field, easing the collection of the generated carriers. This helps identifying any issues regarding to the electric field in the absorber layer. For multi-junction solar cells we use additional bias lights to saturate

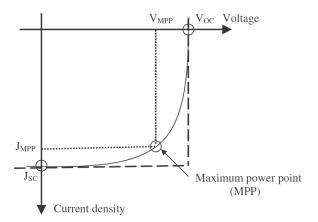


Figure 2.7: Typical I-V curve of a μ c-Si:H solar cell under illumination. The open-circuit voltage $(V_{\rm oc})$ and the short-circuit current density $(J_{\rm sc})$ are indicated, as well as the maximum power point corresponding to the maximum current density J_{MPP} and maximum voltage V_{MPP} .

the subcells not to be measured, so that—all the subcells being interconnected in series—the measured current always corresponds to the most limiting subcell [Burdick 86]. An appropriate choice of the bias-lights spectra and intensities is thus very important. Voltage biasing can also be applied during multi-junction solar cell EQE measurement to put the subcell closer to the short-circuit conditions (*i.e.* to compensate for the voltage generated by the other biased subcells) [Meusel 03]. A white dielectric back-reflector is simply pressed against the back-contact of cell during the measurement. Also the beam size of the monochromatic light is small $(1 \times 2 \text{ mm}^2)$ compared to the solar cell.

Raman spectroscopy

Raman spectroscopy is a very fast and non-destructive spectroscopic technique used to probe the μc -Si:H crystallinity. It relies on the inelastic scattering of a monochromatic light with the silicon medium, inducing a shift in the photon energy which is characteristic of the phase probed. A Renishaw, System 2000 Raman spectrometer was used to measure the Raman crystallinity factor (ϕ_c) of the μc -Si:H layers, assuming the Raman scattering cross-section of c-Si over a-Si was unity [Droz 04]. The evaluation of ϕ_c was then simply obtained through the formula

$$\phi_{\rm c} = \frac{I_{510} + I_{520}}{I_{480} + I_{510} + I_{520}},\tag{2.2}$$

where I_x is the integrated intensity obtained with a Gaussian fit centered at x cm⁻¹. All the spectra were measured in the backscattering geometry using the 514.5 nm emission line of an argon ion laser. The characteristic Raman collection depths in a-Si:H and μc -Si:H at this wavelength are around 50 nm and 150 nm respectively. Measurements were done directly

on the solar cells through the glass/front ZnO stack for p-side values and through the back contact for n-side values.

FTIR and FTPS

Fourier transform infrared spectroscopy (FTIR) is a non-destructive technique to provide chemical bonding information via absorption spectra. The method is typically used for a-Si:H to evaluate the microstructure factor that relates the density of micro-voids in the material. For μc -Si:H, the method is interesting to observe the crystalline grain boundaries, which can be well passivated by a-Si:H tissue, or poorly passivated by hydrogen, or even observe post-deposition oxidation issues [Smets 08, Bronneberg 11].

Fourier-transform photocurrent spectroscopy (FTPS) is a method to measure the Urbach slope (which is a measure of bandtails disorder) and the defect-related absorption of silicon materials. The technique was first demonstrated directly on μc -Si:H solar cells by [Vanecek 02]. A simple schematic of the FTPS setup is shown in Figure 2.8.

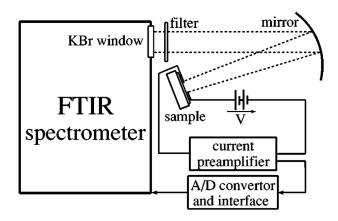


Figure 2.8: FTPS experimental setup (taken from [Vanecek 02]).

The absorption coefficient of low-energy (sub-bandgap) photons gives important information on the electronic quality of the material. The value of the optical absorption coefficient at photon energy of 0.8 eV is assumed to scale with the density of the μc -Si:H i-layers. FTPS was performed directly on our single-junction μc -Si:H p-i-n solar cells. The measurement being very sensitive to the type of ZnO used (variations of light diffusion and level of doping) a careful attention was given to make sure every cell was prepared using the same type of back- and front-contacts. The method being relative, calibration of the absorption curves was performed at 1.35 eV at the corresponding absorption coefficient of crystalline silicon of 235 cm $^{-1}$. Both FTIR and FTPS were done using a Nicolet 8700 spectrometer.

Influence of the deposition pressure and silane depletion on μc -Si:H quality and solar cell performance

The growth of μc -Si:H by PECVD is investigated in an industrial-type parallel plate R&D KAI reactor to study the influence of pressure and silane depletion on material quality using VHF (40.68 MHz) and an interelectrode distance of 22 mm. Single-junction solar cells with intrinsic layers prepared at high pressures and in high silane depletion conditions exhibit improvemed performances, reaching 8.2% efficiency. Further analyzes show that better cell performance are linked to a significant reduction of the bulk defect density in intrinsic layers. These results can be partly attributed to lower ion bombardment energies due to higher pressures and silane depletion conditions, improving the microcrystalline material quality. Layer amorphization with increasing power density is observed at low pressure and in low silane depletion conditions. A simple model for the average ion energy shows that ion energy estimates are consistent with the amorphization process observed experimentally. Finally, the material quality produced in a novel regime for higher rate deposition is reviewed on the basis of these findings.

3.1 Introduction

A wide range of parameters influences the deposition conditions and hence the material quality of μc -Si:H. This includes hardware parameters such as electrode geometry [Niikura 04, Kunii 08, Noda 03], interelectrode distance [Amanatides 02, Nakano 06, Rech 06] and operating frequency [Howling 92, Schwarzenbach 96, Sansonnens 98]; it also includes process parameters, which are easily adjustable for a given reactor, such as power density, pressure, substrate temperature and input gas flows [Strahm 07b, Niikura 07, Hamers 00, Kondo 00, Kalache 03].

Substrate morphology and chemistry has been shown to be important as well [Nasuno 01, Bailat 02, Vallat-Sauvain 05, Python 08]. Thus, much of the research effort is directed towards the understanding of how these externally adjustable parameters affect the internal physical plasma characteristics upon which the material quality of μc -Si:H ultimately depends.

Chapter 3. Influence of the deposition pressure and silane depletion on μc -Si:H quality and solar cell performance

In Section 3.2 we present different pressure and silane depletion conditions for the deposition of the μc -Si:H i-layer of single-junction solar cells. We show that by increasing the pressure and modifying the hydrogen flow rate ($\Phi_{\rm H_2}$), the μc -Si:H solar cell performance can be greatly improved. Section 3.3 presents structural material characterization of deposited μc -Si:H layers, showing that these improvements in cell performance are related to a reduction of the bulk material defect density, as evaluated by Fourier-transform photocurrent spectroscopy (FTPS). Furthermore, amorphization of the μc -Si:H is also revealed under low-pressure deposition conditions. In Section 3.4 an interpretation in terms of ion bombardment energy is proposed and supported by a simple model. Based on these findings, the material quality deposited in a novel regime for high-rate μc -Si:H deposition proposed in a recent publication [Strahm 07b] is reviewed.

3.2 Study of μc -Si:H deposition conditions in a CCP-VHF discharge

In this chapter, very high frequency (40.68 MHz) PECVD (VHF-PECVD) is used in a R&D industrial-type KAI-S reactor. Details the reactor can be found in Section 2.1. The shower-head electrode is suspended at 24.5 mm from the grounded electrode and the 0.5 mm-thick substrates are loaded on top of a 2 mm-thick aluminum plate on the bottom of the reactor. VHF power is supplied via a 40.68 MHz generator, feeding the power through an automatic matching-box connected directly to the center of the cathode. The dc self-bias voltage $V_{\rm dc}$ is measured along with the peak-to-peak voltage $V_{\rm pp}$ with a calibrated high-impedance capacitive gauge on the cathode. Isothermal heating is obtained in the deposition chamber and the temperature T is fixed at 180 °C for all depositions in this study.

Standard p-i-n solar cells were prepared to evaluate the different μc -Si:H layers. Standard μc -Si:H p- and n- layers were used. The front contact was a Z5 textured ZnO thin film, grown on a Schott AF 45 glass substrate, obtained through a modified LPCVD process further treated by a 60' argon-based plasma in IPL (more details in Section 2.1). Solar cells were deposited in a single-chamber process KAI-S reactor, with an i-layer layer approximately 1.2 μ m thick. The patterned cells were 0.25 cm² each, and the back contact was a ZnO thin film grown using LPCVD as well, covered with a white dielectric reflector.

A Raman spectrometer was used to measure the Raman crystallinity factor (ϕ_c) of the μc -Si:H layers using the 514.5 nm emission line of an argon ion laser (cf. Section 2.3 for more details).

3.2.1 Influence of the deposition pressure

The first parameter we studied in the deposition of μc -Si:H material was the pressure p: layers were deposited at 1.2, 2.5 and 3.5 mbar. The rf source power was kept approximately constant across the three deposition regimes and the silane concentration c was below 5% in the three cases. c is defined here in terms of the input flow rates as $c = \Phi_{\text{SiH}_4}/(\Phi_{\text{SiH}_4} + \Phi_{\text{H}_2})$, where Φ_{X} is the input flow rate of gas X in sccm. In each deposition regime c was adjusted in order to have

a Raman crystallinity factor ϕ_c of 50%–60% for the *i*-layer.

In order to clearly separate the effect of pressure and silane depletion, the three deposition regimes had similar depletion conditions. It has been argued that the relevant parameter for the growth of μc -Si:H is the actual silane concentration in the plasma $c_{\rm p}$, which is directly related to the ratio of atomic hydrogen over silicon radicals fluxes to the growing film surface, and not only the silane input concentration [Strahm 07b]. The parameter $c_{\rm p}$ can be estimated with knowledge of the input silane concentration c and silane depletion c:

$$c_{\rm p} = c(1 - D).$$
 (3.1)

While c is readily available, D—which is a function of the plasma dissociation rate and gas residence time—has to be estimated experimentally. As detailed in [Strahm 07b], assuming uniform deposition and no loss of silicon atoms through polysilanes or powder formation, one can simply evaluate D by comparing the actual deposition rate R to the maximum possible deposition rate R_{max} (corresponding to D=1) obtained for a given silane input flow and reactor size through the formula [Strahm 07b]:

$$\frac{R}{R_{\text{max}}} = \frac{D}{1 + c(1 - D)},\tag{3.2}$$

with R_{max} defined as

$$R_{\text{max}} = 0.0962 \times \frac{\Phi_{\text{SiH}_4}}{A} [\text{Å.s}^{-1}],$$
 (3.3)

where A is the total deposition area in the PECVD reactor in m^2 . Inserting the values for the three deposition regimes in Equation 3.3, silane depletion fractions of around $45 \pm 10\%$ are obtained. This is an indication that the silane depletion is low and approximately the same in the three μc -Si:H deposition regimes. We stress that for the three deposition regimes at low silane depletion, the plasma potential measured with the voltage probe is the same within a 10% error margin. Consequently, our experiment investigates only the the effect of ion energy reduction, or a plasma chemistry change, due to pressure.

This model is valid provided the plasma conditions are homogeneous and radical gas-phase reactions can be neglected [Strahm 07b]. We verified in all deposition conditions the spatial homogeneity of ϕ_c and R of the the μc -Si:H layers. A homogeneity better than $\pm 10\%$ was found in all process regimes. The only exception was the high depletion deposition regime at 2.0 mbar (discussed in Section 3.2.2), where deviations were observed at the borders of the deposition surface. For this reason high depletion regimes at pressures higher than 2.0 mbar were not included in this study. Polysilane and powder formation cannot be ruled out, especially in the highest pressure and silane depletion conditions. However, because of the good spatial homogeneity, they should be limited. In addition, as can be verified by a simple one-dimensional plasma model [Sansonnens 00], uniform deposition using this gas flow configuration can be achieved provided the pressure drop $\Delta p/p$ across the reactor

Chapter 3. Influence of the deposition pressure and silane depletion on μc -Si:H quality and solar cell performance

remains small, which is verified for areas smaller than 0.5 m^2 , even with pumping done along a single side. The reactor size in this study was 0.26 m^2 .

Table 3.1 details the deposition conditions of the intrinsic layer of solar cells that were deposited with the three regimes described in the previous paragraph.

Table 3.1: Summary of the deposition conditions for the i-layers in this section using a relatively high Φ_{H_2} . Both the rf voltage V_{rf} , deduced from V_{pp} measurement, and the self-bias V_{dc} are indicated.

p (mbar)	Φ _{SiH4} (sccm)	Φ _{H2} (sccm)	c (%)	R (Å s ⁻¹)	R/R _{max}	D	P_d (W cm ⁻²	V _{rf} (V)	V _{dc} (V)
1.2	49	1250	3.8	2.9	0.34	0.35	0.13	280	8
2.5	64	1140	5.3	5.2	0.50	0.51	0.15	260	5
3.5	41	1566	2.6	3.2	0.47	0.47	0.17	290	6

The I-V curves from the best cells obtained in the three regimes are shown in Figure 3.1. Major improvements are observed for the cells prepared at higher pressure: V_{oc} , FF and

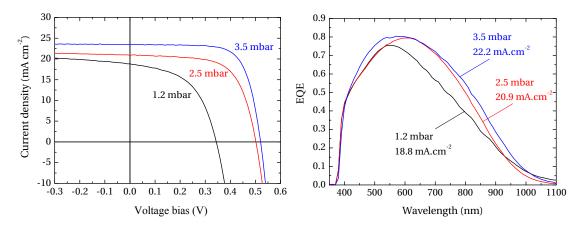


Figure 3.1: I-V curves (left) and external quantum efficiencies (right) of μ c-Si:H p-i-n cells prepared at 1.2, 2.5 and 3.5 mbar.

 $J_{\rm sc}$ all increase significantly with pressure, ranging from 0.34 to 0.52 V, 52 to 72% and from 18.8 to 22.2 mA cm⁻², respectively. It is worth noting here that only the i-layer deposition conditions were changed in order to minimize the differences in the cells not strictly linked to the absorber layer. For this reason an identical intrinsic μc -Si:H buffer layer at the p-i interface about 100 nm thick was used systematically in all deposition regimes to avoid the influence of the deposition pressure on the underlying p-layer and subsequent p-i interface modification.

Another interesting feature of higher i-layer deposition pressure is the significant improve-

ment of the spectral response in the red and infrared spectral region as shown in Figure 3.1. Considering that the crystalline volume fractions of the intrinsic layers are very similar, the changes could be attributed to modifications in the microstructure. Indeed, a dependence of solar cell performance on pressure was already observed in the case of layers deposited at a high rate, and the observed differences were attributed to a denser microstructure with larger grains along with a reduction in post-deposition oxidation [Matsui 03b, Matsui 04, Kondo 05]. However, all the cells prepared in our study were remeasured and did not show any significant post-deposition oxidation, even several months after deposition, with the highest loss observed being less than 3% of the total $J_{\rm sc}$. This may also indicate that the intrinsic layers have similar film densities.

3.2.2 Influence of the hydrogen flow rate and silane depletion

Recently it was shown that it is possible to increase the silane depletion, and therefore the deposition rate of μc -Si:H, by increasing the gas residence time [Strahm 07c]. This approach allows us to keep the rf power density relatively low compared to other deposition processes [Smets 08], as summarized in Figure 3.2.

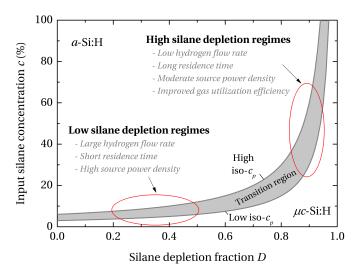


Figure 3.2: Identification of high- and low- silane depletion regimes in the plot of the a-Si:H/ μ c-Si:H transition zone as a function of the silane depletion fraction D and the silane input flow rate concentration c.

However, the question of whether these process conditions allow for the deposition of device-grade μc -Si:H material was not addressed. Here, two additional regimes were developed in order to study the effects of silane depletion on μc -Si:H deposition and material quality, and are presented in Table 3.2.

The first deposition regime with high silane depletion was developed at a pressure of 1.2 mbar

Chapter 3. Influence of the deposition pressure and silane depletion on μc -Si:H quality and solar cell performance

Table 3.2: Summary of the deposition conditions for the *i*-layers in this section using a lowered Φ_{H_2} . Both the rf voltage V_{rf} , deduced from V_{pp} measurement, and the self-bias V_{dc} are indicated.

p (mbar)	Φ_{SiH_4} (sccm)	$\Phi_{ m H_2}$ (sccm)	c (%)	$R \\ (\text{Å s}^{-1})$	R/R _{max}	D	P_d (W cm ⁻²	<i>V</i> _{rf}) (V)	V _{dc} (V)
1.2	49	190	20.6	6.5	0.77		0.15	225	2
2.0	75	75	50.0	8.9	0.61		0.20	380	5

in order to establish a comparison with the low silane depletion regime at the same pressure (discussed previously). The parameters of the deposition regime at low silane depletion were kept constant but the input hydrogen flow, and thus the total flow, were lowered following [Strahm 07c]. This causes on one side an increase in c, but more importantly it increases the gas residence time in the plasma reactor, allowing for a larger fraction of silane to be dissociated, and hence increasing D. In fact, only minor adjustments are necessary to the rf input power in order to keep ϕ_c unchanged. This can be explained following Equation (3.1): the increase in c—which usually leads to more amorphous material—is offset by an increase in D so that the relevant parameter for μc -Si:H growth, c_p , remains unchanged. By reducing $\Phi_{\rm H_2}$ by a factor of 7 (raising the silane concentration to 21%), and slightly increasing the power density, the silane depletion goes up to $80 \pm 5\%$ which explains the enhanced growth rate observed in these regimes, going from $R = 2.9 ~\rm \AA \, s^{-1}$ to $R = 6.5 ~\rm \AA \, s^{-1}$ in this case.

A second deposition regime with a high silane depletion was developed at a pressure of 2.0 mbar and a silane concentration of 50%, further increasing the deposition rate up to $R = 8.9 \, \text{Å} \, \text{s}^{-1}$. The silane depletion fraction is estimated in this second case to $70 \pm 5\%$. Tests at higher pressures have been made; however, powder formation increased significantly and no stable process was found.

Solar cells were deposited with intrinsic layers prepared in the two regimes described above, near the transition region with a ϕ_c of about 50%–60%. The I-V curves from the best cells obtained in those two regimes are shown in Figure 3.3. For comparison the cell deposited at 1.2 mbar under low silane depletion conditions is reproduced as well. Improvements are observed for cells prepared in higher silane depletion conditions. $V_{\rm oc}$, FF and $J_{\rm sc}$ are all increased significantly, going from 0.34 to 0.48 V, from 52 to 66% and from 18.8 to 21.1 mA cm⁻², respectively, and this despite the increase in deposition rate, which is typically associated with a decreases of the μc -Si:H material quality and solar cell efficiency [Gordijn 06b]. The spectral responses of these cells show a behavior similar to that observed for the cells deposited at different pressures. The increase in silane depletion mainly affects the infrared part of the spectrum, increasing the EQE at longer wavelengths for comparable cell thicknesses.

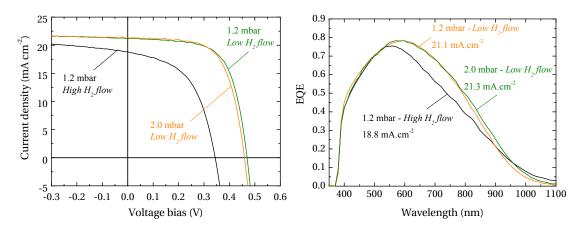


Figure 3.3: I-V curves (left) and external quantum efficiencies (right) of μ c-Si:H p-i-n cells prepared at 1.2 (low and high silane depletion) and 2.0 mbar.

3.3 Material characterization

3.3.1 Defect density of the μc -Si:H intrinsic layer

In order to understand the origin of the improvement of the solar cells with higher deposition pressure and higher silane depletion, the bulk material quality of the absorbing μc -Si:H layer was further investigated through FTPS measurements [Vanecek 02].

The absorption coefficient of low-energy (sub-bandgap) photons gives important information about the electronic quality of the material: the concentration of dangling bonds, *i.e.* density of defects or recombination centers have a significant impact on the absorption at 0.8 eV, which gives an estimation of the midgap defect density. More details are given in Section 2.3. The measurement being very sensitive to the type of ZnO used (variations of light scattering and doping level), careful attention was given to ensure that every cell was prepared using the same type of back- and front contacts.

Figure 3.4 presents the FTPS absorption curves of all the μc -Si:H p-i-n solar cells prepared at 1.2, 2.5 and 3.5 mbar low silane depletion regimes and 1.2 and 2.0 mbar high silane depletion regimes presented in the previous section. The value of the FTPS absorption coefficient at 0.8 eV correlates consistently with solar cell efficiencies [Gordijn 06b]. For instance, the solar cell whose intrinsic layer was prepared at 3.5 mbar shows a sub-bandgap absorption coefficient significantly below that of the cells whose intrinsic layer were deposited at 1.2 and 2.5 mbar. At 0.8 eV a difference of more than one order of magnitude is observed, indicating that the defect density of the material is indeed significantly lowered when deposited at higher pressure. The correlation with the overall electrical cell performance is clear: low mid-gap defect density material leads to higher $V_{\rm oc}$, FF and $J_{\rm sc}$. Solar cells were deposited on other textured ZnO (Z1) as well and the same trend was observed, i.e. the defect density decreased as the pressure increased, indicating that this result is independent of the substrate used.

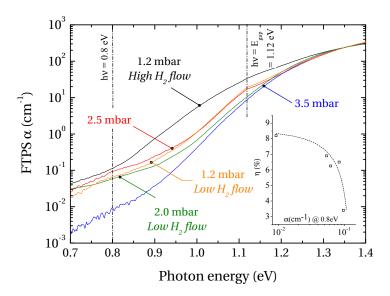


Figure 3.4: Sub-bandgap absorption coefficient obtained by FTPS measurements on μ c-Si:H p-i-n solar cells prepared at 1.2, 2.5 and 3.5 mbar low silane depletion regimes and 1.2 and 2.0 mbar high silane depletion regimes. All cells had the same ZnO as back and front contacts. The inset shows the efficiency as a function of the absorption coefficient at 0.8 eV. The dotted line is a guide to the eye.

The solar cell improvement observed upon increasing the silane depletion can be correlated with FTPS measurements as well, showing that the cell deposited at high silane depletion at 1.2 mbar has a lower defect absorption value than that deposited at low silane depletion.

The authors are led to believe that most of the defects are located within the crystalline grains themselves rather than at the grain boundaries. This hypothesis is supported by the fact that post-deposition oxidation, which is not observed in any of our cells, has shown to be related to poor grain surface passivation [Smets 08].

We interpret the difference in material quality observed with varying pressure and silane depletion as an indication that ion bombardment energy, among other plasma mechanisms, plays an important role in the deposition process. As the deposition pressure is lowered, the capacitive sheaths become less collisional, allowing more ions to impinge on the substrate's surface with higher energy, which in turn is detrimental to the material quality. In the case of increasing silane depletion, achieved by reducing the hydrogen and total gas flow rate, it will be shown that a reduction of ion bombardment is the result of decreasing time-averaged plasma potential (cf. Figure 3.6), although it is unlikely to entirely explain the material and cell improvement, as will be discussed in Section 3.4.

3.3.2 Amorphous to microcrystalline transitions

To support our ion bombardment interpretation, we investigated the influence of power on the amorphous to microcrystalline transition in three regimes. Starting with the deposition parameters used for the solar cells with a Raman crystallinity in the "transition zone" (*i.e.* ϕ_c of around 50%), the power was increased and decreased in order to completely cover the transition zone. The results are given in Figure 3.5 for the three deposition regimes: at 1.2 mbar in high and low silane depletion conditions, and at 3.5 mbar in low silane depletion conditions.

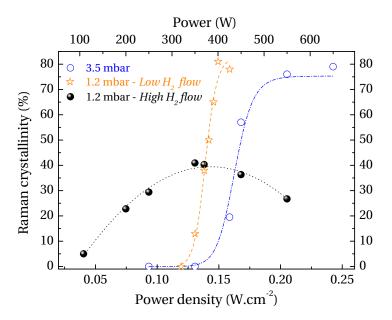


Figure 3.5: Raman crystallinity factor as a function of input power for three regimes: at 1.2 mbar (low and high silane depletion) and 3.5 mbar. The dashed and dotted lines are guides to the eye.

When the power density is varied,the three regimes exhibit quite different behaviors. At 3.5 mbar an increase in power density results in a monotonic increase in crystallinity, going, as expected, from a completely amorphous phase at a low power of 0.14 W cm⁻², to highly crystalline material at high power, *i.e.* ϕ_c =79% at 0.25 W cm⁻². On the other hand, at 1.2 mbar and in low silane depletion conditions the crystallinity first increases between 0.04 and 0.14 W cm⁻², going from 29 to 41%, and then steadily decreases to 27% at 0.21 W cm⁻². At the same pressure of 1.2 mbar, but in high silane depletion conditions, the transition curve is again recovered and high values of ϕ_c of around 80% are reached.

The significant differences observed here between these regimes may be due to multiple factors, among which powder formation or ion bombardment energy seem to be the most reasonable in this context [Strahm 07a]. In the 1.2 mbar regime, the silane partial pressure is lower and powder formation should be less likely. For this particular reason, we suspect that the decrease in crystallinity at higher P_d observed at lower pressure is due to stronger ion bombardment which can induce amorphization. At 3.5 mbar the capacitive sheaths being

Chapter 3. Influence of the deposition pressure and silane depletion on μc -Si:H quality and solar cell performance

more collisional, it is expected that the ions impinging upon the substrate's surface will to lose a larger portion of their average kinetic energy.

It should also be mentioned here that because of the reactor's geometry, which is close to symmetric, ion bombardment is intrinsically higher compared to a typical asymmetric laboratory reactor due to the area law [Lieberman 89]. This may partly explain why amorphization can be observed even at moderate power densities, as in our case.

The fact that, in Figure 3.5, the transition measured for the deposition regime at 1.2 mbar in high silane depletion conditions does not show a decrease in crystallinity is an indication that ion bombardment is reduced as well. However, in contrast to the measurements performed at different pressures, the origin of the reduced ion energy as silane depletion is increased is not straightforward. To understand this effect we performed a supplementary set of plasma potential measurements as a function of hydrogen flow rate in order to get independent confirmation that an actual voltage drop occurs upon decreasing the hydrogen flow. This can be seen clearly in Figure 3.6, where the time-averaged plasma potential (measurement detailed in Section 3.4) and self-bias voltage generated on the cathode decrease with decreasing hydrogen flow.

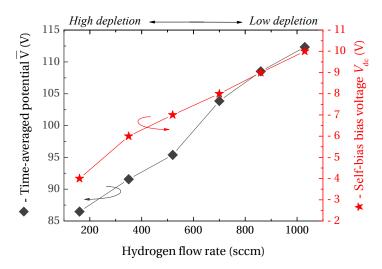


Figure 3.6: Time-averaged plasma potential (black diamonds) and DC bias voltage (red stars) as a function of the hydrogen flow rate in the 1.2 mbar regime.

3.4 Simple model for ion bombardment energy

In this section, we review the experimental evidence of the benefits of using increased pressure and depletion conditions for the deposition of high-quality μc -Si:H, within the range of our study. Evaluation of important plasma parameters, such as ion bombardment energy and electron temperature, is shown to provide some clues to the improvements observed.

In order to assess the reproducibility of the processes developed in different pressure and silane depletion conditions, several solar cells (a minimum of four to a maximum of sixteen) were deposited under each deposition regime. The average efficiencies obtained in these regimes are given in Figure 3.7. Again, there is a clear trend indicating that deposition of

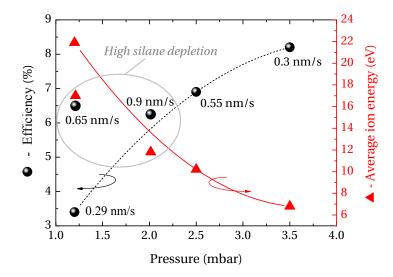


Figure 3.7: Average solar cell efficiency as a function of deposition pressure and silane depletion for the intrinsic layer (black spheres). The average ion energy was evaluated for each deposition regime (red triangles) based on a simple model detailed in Section 3.4. The lines are a guide to the eye for the low silane depletion regimes.

 μc -Si:H intrinsic layers at higher pressure is beneficial for the overall performance of p-i-n solar cells. In the same figure, average efficiencies of solar cells deposited in the two regimes in high silane depletion conditions appear. The estimated average energy \mathcal{E}_i of ions impinging upton the surface is indicated as well. \mathcal{E}_i is calculated in the case of collisional sheaths as

$$\mathcal{E}_{\rm i} \approx 0.62 \, \frac{\lambda_{\rm i}}{s_{\rm m}} \, \overline{V_p} \,, \tag{3.4}$$

where λ_i is the mean free path, s_m the sheath length and $\overline{V_p}$ the time-averaged plasma potential [Liebermann 05]. In our case $V_{\rm dc}$ is small compared to $V_{\rm pp}$ (< 3%); hence, the capacitive-sheath approximation [Chapman 80, Köhler 85] predicts the time-averaged potential $\overline{V_p}$ as

$$\overline{V_p} = \frac{1}{2}(V_{\rm rf} + V_{\rm dc}) \approx \frac{V_{\rm rf}}{2} \equiv \frac{V_{\rm pp}}{4}.$$
 (3.5)

The ratio $s_{\rm m}/\lambda_{\rm i}$ is important as it gives the average number of collisions an ion undergoes while crossing the sheath. The mean free path has been evaluated as $\lambda_{\rm i} = (n_{\rm g}\sigma)^{-1}$, with $n_{\rm g}$ the gas density in the reactor, and σ the collision cross section. As discussed by Perrin *et al.* [Perrin 96], the Langevin model becomes inadequate to describe ion-molecule collision rates when the relative kinetic energy of the colliding species exceeds a few eV. For these high ion energies,

Chapter 3. Influence of the deposition pressure and silane depletion on μc -Si:H quality and solar cell performance

typically found in the high-voltage sheaths of capacitively coupled plasmas, charge-transfer collisions are dominant and the cross section of this interaction is best represented by the hard-sphere limit, *i.e.*:

$$\sigma_{\rm HS} = \pi R_{\rm HS}^{2},\tag{3.6}$$

with $R_{\rm HS}$ the hard-sphere collision radius. Estimations of $\sigma_{\rm HS}$ for rare ions colliding with silane molecules, namely $\sigma_{\rm HS}({\rm Ar}^+{\rm -SiH_4})=24~{\rm Å}^2$ and $\sigma_{\rm HS}({\rm He}^+{\rm -SiH_4})=16~{\rm Å}^2$, should give a fair approximation of the expected cross section values for silane and hydrogen ions colliding with silane molecules. In order to have a rough estimate in our model, we simply used an averaged value for the charge-transfer collision cross section of $\sigma_{\rm HS}=20~{\rm Å}^2$.

The sheath thickness $s_{\rm m}$ did not appear to be significantly affected by the changes in pressure in the range of our study, and thus was taken to be constant at 1 mm in the ion energy calculation. We did, however, check that our observations were consistent with sheath thickness calculations made using a simple matrix sheath model [Schwarzenbach 96, Liebermann 05]. Considering a high-voltage sheath ($V_{\rm rf}\gg T_{\rm e}$), the potential Φ in the sheath is highly negative with respect to the plasma–sheath edge. Hence, the time averaged electron density becomes negligible in this zone ($n_{\rm e}(x)=n_{\rm es}e^{\Phi/T_{\rm e}}\to 0$) and only ions are assumed to be present in the sheath. Assuming a uniform ion density in this region, integration of Poisson's equation over the time-averaged sheath yields

$$s_{\rm m} = \sqrt{\frac{2\varepsilon_0 \overline{V_{\rm p}}}{e n_{\rm s}}} \approx \sqrt{\frac{\varepsilon_0 V_{\rm rf}}{e n_{\rm s}}}.$$
 (3.7)

However, since we could not measure electron density ($n_{\rm e}$), we made use of the formulas from the simple model of Strahm *et al.* [Strahm 07b] to evaluate it, based on the silane dissociation efficiency η as deduced from the $R/R_{\rm max}$ ratio, the electron impact dissociation of SiH₄ rate constant k and the pumping speed a. Calculations led to thicknesses of 1.1 mm for both the 1.2 and 2.5 mbar deposition regimes, and 1.3 mm for the 3.5 mbar regime.

It can be seen that the ion bombardment energy ranges between 20 eV and 5 eV, for which previous publications [Kondo 03a, Smets 06] already showed that these ion bombardment energies significantly affect crystallinity, thus further supporting our interpretations. The average ion energy has been estimated as well for the deposition regimes in high silane depletion conditions. It appears that in both cases ion energy is reduced as a result of a decrease in electron density, as measured and reported in the previous paragraph. The average value of ion energy computed using Equation (3.4) correlates well with the observed improvement in efficiency. For instance, they are in qualitative agreement with ion values measured in similar conditions [Nunomura 08].

In general, the improvement of the electrical properties of the cells may be due to the presence of a denser microstructure and larger grains as a result of lower ion bombardment energy, as previously observed [Kalache 03, Lebib 05, Matsui 03b, Gordijn 06a]. Local amorphization of

the grains through ion bombardment is likely caused by heavy ions through an ion-induced Si bulk displacement mechanism [Smets 06]. Also, regarding capacitively coupled VHF SiH₄/H₂ discharges in this range of pressure, previous studies [Nunomura 07, Nunomura 08] would tend to suggest that the ions that are most likely responsible for this amorphization process are the monosilicon hydride ion group SiH_m⁺ and polysilicon hydride ion groups Si_{n≥2}H_m⁺.

However, for the process regime at 1.2 mbar in high silane depletion conditions, the reduction of ion bombardment energy seems small compared to the improvement in cell efficiency. This observation points towards the presence of other plasma mechanisms that could improve μc -Si:H material quality. According to a recent publication, a reduction in electron temperature T_e can improve the material quality of μc -Si:H, by changing the relative contributions of silane radicals contributing to the growth: this leads to a reduction of impinging flux of short lifetime radicals ($\Gamma_{SiH_{x=2}}$) upon the growing film compared to the more favorable SiH₃ radicals (Γ_{SiH_3}) hence reducing the dangling bond density [Niikura 07]. We qualitatively evaluated the T_e by comparing two molecular hydrogen emission lines H_2 G_0B_0 and H_2 Fulcher by optical emission spectroscopy [Strahm 07a, Fantz 98, Fantz 06]. The changes observed in the ratio of the two emission lines when increasing silane depletion at 1.2 mbar indicate a slight decrease in T_e . However, the changes being small and sometimes within the error of the measurement, at this point it is not clear whether some of the results can be attributed to changes in plasma chemistry.

3.5 Conclusion

Growth of μc -Si:H thin films was studied in an industrial-type medium-area KAI-S PlasmaBox system to evaluate the importance of pressure and silane depletion on material quality using VHF with $d_{\rm gap}$ = 22 mm.

Single-junction μc -Si:H p-i-n solar cells were prepared with an intrinsic layer deposited between 1.2 and 3.5 mbar near the transition region, in low and high silane depletion regimes. For roughly the same crystallinity, it is observed that solar cells made at higher pressures and silane depletion conditions exhibit significantly higher performances within the range of our study. FTPS measurements of μc -Si:H intrinsic layers embedded within solar cells concur with this observation: with increasing pressure and silane depletion the defect density, is significantly lowered, which is an indication that the electronic material quality is improved. Amorphous to microcrystalline transitions as a function of input power density and calculations of the average ion energy impinging on the substrate, both support the hypothesis that ion bombardment is responsible for the observed differences.

4 Highlighting the contributions of two different phases of μc -Si:H material to overall solar cell performances

In this chapter, a qualitative model that explains how plasma processes act on the properties of μc -Si:H and on the related solar cell performance is presented. Evidence for the growth of two different material phases is presented. The first phase, which gives signature for bulk defect density, can be obtained at high quality over a wide range of plasma process parameters and dominates cell performance on flat substrates. The second phase, which consists of nanoporous two-dimensional regions, typically appears when the material is grown on substrates with inappropriate roughness, and alters or even dominates the electrical performance of the device. The formation of this second material phase is shown to be highly sensitive to both deposition conditions and substrate geometry, especially at high deposition rates. This porous material phase is likely more prone to the incorporation of contaminants present in the plasma during film deposition, and leads to solar cells that are unstable with respect to exposure to humidity and post-deposition oxidation. We further demonstrate how the influence of defective zones can be mitigated by suitable plasma processes and silicon oxide doped layers to reach high-efficiency, stable, thin film silicon solar cells.

4.1 Introduction

Improving light management is one of the key steps to increasing the efficiency of thin-film silicon solar cell devices. Light management requires minimum parasitic absorption and optimized light scattering by the substrate texture to allow for maximum light trapping in the thin absorber layers [Müller 04, Boccard 10, Berginski 07, Nicolay 09, Sai 10]. However one of the limitations of the conventional thin-film silicon solar cell design comes from the inherent low resilience of μc -Si:H deposited on substrates with sharp textures. Indeed, during the growth, shadowing effects can lead to the creation of low-quality porous regions resulting in undesired localized current drains in the device. This degrades the overall performance and reliability of the cells [Knoesen 95, Nasuno 01, Finger 03, Python 08, Li 09, Boccard 11] and hence discards potentially better morphologies at the expense of light trapping.

In this chapter, we address the specific issue of obtaining high-quality and resilient μc -Si:H

Chapter 4. Highlighting the contributions of two different phases of μc -Si:H material to overall solar cell performances

through plasma-enhanced chemical vapor deposition (PECVD) on challenging morphologies at high deposition rates. In Section 4.2 the role of the plasma conditions on the formation of the localized nanoporous phase is first determined based on single-junction μc -Si:H solar cell results and advanced material characterization. In Section 4.3 we discuss the interplay of the substrate morphology with the formation of nanoporous regions. It is observed that the use of silicon-rich silicon oxide (SiO $_x$) doped layers results in improved cell performance on rougher substrates. In Section 4.4 additional experiments regarding material stability versus humidity exposure also provide insight into the importance of both deposition rate and substrate morphology for obtaining dense μc -Si:H material. This brings a key new understanding of the role of the plasma conditions in influencing the growth of two distinct μc -Si:H material phases, both of which can drive solar cell performance. In more general terms, any functional electronic device using μc -Si:H material or layers deposited using similar deposition techniques could be affected by the phenomenon.

4.2 Role of plasma process conditions on material porosity

Optimized cell-design techniques were recently introduced to increase the resilience of thinfilm silicon solar cells to substrate morphology; through the use of SiO_x doped layers, high performance was retained even on rough substrates [Despeisse 10, Cuony 10, Cuony 12]. Here we investigate the role of plasma conditions on the formation of two distinct μc -Si:H material phases—and more particularly on the porous regions—at a high deposition rate. We also show that the use of SiO_x doped layers can buffer the detrimental effect of this material phase and restore device electrical performance.

4.2.1 SiO_x doped layers in μc -Si:H solar cells deposited at a high-deposition rate

Both the front and back contacts are made of LPCVD ZnO. Under our specific LPCVD conditions, as-grown ZnO naturally develops randomly distributed pyramidal-shaped structures, allowing for strong light scattering and efficient light trapping in the silicon absorber layers [Nicolay 09]. However, V-shaped valleys with narrow opening angles can become a critical obstacle with current silicon-deposition technologies, as porous defective material easily forms above these regions [Python 09], as can be seen in Figure 4.1. For this reason we have developed a smoothening procedure for our as-grown LPCVD ZnO through the use of a plasma treatment [Bailat 06, Boccard 12a]. This is done to ease the growth of the μc -Si:H by going from V-shaped to U-shaped structures with lower average ZnO facet inclination. This leads to improved cell electrical parameters such as $V_{\rm oc}$ and FF at the expense of reduced light trapping and $J_{\rm sc}$. In this study the root-mean-square roughness of the 4.5- μ m-thick front LPCVD ZnO (Z5) front electrode decreases with increasing plasma treatment time in the IPL system (more details in Section 2.1), going from 170 nm (Z5 20') to 120 nm (Z5 40') to 100 nm (Z5 60'). This plasma treatment thus provides us with varying substrate morphologies, and allows us to study more systematically the development of porous material and the specific

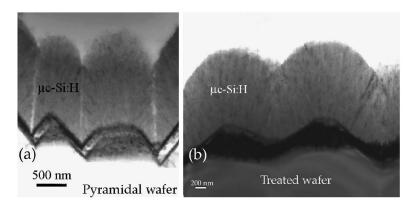


Figure 4.1: TEM micrograph cross section of a μ c-Si:H p-i-n solar cell deposited on a pyramidal wafer (left) and a treated wafer (right). The picture was taken from [Python 09].

role of the SiO_x doped layers.

Single-junction μc -Si:H p-i-n solar cells were prepared in our in-house VHF PECVD reactor with a KAI-M PlasmaBox ($49 \times 60 \text{ cm}^2$ powered electrode area) at a deposition temperature of 180 °C and an interelectrode distance of 12.5 mm. The 100 nm thick p-i interface was kept identical and deposited using VHF at 5.5 mbar and a low rate of around 3 Å s^{-1} for all of the cells. Intrinsic μc -Si:H layers 1.7 μ m were then deposited at a constant high rate of 10 Å s^{-1} on top of the buffer layer. The hydrogen input flow rate (Φ_{H_2}) was varied from 2000 to 300 sccm and the feed-in power density was adjusted accordingly to get similar Raman crystalline fractions across the series while all other parameters were held constant. A reduction of only 20% in power density was required when reducing Φ_{H_2} from 2000 to 300 sccm, to compensate for increased residence time, thanks to a quite high level of silane depletion [Strahm 07b].

Silane depletion (D) was evaluated by tunable IR laser spectrometry, allowing the analysis of the rotovibrational absorption lines of silane directly through the exhaust line of the deposition system [Bartlome 09]. This allows for the estimation of the silane concentration in the plasma (c_p) and the expected film growth rate. Powder formation was diagnosed using visible laser light scattering in the exhaust line of the reactor and optical emission spectroscopy. Trimethylboron and phosphine gases were used for p-type and n-type doping, respectively, and SiO_x doped layers were obtained by adding CO_2 to the deposition gas mixtures. Table 4.1 summarizes the deposition conditions used.

With reduced Φ_{H_2} , the gas residence time lengthens and D increases from 80 to 85%, as measured from our IR laser-based silane sensor. Secondary gas-phase reactions and powder formation are also favored with reduced Φ_{H_2} . More details of this such plasma processes can be found in Section 6.3 and in [Parascandolo 10a]. The lowest Φ_{H_2} plasma conditions could not be further investigated as the new process pumps installed did not allow us anymore to reach such high pressure with this limited amount of gas flow rate.

Chapter 4. Highlighting the contributions of two different phases of μc -Si:H material to overall solar cell performances

Table 4.1: Deposition parameters of the i-layer for the Φ_{H_2} series for a constant growth rate of $10\,\text{Å}\,\text{s}^{-1}$. The silane input flow rate (Φ_{SiH_4}), depletion (D), concentration in the plasma (c_p)—as measured with IR laser in the exhaust line—and the gas residence time without the plasma are also indicated.

Freq.	R (Å s ⁻¹)	p (mbar)	Φ _{SiH4} (sccm)	Φ _{H2} (sccm)	P_d (W cm ⁻²	R/R _{max} 2) (%)	D (%)	<i>c</i> _p (%)	$ au_{ m res.}$ (s)
VHF				300	0.34	54	-	-	1.74
				600	0.35	54	85	2.3	1.01
	10	5.5	120	800	0.37	54	84	1.9	0.79
				1200	0.39	54	83	1.5	0.55
				2000	0.40	54	80	1.1	0.34

Figure 4.2 shows the resulting conversion efficiencies of solar cells with standard μc -Si:H or SiO_x p-type and n-type doped layers on the smoothest substrate of the study, the Z5 60'.

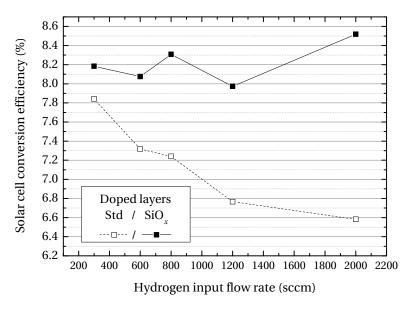


Figure 4.2: Conversion efficiency of solar cells deposited on Z5 60' with standard μc -Si:H (empty symbols) and SiO_x (filled symbols) doped layers for increasing Φ_{H_2} during i-layer deposition.

A clear trend can be observed for the solar cells prepared with μc -Si:H doped layers, with an efficiency drop from 7.8 to 6.6% as $\Phi_{\rm H_2}$ is increased due to a steady drop of $V_{\rm oc}$ from 0.48 V to 0.44 V and FF from 66.3 to 61.5%. The efficiency remains above 8.0% when ${\rm SiO}_x$ doped layers are used, with $V_{\rm oc}$ and FF up to 0.51 V and 70.2%, respectively. A striking difference appears when using ${\rm SiO}_x$ doped layers, as the device electrical performance is independent of $\Phi_{\rm H_2}$ during intrinsic layer deposition.

4.2.2 In depth μc -Si:H material characterization

To clarify the origin of the efficiency trend observed with μc -Si:H doped layers and the effect of SiO_x layers, advanced materials characterization was carried out.

Raman spectrometry

A Raman spectrometer was used to measure the Raman crystallinity factor (ϕ_c) of all the μc -Si:H solar cells using the emission lines of both Ar⁺ (514 nm) and He-Ne (633 nm) lasers for penetration depths of around 150 nm and 1 μ m, respectively, into the μc -Si:H material (see Section 2.3 for more details). Measurements were made directly on the solar cells through the glass/front ZnO stack for p-side values and through the back contact for n-side values. The measurements are reported in Figure 4.3. We see with the green laser measurements that

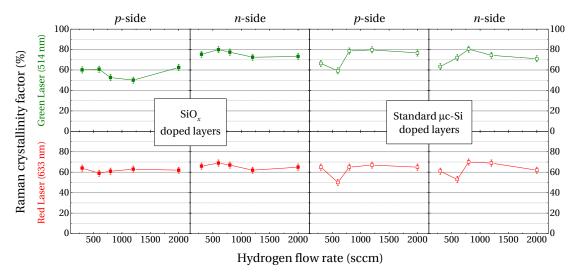


Figure 4.3: Raman crystallinity factor of all the solar cells prepared in this study, using the SiO_x μc -Si:H doped layers (left) and standard doped layers (right). Measurement were made with both a green laser (top) and a red one (bottom) for penetration depths of around 150 nm and 1 μm , respectively, into the μc -Si:H material.

cells with the SiO_x doped layers present slightly lower ϕ_c values from the p-side of the cell compared to cells incorporating the standard μc -Si:H doped layers. This difference is in fact related to the lower crystalline fraction of the doped layers themselves. Indeed, while our standard μc -Si:H doped layers have typical ϕ_c values of around 75% or above, SiO_x doped layers have lower values of around 30–40% and the green laser is more sensitive to interface variations because of its shorter penetration depth. The i-layer itself is not really affected as confirmed from the red laser measurements done on both sides of the cells: the mean ϕ_c value from the n-side goes from 65% with the standard doped layers to 66% with the SiOx ones, and from the p-side it is 62% in both cases. Furthermore, very high and similar EQE values are observed in the blue region of the spectrum for all the cells presented, indicating

Chapter 4. Highlighting the contributions of two different phases of μc -Si:H material to overall solar cell performances

the presence of a p-i interface of relatively high crystallinity (more details in Section 8.2.1). We conclude that the differences in the solar cell performances cannot be related to a change in the crystalline fraction of the material.

μc -Si:H bulk phase quality

Some reports claim there is a direct relationship between the crystallographic orientation of μc -Si:H and the associated solar cell performance when going from random to (220) preferential orientation [Matsui 02, Saito 11]. However, this interpretation is still under debate [Schicho 12], as the preferentially oriented μc -Si:H was observed when deposited on flat structures, while actual μc -Si:H solar cells are deposited on rough substrates. X-ray diffraction analysis on the μc -Si:H p-i-n cells co-deposited on AF 45 glass is presented in Figure 4.4. Although we observe a preferential (220) orientation for all films, there is no trend with respect

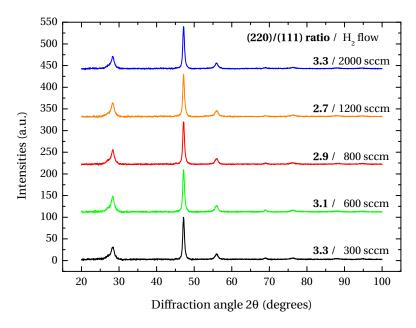


Figure 4.4: X-ray diffraction patterns of μ c-Si:H deposited on glass with increasing Φ_{H_2} . The ratio of the (220) to (111) peak heights is indicated for each deposition condition.

to Φ_{H_2} , and cell performance increases.

Fourier-transform infrared (FTIR) vibrational spectra were compared for layers deposited at $10~\text{Å}\,\text{s}^{-1}$ on polished wafers using both the highest and lowest Φ_{H_2} . The spectra are compared to high-quality μc -Si:H material deposited at a lower rate of $3~\text{Å}\,\text{s}^{-1}$ using RF at 9.0 mbar (see details in Section 5.4.1). Relevant parts of the spectra are shown in Figure 4.5.

In particular we did not detect the presence of narrow high stretching modes, which are a signature of poorly passivated grain boundaries susceptible to post-deposition oxidation [Smets 08, Bronneberg 11], even for the material with the worst solar cell performance in the series. All

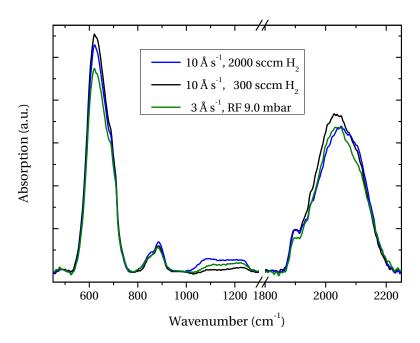


Figure 4.5: FTIR absorption spectra of μc -Si:H deposited on polished c-Si substrates at $10\,\mathrm{\AA\,s^{-1}}$ with 2000 sccm H_2 (blue line) and 300 sccm H_2 (black line), and at a low rate of $3\,\mathrm{\AA\,s^{-1}}$ (green line).

three materials had very similar structural features and a hydrogen content of around 5%. As a result the method could not discriminate between layers of high- and low-quality material.

The mid-gap density of states was quantified through Fourier-transform photocurrent spectroscopy (FTPS) performed directly on the cells [Vanecek 02] FTPS sub-bandgap absorption curves for three solar cells with standard doped layers are plotted in Figure 4.6.

The same absorption coefficient at 0.8 eV is observed for all $\Phi_{\rm H_2}$ conditions, indicating that all intrinsic layers have the same bulk defect density. Similar defect densities were measured on devices with ${\rm SiO}_x$ doped layers as well. All the characterization tools used here probe bulk material properties and show that $\Phi_{\rm H_2}$ has no significant influence on the bulk quality of the deposited μc -Si:H material, despite the observed cell efficiency trend.

Intrinsic stress measurements were also performed via the wafer-bending method on wafer strips for all layers deposited with varied $\Phi_{\rm H_2}$ but no trend was observed either, as all samples exhibited similar compressive stress values of around -110 MPa (see details in Section 7.5).

Cross-section SEM imaging of the μc -Si:H solar cells

Scanning electron microscope (SEM) cross section images of solar cells were taken for both the highest and lowest $\Phi_{\rm H_2}$ conditions with standard and ${\rm SiO}_x$ doped layers. A Philips XL-30 field-emission gun environmental scanning electron microscope (FEG-ESEM) with an accel-

Chapter 4. Highlighting the contributions of two different phases of μc -Si:H material to overall solar cell performances

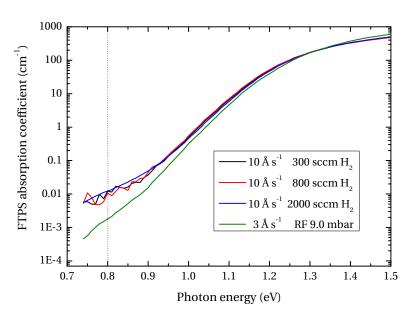


Figure 4.6: Sub-bandgap absorption coefficient obtained by FTPS on μc -Si:H p-i-n solar cells with their intrinsic layers deposited at $10\,\mathrm{\mathring{A}}\,\mathrm{s}^{-1}$ with $300\,\mathrm{sccm}\,H_2$ (black line), $800\,\mathrm{sccm}\,H_2$ (red line) and $2000\,\mathrm{sccm}\,H_2$ (blue line), and at a low rate of $3\,\mathrm{\mathring{A}}\,\mathrm{s}^{-1}$ (green line) on Z5 60' substrates.

erating voltage ranging between 5 to 30 kV was used to qualitatively evaluate the formation of nanoporous regions in the material. The SEM images in Figure 4.7 show that deposition with high Φ_{H_2} gives rise to nanoporous regions (visible as vertical black lines) which are less prevalent in the dense material obtained with low Φ_{H_2} .

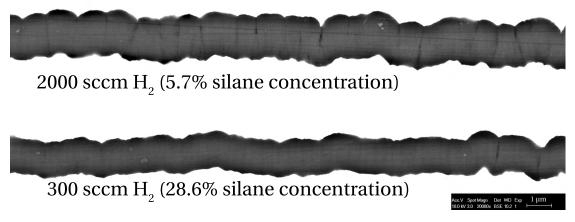


Figure 4.7: SEM images of μ c-Si:H p-i-n solar cells with their i-layers deposited at 10 Å s⁻¹ using Φ_{H_2} =2000 sccm (top) Φ_{H_2} =300 sccm (bottom) with SiO_x doped layers on the smoothest substrate Z5 60'.

The performance variation versus Φ_{H_2} is most likely due to the formation of this nanoporous

material phase, which develops from the bottom of the V-shaped valleys where the silicon growth fronts encounter each other during film deposition, and can locally increases the recombination current.

μc -Si:H material analysis conclusion

Even though the plasma deposition conditions described earlier may provide very similar bulk material properties, the best conditions (low $\Phi_{\rm H_2}$) hinder the development of nanoporous zones and result in the deposition of denser μc -Si:H material. The contribution of these defects to the bulk material properties (*i.e.* the FTPS absorption value at 0.8 eV) was shown not to be significant, and the porous areas can be considered as two-dimensional surfaces within the device. These results demonstrate that cell performance with regular μc -Si:H doped layers is strongly dominated by this nanoporous material phase in the intrinsic layer, which is shown to be much more sensitive to the plasma deposition conditions than the bulk μc -Si:H material quality itself.

4.3 Interplay between substrate roughness and PECVD process

We discuss in this section the impact of substrate roughness and morphology on the formation of the nanoporous material phase. The previous device on Z5 60' was co-deposited on two rougher substrates, Z5 40' and Z5 20'. Figure 4.8a summarizes the cell conversion efficiencies obtained on all substrates for both types of doped layers.

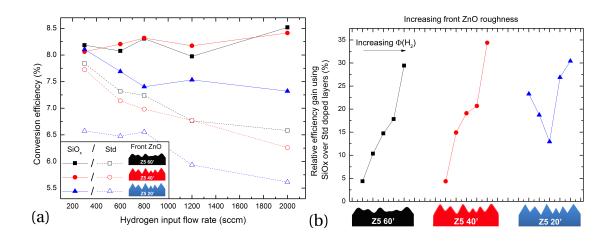


Figure 4.8: (a) Conversion efficiencies of solar cells with standard (empty symbols) and SiO_x (filled symbols) doped layers on ZnO front electrodes of increasing roughness through reduced plasma treatment time: 60 minutes (black), 40 minutes (red), 20 minutes (blue). (b) Relative increase in conversion efficiency of μc -Si:H solar cells is evaluated when standard doped layers are substituted with SiO_x layers for the three different front ZnO.

Chapter 4. Highlighting the contributions of two different phases of μc -Si:H material to overall solar cell performances

Significant gains are again observed when using SiO_x doped layers thanks to increased $V_{oc} \times FF$ values. With these SiO_x layers the losses are small, indicating that the detrimental nanoporous-phase contribution is buffered, and suggesting a mechanism in which local current drains (shunts) are quenched [Despeisse 10].

The relative performance increase when going from the standard to the SiO_{x} doped layers on all three substrates of this series is presented in Figure 4.8b. For the two rougher substrates, the trend with respect to $\Phi_{\mathrm{H}_{2}}$ is similar, but stronger, than that observed for the smoothest substrate Z5 60'. Cell performance is again less sensitive to the intrinsic layer plasma deposition conditions. For low $\Phi_{\mathrm{H}_{2}}$, relative efficiency gains of 4 to 23% are observed, while for the highest flows they range from 29 to 34%. In the case of the roughest ZnO front electrode, the relative increase is more constant over the whole range of $\Phi_{\mathrm{H}_{2}}$: as the nanoporous phase is promoted by sharp front-electrode features, the performance recovery thanks to the SiO_{x} doped layers is emphasized.

These observations show that the extent of this porous material is affected by the roughness and sharpness of the underlying substrate on which the film grows. The discriminant role of the textured substrate is essential to properly evaluate μc -Si:H deposition regimes. It is suspected that cells deposited on a substrate even smoother than the Z5 60' studied here, such as flat or optimized sputter-etched ZnO, should not be affected by $\Phi_{\rm H_2}$ conditions as the secondary phase will not be promoted by the morphology. As a result, cell performance should be limited and driven only by the bulk material quality: under these conditions clear trends of cell performance with regard to bulk defect density were observed [Gordijn 06a].

4.4 Material stability and evidence of the nanoporous phase

 μc -Si:H films are known to be more sensitive to oxidation and in-diffusion of atmospheric gases than their amorphous counterparts [Veprek 83, Finger 03]. The performance stability of films embedded in solar cell devices that have been stored simply in air has been studied as well [Finger 03, Matsui 03b, Frammelsberger 10, Boccard 11] and is referred to hereafter as dark degradation.

All the previous cells were remeasured after 11 months of being stored in the dark in the air without being encapsulated. No loss of current was observed in any of the cells, as all of the $J_{\rm sc}$ variations were within 2.5%. The most striking differences appear in the $V_{\rm oc}$, as it strongly decreases with dark degradation for standard μc -Si:H doped layers. The average relative $V_{\rm oc}$ reduction increases from 4.5% on Z5 60', to 5.5% on Z5 40', and to 15.9% on Z5 20'. A maximum loss of 27.4% is observed for μc -Si:H material deposited using high $\Phi_{\rm H_2}$ conditions on Z5 20', *i.e.* the conditions resulting in the highest density of the nanoporous phase. Using ${\rm SiO}_x$ doped layers, the $V_{\rm oc}$ is stable for all of the cells, degrading 2.8% at most. It could be that the mixed-phase nature of ${\rm SiO}_x$ helps the doped layers act as a barrier to in-diffusion of atmospheric contaminants compared to standard μc -Si:H(higher ϕ_c), as an a-Si:H buffer layer at the p-i interface of an n-i-p device was proven to be effective in this regard [Taira 03].

We present in this section an additional set of experiments demonstrating the presence of porous material in the solar cells. As-deposited non-encapsulated μc -Si:H cells with SiO $_x$ doped layers, were subject to a (non-standard) damp-heat cycle (100% humidity, 50 °C) for five days to simulate accelerated dark degradation. The cells were then annealed at 180 °C to induce water vapor desorption, which restored their performances to close to their initial values. Relative variations of both $V_{\rm oc}$ and FF are an indication of the susceptibility of μc -Si:H to water vapor incorporation, as it is favored through the nanoporous zones, while $J_{\rm sc}$ is mostly unaffected by the damp-heat/annealing cycle. Figure 4.9 shows the average value of $V_{\rm oc} \times FF$ over 10 to 16 cells deposited with increasing growth rates of 3, 9 and 12 Å s⁻¹ using VHF on top of two different substrates: a Z5 60' and a thinner (1 μ m) untreated layer ZnO (Z1) with more dopant. Major morphological differences between these two substrates are the size of the pyramids (700 nm and 180 nm) and the average facet inclinations (18nm and 30nm; see inset in Figure 4.9). Z1 exhibits a higher density of sharper valleys, hence promoting the presence of porous material.

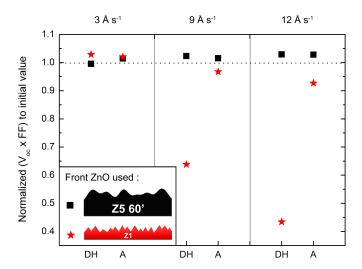


Figure 4.9: $V_{\rm oc} \times FF$, normalized to their initial values, of single-junction p-i-n μ c-Si:H solar cells after the damp-heat experiment (DH) and annealing step (A) for three growth rates. Cells were co-deposited on two different ZnO front electrode morphologies: a smoothened substrate, Z5 60' (black squares), and a substrate with a high density of sharp pyramidal features, Z1 (red stars). Plotted values are averaged over 10 to 16 cells (see text).

While good stability with regard to damp-heat testing is observed for the cells deposited on the smoothest substrate, Z5 60', major differences appear on Z1. At a low growth rate of 3 Å s⁻¹ damp-heat experiments do not lead to a decrease of the electrical performance of cells grown on any substrate. Above this growth rate, cell performance on Z1 is strongly affected by the damp-heat test, with a $V_{\rm oc} \times FF$ reduction of 35% at 9 Å s⁻¹ and above 55% at 12 Å s⁻¹. We observe as well that annealing recovers almost all of the losses induced by the damp-heat test. In contrast, Z5 60' allows for the growth of highly stable material, thanks to a much smoother morphology that reduces nanoporous phase formation. In all cases,ZnO instability accounts

Chapter 4. Highlighting the contributions of two different phases of μc -Si:H material to overall solar cell performances

for some of the variaion observed in FF values. However, comparing different devices with the same front and back ZnO gives a direct comparison of the actual impact of μc -Si:H intrinsic layer instability. It is worth mentioning here that as Z1 is more doped than Z5, it is also less sensitive to degradation with respect to humidity exposure [Steinhauser 11].

This original method for simulating accelerated dark degradation demonstrates the importance of both deposition rate and surface morphology on the formation of the μc -Si:H secondary, nanoporous phase. Increased porosity is observed at high growth rates and is clearly related to the substrate sharpness and the density of potential sites for void formation.

4.5 On the role of the SiO_x doped layers

From this study, we conclude that SiO_x doped layers reduce the negative impact of substrate-induced nanoporous regions on cell electrical performance. Figure 4.10 summarizes simply the observations made in this study.

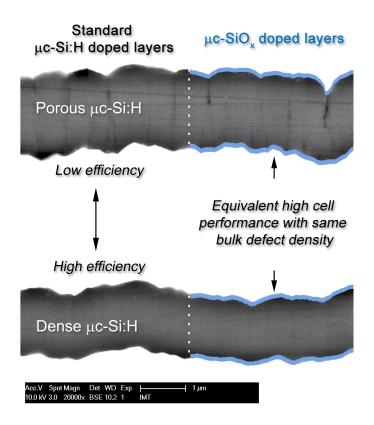


Figure 4.10: SEM images of μ c-Si:H p-i-n solar cells with their i-layers deposited at 10 Å s⁻¹ using Φ_{H_2} =2000 sccm (top) Φ_{H_2} =300 sccm (bottom) with SiO_x doped layers on the smoothest substrate Z5 60'. Performance recovery in cells with porous intrinsic layers, made with high Φ_{H_2} , is obtained through the use of doped SiO_x layers in place of doped μ c-Si:H layers.

The use of SiO_x doped layers allows the electrical performance of solar cells with porous intrinsic layers to match that of cells with denser intrinsic material with similar bulk defect densities. This is further supported by the observation of almost constant solar cell efficiencies on Z5 60' and Z5 40' in Section 4.2, independent of the $\Phi_{\rm H_2}$ used, which is consistent with the identical bulk properties exhibited by the different intrinsic layers. We demonstrated that the electrical gain obtained when using SiO_x doped layers is related, at least partly, to the presence of the substrate-induced nanoporous phase which can be aggravated by the deposition conditions. This performance enhancement may come from a shunt-quenching effect as already proposed [Despeisse 10].

Another possibility is that there is a reduction of boron cross-contamination from the underlying p-layer. This hypothesis is corroborated by electric-field profile measurements in μc -Si:H p-i-n solar cells done by cross-sectional scanning kelvin probe microscopy, in which negative charges at the cluster boundaries are speculated to be related to the presence of activated boron [Dominé 07]. We showed here as well that the use of SiO_x doped layers alone is not sufficient to completely negate the influence of this porous defective material phase. In order to reach high-efficiency thin-film silicon solar cells, further optimized substrate morphologies, SiO_x layers and intrinsic μc -Si:H deposition processes—especially at high growth rates—are all required.

Regarding the formation of the nanoporous phase, clear identification of the critical plasma parameters promoting its appearance is mandatory to gain further insights into plasma-surface interactions (control of incident radical flux, ion bombardment energy, densification processes, shadowing and re-emission processes for coverage and filling considerations etc.), as bulk material quality alone was proven here not to be sufficient for reaching high-efficiency solar cells.

4.6 Conclusion

This chapter highlights a fundamental aspect of μc -Si:H deposition on highly textured substrates: two different phases of μc -Si:H material contribute to overall solar cell efficiency, both of which can drive cell performance. Defective localized nanoporous regions were found to be significantly more sensitive to plasma process conditions and to substrate morphology than the bulk phase. Although FTPS and FTIR are the preferred opto-electrical characterization tools to determine μc -Si:H quality and identify optimum intrinsic layer process conditions, we clearly demonstrated that they are not sufficient to fully relate device performance to material quality. This becomes especially relevant when depositing on substrates with sharp features, which are essential for achieving optimum light trapping and optical performance. On such substrates, and depending on plasma conditions, it is a challenge to deposit dense material at a high deposition rate, which is a prerequisite for achieving high electrical performance and, ultimately, high conversion efficiency. Optimized SiO $_x$ doped layers were demonstrated to improve the resilience of μc -Si:H solar cell performance against these nanoporous regions.

5 Comparison of plasma excitation frequencies for the growth of high-quality μc-Si:H *i*-layers

This chapter details a comparative study of 13.56 MHz (RF) versus 40.68 MHz (VHF) excitation frequencies for the growth of very high-quality μc -Si:H for use as an absorber layer in thin-film silicon solar cells. We demonstrate improved transport properties of the μc -Si:H absorber layer when grown using RF instead of VHF. For both of the interelectrode distances evaluated in this study, RF leads to better-performing single-junction and multi-junction solar cell devices. FTPS absorption measurements reveal that very low bulk defect density μc -Si:H can be grown using either RF or VHF. However, we show that μc -Si:H grown on rough substrates using RF is more dense than μc -Si:H grown using VHF. As a result, while RF cell performance is driven mainly by the bulk material quality, VHF cell performance is limited by secondary defective nanoporous regions

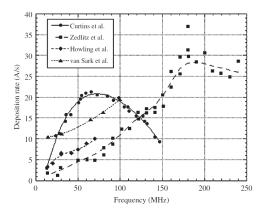
5.1 On the use of very-high frequency in capacitively coupled plasmas

Ever since intrinsic μc -Si:H was recognized as a potential active layer in thin-film silicon solar cells [Meier 94b] (see details in Section 1.4), major efforts have been made to find ways to increase both its quality and its deposition rate. While a broad range of plasma approaches was undertaken to study silane-based plasmas and the deposited layers, capacitively coupled reactors remain the best tools to deposit high-quality a-Si:H and μc -Si:H to date. They have the advantage of providing good deposition homogeneity over large surface areas. Within this technology, major developments were undertaken to improve the deposition conditions and the analysis of silicon-based deposited materials.

In particular, it has been observed that the excitation frequency of capacitively coupled plasmas (CCPs) has considerable effects on the plasma parameters, within the HF and VHF bands (3—300 MHz). While the radio frequency of 13.56 MHz became very common and standard in CCP applications, the use of higher frequencies for silane-based plasmas started to appear in the group of Prof. W. E. Spear in the 1980s with the deposition of μc -Si:H at 40.68 MHz [Willeke 83]. However, it was only later that higher frequencies were demonstrated

Chapter 5. Comparison of plasma excitation frequencies for the growth of high-quality μc -Si:H i-layers

to provide significant advantages over the regular 13.56 MHz frequency: the group of Prof. A. Shah in Neuchâtel first reported that an increase in the plasma frequency allows for higher deposition rates of a-Si:H, going from 3 to 20 Å s $^{-1}$ at constant source power, with only minor degradation of the material quality [Curtins 87]. Howling $et\ al$. [Howling 92] also reported a significant increase in the a-Si:H growth rate in the 13.56–70 MHz range, but carefully kept the actual power coupled into the plasma constant (so that the matching network losses were not taken into account). Both in hydrogen [Heintze 93] and silane-based [Heintze 96] plasmas, higher excitation frequencies were shown to provide a higher ion density and ion flux towards the substrates, along with a reduction the ions' maximum energy, keeping the effective power in the plasma constant. The resulting larger population of ions with moderate energy was thought to be responsible for this improvement. Figure 5.1 summarizes these observations.



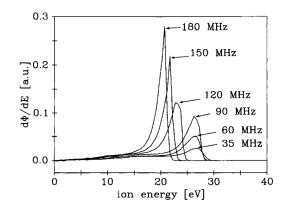


Figure 5.1: Left: Increased a-Si:H deposition rate observed with the use of higher plasma excitation frequencies [Meillaud 09]. Right: Energy distribution of ions impinging on the substrate in low-pressure SiH₄/H₂ plasmas measured with a retarding grid analyzer [Heintze 96].

Those gains are attributed to a more efficient radio frequency power coupling as the plasma excitation frequency approaches the electron-neutral collision frequency for momentum transfer. Higher excitation frequencies significantly alter the plasma electron energy distribution function (EEDF) so that the high-energy tail of the distribution is more populated. With more high-energy electrons available, the ionization rate of silane molecules improves and the plasma density increases. This translates directly into an increase in the silane dissociation efficiency by electron impact, providing more radicals to the growing film [Curtins 87, Keppner 95]. The sheath also becomes thinner with increasing frequency [Kroll 94], which implies that fewer reactive radical are lost before they can reach the growing film.

Power dissipation in the plasma changes significantly with increasing frequency: more power is dissipated in the bulk of the plasma and less in the sheaths, leading to a lower electrode voltage ($V_{\rm pp}$) and sheath voltage [Howling 92, Kroll 94, Keppner 95, Perrin 00]. As a consequence, the use of higher excitation frequencies also results in a reduction of ion acceleration in the sheath,

leading to a lower ion bombardment energy on the growth surface. This may explain why lower stress was observed in a-Si:H films deposited with higher excitation frequencies [Dutta 92].

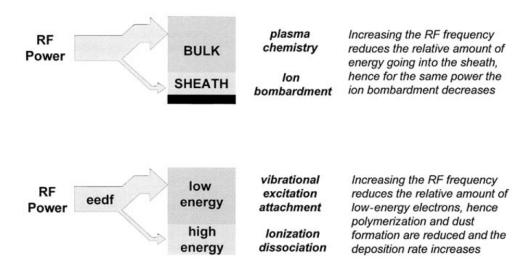


Figure 5.2: Influence of a higher plasma excitation frequency in CCP RF discharges on the power dissipation (higher P_{bulk}/P_{sheath} ratio) and the EEDF. Higher frequencies favor more high-energy electrons and fewer low-energy collisions (image taken from [Perrin 00]).

A study also demonstrated that a higher excitation frequency raises the power threshold above which powder formation occurs in silane-based plasmas [Dorier 92]. However it should be noted here that the study was done at a very low pressure of 0.3 mbar. At much higher pressures (1–30 mbar), secondary reactions are promoted over the diffusion of radicals to the substrate. As a result, it is possible that a higher silane dissociation, thanks to the use of a higher excitation frequency, could in fact favor powder formation in the plasma.

Regarding μc -Si:H specifically, the application of higher frequencies was also shown to provide favorable growth conditions [Oda 88, Prasad 89, Finger 94] and better nucleation [Tzolov 97]. The conditions for growing crystallites are favored thanks to a higher plasma density, higher silane dissociation efficiency and reduced ion energy. The selective etching of the disordered material is improved, allowing the crystallites to develop more rapidly. A reduction of ion bombardment energy is important as well to limit strong ion-bulk interactions, that can eventually lead to amorphization [Smets 06], and to reduce the defect density of the material [Gordijn 06b].

High-Pressure Depletion (HPD) regimes (>1–2 mbar) were developed [Guo 98] to increase the deposition rate while keeping good material quality. This improvement is due to an increase in plasma density associated with a further reduction of the ion bombardment energy—as ions undergo charge transfer and elastic collisions in the sheath—and a decrease in the electron temperature [Kondo 03b, Matsui 03b, Niikura 07]. Indeed, while SiH_3 radicals can be created by the electron-impact dissociation of SiH_4 at a relatively low energy of 8.75 eV, shorter-

Chapter 5. Comparison of plasma excitation frequencies for the growth of high-quality μc -Si:H i-layers

lifetime radicals (SiH $_{x\leq 2}$), which are detrimental for the growth of good-quality material, can be created directly from the same mechanism with higher energy electrons of around 9.5 eV or more. To better understand those deposition regimes, a lot of attention was also given to the characterization of capacitively coupled hydrogen plasmas and their dependence on frequency, pressure and power [Amanatides 01, Jolly 05, Marques 07, Nunomura 07].

However, with HPD regimes now being considered, the question still remains whether the excitation frequency can have a significant role in μc -Si:H material quality for thin-film silicon solar cells. For this reason, we present in this chapter a comparative study of 13.56 MHz (RF) and 40.68 MHz (VHF) for the realization of single-junction μc -Si:H solar cells in an industriallike KAI-M system. Section 5.2 presents results obtained using a large interelectrode distance of 22.5 mm. Three i-layer growth rates are evaluated with thicknesses from roughly 1 to 2.5 µm to evaluate the quality of the μc -Si:H. We show that the use of RF leads to better-performing solar cell devices overall, with improved V_{oc} and FF even for thicker cells, indicating reduced recombination in the i-layer. Section 5.3 reports a similar comparative study using a smaller interelectrode distance of 12.5 mm instead. We first review the RF deposition, showing that the hydrogen flow rate (Φ_{H_2}) does not have a significant impact on the deposited material quality. A clear benefit of using higher pressures for increased growth rate is shown: similar performances and defect densities are obtained for μc -Si:H deposited at 5 Å s⁻¹ and for the best material deposited at 3 Å s⁻¹. Using VHF we see that the cell performance is less dependent on the deposition pressure. Eventually, combining the μc -Si:H bulk defect density study with a damp-heat analysis in Section 5.4.2, we show that while i-layers prepared using RF have similarly low bulk defect density as VHF-prepared layers, they are also denser. The reduction of nanoporous regions is clearly evidenced by the $V_{\rm oc}$ stability of solar cell devices deposited on both smooth and rough surfaces. While these defective nanoporous regions tend to limit the VHF cells' efficiencies, RF cells are limited mainly by the bulk quality of the i-layer. Some hypotheses are given to explain these differences.

5.2 22-mm-gap reactor configuration

The first part of this section presents a comparison of RF and VHF for the growth of high-quality μc -Si:H for use as an absorber layer in single-junction solar cells. This first standard-interelectrode gap study was led at the time by Dr. Andrea Feltrin.

All the results presented here were obtained using an in-house plasma-enhanced chemical vapor deposition (PECVD) reactor with dual KAI-M PlasmaBox chambers, namely Chamber A and Chamber B. Standard μc -Si:H p- and n-doped layers were deposited in Chamber A using VHF and an interelectrode gap of 12.5 mm, and were kept strictly the same throughout the entire study, so that only the i-layer itself was modified. The latter was grown in Chamber B. This configuration brings multiple advantages such as:

i More freedom with the Chamber B hardware parameters such as frequency and interelec-

trode gap.

- ii Not having to expose the samples to air between the p-layer and the i-layer deposition.
- iii A possible reduction of *p-i* interface problems due to boron cross-contamination during the evaluation of different plasma regimes that can interact differently with the plasma chamber.
- iv Limitation of residual-cleaning-gas contamination of the *i*-layer as compared to the case where the growth happens in Chamber A after it is dry cleaned after the *p*-layer [Hrunski 08].

The i-layer was grown in Chamber B using the standard interelectrode distance of 24.5 mm. Taking into account the standard aluminum loading plate thickness of 2 mm, this leads to an effective interelectrode gap of 22.5 mm. The chamber temperature was kept at 180 °C for all silicon layer depositions. Since the plasma deposition chamber seasoning can also affect the starting conditions for the growth of the deposited material, both chambers of the reactor were entirely cleaned after each deposition with SF₆+O₂—and later on NF₃+Ar mixtures—to ensure good reproducibility of these tests. 0.5-mm-thick AF45 glass substrates from Schott AG were coated with LPCVD ZnO treated for 60' (Z5 60') in the IPL system. This substrate was chosen as a reference substrate as its morphology provides optimal performance for μc -Si:H single-junction solar cells.

5.2.1 Standard-gap deposition regimes

Based on previous experience with the KAI-S system (see Section 3.2), a relatively high deposition pressure of 3.0 mbar was chosen in the KAI-M when using VHF for this study. Regarding RF regimes, a reduced deposition pressure of 2.0 mbar was first evaluated. This was, however, discarded because of the relatively low solar cell performances (around 7% efficiency) observed despite a low growth rate (R) of 1.7 Å s⁻¹. Based on the literature [Roschek 03, Kilper 05, Rech 06] and some first tests, a higher deposition pressure of 5.0 mbar was chosen for the RF regimes with the 22.5 mm gap.

Three growth rates of the i-layer were evaluated for both frequencies, ranging from relatively low to moderate values, i.e. 1.6 to 3.8 Å s⁻¹. All the plasma regimes presented were tailored to give a Raman crystallinity factor of around 60% in the cell, which is known to be optimal for solar cell performance [Vetterl 00, Johnson 08b, Ellert 12]. In this study the hydrogen flow ($\Phi_{\rm H_2}$) was kept constant at 2000 and 2500 sccm for VHF and RF, respectively. A p-i buffer layer of 100 nm was always deposited using the lowest growth rate out of the three evaluated for each excitation frequency. This was done in order to limit the influence of the various deposition regimes on the underlying p-layer and subsequent p-i interface modification. The inherent crystallinity gradient along the growth direction was simply controlled through silane compensation, with $\Phi_{\rm SiH_4}$ flow increase adjustment over the thickness. The regimes that were developed and used in this study are detailed in Table 5.1.

Chapter 5. Comparison of plasma excitation frequencies for the growth of high-quality μc -Si:H i-layers

Table 5.1: Deposition parameters of the i-layer for both RF and VHF using the standard interelectrode gap of 22.5 mm. Silane dissociation efficiency as evaluated from R/R_{max} is also indicated.

Freq.	p (mbar)	Φ _{H2} (sccm)	R (Å s ⁻¹)	P_d (W cm ⁻²)	Φ _{SiH4} (sccm)	R/R _{max}	c_p (%)	$ au_{ m res.}$ (s)
VHF	3.0	2000	1.6	0.08	32	0.33	1.04	0.35
			2.7	0.10	37	0.49	0.92	0.35
			3.8	0.13	52	0.49	1.28	0.35
RF	5.0	2500	1.7	0.10	26	0.44	0.58	0.47
			2.6	0.15	37	0.47	0.77	0.47
			3.5	0.20	47	0.50	0.92	0.47

We can observe that, using this specific configuration, an increase in power density of 25 to 35% is required when using RF compared to VHF to reach a similar deposition rate for a material grown at the transition regime. Note that power densities indicated here do not refer to the real power coupled to the plasma, but only the input power as indicated from the generator; they do not take into account losses in the matching network circuit. In terms of silane dissociation efficiency, comparable values were obtained for both frequencies for all growth rates evaluated here except for the $1.6~{\rm \AA\,s^{-1}}$ regime using VHF. The electrical performance of the solar cells was then studied as a function of the absorber layer thickness, and the results are presented in the next section.

5.2.2 Analysis of solar cell performance

We present here single-junction μc -Si:H solar cell performance as a function of the i-layer growth rate for both excitation frequencies. The electrical performance will be analyzed for three thicknesses, so that we can more precisely evaluate charge carrier transport efficiency and the relative amount of bulk recombination losses [Vetterl 01].

For clarity, only the best cell results are reported in this section. However, tables in Appendix A summarize for each optimized deposition regime the best solar cell performance obtained along with the mean value of the 10 best cells for both $V_{\rm oc}$ and FF. An average value for short-circuit current density ($J_{\rm sc}$) and the efficiency η cannot be calculated since $J_{\rm sc}$ is not measured for all cells but only for the best one, as a single measurement takes a long time.

Looking first at the cells grown using VHF, we observe in Figure 5.3 that the $V_{\rm oc}$ of these cells gradually decreases with i-layer thickness for the low and intermediate growth rates. The $V_{\rm oc}$ never exceeds 515 mV, and the highest value of 513 mV is obtained for the intermediate growth rate for the thinnest i-layer evaluated here. For the VHF cells prepared at 3.8 Å s⁻¹, the $V_{\rm oc}$

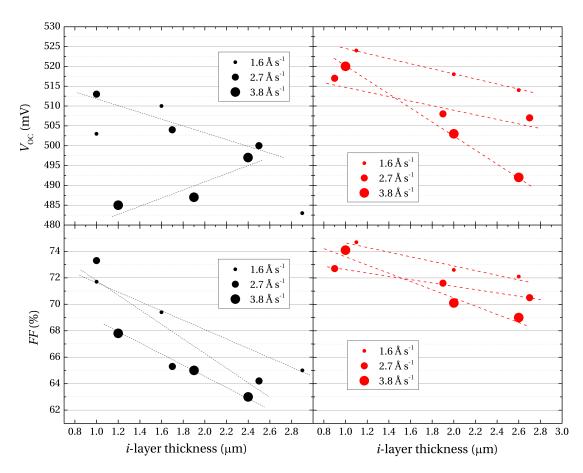


Figure 5.3: V_{oc} and FF values of the best solar cells with i-layers grown using RF (red circles) or VHF (black circles) for three thicknesses and three growth rates.

surprisingly increases with i-layer thickness. Although we do not have a clear explanation for this, we hypothesize that it could be related to the formation of nanoporous regions: while they typically lead to very detrimental electrical effects for very thin i-layers, the increased thickness may allow the regions to close, reducing $V_{\rm oc}$ losses induced by connecting such defective regions directly with the ZnO back contact. On the other hand, with RF, a significant $V_{\rm oc}$ improvement overall is evident for all three growth rates. For thin devices, values are always above 515 mV, which could never be attained using VHF. When grown at the lowest deposition rate, the $V_{\rm oc}$ only barely decreases with i-layer thickness, with 2.6- μ m-thick device still reaching 515 mV. A steeper decrease in $V_{\rm oc}$ is observed for the highest growth rate, which can be attributed to a deterioration of the i-layer bulk material quality and increased recombination.

Figure 5.3 shows significantly lower FF for VHF compared to RF for all devices, especially thicker ones. Indeed, with VHF, increased thickness decreases FF rapidly to values that are below 66% for thicknesses above 2.4 μ m, whatever the growth rate. At 3.8 Å s⁻¹ the FF values are all very low, ranging from only 68% for the thinnest cell, to 63% for the thickest. When RF is used to grow the i-layers, the FF reduction with increasing thickness is not as large:

Chapter 5. Comparison of plasma excitation frequencies for the growth of high-quality μc -Si:H i-layers

FF is always above 69% even for the thickest i-layers with the highest growth rate. This observation supports the idea that the μc -Si:H grown under those conditions exhibits much better carrier transport properties. This FF improvement can come from either a reduction of carrier recombination losses in the i-layer or near the interfaces, or a decrease of shunting issues originating from nanoporous regions appearing in the material.

Looking now at the $J_{\rm sc}$ in Figure 5.4, we see different behaviors as a function of the growth rate for the VHF cells. While a quasi-linear increase in $J_{\rm sc}$ can be observed for the low and intermediate rates, for the largest growth rate $J_{\rm sc}$ decreases slightly. On the other hand, for the RF cells, $J_{\rm sc}$ steadily increases with thickness for all three growth rates.

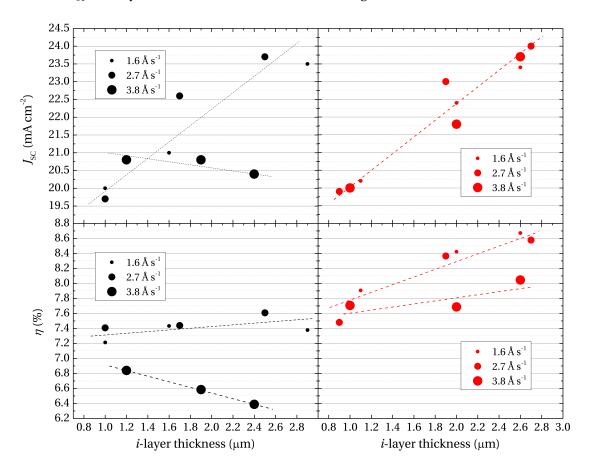


Figure 5.4: J_{sc} (as measured from EQE measurement) and efficiency of the best cells with i-layers grown using RF (red circles) or VHF (black circles) for three thicknesses and three growth rates.

By taking a closer look at the EQE measurements shown in Figure 5.5, interesting information can be retrieved about the $J_{\rm sc}$ behavior. For all μc -Si:H solar cells with their i-layers grown using VHF, the EQE is reduced in the blue region of the spectrum with either both increased deposition rate and thickness. Although the effect is small, it appears systematically. This observation indicates that, despite having an optimal Raman crystalline fraction and a similar p-i interface, μc -Si:H i-layers grown with VHF cannot handle charge transport properly.

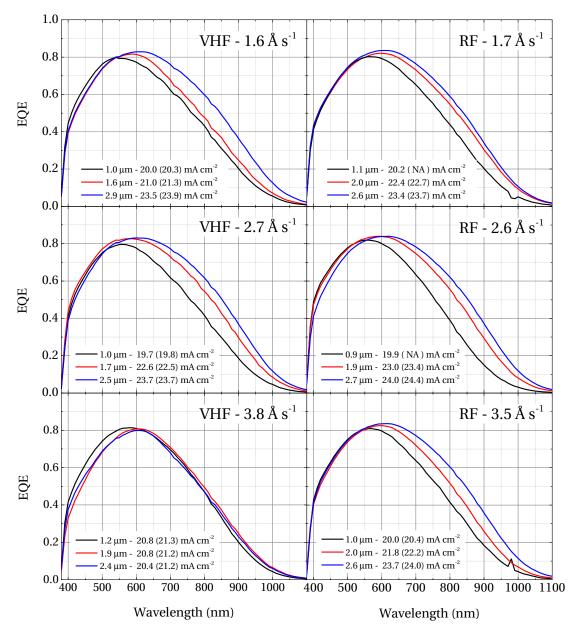


Figure 5.5: External quantum efficiencies of all of the cells presented in this section. Cells were prepared using VHF (left) or RF (right) with increasing i-layer thicknesses and growth rates.

Looking only at the fastest growth rate, we observe furthermore a strong reduction of the EQE in the IR for cells prepared using VHF. In this case, growing a thicker absorber layer does not lead to the expected $J_{\rm sc}$ enhancement through improved IR response, as observed in all other regimes: Instead, cells with all three thicknesses exhibit a $J_{\rm sc}$ below 21 mA cm⁻² with nearly overlapping EQE curves, and with the thickest cell even leading to the worst effective $J_{\rm sc}$ (20.4 mA cm⁻²). Charge extraction may be limited by a higher recombination rate or by

Chapter 5. Comparison of plasma excitation frequencies for the growth of high-quality μc -Si:H i-layers

a reduced electric field in the i-layer. Furthermore with increasing absorber thickness, the transport length needed to extract charge also increases, worsening the charge extraction efficiency.

On the other hand, the μc -Si:H cells prepared using RF exhibit better EQEs overall. The blue region shows little or no decrease for very thick i-layers and higher growth rates. A steady improvement of the EQE in the IR is also observed for thicker i-layers, even for the highest growth rate. These observations indicate that carrier transport is improved in μc -Si:H i-layers by reducing the frequency from 40.68 to 13.56 MHz.

It is interesting to put these results into perspective with solar cells co-deposited on standard Asahi U-type front TCOs. These coated glass substrates were evaluated only for the RF regimes with the lowest and intermediate growth rates. Before proceeding with the p-i-n cell deposition, these substrates were pre-coated with a thin ZnO cap layer of around 10 nm in thickness to protect them from the p-(μc -Si:H)-layer hydrogen-rich plasma conditions that would otherwise lead to a chemical reduction of the SnO₂:F surface [Schade 84, Sato 93]. We can see in Figure 5.6 that, similar to the VHF regimes on Z5 60', an increase of the i-layer thickness leads to a systematic decrease in the blue region of the spectral response and to little or no gain in the IR.

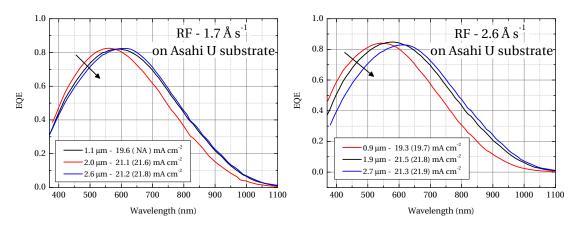


Figure 5.6: External quantum efficiencies of μc -Si:H solar cells on Asahi U-type substrates (protected by a thin cap of sputtered ZnO) prepared using RF, three increasing thicknesses and low and moderate growth rates of $1.7\,\mathrm{\AA\,s^{-1}}$ and $2.6\,\mathrm{\AA\,s^{-1}}$, respectively.

This is a very distinctive behavior from what is observed on Z5 60' for those specific growth regimes. We suspect that the transport properties of the i-layer are negatively impacted when grown on this front TCO due to its morphology (i.e. the presence of relatively sharp small features with narrow opening angles), which may favor the formation of nanoporous zones in the material when the growing fronts encounter during the growth. A SEM micrograph of such SnO_2 substrate shown in Figure 5.7 indeed demonstrates the presence of small, sharp features.

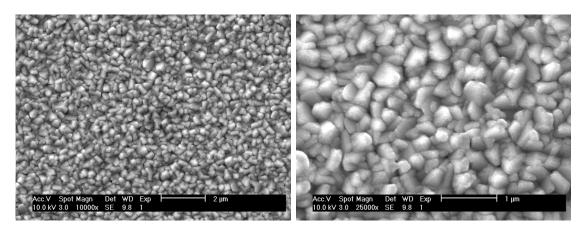


Figure 5.7: Plan-view SEM micrographs of an Asahi U-type substrate at a magnification of $10\,000\times$ (left) and $25\,000\times$ (right).

The Z5 60' on the other hand provides a smoother surface (see details in Section 2.1), ranging from small V-shaped to very large U-shaped valleys, hence limiting the density of porous zones in the material. It should be noted that the reduced light-trapping efficiency of the Asahi U-type substrate may only partly explain the saturation behavior observed for long wavelength: although the benefit from an increased i-layer thickness should be smaller than on a Z5 60', for which the large features allow for better long-wavelength light scattering, it should nevertheless be present. Overall, Asahi U-type substrates lead to a saturation of the $J_{\rm sc}$ with i-layer thickness so that the efficiency is much more limited on these substrates, reaching a plateau above 2.0 μ m, with a maximum value of 7.6%.

5.2.3 Conclusion

We have shown that μc -Si:H solar cells perform better with their i-layers deposited using RF compared to VHF for relatively low growth rates between 1.6 and 3.8 Å s⁻¹. V_{oc} and FF values do not decrease as quickly as with VHF with increasing i-layer thickness, so that a steady increase in efficiency is observed: The relative amount of bulk recombination losses is lower for the RF material. Furthermore VHF cells exhibit charge carrier extraction problems as shown from the EQE analysis, with a decrease in the blue part of the spectrum and little to no gain in the IR. Similar reduced transport properties are also observed for cells grown using RF but on rougher Asahi U-type substrates. We suggest that this behavior come from nanoporous regions that form during the growth of the μc -Si:H due to differences in the deposition process parameters—here, different frequencies—or to inadequate substrate morphology characteristics.

5.3 12-mm-gap reactor configuration

For this study, we reduced the reactor gap to 12.5 mm thanks to an aluminum spacer inserted at the bottom of chamber B, in which the i-layer growth is analyzed. A simple representation of this configuration is depicted in Figure 5.8.

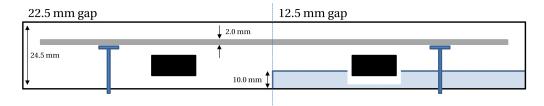


Figure 5.8: Cross-sectional view of the aluminum spacer installed at the bottom of the reactor to reduce the interelectrode gap from 22.5 mm (left) to 12.5 mm (right). The drawing is not to scale.

Since Chamber A was not modified, we could easily keep our regular μc -Si:H doped layers, so that only the i-layer was varied. Multiple series were prepared for both excitation frequencies: $\Phi_{\rm H_2}$, pressure and growth rate were varied. The two frequencies were not evaluated in parallel since changing between them required both hardware (RF generator and matching network circuit) and software modification. As a result we ran all of the experiments at 13.56 MHz before those at 40.68 MHz. For all of the studies presented hereafter, for which the ilayer was deposited in Chamber B, the differential pumping, which is a core aspect of the PlasmaBox concept [Bubenzer 90], was turned off. This decision was motivated by some advantages that are described in Appendix B.

5.3.1 13.56 MHz excitation frequency

In this subsection we present three of the main deposition regime series that were developed and optimized for the μc -Si:Hi-layers. We first show that the hydrogen flow rate does not impact solar cell performance in the range used for this particular low-gap study. Then a growth rate series, going from 3 to 8 Å s $^{-1}$ at a constant pressure, is presented along with a defect density analysis. Finally, a pressure series at a growth rate of 5 Å s $^{-1}$ is presented. All cells were had a similar i-layer thickness of around 1.2 μm .

H_2 flow rate series at a constant growth rate of 3 Å s⁻¹

When we lowered the gap from 22.5 to 12.5 mm we also increased the deposition pressure which was previously set at 5 mbar for this frequency. A few trials were done at 8.0, 9.0 and 10.0 mbar with a target growth rate of 3 Å s⁻¹. We found that 9.0 mbar was optimal in terms of cell performance, with an efficiency of around 8.5% for a 1- μ m-thick one micron thick μ c-Si:H solar cell. Based on our previous observations in the KAI-S (see Section 3.2.2), we decided to

first evaluate the influence of the total flow rate and silane depletion on cell performance for this low-gap configuration under high-pressure conditions. Process homogeneity over the whole area was also studied.

Using a deposition pressure of 9.0 mbar, we varied $\Phi_{\rm H_2}$ from 3000 to 1200 sccm, *i.e.* from the maximum value of the mass flow controller to the minimum value, ensuring that we could maintain the desired pressure (we even switched off the roots pump). Before depositing the solar cells, we first optimized the Raman crystallinity of the μc -Si:H i-layer along with the growth rate by simply depositing single layers on glass with a p-(μc -Si:H) seed layer. We observed that, in this high-pressure regime, $\Phi_{\rm H_2}$ does not have a strong influence on the Raman crystallinity (ϕ_c) nor on the growth rate, so we increased the silane flow rate ($\Phi_{\rm SiH_4}$) just slightly for crystallinity compensation in the cell. The goal was to have similar ϕ_c for each regime, so that the variation in cell performance reflects the differences in material quality rather than in the crystallinity. The cells were prepared on Z5 60' substrates with an i-layer thickness of 1.2 μ m. The i-layer deposition regimes are detailed in Table 5.2 along with the measured ϕ_c from both sides of the cells.

Table 5.2: Deposition parameters of the i-layer as a function of the hydrogen input flow rate, using RF, a growth rate of $3 \,\text{Å} \,\text{s}^{-1}$, a gap distance of 12.5 mm. The silane dissociation efficiency (as evaluated from R/R_{max}), gas residence time without plasma and Raman crystallinity factors as measured from both the p- and n- sides of the cell are also indicated.

Freq.	R (Å s ⁻¹)	p (mbar)	P_d (W cm ⁻	$\Phi_{\rm H_2}$ 2)(sccm)	Φ _{SiH4} (sccm)	R/R _{max}	c_p (%)	$ au_{ m res.}$ (s)	p -/ n - ϕ_c (%)
		1200	31	0.63	0.93	0.97	52 / 55		
				1650	32	0.61	0.74	0.71	55 / 57
RF	RF 3 9.0	0.15	2100	33	0.59	0.63	0.56	69 / 61	
				2500	34	0.57	0.57	0.47	69 / 64
				3000	35	0.55	0.51	0.39	73 / 70

We can see that under these conditions the crystalline fraction of the i-layers increases with increasing $\Phi_{\rm H_2}$; despite the slight $\Phi_{\rm SiH_4}$ compensation, the desired constant ϕ_c over the series was not obtained. Nevertheless the comparison remains relevant as all ϕ_c are within 11% (absolute) of the mean value of 62%. Based on our experience, overall cell performance should not be dramatically influenced by the limited ϕ_c variation here, with the $V_{\rm oc}$ losses being roughly compensated by the $J_{\rm sc}$ increases. In terms of homogeneity over the deposition area, $\Phi_{\rm H_2}$ itself did not have a significant impact: the thicknesses and Raman crystalline fractions were observed to be very close for the very low- and high- flow conditions tested. We also observe that the gas residence time gradually decreases with increasing total gas flow as expected, leading to an effective reduction of the silane dissociation efficiency as evaluated from $R/R_{\rm max}$. Figure 5.9 summarizes the cells performances obtained for this series.

Chapter 5. Comparison of plasma excitation frequencies for the growth of high-quality μc -Si:H i-layers

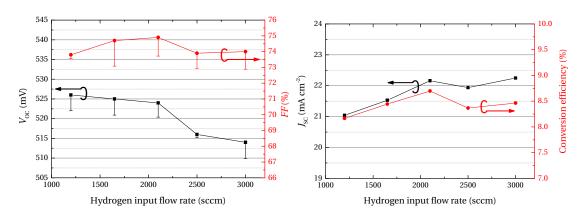


Figure 5.9: Performance of μ c-Si:H solar cells as a function of the hydrogen input flow rate, using RF, a growth rate of $3\,\text{Å}\,\text{s}^{-1}$, a gap distance of 12.5 mm and a deposition temperature of 180 °C. Left: V_{oc} and FF values, with both the best (symbols) and the mean values (bars) out of the 10 best cells. Right: J_{sc} and conversion efficiency of the corresponding best cells.

With increasing $\Phi_{\rm H_2}$ both the maximum and mean values of the $V_{\rm oc}$ are decreased by 12 mV, going from 526 to 514 mV and from 522 to 510 mV, respectively. While significant, this small loss can be ascribed to the associated crystallinity increase of the μc -Si:H i-layer, as a direct correlation between the two was already observed [Vetterl 00, Droz 04, Johnson 08b]. Regarding the FF, the values are quite stable and high: the mean value out of the 10 best cells on each substrate varies by only 0.5% around an average value of 73.2%. The influence of the i-layer crystalline fraction is evident in the $J_{\rm sc}$, as it steadily increases with $\Phi_{\rm H_2}$ going from 21.0 to 22.3 mA cm⁻². Overall, the efficiency is stable, as the losses in $V_{\rm oc}$ are counter-balanced by the associated $J_{\rm sc}$ gains: the mean value is 8.4%, with the best value of 8.7% obtained at 2100 sccm and the lowest value of 8.2% obtained at 1200 sccm.

As a result we conclude that under high-pressure conditions using RF, $\Phi_{\rm H_2}$ does not have a significant impact on the μc -Si:H quality, the solar cell performance or the homogeneity.

Growth rate series at constant pressure

Thanks to the reduced interelectrode distance, higher-deposition-rate regimes should be reachable while limiting powder formation [Takai 01, Parascandolo 10b, Strahm 10]. We here present the performance of solar cells with 1.2-µm-thick i-layers prepared at a constant pressure of 9.0 mbar with RF, for increasing growth rates of 3, 5 and 8 Å s⁻¹. The highest $\Phi_{\rm H_2}$ value of 3000 sccm was retained in order to limit powder formation for increased $\Phi_{\rm SiH_4}$. The p-i interface was kept the same with a buffer layer of around 100 nm in thickness deposited at a growth rate of 3 Å s⁻¹. This was done to focus on the quality of the bulk material and to be less sensitive to possible interface issues arising from higher power plasma regimes on top of the p-layer.

The deposition regimes are detailed in Table 5.3.

Table 5.3: Deposition parameters of the i-layer as a function of the growth rate, using RF, a constant deposition pressure of 9.0 mbar and a gap distance of 12.5 mm. The silane dissociation efficiency (as evaluated from R/R_{max}) and gas residence time without plasma are also indicated.

Freq.	p (mbar)	Φ _{H2} (sccm)	$R \\ (\text{Å s}^{-1})$	Φ _{SiH4} (sccm)	P_d (W cm ⁻²)	R/R _{max}	<i>c</i> _p (%)	$ au_{\mathrm{res.}}$ (s)
			3	35	0.15	0.56	0.51	0.39
RF 9.0	3000	5	54	0.34	0.60	0.70	0.39	
			8	82	0.56	0.63	0.96	0.39

The required power density becomes very large for increased growth rate when using RF, going from 0.15 to 0.56 W cm $^{-2}$, which is nearly the highest value we allowed our system. $R/R_{\rm max}$ increases slightly, going from 56 to 63% in absolute values, with increased silane and power density.

Figure 5.10 summarizes the cell performances obtained for this series.

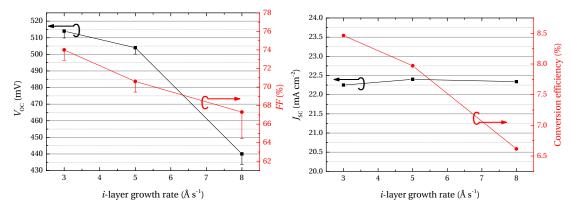


Figure 5.10: Performance of μ c-Si:H solar cells as a function of their i-layer growth rate using RF, a constant deposition pressure of 9.0 mbar and a gap distance of 12.5 mm. Left: V_{oc} and FF values, with both the best (symbols) and the mean values (bars) out of the ten best cells. Right: J_{sc} and conversion efficiency of the corresponding best cells.

Both the $V_{\rm oc}$ and the FF mean values are significantly reduced with increasing i-layer growth rate, going from 510 to less than 435 mV and from 72.9 to 64.4%, respectively. As a result, the efficiency steadily decreases from 8.5% at 3 Å s⁻¹ to 8.0% at 5 Å s⁻¹ and to a very low 6.6% at 8 Å s⁻¹.

To complement these results, the defect density of the bulk material was analyzed by Fourier-transform photocurrent spectroscopy (FTPS) and is presented in Figure 5.11.

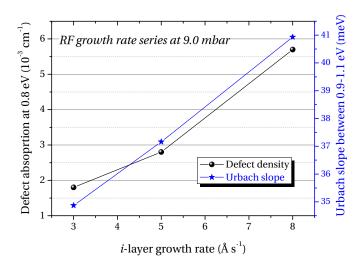


Figure 5.11: FTPS defect-related absorption value at 0.8 eV of μ c-Si:H solar cells prepared using RF at a constant pressure of 9.0 mbar for increasing growth rates of 3, 5 and 8 Å s⁻¹.

At a constant pressure of 9.0 mbar, increasing the growth rate of the i-layer leads to an almost linear increase of defect absorption. This can be interpreted as a direct consequence of the increased ion bombardment associated with the elevated power density required [Gordijn 06a]. However the exact origin of the defects cannot be elucidated with this measurement as μc -Si:H is a heterogeneous material: these defects could be within the grains, at the grain boundaries or at the conglomerate boundaries as well [Bailat 04, Meillaud 08]. Looking at the Urbach energy value (deduced from the slope of the absorption coefficient), we see a similar increase from 35 to 41 meV, indicating more structural disorder in the material, i.e. strained bonds.

To conclude, when using RF, increasing the deposition rate from 3 to 8 Å s⁻¹ by simply adjusting Φ_{SiH_4} and the power density leads to strong losses in μc -Si:H solar cell performance, which are attributed to an increase of the defect density and structural disorder of the bulk material.

Pressure series at a growth rate of 5 Å s^{-1}

We will now review the influence of the deposition pressure on μc -Si:H solar cell performance while keeping the growth rate constant at $5\,\text{Å}\,\text{s}^{-1}$ and still using RF. This deposition rate was chosen based on the results of the previous section, which showed a significant degradation of the material quality with deposition rate. As in the previous section, the p-i interface was always the same and was deposited a lower growth rate of $3\,\text{Å}\,\text{s}^{-1}$ to limit possible interface issues and to concentrate on the bulk material. The highest Φ_{H_2} value of 3000 sccm was again retained in order to limit powder formation.

Table 5.4 lists the deposition parameters of the optimized regimes.

With increasing pressure, the required power density becomes much more important to get a

Table 5.4: Deposition parameters of the *i*-layer as a function of deposition pressure, using RF, a constant growth rate of $5 \, \text{Å} \, \text{s}^{-1}$ and a gap distance of 12.5 mm. The silane dissociation efficiency (as evaluated from R/R_{max}), gas residence time without plasma and Raman crystallinity factors as measured from both p- and n- sides of the cell are also indicated.

Freq.	$R \\ (\text{Å s}^{-1})$	$\Phi_{ m H_2}$	p (mbar)	Φ _{SiH4} (sccm)	P_d (W cm ⁻²	$(2)^{R/R_{\text{max}}}$	<i>c</i> _p (%)	$ au_{ m res.}$ (s)	<i>p-/n-</i> φ _c (%)
		3000	6	56	0.29	0.58	0.77	0.26	68 / 78
RF	5		9	54	0.34	0.60	0.70	0.39	59 / 67
			12	55	0.40	0.59	0.73	0.52	71 / 68
			15	60	0.49	0.54	0.89	0.65	76 / 70

similar growth rate while staying in the a-Si:H/ μc -Si:H transition region. $R/R_{\rm max}$ is quite constant over the series but decreases slightly for the highest pressure. With increasing pressure, gas-phase reactions are favored so that silane radicals contribute more to the formation of polysilanes and powder in the plasma than to the growing silicon film [Takai 01, Strahm 10].

As can be seen in Figure 5.12, both the $V_{\rm oc}$ and the FF increase substantially with increasing pressure. Unexpectedly, the cell prepared at 9.0 mbar has a slightly more amorphous-rich

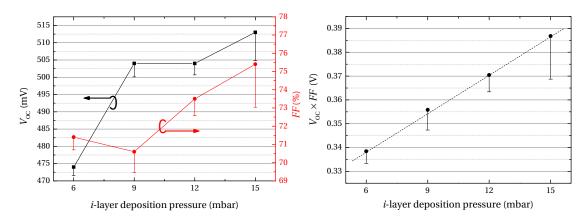


Figure 5.12: V_{oc} and FF (left) and $V_{oc} \times$ FF (right) for μc -Si:H solar cells whose i-layer was deposited using RF at 5 Å s^{-1} with increasing pressures. Both the best (symbols) and the mean values (bars) of the 10 best cells are shown.

p-i interface, which explains why the $V_{\rm oc}$ is higher, associated with a small FF loss. This overall enhancement is seen more clearly in $V_{\rm oc} \times FF$, which steadily increases with pressure. In Figure 5.13 we observe that all $J_{\rm sc}$ values are very similar (around 22.7 mA cm $^{-2}$), except for the more a-Si:H-rich solar cell deposited at 9.0 mbar, which exhibits some losses especially in the blue region due to the lower crystalline fraction (see Section 8.2.1). As a direct result of the gains in both $V_{\rm oc}$ and FF, the cell performance significantly increases from 7.7% at 6.0 mbar to 8.7% at 15.0 mbar.

Chapter 5. Comparison of plasma excitation frequencies for the growth of high-quality μc -Si:H i-layers

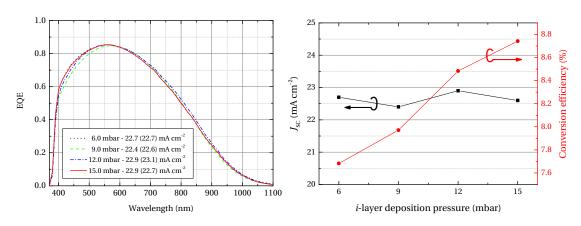


Figure 5.13: External quantum efficiencies of the best μ c-Si:H solar cells whose i-layer was deposited using RF at 5 Å s^{-1} and at increasing pressures (left), and the corresponding values of J_{sc} and conversion efficiency (right).

A defect density analysis was done on this series as well and is presented in Figure 5.14. A clear

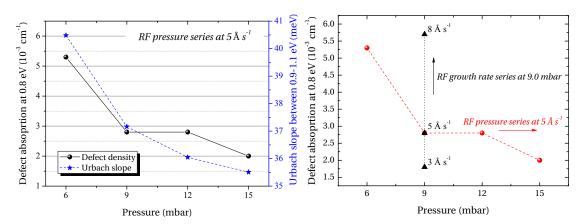


Figure 5.14: FTPS defect absorption value at 0.8 eV for the solar cells prepared using RF at $5\,\text{Å}\,\text{s}^{-1}$ with increasing deposition pressure (left) and a compared to the previous growth rate series at a constant pressure of 9.0 mbar (right).

decrease in defect absorption can be observed with increasing pressure, as the absorption value at $0.8~{\rm eV}$ goes from $5.3\times10^{-3}~{\rm cm}^{-1}$ at $6.0~{\rm mbar}$ to $2.0\times10^{-3}~{\rm cm}^{-1}$ at $15.0~{\rm mbar}$. The Urbach slope also decreases from $40.9~{\rm to}~34.9~{\rm meV}$. As discussed in Section 3.4, such an improvement in bulk material quality can result from a reduction in the average ion-bombardment energy thanks to the increased pressure [Kalache 03, Lebib 05, Matsui 03b, Gordijn 06a]: as the ions are accelerated within the collisional sheath they undergo more and more charge transfer reactions and elastic collisions.

This section has shown that increasing the deposition pressure can be beneficial for μc -Si:H material quality as demonstrated by the superior electrical performance and the decreased

bulk defect density as measured with FTPS.

5.3.2 40.68 MHz excitation frequency

Using the same interelectrode distance of 12.5 mm, we now present the results obtained using 40.68 MHz instead of 13.56 MHz. The focus was on using put on a moderate growth rate of $3 \, \text{Å} \, \text{s}^{-1}$ comparable to what was obtained using RF. Again all the cells presented here have a similar i-layer thickness of around 1.2 μ m.

To achieve a proper comparison between the frequencies, two deposition pressure series were prepared, each going from 3.0 to 9.0 mbar with 1.5 mbar increments: in the first, $a\Phi_{\rm H_2}$ was set at a high value of 2500 sccm, and in the second, the lowest amount of $\Phi_{\rm H_2}$ that would sustain the desired pressure was used. Then, deposition regimes with higher growth rates of 5 and 8 Å s $^{-1}$ were also developed.

In order to get the optimum Raman crystallinity and growth rate, all deposition regimes were again first tuned on top of AF45 glass substrates with a p-layer acting as a seed layer. The cells were then prepared on Z5 60'.

Pressure series at a constant growth rate of 3 Å s⁻¹

Based on our observations using VHF and a standard 22.5 mm gap, we decided to re-evaluate the influence of $\Phi_{\rm H_2}$ on the associated silane depletion conditions and solar cell performance. Table 5.5 summarizes the relevant deposition parameters.

At high $\Phi_{\rm H_2}$, the silane dissociation efficiency η_D , as evaluated from $R/R_{\rm max}$, increases with pressure: starting from a low value of 28% at the lowest pressure of 3.0 mbar, it steadily improves with increasing pressure and gas residence time, reaching 59% at 9.0 mbar. As a consequence, the silane gas utilization efficiency is increased, reducing the required $\Phi_{\rm SiH_4}$ from 70 to only 33 sccm. It is interesting to note that a higher power was also required at the lower pressures to reach the target growth rate; this compensated for the lower residence time and plasma density. On the other hand, all deposition regimes developed with the lowest possible $\Phi_{\rm H_2}$ show increased gas residence time and high silane utilization efficiencies ranging from 65 to 69%.

All of the detailed processes in Table 5.5 were subsequently used for μc -Si:H solar cell fabrication, with the exception of the 3.0 mbar regime using low $\Phi_{\rm H_2}$. The performances of the associated solar cells are shown in Figure 5.15. The same scales were used for comparison between the two $\Phi_{\rm H_2}$ series.

The solar cells prepared using high $\Phi_{\rm H_2}$ conditions exhibit poor performance for relatively low pressures of 3.0 and 4.5 mbar. This is due to reduced $V_{\rm oc}$ and FF values of around 470 mV and below 69%, respectively. At 6.0 mbar and higher, $V_{\rm oc}$ lies between 490 and 500 mV, and FF

Chapter 5. Comparison of plasma excitation frequencies for the growth of high-quality μc -Si:H i-layers

Table 5.5: Deposition parameters of the i-layer as a function of the deposition pressure, using VHF, a constant growth rate of $3\,\text{Å}\,\text{s}^{-1}$ and a gap distance of 12.5 mm. The silane dissociation efficiency (as evaluated from R/R_{max}), gas residence time without plasma and Raman crystallinity factors as measured from both p- and n- sides of the cell are also indicated. Recipes were optimized for a constant Φ_{H_2} of 2500 sccm (top), and the lowest possible Φ_{H_2} needed to reach the target pressure (bottom).

Freq.	R (Å s ⁻¹)	Φ _{H2} (sccm)	p (mbar)	Φ _{SiH4} (sccm)	P_d (W cm ⁻²	$(2)^{R/R_{\text{max}}}$	<i>c</i> _p (%)	$ au_{ m res.}$ (s)	<i>p-/n-</i> φ _c (%)
			3.0	70	0.14	0.28	1.95	0.15	58 / 64
		2500	4.5	59	0.18	0.33	1.53	0.23	59 / 66
VHF	3		6.0	44	0.11	0.44	0.96	0.31	59 / 63
			7.5	38.5	0.14	0.50	0.74	0.39	68 / 72
			9.0	33	0.15	0.59	0.53	0.47	66 / 69
		350	3.0	29	0.14	0.67	2.40	1.05	NA
		500	4.5	28	0.11	0.69	1.57	1.13	64 / 68
VHF	3	1100	6.0	30	0.12	0.65	0.92	0.70	74 / 83
		1500	7.5	30	0.13	0.65	0.68	0.66	68 / 78
		1700	9.0	30	0.19	0.65	0.60	0.69	52 / 67

between 71 and 73%. At 9.0 mbar a decrease in $V_{\rm oc}$ and $J_{\rm sc}$ is observed despite i-layer thickness and crystalline fraction similar to that at 6.0 mbar. This could be related to an increase in the nanoporous phase, but this hypothesis is unconfirmed. This pressure-dependent performance behavior is not seen when we use the lowest $\Phi_{\rm H_2}$. Indeed, looking at Figure 5.15, we see that all parameters are quite stable whatever the pressure: FF is quite high—around 71%—and the $V_{\rm oc}$ is always around 495 mV except for at 6.0 mbar. However this last result can be explained by the fact that the crystalline fraction of this cell is much higher (74% and 83% when measured from p- and n- sides respectively) than those of the three others .

The reason why the cells prepared under high $\Phi_{\rm H_2}$ conditions show reduced performance at the lower 3.0 and 4.5 mbar pressures may come from the high power required to grow a material with the required crystallinity at such a growth rate. These conditions have higher ion-bombardment energy, which can favor the creation of additional defects. This deterioration in material quality is corroborated by FTPS defect density measurements that were performed on both series and are presented in Figure 5.16. The two cells prepared at low pressures with high $\Phi_{\rm H_2}$, leading to the worst performances, have the most defective *i*-layers. The difference is quite clear between these two regimes, which led to solar cells with defect-related absorption coefficients above $3.3 \times 10^{-3}~{\rm cm}^{-1}$, and the rest of the cells with $\alpha(0.8~eV)$ values ranging between $2.3~{\rm and}~1.4 \times 10^{-3}~{\rm cm}^{-1}$.

From this experiment we see that $\Phi_{\rm H_2}$ does not influence the *i*-layer material quality above 6.0 mbar. All of these regimes provide μc -Si:H solar cell conversion efficiencies between 7.9

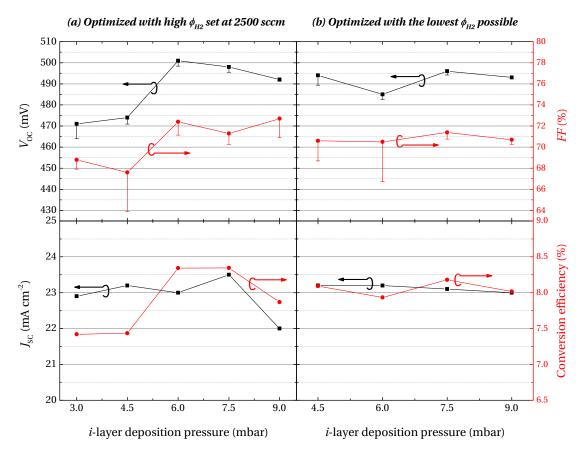


Figure 5.15: Top: Best V_{oc} and FF values as a function of deposition pressure for solar cells whose optimized i-layer was deposited using VHF with Φ_{H_2} at a relatively high value of 2500 sccm (left) and with the lowest Φ_{H_2} possible (right). Bottom: Corresponding J_{sc} and conversion efficiencies of the best solar cells.

and 8.3%, and relatively low defect densities, whereas the use of high $\Phi_{\rm H_2}$ at pressures below 4.5 mbar leads to low $V_{\rm oc} \times FF$ and efficiencies of 7.4%, and is clearly associated to an increase in the bulk material defect density as assessed by FTPS.

Growth rate series at constant pressure

Based on the results presented in the previous section, a growth rate series was also performed using the most promising regime, *i.e.* the regime at 7.5 mbar with high $\Phi_{\rm H_2}$ conditions, which limits powder formation even at high deposition rates. The *i*-layer deposition parameters of the newly developed regimes at 5 and 8 Å s⁻¹ are presented in Table 5.6.

At this constant pressure and similar gas residence time, the silane dissociation efficiency is always in the range of 50–60% for the three growth rates. We note that the power required to go from 3 to 8 Å s⁻¹ is, as expected, much lower using VHF instead of RF. While the 7.5 mbar VHF

Chapter 5. Comparison of plasma excitation frequencies for the growth of high-quality μc -Si:H i-layers

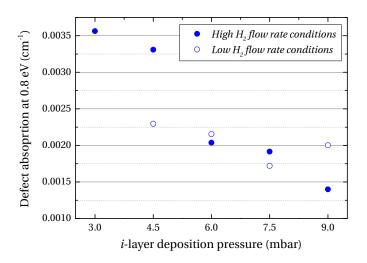


Figure 5.16: FTPS defect absorption value at 0.8 eV as a function of the deposition pressure of of μc -Si:H solar cells whose optimized i-layer was optimized using VHF with Φ_{H_2} at relatively high value of 2500 sccm (filled circles) and with the lowest Φ_{H_2} possible (empty circles).

Table 5.6: Deposition parameters of the i-layer as a function of growth rate using VHF, a constant pressure of 7.5 mbar and a gap distance of 12.5 mm. The silane dissociation efficiency (as evaluated from R/R_{max}), gas residence time without plasma and Raman crystallinity factors as measured from both p- and n- sides of the cell are also indicated.

Freq.	p (mbar)	Φ _{H2} (sccm)	R (Å s ⁻¹)	Φ _{SiH4} (sccm)	P_d (W cm ⁻	R/R_{max}	<i>c</i> _p (%)	$ au_{ m res.}$ (s)	p -/ n ϕ_c (%)
			3	39	0.14	0.50	0.77	0.39	68 / 72
VHF	7.5	2500	5	49	0.20	0.61	0.80	0.39	65 / 74
			8	86	0.34	0.60	1.30	0.39	70 / 69

regime uses only 5% lower power density than the 9.0 mbar one using RF regime at 3 Å s $^{-1}$, 65% less power is required for both the 5 and 8 Å s $^{-1}$ regimes.

Looking at the conversion efficiency summary in Figure 5.17, we see that the use of RF over VHF for lower growth rates ($R \le 5 \, \text{Å} \, \text{s}^{-1}$) leads to better-performing μc -Si:H solar cell devices. Although not represented on the graph, we stress that we could never reach comparable efficiencies when using VHF compared to RF for low rates of around $3 \, \text{Å} \, \text{s}^{-1}$, whatever the VHF regime.

For a growth rate of around $5\,\text{Å}\,\text{s}^{-1}$, comparable conversion efficiencies of 8.0 and 8.1% are obtained for cells prepared with RF and VHF, respectively. As seen in the Section 5.3.2, an increase in pressure when using RF is favorable, and led to an increased efficiency of 8.5%.

At a rate of $8\,\text{Å}\,\text{s}^{-1}$ the VHF cell performs much better than the RF cell, with a 7.4% conversion efficiency compared to a 6.6% efficiency. We observe an increase in both V_{oc} and FF, which

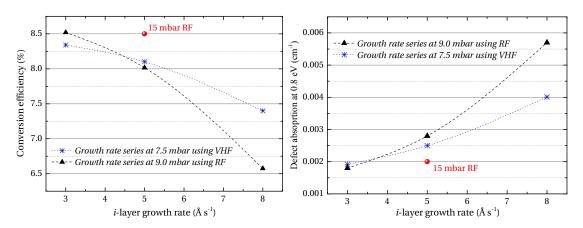


Figure 5.17: Left: Best conversion efficiencies of μc -Si:H solar cells prepared using either VHF at 7.5 mbar (blue stars) or RF at 9.0 mbar (black triangles), as a function of deposition rate. Right: Corresponding FTPS defect-related absorption. The beneficial effect of a higher deposition pressure of 15 mbar using RF has on the μc -Si:H quality is also shown.

go from 440 to 473 mV and 67 to 70%, respectively. This gain is associated with a decrease in defect absorption as measured by FTPS—it is reduced from $5.7 \times 10^{-3}~\rm cm^{-1}$ to $4.0 \times 10^{-3}~\rm cm^{-1}$. The significantly higher power density required to reach higher deposition rates when using RF is thought to be responsible for this result, hence favoring VHF for rates of 5–8 Å s⁻¹ and above.

5.3.3 Conclusion

A comparative study of 13.56 MHz and 40.68 MHz for the growth of high-quality μc -Si:H in a chamber with an electrode gap of 12.5 mm again shows that the use of 13.56 MHz leads to better-performing cells. While i-layers prepared using VHF have a similarly low bulk defect density, the associated cell performances are always subpar. However, for increased growth rates, VHF starts to become attractive as less input power is required, favoring the growth of μc -Si:H material with a low bulk defect density.

5.4 Material analysis and stability study

In this section we review the performance of the solar cells prepared using 13.56 or 40.68 MHz and analyze their material properties. First, we compare the bulk defect density of the cells. We also present an additional damp-heat analysis, demonstrating the ability to differentiate between dense and porous μc -Si:H.

5.4.1 FTPS comparison of cells prepared using RF and VHF

The defect-related absorption coefficients, as obtained from FTPS measurements, of all of the cells prepared in the previous sections using an interelectrode distance of 12.5 mm are summarized in Figure 5.18.

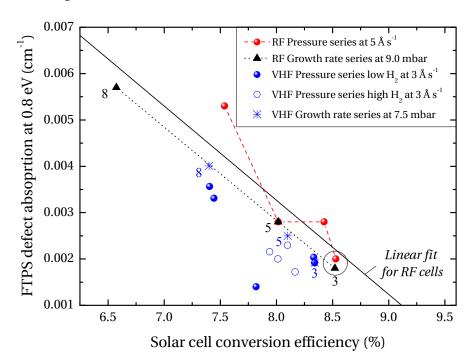


Figure 5.18: FTPS defect-related absorption coefficient at 0.8 eV as a function of the corresponding μc -Si:H solar cell conversion efficiency. The blue circles, spheres and stars correspond to those prepared using VHF, while the rest are prepared using RF. The dotted lines are simply guides to the eye.

The LPCVD ZnO contacts and the doped layers were kept strictly identical throughout the series so that the differences observed in the 0.8 eV absorption coefficient relate only to the material quality of the 1.2- μ m-thick *i*-layer. We observe that all of the cells prepared using RF exhibit a clear trend between their conversion efficiency versus the measured *i*-layer bulk defect absorption. Indeed, with decreasing growth rate and increasing pressure, a quasilinear relationship between the bulk defect density and the solar cell efficiency is established. Furthermore, two RF regimes—one with cells prepared at 3 Ås⁻¹ using 9.0 mbar and one with cells prepared at 5 Ås⁻¹ using 15.0 mbar—lead to a similar low defect-related absorption coefficient of around 2 × 10⁻³ cm⁻¹, which, in turn, leads to a similar solar cell efficiency of 8.5% (circled in Figure 5.18).

In contrast, the cells prepared using VHF do not have such a clear relationship with respect to FTPS defect density. Despite the growth of a high-quality μc -Si:H bulk material with a comparable or even lower bulk defect density than that of materials grown using RF, the

associated solar cell conversion efficiency remains always lower for $R < 8~\rm{\AA\,s^{-1}}$. The i-layer with the lowest defect-related absorption coefficient of $1.4 \times 10^{-3}~\rm{cm^{-1}}$, obtained at $3~\rm{\AA\,s^{-1}}$ using the highest $\Phi_{\rm H_2}$ conditions with VHF, leads to only average solar cell performance with a conversion efficiency of 7.8% despite an adequate Raman crystalline fraction. This demonstrates that bulk defect density alone does not drive solar cell performance.

In other words, although bulk defect density plays a determining role on the conversion efficiency of cells prepared using RF, low defect density is insufficient for high-performance cells prepared using VHF. These cells typically perform worse than their RF-prepared equivalents because of nanoporous-phase development. This hypothesis will be confirmed in the next section.

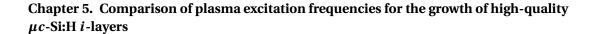
5.4.2 Stability study of μc -Si:H-based solar cells

We present in this section an additional set of experiments demonstrating the presence of nanoporous material in the solar cells prepared using VHF. Similarly as in Section 4.4, asdeposited, non-encapsulated μc -Si:H cells prepared using either RF or VHF were subjected to annealing for 1h30' at 180 °C under nitrogen flow, followed by exposure to (non-standard) damp heat (100% humidity, 50 °C) for two days to simulate accelerated dark degradation, *i.e.* degradation of solar cell performance under ambient atmosphere. This was done for single-junction μc -Si:H single-junction solar cells deposited on smooth Z5 60' and for micromorph tandem cells where the μc -Si:H bottom cell was grown on a more textured surface, a Z2 2', in order to trap sufficient light in the tandem cell structure. All of the top cells were co-deposited in one run in the large-area KAI-S system.

For this experiment the standard interelectrode distance of 22.5 mm was used. Three deposition regimes were optimized at 3.3 mbar using VHF with varying growth rates: 3.0, 4.5 and $7.0\,\text{Å}\,\text{s}^{-1}$. A higher pressure of 5.0 mbar was also tried for the growth rate of $4.5\,\text{Å}\,\text{s}^{-1}$ but did not give better results than 3.3 mbar. For comparison, similar regimes with RF were evaluated as well. However, only the growth rates of 3.0 and $4.5\,\text{Å}\,\text{s}^{-1}$ could be evaluated at 5.0 mbar, as $7.0\,\text{Å}\,\text{s}^{-1}$ was not achievable with this interelectrode gap (too much power would have been required). At $4.5\,\text{Å}\,\text{s}^{-1}$, using RF, a higher pressure of 7.5 mbar was evaluated as well and led to a better-performing cell with a significantly reduced defect density $(4.7\times10^{-3}~\text{cm}^{-1}~\text{for} 5.0~\text{mbar})$ compared to $2.7\times10^{-3}~\text{cm}^{-1}$ for 7.5 mbar).

The cells were successively measured after their preparation, after annealing, and after the damp-heat test. The V_{oc} evolution of the micromorph cells is shown in Figure 5.19.

Increasing the growth rate of the bottom cell using VHF significantly aggravates the sensitivity of the tandem-cell $V_{\rm oc}$ to damp heat: after damp-heat exposure, respective losses of 30, 100 and 380 mV are observed for the best cells grown at 3.0, 4.5 and 7.0 Å s⁻¹, respectively. Looking at the $V_{\rm oc}$ median value, the losses are even worse, reaching 24, 166 and 495 mV, respectively. On the other hand, when bottom cells are grown using RF, stable behavior is observed for



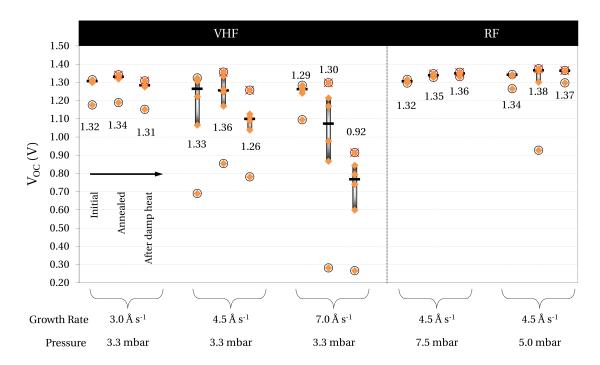


Figure 5.19: V_{oc} of micromorph cells in the initial state, after the annealing and after damp-heat exposure. The cells were deposited on Z2 2' and the bottom cell was deposited with varying pressures and growth rates.

micromorph cells at $4.5 \, \text{Å} \, \text{s}^{-1}$: the median value after the damp-heat test even increases by 43 mV at 5.0 mbar and 22 mV at 7.5 mbar. Since the single-junction a-Si:H subcell in these micromorph devices was also stable with regard to damp-heat exposure, we conclude that the material grown using VHF at 3.3 mbar is much more porous than that grown using RF.

The $V_{\rm oc}$ evolution of the single-junction solar cells on a smoother substrate (Z5 60') is shown in Figure 5.20. We observe that, in this case, the damp-heat experiments induce negligible $V_{\rm oc}$ losses. This can be explained by the fact that the smoother substrate morphology leads to a reduced density of nanoporous zones as compared to the sharper morphology that is present in the micromorph cells after the a-Si:H top-cell growth on Z2 2'. Nevertheless, small variations of $V_{\rm oc}$ within the range of 15–25 mV are still observed with VHF on such substrates. For the μc -Si:H material grown using RF, on the other hand, the $V_{\rm oc}$ is not perturbed at all throughout the whole experiment and remains within the measurement error.

 $J_{\rm sc}$ remains stable throughout the experiment for all micromorphs subcells and single-junctions cells except for the 7.0 Å s⁻¹ VHF cell, which could not be properly measured after the dampheat test. In particular there was no EQE loss observed in the IR similar to previous reports [Matsui 03b, Matsui 04]. We ascribe this difference to the oxidation of nanoporous-phase zones rather than the grain boundaries themselves within the large conglomerates which impedes charge extraction and collection.

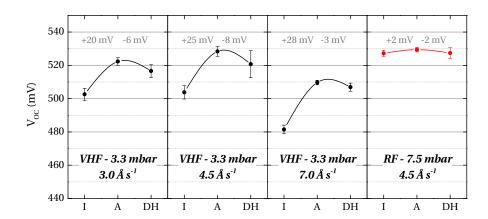


Figure 5.20: Mean V_{oc} of the 10 best single-junction μc -Si:H solar cells on Z5 60' deposited with varying pressures and growth rates in the initial state (I), after annealing (A) and after damp-heat exposure (DH).

Although we cannot yet explain why the use of RF leads to the growth of more dense and compact μc -Si:H material, some hypotheses can be proposed. One possible explanations is an increase in ion bombardment. Since the use of a lower excitation frequency leads to an increase of higher-energy ion flux towards the film, it could help densify the growing surface. However, we have seen that deposition pressure can also greatly influence the ions' energy as they are accelerated through the collisional sheath. Unfortunately, under those high-pressure conditions, we are not able to measure the energy distribution function of bombarding ions arriving on the substrate (retarding field analyzers work only for plasmas with relatively low pressure ≤ 1 mbar).

Another possible role of a reduced frequency in the growth of denser material may be related to the sheath thickness. Indeed, as discussed in Section 5.1, an increase in the excitation frequency was shown to reduce the sheath thickness [Kroll 94]. As a result, the relative contribution of more highly reactive radicals, such as SiH_2 , to the growth surface would be enhanced—since their losses would be reduced in the sheath region—which would in return favor the growth of a more porous material. Lastly, studies on the SiH_3 and SiH_2 generation profiles in the plasma may point toward a higher generation of highly reactive radicals near the sheaths rather than in the bulk when using higher excitation frequencies inducing a larger contribution of these sylylenes to the growing film [Keppner 95, ur Rehman 11], which is detrimental for the material density.

We have shown in this section that the μc -Si:H material grown using VHF is very porous and susceptible to water vapor ingress as compared to the material grown using RF. This tendency towards porous material is particularly detrimental in micromorph solar cells because rough substrates—like LPCVD ZnO with an a-Si:H top cell grown on it—promote the formation of the nanoporous regions. On smoother substrates, smaller but still significant differences are observed.

5.4.3 Conclusion and current view

In summary, both RF- and VHF-prepared cells can have a very low bulk defect density of around $2 \times 10^{-3}~\rm cm^{-1}$. However despite similar or even better bulk material quality, the conversion efficiency of VHF-prepared cells is always lower than RF-prepared cells. A dampheat study indicated that the μc -Si:H i-layer material obtained using RF better withstands water-vapor exposure on rough substrate morphologies. This indicates that the material grown using RF is more dense when deposited on rough surfaces, with significantly less severe nanoporous regions (they are smaller either in size or gravity). As a result, the performance of RF-prepared cells is dominated mainly by the bulk material quality and less by the nanoporous phase, as in VHF-prepared cells.

Based on our observations in this chapter, we summarize our current view of the growth of high-quality μc -Si:H deposited using either RF or VHF and the role of the SiO_x doped layers (seen in Section 4.5) in actual solar cells in Figure 5.21.

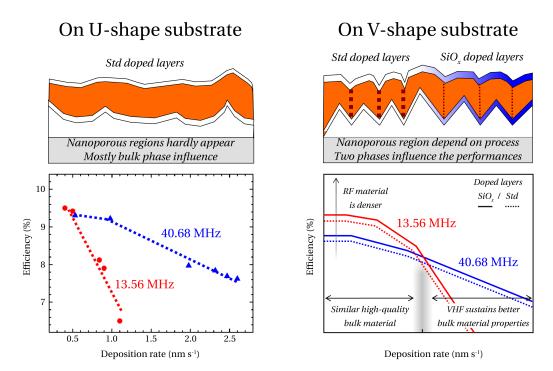


Figure 5.21: Simplified view of μ c-Si:H growth on U-shape vs V-shape substrate morphologies. While on U-shape substrates (such as sputtered etch ZnO) the cells performances are mainly determined by the bulk phase, on V-shape substrates they also rely on the density of the nanoporous regions formation. In this case the use of RF over VHF has the advantage to provide a denser material, hence leading to better material. However, for higher growth rates, the bulk phase becomes defective quicker, hence favoring VHF in this case. SiO_x doped layers can help alleviate the electrical performances of the nanoporous regions but cannot eliminate them. Graph in the bottom left is adapted from a graph given by the group of Jülich during the FP6 EU ATHLET project.

5.5 Conclusions

In this chapter, we examined the role of the excitation frequency on μc -Si:H material quality for application in thin-film silicon solar cells. We demonstrated that the lower 13.56 MHz frequency provides better solar cells for interelectrode distances of 22.5 and 12.5 mm—and for moderate growth rates of around 5 Å s⁻¹ or less. Better carrier transport was observed with increasing i-layer thickness using RF, permitting higher $V_{\rm oc}$ and FF together with larger $J_{\rm sc}$. Furthermore, increasing the pressure with RF improved bulk material quality, allowing for the growth of μc -Si:H material with a similar defect density at 5 Å s⁻¹ at 15.0 mbar and at 3 Å s⁻¹ at 9.0 mbar.

While both frequencies allow for the growth of very good bulk material quality, as assessed by FTPS measurements, the corresponding efficiencies of the cells prepared using 40.68 MHz were always low compared to those of the cells prepared using 13.56 MHz, within the range of our study. This observation suggests that a parameter besides bulk defect density impedes carrier transport in solar cells prepared using VHF. A higher density of nanoporous regions was deduced from damp-heat experiments in the cells grown using VHF, which showed strong $V_{\rm oc}$ instabilities; this was not observed with RF. These porous zones contribute significantly to reduced μc -Si:H solar cell performance, especially when the morphology favors the appearance of such zones.

Although no clear physical explanation was offered for the exact role of the plasma excitation frequency on the μc -Si:H material density, some hypotheses were provided to explain why the use of RF leads to more dense and compact material. A larger population of high-energy ions could help to densify the growth surface, or a reduction in proportion of highly reactive radicals (*e.g.* SiH, SiH₂) contributing to the growth of the film. In the latter case, it could be related to (i) a change in the generation of radicals favoring monoradicals (*e.g.* SiH₃, Si₂H₅), (ii) gas-phase reactions involving short-lived radicals or (iii) an increase of the sheath thickness, reducing the proportion of highly reactive radicals (*e.g.* SiH, SiH₂), (iv) a change in the generation profile of short-lived highly reactive radicals, favoring their creation near the sheaths with increasing excitation frequency, which in return enhances their detrimental contribution for the growth of a dense μc -Si:H film.

It is important, however, to put these results into perspective with current thin-film silicon technology requirements both in terms of substrate texturing and material deposition rate: while denser material deposited at a lower rate may be favorable in micromorph cells—as a highly textured substrate is necessary for generating high currents—the use of deposition regimes more prone to the growth of nanoporous regions but that still yield high-quality bulk material at very high growth rates may be desirable in certain cases. For instance, in triple-junction a-Si:H/ μc -Si:H solar cells, much thicker μc -Si:H i-layers are required and the constraints on the a-Si:H top-cell current are also relaxed, allowing for the use of front TCOs with smoother morphologies. This, in turn, allows for the growth of high-quality material without significant nanoporous zones, hence favoring the use of VHF.

6 High deposition rate of device-grade μc-Si:Η

In this chapter we review our efforts to improve the material quality of μc -Si:H layers deposited at high deposition rates in an industrial-type KAI-M reactor for application in thin-film solar cells. A significant part of the results presented in this chapter were obtained within a large European collaborative project supported by the EU's Seventh Framework Programme for Research (FP7) in the area of energy. Hence, this FP7 EU PEPPER 3-year project will first be briefly summarized in Section 6.2 before the key points and main achievements are given in the next sections. Section 6.3 reviews how both hydrogen flow rate and pressure influence secondary gas-phase reactions in the plasma and solar cell performance. We show that plasma conditions at the onset of significant powder formation lead to better-performing μc -Si:H solar cells. Section 6.4 discusses the crucial interplay between the μc -Si:H growth rate and the substrate morphology with regard to the formation of nanoporous regions. In Section 6.5, we highlight the important role of a reduced interelectrode gap, which leads to lower defect-related absorption and improved μc -Si:H solar cell performance with the absorber layer deposited at higher rates. Section 6.7 presents the growth kinetics controlling the film properties and some simulations performed in collaboration with University of Patras.

6.1 Introduction

As discussed earlier in Section 1.3, to lower production costs and increase the conversion efficiency of TF Si solar modules, the deposition of high-quality μc -Si:H at an increased rate and on textured substrates that guarantee efficient light trapping is critical. While higher deposition pressure regimes have been identified as an interesting approach to deposit improved-quality μc -Si:H material at higher growth rates [Guo 98, Kondo 00, Matsui 03b, Mai 05, Sobajima 08], they also tend to favor secondary gas-phase reactions in the plasma and powder formation. Above a certain threshold, such reactions thus lead to a reduction in the silane gas utilization efficiency, strong inhomogeneity, instabilities over time, possible pump failure and down times. Another way to get high-quality i-layers at an increased deposition rate is to further increase the plasma excitation frequency, as already discussed in Section 5.1, since this improves the silane dissociation efficiency and reduces the ion bombardment on the growing film.

However, this approach leads to significant complications for up-scaling, as electromagnetic non-uniformities, such as the standing-wave effect [Lieberman 02, Sansonnens 06], start to play a major role on the actual plasma conditions.

For these reasons, a lot of research has recently been done to combine increased pressure and moderately high plasma excitation frequency in conventional capacitive discharges, while minimizing powder formation. For instance, a reduction of the interelectrode gap ($d_{\rm gap}$) was shown to bring significant advantages since it allows for a high-density plasma while limiting secondary gas-phase reactions in the plasma, hence favoring the growth of device-grade a-Si:H [Isomura 02] and μc -Si:H [Nakano 06, Strahm 10] at high rates.

However, at these high rates, the formation of nanoporous regions on rough surfaces remains a problem as will be seen in this chapter. The substrate morphology is very important to grow μc -Si:H without any structural defects but becomes even more critical at very high deposition rate. Hence we will see that a morphology which is good for a process at 3 Å s⁻¹ will be very detrimental for higher rates. For instance, sputter-etched ZnO from Jülich is known to provide an excellent surface morphology for the growth of μc -Si:H allowing for very high $V_{\rm oc}$ and FF. As a direct consequence very high deposition rates regimes could be developed more "easily" on this smooth electrode, as compared to LPCVD ZnO (that would favor the formation of nanoporous regions), so that very good single-junction μc -Si:H solar cells could be obtained. However, LPCVD ZnO provides more potential in terms of light-trapping, in particular for micromorphs where a high top cell current is desirable, hence forcing us to develop more the plasma regimes to limit the secondary defective phase formation.

The present work is part of this effort and seeks a deeper understanding of the main requirements for the deposition of high-quality μc -Si:H at very high growth rates above $10\,\text{Å}\,\text{s}^{-1}$. Most of the results presented in this chapter were obtained together with Dr. G. Parascandolo and Dr. K. Söderström.

6.2 PEPPER project

Entitled "Demonstration of high performance Processes and Equipments for thin film silicon Photovoltaic modules Produced with lower Environmental impact and Reduced cost and material use", the FP7 EU PEPPER project [PEPPER 10] is a joint effort involving European laboratories and companies. The goals of the project are to develop a new generation of production lines and demonstrate and partially implement a new technology that will (i) reduce the cost of ownership associated with the fabrication of tandem modules to $0.5 \leqslant /W_p$, (ii) increase module output power to 157 Wp stabilized (corresponding to a conversion efficiency of 11%) and (iii) reduce the environmental impact of the fabrication process with the target of 20% lower energy-payback time.

The breakdown of the different task forces necessary to achieve these goals is shown in Figure 6.1, indicating all the work packages (WPs) and their interactions.

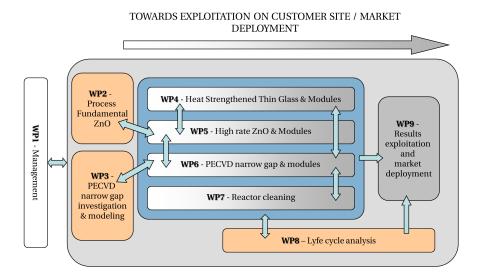


Figure 6.1: PEPPER project work packages.

EPFL was involved, among others, in WP3 "Investigation, modeling and understanding of the different plasma regimes in narrow-gap electrode configurations". This WP investigates in depth plasma regimes for the growth of high-quality μc -Si:H i-layers as a function of $d_{\rm gap}$ with a focus towards high deposition rates of 1.2–1.5 nm s $^{-1}$. Many results were shared with the University of Patras (Greece) in order to assist them with the development of a comprehensive model for parallel-plate PECVD and numerical simulations. This was done to develop a better understanding of the complex interactions between the deposition parameters, the plasma characteristics and, ultimately, the material and solar cell device properties. Cooperation with WP2, which involves the development and understanding of the LPCVD ZnO electrodes (EPFL), was also required, as there is a strong interplay between the front ZnO morphology and the deposited material quality. Finally, a combined effort with WP6, which developed a next-generation industrial reactor (TEL Solar), was also necessary to transfer the knowledge acquired to industry. The main results of WP3 are presented in this chapter.

6.3 Influence of pressure and hydrogen flow

In this section we review the influence of both the deposition pressure and hydrogen flow rate ($\Phi_{\rm H_2}$) on the performance of μc -Si:H solar cells when deposited at a high rate of 1 nm s $^{-1}$. Some of the conditions described here were already shown in Chapter 4. However, the present investigation goes further in the analysis of the plasma regimes. We show that depositing closer to conditions that favor secondary gas-phase reactions is not detrimental to material quality and eventually leads to better-performing μc -Si:H solar cells. This study was done with Dr. Gaetano Parascandolo and Dr. Richard Bartlome and can be found in detail in [Parascandolo 10a].

For this study we used the KAI-M reactor operating at VHF with $d_{\rm gap}=12$ mm. For each of the processes developed, a similar i-layer growth rate of 1 nm s $^{-1}$ was targeted. The silane flow rate ($\Phi_{\rm SiH_4}$) was kept constant at 120 sccm while $\Phi_{\rm H_2}$ was decreased, so that gas residence time increased. The source power density was slightly adjusted to get the same Raman crystallinity factor (ϕ_c) and growth rate (R). Silane depletion (D) was monitored by an IR laser spectrometer in the exhaust line, and powder formation was evaluated by visible laser light scattering (LLS) directly behind the pumping grid of the PlasmaBox (cf. details in Section 2.2). The deposition conditions for the $\Phi_{\rm H_2}$ series done at a constant pressure of 4.5 mbar are detailed in Table 6.1.

Table 6.1: Process details using VHF at 4.5 mbar with input silane concentration c, silane depletion, silane concentration in the plasma c_p , estimated growth rate R_{est} , actual growth rate R, LLS measurement of powder in the exhaust and residence time (τ) .

Process	Φ _{H2} (sccm)	c (%)	D (%)	c_p (%)	$R_{\text{est.}}$ (Å s ⁻¹)	$R (Å s^{-1})$	LLS (mV)	$ au_{ m res.}$ (s)
A	2500	4.6	75.1	1.1	13.6	9.7	43.6	0.23
В	2000	5.7	77.6	1.3	14.0	10.0	73.0	0.28
C	1600	7.0	80.2	1.4	14.5	10.0	114.3	0.35
D	1200	9.1	81.8	1.7	14.8	10.0	136.4	0.45
E	800	13.0	86.6	1.8	15.7	10.0	267.6	0.65

Only minor adjustments of the source power density were required (going from 0.36 to $0.35\,\mathrm{W\,cm^{-2}}$) with decreasing $\Phi_{\mathrm{H_2}}$, while the decrease in residence time led to an enhancement of silane dissociation efficiency, going from 75 to 87%. The estimated deposition rate ($R_{\mathrm{est.}}$) is based on the silane depletion fraction and the assumption that all the dissociated silane contributes to the film growth [Strahm 07b, Bartlome 09]. While a relative increase of 15% is observed for $R_{\mathrm{est.}}$, R which was obtained from layer thickness measurements, stayed constant at 1 nm s $^{-1}$. This increased discrepancy, shown in Figure 6.2a, is due to an increase of silane radicals lost to the formation polysilane or powder, which do not contribute to film growth. The significant increase in powder formation is also confirmed by the LLS measurements, which are summarized in Figure 6.2a as well.

Time-resolved optical emission spectroscopy was used to observe the integrated intensity of the H_2 Fulcher lines (600–630 nm), which is proportional to the electron density [Strahm 09], and the results for processes A to E are shown in Figure 6.2b. A clear difference can be seen going from a powder-free regime (process A, high Φ_{H_2}) to a dusty regime (process E, low Φ_{H_2}): a clear signature of powder formation is observed with a periodic oscillation of the electron density. Clusters form in the plasma and accumulate negative charges while they grow, reducing the electron density. As soon as such clusters are large enough, that they can no longer be confined in the plasma, neutral drag forces expel them from the reactor, allowing the electron density to rise again [Bouchoule 91, Stoffels 95, Johnson 08a].

Although we used deposition conditions close to the onset of large powder particles, we could

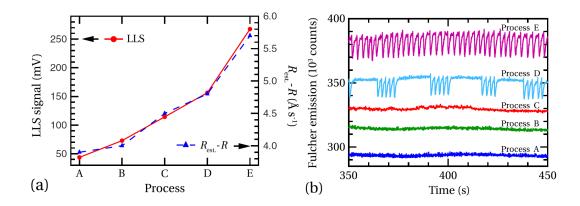


Figure 6.2: (a) Evolution of the LLS signal and difference between the estimated growth rate, obtained from the silane depletion measurement, and the actual growth rate for processes A to E. (b) Time evolution of the H_2 Fulcher emission intensities for processes A to E.

not actually find any powder after the deposition on the large-area aluminum plate for all deposition conditions detailed in this section. Powder is rather typically observed near the exhaust at the pumping grid or near leaks that can be present in the reactor (cf. Appendix B).

A similar plasma study was performed for increased pressures of 5.5 mbar and 7.0 mbar. Φ_{SiH_4} was kept constant at 120 sccm, so that only the power density was varied to keep the same growth rate of 1 mm s $^{-1}$ and the same ϕ_c . Similar observations were made with regard to secondary gas-phase reactions with decreasing Φ_{H_2} , and increased pressure also led to an increase of powder formation as expected from a silane partial pressure increase.

These deposition regimes were used to evaluate the μc -Si:H material quality directly in single-junction μc -Si:H solar cells on Z5 45'. The i-layer thickness was kept at 1.8 μ m and standard μc -Si:H doped layers were used. Figure 6.3 summarizes the conversion efficiencies of these cells.

We see that plasma conditions at the onset of powder formation, with increased silane input concentration, lead to better-performing solar cells. Indeed, regime E, the dustiest one, led to the highest solar cell efficiency (7.1%) of the 4.5 mbar series. As already seen in Chapter 4 for the 5.5 mbar series, we explain that these performance gains are due to a denser μc -Si:H material. At this point, however, it remains difficult to relate the improvement of the material density only to plasma conditions favoring powder formation. We also observe that increased pressure is indeed favorable for solar cell performance, although in this case, the gains could also be ascribed to a reduction of the ion bombardment energy.

Powder is known to greatly influence the plasma parameters and power transfer because of the additional electron energy loss mechanism [Dorier 92, Hollenstein 00]. Although the exact mechanisms involved in the particle charging processes in dusty plasmas remain under investigation, particle formation and charging typically lead to a more resistive *rf* discharge and the

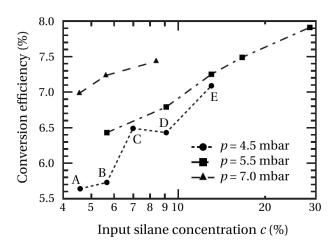


Figure 6.3: Single-junction μ c-Si:H solar cell conversion efficiency as a function of the i-layer deposition pressure and input silane concentration (varying Φ_{H_2}) for a constant high deposition rate of l nm s $^{-1}$.

electron temperature is thought to rise to compensate for the additional electron losses at the clusters [Fridman 96, Takai 00, Takai 01]. It is worth mentioning here that some simulation studies [McCaughey 89, McCaughey 91, Wang 97] showed an opposite effect resulting from the presence of charged particles in the plasma: particles lead to a depletion of the high-energy tail of the electron energy distribution (due to Coulomb scattering from the Debye shield surrounding the particles), effectively reducing the electron temperature (T_e). Furthermore, exactly how T_e affects the growth remains unclear: while it is typically assumed that a lower T_e is favorable to increase the $\Gamma_{SiH_3}/\Gamma_{SiH_{x\leq 2}}$ radical generation ratio [Niikura 07] (as typically observed for the growth of high-quality a-Si:H), experimental studies have suggested the opposite—a higher T_e would be favorable for μc -Si:H [Nakano 06].

Sylene radical (SiH₂) is known to react very rapidly with SiH₄ to give disilane—especially under high-pressure conditions. In this case, the μc -Si:H material is denser for an increased silane concentration in the plasma, meaning SiH₂ radicals are indeed less likely to reach the surface since they have more chance to find a SiH₄ molecule to react with before that (such reaction will be further corroborated by first plasma simulations presented in Section 6.7.2). Another way to explain a possible reduction of short-lived silane radicals such as SiH₂, SiH or Si, reaching the growing film is that under high-pressure conditions they can react very quickly either with higher-order polysilane Si_nH_{2n+2} molecules (with $n \ge 3$) to form polymerized species [Kawasaki 97], or with already-formed larger clusters, hence effectively reducing their chance to stick on the growing silicon surface.

Other possible explanations for the formation of nanoporous zones, such as a change in the sheath thickness or the silane radical generation profiles, cannot be ruled out at this point. Proper $V_{\rm pp}$ measurements could unfortunately not be done during our study, so that we cannot link a time-averaged plasma potential reduction with decreasing $\Phi_{\rm H_2}$ as in Section 3.4.

More in-depth plasma analysis is thus required: impedance measurement in post-match conditions and the use of deposition-tolerant rf biased Langmuir probes would greatly help in investigating the most critical plasma parameters (e.g. impedance modifications, harmonics analysis, ion and electron densities, electron temperature), and thus in understanding the main plasma requirements for the deposition of high-quality μc -Si:H at high rates.

6.4 Impact of the substrate morphology

In this section we review the influence of the substrate morphology on the performance of μc -Si:H solar cells. More specifically, we demonstrate the fact that although some morphologies are suitable for low-deposition-rate processes, they can become strongly unfavorable for higher growth rates. Indeed, the sharpness of the substrate strongly influences the growth dynamics, favoring the rise of nanoporous-phase material.

6.4.1 On the sharpness of the LPCVD ZnO front contacts

For the present study, μc -Si:H solar cells were deposited on different LPCVD ZnO front contacts with varying morphologies. As already discussed in Section 2.1, the morphology can be smoothened through the application of an argon-based plasma treatment [Bailat 06], reducing the overall sharpness of the features while keeping their size similar. Figure 6.4 presents the atomic force microscopy (AFM) topographic images of such substrates.

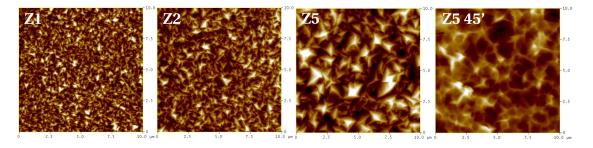


Figure 6.4: AFM topographic images of some of the LPCVD ZnO front contacts used in this study.

Table 6.2 summarizes the parameters which describe the texture of each substrate used in this study. The root mean square of the surface roughness (σ_{RMS}), measured via AFM, together with the average facet inclination are given to describe the sharpness of the substrate features [Cuony 11]. The size of these ZnO pyramidal features is also directly related to their spatial density on the substrate surface as can be seen in the corresponding AFM topographic images.

Table 6.2: Details of the ZnO substrates used for the present study and main parameters describing their surface morphologies. As-deposited Z5 is presented simply for reference, as it was not used for solar cells in this section. For more details, please refer to Section 2.1

Substrate	Z1	Z2	<i>Z</i> 5	Z5 20'	Z5 45'
Thickness (µm)	1.3	2	5.0	< 5.0	<5.0
$\sigma_{\rm RMS}$ (nm)	49	79	184	168	106
Pyramid size (nm)	160	250	600	600	600
Average facet inclination (°)	30	40	45	-	18
Ironed surface (%)	142	155	167	137	115

6.4.2 Single-junction μc -Si:H solar cells

Single-junction μc -Si:H solar cells were deposited on four substrates (Z1, Z2 2', Z5 20' and Z5 45') with three μc -Si:H i-layer VHF PECVD processes at 5.5 mbar with increasing deposition rates R of 3, 9 and 12 Å s⁻¹. The $V_{\rm oc} \times FF$ values of these devices—which account for the overall electrical performance of the devices—is plotted versus R in Figure 6.5a. As expected, a reduction of this product is observed i) for each substrate with increasing R, due to increased bulk defect density as measured via FTPS (going from roughly 2 \times 10⁻³ to 7 \times 10⁻³ cm⁻¹, cf. Figure 6.6b) and ii) for each given R when using a sharper substrate. In Figure 6.5b, the $V_{\rm oc} \times FF$ value is normalized for each substrate with respect to the value obtained for the lowest R of 3 Å s⁻¹. We see that the relative losses versus R are more severe on sharp substrates, indicating that the substrate morphology becomes more critical when increasing R.

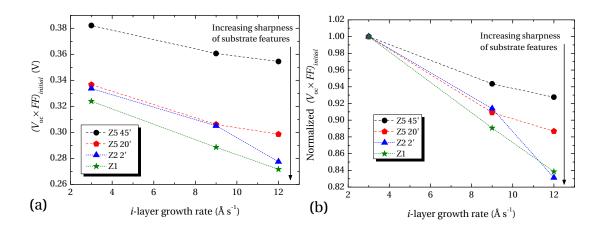


Figure 6.5: (a) $V_{\rm oc} \times FF$ values for devices deposited on the four substrates of Table 6.2 versus R of the i-layers. (b) Same data in (a), but normalized with respect to device performance at the lowest R for each substrate.

In order to get more insight into the relationship between R and substrate morphology, we studied the electrical stability of devices versus dark degradation, *i.e.* degradation of non-encapsulated devices stored in air that is related to water vapor absorption in porous material. Devices were subject to five days of (non-standard) damp-heat tests performed at 50 °C and 100% humidity to simulate accelerated dark degradation (see Section 4.4). Contributions of ZnO to device instability are not excluded but do not influence our results, as we compare device stability versus R for each substrate. After damp-heat tests, the devices were annealed to restore performance upon water vapor desorption.

In Figure 6.6a the $V_{oc} \times FF$ values after a damp-heat test of devices deposited on Z5 45', Z2 2' and Z1 are plotted versus R and are normalized with respect to initial performance.

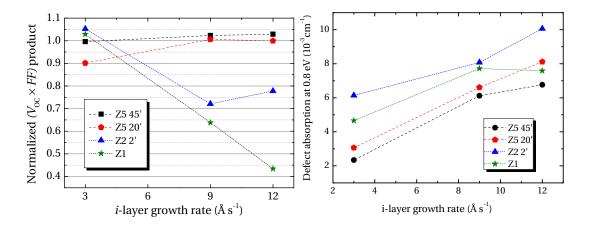
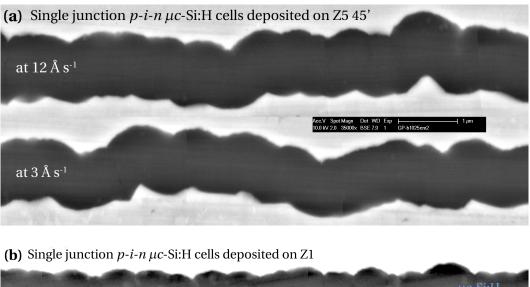


Figure 6.6: (a) Stability with respect to damp heat of the electrical performance of μ c-Si:H solar cells deposited on Z5 45', Z5 20', Z2 2' and Z1 plotted versus i-layer R. The $V_{oc} \times$ FF values are normalized to the initial value, for each substrate and R. (b) FTPS defect absorption value at 0.8 eV of the corresponding solar cells.

We observe that the performance of all devices deposited at $R=3~\rm \AA\,s^{-1}$ is quite insensitive to damp heat, independent of the substrate. Only the cell prepared on Z5 20' shows an unexpected 10% degradation. At higher R, the devices deposited on Z1 and Z2 2' substrates are highly unstable and lose up to 40% of their initial performance, which is not the case for those deposited on smoothed Z5 45' and Z5 20'. Performances were mostly restored upon annealing on all substrates and for all R (not shown). $V_{\rm oc}$ and FF separately display the same behavior as their product (not shown), but it is the instability of FF that mainly drives electrical performance losses, $V_{\rm oc}$ variations being smaller that 10% for all substrates and R. We can also confirm from Figure 6.6b that the bulk quality, as measured with FTPS, is not correlated with stability. Indeed, a much higher defect-related absorption does not lead to a larger damp-heat instability on smooth substrates (cf. R=12 and $3~\rm \AA\,s^{-1}$). $J_{\rm sc}$ was not affected by the experiment.

Further insight is given by cross-sectional SEM images of μc -Si:H films deposited on smooth

Z5 45' and sharp Z1 substrates at 3 and 12 $\text{Å} \, \text{s}^{-1}$, shown in Figure 6.7.



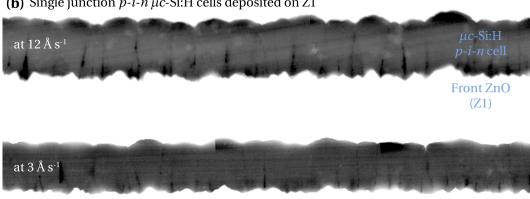


Figure 6.7: Cross-sectional SEM micrographs of μ c-Si:H cells deposited at a high rate of 12 Å s⁻¹ on (a) a smooth Z5 45' and (b) a Z1 with a higher density of sharp pyramids (b).

Films deposited on Z5 45' appear very homogeneous, without any porous regions, and are indistinguishable for the two deposition regimes. On the other hand, although films deposited at $3\,\text{Å}\,\text{s}^{-1}$ on Z1 display a large density of linear nanoporous regions (dark zones in the SEM images) as expected, much larger regions of porous material develop during high-rate growth at $12\,\text{Å}\,\text{s}^{-1}$. This means that the effect of the substrate is not only geometrical: V-shaped valleys favor the formation of cracks, but also influence the film growth dynamics. Instability to damp heat together with the above SEM images, suggests that sharp substrate features act as a morphological barrier to the high-rate growth of compact μc -Si:H films, thus resulting in porous layers whose electrical properties are strongly affected by water vapor ingress.

6.4.3 Filtered μc -Si:H solar cells

In the previous section, we have showed that the influence of the substrate morphology on the performance of μc -Si:H solar cells depends on the PECVD process itself. Here we will focus on studying the effect of "pinching" that typically appears after the a-Si:H top cell in micromorph devices. To investigate this specific pinched morphology on the bottom-cell performance, two pairs of substrates were added in the three deposition runs made at different R presented in the last section. These substrates were i) a Z1 and a Z2 covered with a p-i-n a-Si:H top cell with a 220-nm-thick i-layer suitable for micromorph cells, and ii) a Z1 and a Z2 covered with a similarly thick but conductive n-(a-Si:H) layer [Kluth 09] whose light absorption is similar to that of an a-Si:H top cell and whose surface faithfully reproduces the morphology of the substrates. With substrates ii) we obtained "filtered" single-junction μc -Si:H devices which are expected to simulate the electrical and optical behavior of the bottom cell in a tandem device.

As shown in Figure 6.8, a severe relative loss of electrical performance with increasing R is observed on filtered cells; $V_{\rm oc} \times FF$ decreases 2–3 times more than on non-filtered cells. Moreover, filtered solar cells are observed to be more unstable in damp heat tests than the

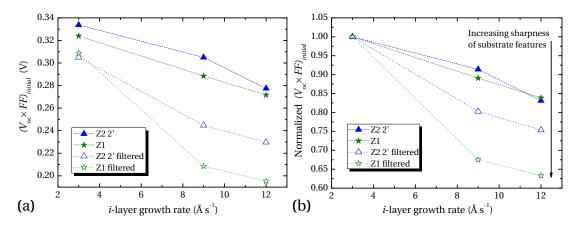


Figure 6.8: (a) Initial $V_{oc} \times FF$ values for devices deposited on Z1 and Z2 substrates (filled symbols, same as in Figure 6.5a) and filtered Z1 and Z2 (empty symbols) versus R of he i-layers. (b) The data in (a) are normalized with respect to device performance at the lowest R, for each substrate.

corresponding non-filtered devices, with $V_{\rm oc}$ variations of up to 20% with respect to the initial value for $R = 12 \,\rm \AA\,s^{-1}$. On the basis of these observations, we expect the top-cell morphology to similarly negatively impact the initial $V_{\rm oc}$ and its stability in micromorph devices.

This expectation is confirmed from the results in Figure 6.9a: micromorph devices deposited on Z2 2' and Z1 have initial (I) $V_{\rm oc}$ values between 1.30 and 1.35 V, depending on R, which increase by 40 to 60 mV upon annealing (A) under vacuum at 200 °C for 20'.

In Figure 6.9b we plot the $V_{\rm oc}$, before and after annealing, of single-junction μc -Si:H cells

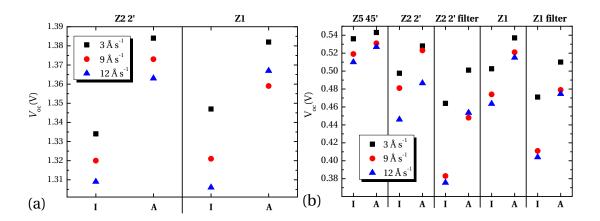


Figure 6.9: (a) Initial $V_{\rm oc}$ (I) and $V_{\rm oc}$ after annealing (A) of micromorph solar cells deposited at different R on Z2 and Z1 substrates. (b) Initial $V_{\rm oc}$ and $V_{\rm oc}$ after annealing of single-junction μ c-Si:H solar cells deposited on Z5 45', Z2 2', Z2 2'filtered, Z1 and Z1 filtered.

deposited on Z5 45', Z2 2', Z2 2' filtered, Z1 and Z1 filtered. The initial $V_{\rm oc}$ s of the micromorph devices in Figure 6.9a are 100 mV lower than expected from the sum of the $V_{\rm oc}$ s of single-junction deposited on optimum Z5 45' substrates and that of a standard top a-Si:H cell ($V_{\rm oc} \approx 900$ mV); considering the $V_{\rm oc}$ s of single-junction cells deposited on Z2 2' and Z1 (Figure 6.9b), the micromorph $V_{\rm oc}$ s are still 50 to 70 mV lower than expected. Such a loss does not come, as is often suggested, from the recombination junction: looking at the $V_{\rm oc}$ s of filtered cells, we see that the top-cell morphology almost totally accounts for the $V_{\rm oc}$ loss in micromorph devices, the effect of the recombination junction being on the order of 10 mV, if present. Moreover, the $V_{\rm oc}$ increase upon annealing is comparable for filtered and micromorph devices. Note that approximately 20 mV of $V_{\rm oc}$ is lost in all cases (compared to sum of the individual sub-cells' $V_{\rm oc}$ s) because of the lower current in the bottom cell as compared to a single-junction cell.

SEM images can help us understand these observations about tandem devices: indeed, the plan-view SEM images in Figure 6.10 demonstrate that our top-cell deposition process does not smooth out the V-shaped valleys of the LPCVD ZnO substrate, but rather gives rise to pinch points with narrowed opening angles. These narrowed openings further increase the potential of large cracks to propagate, mainly due to shadowing, as further confirmed by the cross-sectional view SEM micrographs on cells deposited on Z1 filtered presented in Figure 6.11.

Interestingly, we observe that micromorph devices display improved stability of electrical properties over damp heat/annealing cycles compared to single-junction μc -Si:H and filtered single-junction μc -Si:H solar cells deposited on the same TCO, as shown in Figure 6.12. In this figure, the post-deposition treatment T refers to a H₂ plasma on the completed cells. This treatment serves two purposes: i) it provides an annealing step under vacuum for the

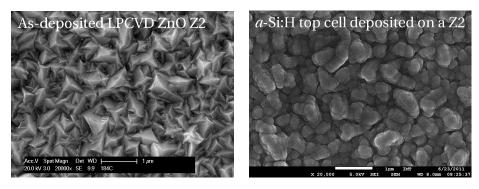


Figure 6.10: Plan-view SEM micrographs at a magnification of 20 000× of a Z2 substrate (left) and a Z2 on top of which an a-Si:H top-cell was deposited (right).

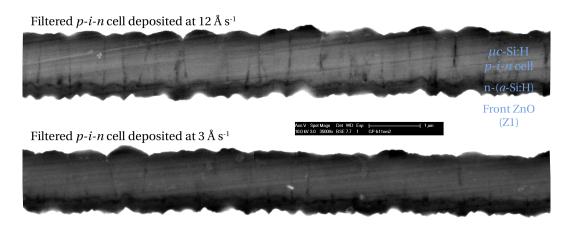


Figure 6.11: Cross-sectional SEM micrographs of μ c-Si:H cells deposited on Z1 filtered at a high rate of 12 Å s^{-1} (top) and at a lower rate of 3 Å s^{-1} (bottom).

 μc -Si:H cell, and ii) it leads to a significant increase in the LPCVD ZnO conductivity as detailed in [Ding 13].

The electrical behavior of the tandem devices is dominated by the a-Si:H top cell which are responsible for roughly two-thirds of the power generated in the devices. This partly explains the better stability of the tandem cells compared to the filtered cells. Still, while the $V_{\rm oc}$ of a tandem cell is roughly the sum of the $V_{\rm oc}$ s of the component sub-cells as previously discussed, the FF depends in a non-trivial way on the contributions of the sub-cells, the current-matching condition and, more generally, the overall device design. Significant efforts are thus currently underway to correctly separate the contributions of the top and bottom cells to the performance of a tandem device. Several methods are being tested in our laboratory, such as the use of filtered μc -Si:H cells, as in the present study, or the development of a current-matching machine [Bonnet-Eymard 13].

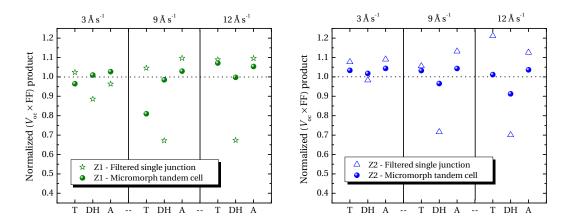


Figure 6.12: $V_{oc} \times FF$ stability of filtered μc -Si:H (stars) and micromorph tandem (marbles) devices with respect to post-deposition treatment (T), damp heat (DH) and annealing (A) versus μc -Si:H i-layer R. The $V_{oc} \times FF$ values are normalized to the initial value for each substrate and R. Devices deposited on Z1 (left) and Z2 (right) are compared.

6.4.4 Conclusion

In this section we examined the interplay between substrate morphology and the PECVD process, showing that a morphology that is compatible with low-deposition-rate processes can be highly detrimental to devices deposited at higher rates. Sharp substrate features enhance the development of nanoporous regions along the film thickness that can then act as bad recombination diodes and reduce device stability. When depositing at a higher rate, the probability of growth precursors finding a favorable site before being incorporated into the film is reduced, and shadowing can further limit the deposition of dense material at the bottom of the valleys. We have shown as well that, for micromorph devices, even on smoother substrates, the a-Si:H top cell typically presents a surface for the μc -Si:H bottom-cell deposition that is highly unfavorable due to pinching points, inducing a significant $V_{\rm oc}$ loss. More in-depth understanding is thus required to grow a dense μc -Si:H material at high deposition rates on rough surfaces.

6.5 Influence of the interelectrode gap

In this section we review the role of the $d_{\rm gap}$ in determining the deposition rate of device-grade μc -Si:H material. During the PEPPER project, we were able to optimize μc -Si:H layers using three different interelectrode distances in our KAI-M reactor, namely 22, 12 and 9 mm. To reach 9 mm we had to modify our aluminum loading plate so that it properly enters the reactor without any risk of the substrate touching the top electrode, even when lifted up by the pins. Grooves were defined in the bottom of the aluminum plate for that purpose as can be seen in Figure 6.13.

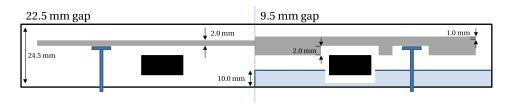


Figure 6.13: Section view of the aluminum spacer installed at the bottom of the reactor to reduce the interelectrode gap from 22 (left) to 9 mm (right). The drawing is not to scale.

For a given $d_{\rm gap}$, we optimized the μc -Si:H i-layer recipe for the highest deposition rate achievable. Practically, we tried to find the best combination of deposition pressure and power density for the highest target growth rate. However, some limitations were observed for a given $d_{\rm gap}$, as too high pressures or $\Phi_{\rm SiH_4}$ led instead to a decrease of the film growth rate. Indeed, above a certain point, as the pressure or $\Phi_{\rm SiH_4}$ is further increased, more polysilane and powder formation is observed, increasing the number of silane radicals that are lost and do not contribute to the growth of the film. A reduction of the interelectrode distance can overcome this issue mainly by promoting surface reactions on the electrodes instead of volume reactions in the plasma that lead to powder formation [Strahm 10].

In Figure 6.14a, we summarize the best $V_{\rm oc} \times FF$ values of μc -Si:H solar cells prepared on Z5 45' that were obtained for each $d_{\rm gap}$, with an emphasis on the highest growth rate achievable. The cells were similar in terms of thickness (1.2–1.3 μ m) and design, with SiO $_x$ doped layers, so that only the i-layer was varied. The cells were annealed before being measured.

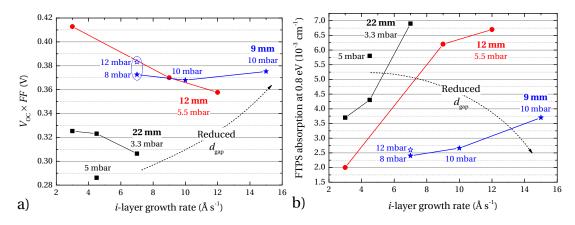


Figure 6.14: (a) Best $V_{\rm oc} \times$ FF values obtained for each $d_{\rm gap}$ using the best deposition pressure found for the highest target growth rate. (b) Associated defect-related absorption value at 0.8 eV as measured by FTPS.

For the largest gap of $d_{\rm gap}$ = 22 mm, we observe that the $V_{\rm oc} \times FF$ values, which are relatively low, drop significantly with increasing R from 3 to 7 Å s⁻¹. Higher growth rates could not be

obtained as a significant fraction of silane radicals are lost to polysilane and dust formation. Narrowing $d_{\rm gap}$ down to 12 mm shifts the formation of powder to a higher pressure threshold, so that an increased deposition pressure of 5.5 mbar could be used without any powder issues. We observe that significantly better-performing devices are obtained for similar R and above, with an increase of roughly 30% in the $V_{\rm oc} \times FF$ values over the same R range. A much higher deposition rate of 12 Å s⁻¹ could also be reached, thanks to reduced secondary gas-phase reactions, allowing for more silane radicals to actually contribute to the growing film. Still, we again observe this trend of decreasing $V_{\rm oc} \times FF$ values for increasing growth rates. Further reduction of $d_{\rm gap}$ to 9 mm allowed us to use even higher pressures such as 8–12 mbar, resulting in improved solar cell performance at larger deposition rates of up to $R=12\,{\rm Å\,s^{-1}}$. A conversion efficiency of 9.3% was obtained for a single-junction μc -Si:H solar cell on Z5 45'. Since we had insufficient time to optimize a new p-SiO $_x$ layer and p-i interface using the narrow gap of 9 mm, we believe $V_{\rm oc} \times FF$ could be even higher.

The defect-related absorption of these μc -Si:H solar cells was measured by FTPS and is shown in Figure 6.14b. This analysis demonstrated that working at higher pressures, with a narrow gap, allows for the deposition of very high quality μc -Si:H material at higher R. By reducing $d_{\rm gap}$ from 22 to 12 mm, we can keep a comparable defect-related absorption value at almost twice the maximum R value. Then, going from $d_{\rm gap} = 12$ to 9 mm and using higher deposition pressures, the defect absorption value is further reduced and an even lower value is finally measured for R= 15 Å s⁻¹ than for 3 Å s⁻¹ in the larger $d_{\rm gap} = 22$ mm configuration. Such improvements can either be attributed to a reduction of ion bombardment, which results from the increased deposition pressure, or to the plasma chemistry favoring SiH₃ radicals, as further discussed in the next section.

6.6 RF vs. VHF with reduced interelectrode distance

As a follow up to the comparative study of excitation frequencies presented in Chapter 5, both RF and VHF were again evaluated but with $d_{\rm gap} = 9$ mm and at a higher growth rate of 7 Å s⁻¹.

A pressure series for the deposition of a 1.3 µm thick i-layer was thus performed for both frequencies and single-junction solar cells results on Z5 45' are presented in Figure 6.15a. It is shown that the deposition pressure does not have a strong impact on the solar cell performances prepared using VHF, with efficiencies remaining quite stable over the range of pressure studied. The bulk defect-related absorption slightly decreases with increasing pressure though, going from 3.3×10^{-3} cm⁻¹ at 6 mbar to 2.2×10^{-3} cm⁻¹ at 12 mbar. On the other hand, the performances of solar cells prepared using RF strongly rely on the deposition pressure, going from only 6% at 6 mbar up to 9.1% at 15 mbar. The quality of the bulk phase, as assessed by the FTPS measurement, is largely improved as well with increasing pressure. We attribute the different behavior to the associated decreasing ion bombardment energy when using VHF and the reduced power density required (≈ 0.25 W cm⁻²) as compared to RF (≈ 0.5 W cm⁻²).

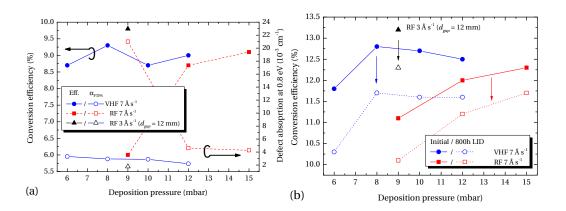


Figure 6.15: (a) Conversion efficiency (filled symbols) and defect-related absorption (empty symbols) of single-junction μ c-Si:H solar cells as a function of deposition pressure using either RF (red) or VHF (blue). (b) Conversion efficiency of co-deposited micromorphs at initial state (filled symbols) and degraded state after 800 h LID (empty symbols). The baseline process using the process at $d_{gap} = 12$ mm, 9 mbar using RF is indicated as a reference (black).

Micromorphs were prepared on as-grown Z5/2 front-contact (cf. details in Section 2.1) with a 220 nm thick a-Si:H top cell deposited in a KAI-M reactor, and had their bottom cell codeposited with the single-junctions. We observe in Figure 6.15b that tandem cells prepared using VHF at pressures equal or above 9 mbar have relatively stable and comparable values both in intial and after 800 hours of LID states. When using RF, a very high pressure of 15 mbar is required in order to get similar conversion efficiency values, demonstrating that the use of VHF using the narrow-gap configuration of $d_{\rm gap}$ = 9 mm is not as detrimental as for $d_{\rm gap}$ = 12 mm and 22 mm (cf. Chapter 5). Indeed, the $V_{\rm oc}$ in this case stays very stable for both excitation frequencies. However, we still notice that the relative degradation is lower with RF thanks to higher FF, which may be an indication that although the bulk material of RF is worse (cf. Figure 6.15a), it is still slightly more dense. The best micromorph stabilized efficiency attained was 12.3% using VHF at 10 mbar and is presented in detail in Section 9.2.

We also evaluated the influence of a reduced $\Phi_{\rm H_2}$ when using VHF at 8 mbar and in this case, going from 2500 sccm to 800 sccm, no improvement in single-junction μc -Si:H solar cell performance was observed, contrary to $d_{\rm gap}$ = 12 mm (cf. Section 6.3). We even observed a slight decrease of the conversion efficiencies, with a reduced $\Phi_{\rm H_2}$, going from 9.3% to 8.7%. It could also be related the shift of the onset of powder formation when using such a narrow gap reactor that prevented us from observing a similar effect.

6.7 Modeling of gas-phase and μc -Si:H film growth mechanisms

To further understand the underlying physics of the growth process and explain some of our experimental observations, simulations were performed by the University of Patras, using a

fluid model for silane-based rf discharges. Different sets of plasma deposition conditions were shared with the University of Patras, within the PEPPER project, and some of the first results are presented here.

6.7.1 On the role of radicals contributing to the growth

The growth of high-quality a-Si:H and μc -Si:H obtained by PECVD relies, to a significant extent, on the surface reaction kinetics of the different silane radicals. It has been observed that the contribution of monoradicals such as SiH₃ and Si₂H₅ is beneficial to obtain a dense film with good conformal step coverage and a smooth surface. Such radicals have only one dangling bond and can diffuse over large distances on the growing surface—almost fully passivated by hydrogen—before finding a suitable silicon dangling-bond to form a Si-Si bond [Tsai 86, Abelson 93]. Such growth is typically referred to as a surface-rate-limited chemical vapor deposition (CVD) process, as opposed to what can happen in a physical vapor deposition (PVD) process in which highly reactive radicals (e.g. SiH₂, SiH, Si) lead to poor step coverage, a rough surface and columnar structures. A grid system was used to measure the sticking coefficients of SiH₃ and Si₂H₅ [Perrin 98]. These observations are summarized in Figure 6.16.

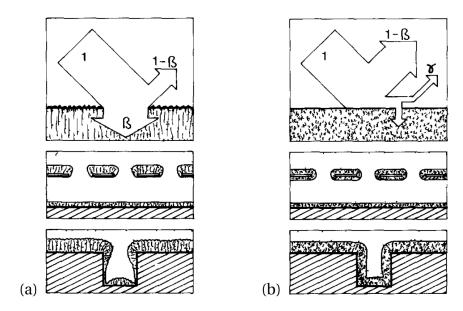


Figure 6.16: General view of surface-reaction processes. In (a) silane radicals have a high surface reaction probability β , leading to poor step coverage, a rough surface and columnar structures. In (b) silane radicals have a low β value leading to CVD-like growth conditions with good conformal step coverage, and a dense and smooth film. The top two figures show the probabilities of re-emission $(1-\beta)$ and recombination at the surface (γ) that produces volatile products (e.g. SiH₄ and Si₂H₆). The middle two figures illustrate the deposition thickness distribution on the grid device used for sticking probability measurement, and the bottom two figures describe the corresponding step coverage. Figure taken from [Schmitt 89].

Another crucial parameter for a-Si:H and μc -Si:H growth, frequently mentioned in this thesis, is the ion bombardment energy, which also affects growth kinetics. It is now commonly accepted that moderate ion energies can favor the growth of a denser microstructure and smoother surfaces for a-Si:H [Drevillon 83, Abramov 98, Dalakos 04, Smets 07], a-SiGe:H alloys [Perrin 89] or μc -Si:H [Bronneberg 12a]. This is especially true when highly reactive radicals are involved in the deterioration of the material, in which case a higher ion bombardment energy can enhance the surface mobility and diffusion of adsorbed radicals on the surface, leading to densification of the material.

6.7.2 Simulations of PECVD of μc -Si:H

To get a more in-depth understanding of the plasma conditions that effectively lead to a good μc -Si:H material quality, we present in this section a first glimpse of the simulation results based on some of the plasma conditions presented in this thesis. Dr. Lefteris Amanatides, from the University of Patras, is in charge of the plasma simulation code development and performed all the analysis. Dr. Spyros Sfikas is also acknowledged for all the simulations and analysis done within the collaboration.

The simulations are based on a two-dimensional code that includes all the main physical and chemical processes that take place during SiH_4/H_2 plasma deposition. Namely, the simulation accounts for gas mixture flow, heat transfer in the reactor, ion and electron masses, momentum and energy balance, gas phase and surface chemistry, and electromagnetic propagation in the rf electrode and plasma. A set of 25 species together with a total number of 112 reactions (85 in the gas phase and 27 surface gas interactions) is included in this version of the model. The chemistry of polysilane formation was also added to the model during the project: all possible polymerization processes were taken into account, including small polysilane formation (up to 12 Si atoms) through negative ions, cations and free radicals. The simulations were performed for the geometry of our PlasmaBox KAI-M reactor. A detailed description of the model can be found in [Lyka 06], and an updated description is given in [Amanatides 11].

VHF hydrogen flow rate series

The $\Phi_{\rm H_2}$ series performed using VHF at a constant pressure of 5.5 mbar and growth rate of $10\,{\rm \AA\,s^{-1}}$ with $d_{\rm gap}$ = 12 mm was chosen for further investigation through simulation. Indeed, we could evidence with this series that reduced $\Phi_{\rm H_2}$ leads to a denser μc -Si:H material on textured substrates (cf. Sections 4.2.1 and 6.3).

The rf voltage on the electrode was scaled in the simulation to match the experimentally observed deposition rate. The ion bombardment energy flux $\phi_{\rm ion}$ was calculated as well. We also report the ratio of the monoradicals SiH₃ and Si₂H₅ over the highly reactive radicals SiH and SiH₂, *i.e.* $\Upsilon = (\text{SiH}_3 + \text{Si}_2\text{H}_5)/(\text{SiH} + \text{SiH}_2)$. The results of the simulations are presented in a condensed form in Table 6.3.

110

$\Phi_{ m H_2}$ (sccm)	Voltage (V)	Power (W)	n_e (10 ¹⁰ cm ⁻³)	$\phi_{\rm ion}$ (mW cm ⁻²)	Υ (10 ³)
300	80	487	2.25	2.52	39.1
600	95	576	2.15	3.15	6.9
800	90	524	1.80	3.47	4.1
1200	105	646	1.80	3.58	2.9

1.55

3.52

2.4

690

Table 6.3: Plasma parameters calculated by the simulation code for the Φ_{H_2} series done using VHF at a constant pressure of 5.5 mbar and growth rate of $10\,\mathrm{\AA\,s^{-1}}$ with $d_{gap}=12$ mm.

We see that Υ significantly increases with low Φ_{H_2} values. The loss of highly reactive silane radicals happens mainly through the following reactions:

$$SiH + SiH_4 \xrightarrow{k_1} Si_2H_5, \text{ with } k_1 = 6.9 \times 10^{-10} \times \left[1 - (1 + 0.44 \times p[\text{mbar}])^{-1}\right] \text{ (cm}^{-3} \text{ s}^{-1}), \text{ and } SiH_2 + SiH_4 \xrightarrow{k_2} Si_2H_6^{**}, \text{ with } k_2 = 2 \times 10^{-10} \times \left[1 - (1 + 0.44 \times p[\text{mbar}])^{-1}\right] \text{ (cm}^{-3} \text{ s}^{-1}).$$

 ${
m Si}_2{
m H}_6^{**}$ can then react with atomic hydrogen to form ${
m Si}_2{
m H}_5$. The rate constants k_1 and k_2 , taken from [Perrin 96], are a function of pressure as the products require third-body stabilization. The increased rate at which SiH and SiH $_2$ are lost is linked to the higher silane density in the reactor. Indeed, the silane concentration in the plasma c_p , as measured by an IR laser spectrometer in the exhaust line, increases going from 1.1% at $\Phi_{\rm H}_2$ =2000 sccm to 2.3% at $\Phi_{\rm H}_2$ =600 sccm, while Y increases by a factor > 2 (recall that c and D increase as well, going from 6 to 17%, and 80 to 85%, respectively over the same $\Phi_{\rm H}_2$ range). c_p could unfortunately not be measured in the lowest $\Phi_{\rm H}_2$ =300 sccm conditions due to experimental limitations (cf. details in Section 4.2.1 and Table 4.1).

RF pressure series

2000

The pressure series performed using RF at a constant growth rate of 5 Å s⁻¹ with $d_{\rm gap}$ = 12 mm was also selected as an interesting set of conditions to perform plasma simulations. In this case, we observe a steady decrease in the μc -Si:H bulk defect-related absorption as the pressure is increased (cf. Section 5.3.1). The results of the simulations are presented in a condensed form in Table 6.4.

As expected, $\phi_{\rm ion}$ decreases with increasing pressure, going from 0.7 mW cm⁻² at 6 mbar to 0.3 mW cm⁻² at 15 mbar. A significant increase in Y with increasing pressure is also observed. Here, the important losses of highly reactive species, such as SiH and SiH₂, are related mostly to an increase in secondary gas-phase reactions with hydrogen which are favored under high-pressure conditions, such as

Pressure (mbar)	Voltage (V)	Power (W)	n_e (10 ⁹ cm ⁻³)	$\phi_{\rm ion}$ (mW cm ⁻²)	Υ (10 ³)
6	220	422	3.35	0.67	26.8
9	160	351	3.20	0.39	40.1
15	110	234	2.25	0.30	148.2

Table 6.4: Plasma parameters calculated by the simulation code for the pressure series using RF at a constant growth rate of $5\,\text{Å}\,\text{s}^{-1}$ with $d_{gap} = 12$ mm.

SiH + H₂
$$\xrightarrow{k_3}$$
 SiH₃, with $k_3 = 2 \times 10^{-12} \times \left[1 - (1 + 0.04 \times p[\text{mbar}])^{-1}\right] (\text{cm}^{-3} \text{ s}^{-1})$, and SiH₂ + H₂ $\xrightarrow{k_4}$ SiH₄, with $k_4 = 3 \times 10^{-12} \times \left[1 - (1 + 0.04 \times p[\text{mbar}])^{-1}\right] (\text{cm}^{-3} \text{ s}^{-1})$.

The rate constants k_3 and k_4 also depend on pressure and are again taken from [Perrin 96]. In Figure 6.17 we compare generation rate profiles of SiH₃ and SiH radicals and their steady-state densities in the plasma. We see that the steady-state profile of SiH radicals is very close to the generation profile. This is due to the highly reactive nature of this radical especially under high-pressure conditions that favor secondary gas-phase reactions and limit its diffusion. On the other hand, the steady-state density profile of SiH₃ radicals has a bell shape. This is an indication that diffusion dominates mass transport and SiH₃ losses are determined mainly by surface reactions.

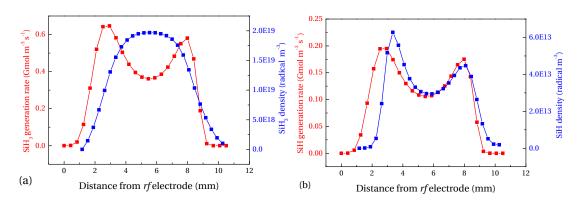


Figure 6.17: Generation profiles and steady-state densities of SiH₃ radicals (a) and SiH radicals (b) using RF at 15 mbar for $R=5\,\text{Å}\,\text{s}^{-1}$ and $d_{gap}=12$ mm (cf. details in text).

In Figure 6.18a the average electron temperature profile is plotted for increasing plasma deposition pressure. The profiles tend to smooth out with increasing pressure, with lower values near the sheaths and higher values in the bulk of the plasma. This is due to the much higher concentration of negative ions at high pressures. Indeed, the density of the most dominant $\mathrm{Si}_2\mathrm{H}_5^-$ anion is about three times higher at 15 mbar as compared to 9 mbar.

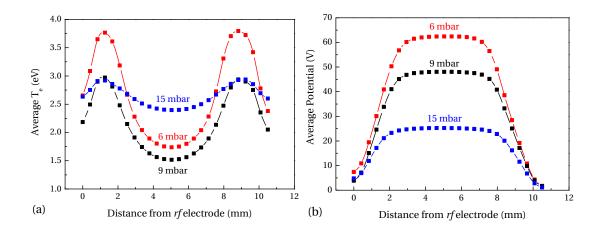


Figure 6.18: (a) Average electron temperature and (b) potential profiles as a function of deposition pressure using RF at 15 mbar for $R=5\,\mathrm{\mathring{A}\,s^{-1}}$ and $d_{gap}=12$ mm (cf. details in text).

These ions are much heavier than electrons and SiH $_3^+$ ions and their transport is much slower. These anions can induce charge separation and strong short-range fields in the bulk of the plasma that tend to heat up electrons, raising their temperature to maintain the quasi-neutral condition. In Figure 6.18b the average plasma potential is seen to decrease with increasing pressure going from \approx 60 V at 6 mbar to \approx 25 V at 15 mbar. With the increase in pressure, we need to decrease the applied rf voltage, which is an input parameter for the simulation, in order to obtain the same deposition rate.

6.7.3 Conclusions and perspectives on the plasma simulations

These are only the first analyses of the set of conditions shared with the University of Patras. The encouraging results highlight the important contributions of the different silane radicals to the growth of the film. In both sets reported improvement in the μc -Si:H quality is associated with an increased $\Upsilon = (SiH_3 + Si_2H_5)/(SiH + SiH_2)$ ratio of radicals contributing to the film growth. An in-depth analysis of these results is still required and will be pursued. Further improvements to validate the simulation code should also be continued (e.g. systematic measurements of $V_{\rm pp}$, $T_{\rm e}$ and actual power coupled into the plasma). Furthermore, the development of a kinetic Monte Carlo code for the simulation of growth kinetics is also underway at the University of Patras. In this code, the species fluxes towards the surface can be imported as an input and simulations should provide important microstructure parameters of the silicon thin films (e.g. ϕ_c , microstructure factor, hydrogen content, roughness, formation of cracks, etc.). The development of such simulation tools are of the utmost importance to TF Si technology in general and for PV in particular, as they elucidate the physics that would otherwise remain hidden from the experimentalist so that a better understanding may hopefully lead to an improved control of the material.

6.8 Conclusion

In this chapter, we demonstrated that an increase in secondary gas-phase reactions, as obtained here with reduced $\Phi_{\rm H_2}$, as well as increase in pressure, both favor the growth of dense μc -Si:H material, leading to better-performing solar cells. The strong interplay between the μc -Si:H growth rate and substrate morphology with regard to the formation of nanoporous regions was also clearly shown. The beneficial effect of reduced interelectrode distances is validated: with a reduction in powder formation, the use of higher pressures becomes accessible, improving gas utilization efficiency and reducing ion bombardment energy at high growth rates. This results in improved material quality, as assessed by FTPS, and very high-performance μc -Si:H solar cells. While the use of RF instead of VHF with the narrow gap configuration led to a more defective bulk phase (requiring very high power densities), which limited the solar cell efficiencies, the cells were also more stable, which suggests that the formation of nanoporous regions formation was less favorable.

In the second half of this chapter, the important role of the contributions of the different silicon radicals to silicon growth were discussed in the framework of simulations performed in collaboration with the University of Patras. In light of the first simulation results discussed, it seems like secondary gas-phase reactions, which are favored at higher pressures, are possibly the main reason for a decrease in the detrimental participation of highly reactive species, such as SiH and SiH_2 . High-pressure plasmas are thus desirable to promote the relative contribution of SiH_3 and Si_2H_5 , provided significant powder formation is not an issue, which can be solved by further reducing the interelectrode distance.

Overall, this chapter evidences the need for better control of the growth kinetics of thin-film silicon, in particular for PV applications, where high growth rates must be combined with highly textured substrates.

7 Intrinsic stress in μc -Si:H

In this chapter, intrinsic compressive stress within μc -Si:H i-layers is evaluated and tentatively correlated to structural characterization of the material or the associated solar cell performance. In Section 7.3, we demonstrate a trend in which low-stress μc -Si:H favors improved cell performance. We observe that increased pressure and depletion tend to reduce intrinsic stress in the material. In Section 7.4, we show that intrinsic stress is closely related to the bulk defect density of μc -Si:H i-layers deposited at the same growth rate, assuming the same Raman crystalline fraction. However, similarly as with FTPS or FTIR spectra, we demonstrate in Section 7.5 that intrinsic stress tests are unable to discriminate between materials with identical bulk quality signature but leading to a porous or a dense material once integrated in an actual solar cell.

7.1 Introduction

Intrinsic stress analysis of thin films gives important clues about their actual growth conditions [Hu 91, Windischmann 91]. Ions with moderate energies significantly improve the quality of deposited *a*-Si:H—by promoting surface diffusion, decreasing the material porosity (density of nanosized voids), and reducing defect density [Hamers 98, Smets 06]. Increasing ion bombardment energy is typically associated with a stress reversal, going from tensile to compressive. However, higher-energy ions can lead to detrimental effects by creating further vacancies within the material (*e.g.* through Si atom bulk displacement) and reducing the growth rate because of ion-sputtering processes.

In particular, hydrogen was shown to play a determining role in the compressive stress build-up towards μc -Si:H nucleation [Kroll 96, Fujiwara 02]: H insertion within the a-Si:H film leads to high Si–Si strained bond density and the creation of more SiH $_n$ (n=1–2) complexes. In view of this, we also understand how high-energy ion bombardment, which can involve H $^+$ implantation, may favor the formation of porous layers and be beneficial for the nucleation of crystallites [Kalache 03]. Interestingly, there is a link between compressive stress in a-Si:H and photodegradation [Stutzmann 85, Powell 02]. Compressive stress can lead to further

weakening of short strained Si-Si bond affecting the kinetics of dangling bonds creation upon light soaking.

Since μc -Si:H quality was shown to be driven by the quality of both bulk and porous zone phases (see Chapter 4), we want to examine whether intrinsic stress on its own can give relevant information about those phases. Different methods exist to evaluate intrinsic stress in μc -Si:H films, namely: (i) the shift of the c-Si mode with Raman spectroscopy (although limited by the penetration depth of the wavelength used), (ii) the broadening of XRD peaks and (iii) the wafer bending method. The latter was chosen as it gives a macroscopic estimation of the stress in our material close to the transition region (Raman crystallinity factor ϕ_c of 60%–70%), as opposed to the other two methods which rely on the stressed crystalline phase only.

7.2 Experimental details

A medium-sized KAI system was used to deposit all the μc -Si:H layers and solar cells in this study (see details in Section 2.1). The KAI-M interelectrode distance was set at 12 mm, the deposition temperature was set at 180 °C, and the excitation frequency was set at 40.68 MHz.

Layers were co-deposited on both Schott AF45 glass substrates and silicon wafer to analyze their properties. Micro-Raman spectroscopy was used to estimate ϕ_c of the μc -Si:H layers [Vallat-Sauvain 06], using the emission line of an Ar⁺ laser at 514 nm. Special care was taken to always have comparable ϕ_c . Spectroscopic ellipsometry measurements were conducted over a wide energy range (0.6–6.0 eV) with a phase-modulated spectroscopic ellipsometer (UVISEL 2 Horiba Jobin Yvon) to precisely assess film thickness and composition on both types of substrate.

Stress measurements were done with μc -Si:H layers deposited on Si(100) wafer strips with an *Ambios XP-2* surface profiler. Wafer strip were 50 × 8 × 0.3 mm³ for the low-deposition-rate regimes (Section 7.3) and 50 × 10 × 0.3 mm³ for the high-rate regimes (Section 7.5) and the pressure series (Section 7.4). Intrinsic stress in the film (σ) was calculated using Stoney's formula

$$\sigma = \frac{1}{6r} \frac{E}{(1-\nu)} \frac{d_{\rm s}^2}{d_{\rm f}},\tag{7.1}$$

with r the radius curvature, approximated here as $r=L^2/8B$ with the wafer strip length L and bow height B (as $L\gg B$), E Young's modulus of silicon, v Poisson's ratio, d_s the substrate thickness and d_f the deposited film thickness [Brenner 49]. The ratio E/(1-v) value was taken as 180.5 GPa as reported in [Brantley 73] for Si(100). Based on the uncertainties in the determination of L, B and d_f , we estimated the error for total stress to be within 20 MPa.

Standard p-i-n solar cells were prepared to evaluate the material quality of approximately 1- μ m-thick μ c-Si:H absorber layers. The front contacts were Z5 45' textured zinc oxide treated

by an argon-based plasma, and the back contacts a Z2 (see details in Section 2.1). The back contacts were also covered with a white dielectric reflector. Open-circuit voltage ($V_{\rm oc}$) and fill factor (FF) were derived from current-voltage curves, obtained using a Wacom AM1.5G solar simulator, and short-circuit current density ($J_{\rm sc}$) was derived from external quantum efficiency (EQE) measurements.

7.3 First observations at low deposition rates

In this section, plasma diagnostic techniques and thin-film material characterization were used to identify the deposition parameters necessary to obtain low-stress μc -Si:H, and to investigate its performance when used as an absorber layer. A relationship between low intrinsic stress in the deposited i-layer and better-performing solar cells is identified.

7.3.1 Plasma deposition conditions

A power series for the deposition of the μc -Si:H i-layer was done at a pressure of 3.5 mbar using VHF. The silane flow (Φ_{SiH_4}) was adjusted to keep comparable ϕ_c of between 50 and 60% within the i-layer for all regimes. Silane dissociation efficiency (D) was evaluated by tunable IR laser spectrometry, allowing the analysis of rotovibrational absorption lines of silane directly through the exhaust line of the deposition system [Bartlome 09]. This allowed for the estimation of both the silane concentration in the plasma (c_p) and the expected growth rate of the film. Powder formation was diagnosed using visible laser light scattering in the exhaust line of the reactor. Table 7.1 summarizes the deposition conditions of the μc -Si:H i-layers that were used in the solar cells and characterized in this section.

Freq.	p (mbar)	P_d (W cm ⁻²)	R) (Å s ⁻¹)	Φ _{SiH4} (sccm)	Φ _{H2} (sccm)	D (%)	<i>c_p</i> (%)	$ au_{ m res.}$ (s)
VHF	3.5	0.05 0.10 0.15	1.4 1.8 2.5	50 53 60	2000 2000 2000	22.9 32.5 34.3	1.9 1.7 1.9	0.23 0.23 0.23
VHF	3.5 7.0	0.10 0.15	2.0 3.7	32 43	800 2500	54.6 41.5	1.7 1.0	0.55 0.45
RF	5.0, 22 mm gap	0.10	1.7	26	2500	-	-	0.47

Table 7.1: Summary of \mu c-Si:H i-layer deposition conditions.

A high silane dilution in hydrogen (Φ_{H_2}/Φ_{SiH_4}) of between 33 and 40 was used to minimize powder formation. The absence of powder was further confirmed by a laser-light scattering experiment and silane depletion measurements, which indicated that all silane dissociated

in the plasma contributed to film growth. Based on these deposition regimes, we developed two new regimes with increased silane depletion—through increased pressure or reduced Φ_{H_2} —which was already identified as an important factor for material quality in previous chapters.

Time-resolved optical emission spectroscopy (OES) was also used as a non-intrusive diagnostic technique [Fantz 98, Howling 07] for the power series. Emission intensities from the $\rm H_2$ Fulcher (600–630 nm) and $\rm G_0B_0$ (461–464 nm) lines were integrated as both originate from electron-impact excitation of the $\rm H_2$ ground state but with different emission-rate-coefficient dependencies on electron temperature $\rm T_e$. Hence the ratio $\rm I_{\rm G_0B_0}/\rm I_{\rm Ful}$ allows us to check $\rm T_e$ variation over time, and in particular from ignition to steady-state equilibrium. SiH* emission (409–423 nm), originating from electron impact SiH₄ excitation, along with proper $\rm H_2^*$ background subtraction, was used to derive information about silane density in the plasma.

Time-resolved OES measurements, presented in Figure 7.1, show that the ratio of hydrogen to silane radicals flowing to the growth surface increases upon increasing the power density from 0.05 to 0.10 and 0.15 W cm⁻², while $T_{\rm e}$ remains constant. This might be an indication

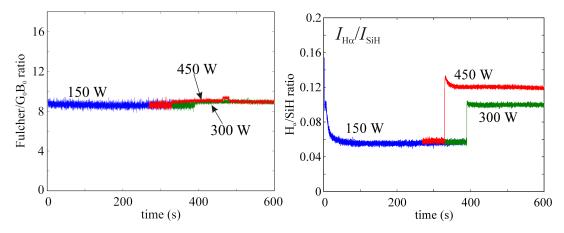


Figure 7.1: Evolution of $I_{G_0B_0}/I_{Ful}$ (left) and H_{α}/SiH (right) emission intensity ratio of a SiH_4/H_2 plasma at a pressure of 3.5 mbar with increasing rf power of 150, 300 and 450 W (corresponding to 0.05, 0.10 and 0.15 W cm⁻² power densities, respectively).

that a change in the plasma chemical composition is responsible for the deterioration of the μc -Si:H material properties. However, modifications of surface reactions on the growing film cannot be excluded.

7.3.2 Material characterization

Intrinsic stress was measured after depositing the μc -Si:H layers using the deposition regimes detailed in Table 7.1. A μc -Si:H p-layer identical to that used within the solar cell devices was systematically deposited before the i-layer to be analyzed, and is included within the total

thickness of 300 nm common to all of these samples. This was done in order to get a good nucleation layer on top of the c-Si native oxide, and to limit differences coming from possible incubation layers that could develop, depending on the deposition regimes.

Figure 7.2 shows μc -Si:H compressive intrinsic stress, as a function of the plasma deposition conditions, with ϕ_c around 60%. We see that intrinsic stress increases for samples deposited at

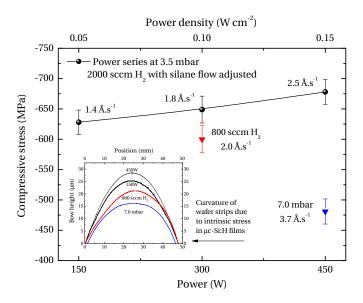


Figure 7.2: Intrinsic stress in μ c-Si:H films deposited on Si(100) wafer strips with various deposition parameters. Inset: Surface profiles of bent wafer strips as measured with profilometer.

higher power densities, for constant $\Phi_{\rm H_2}$ and pressure. Interestingly, for the deposition done at 0.10 W cm⁻², reducing $\Phi_{\rm H_2}$ from 2000 to 800 sccm, and adapting $\Phi_{\rm SiH_4}$ to obtain the same ϕ_c , decreased the stress in the film from -649 to -600 MPa. The most remarkable decrease is observed at 0.15 W cm⁻²: by increasing the pressure to 7.0 mbar stress drops from -678 to -481 MPa.

The power series was repeated with thicker films deposited on single-side-polished c-Si wafers for Fourier transform infrared spectroscopy (FTIR) to get chemical bonding information. This analysis difficult as only thin μc -Si:H films of around 600 nm could be deposited for comparison, as thicker films would immediately peel off when prepared at high power density. The IR spectra show no significant differences between the low- and high-power deposition regimes in terms of hydride stretching modes. In particular we do not see the signature of narrow high-hydride stretching modes (NHSMs) characteristic of hydrogenated crystalline grain boundaries and poor electronic properties [Smets 08]. However, strong Si–O–Si stretching modes (around 1100 cm⁻¹) are observed for the layer deposited at 0.15 W cm⁻² and are completely absent at 0.05 W cm⁻² (Figure 7.3). This indicates that the material deposited at higher power is more porous and susceptible to post-deposition oxidation (all the measurements were done immediately following deposition for all samples).

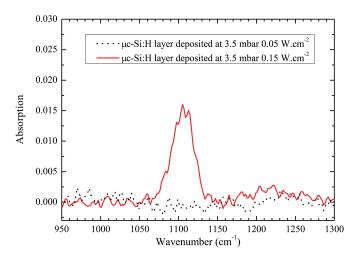


Figure 7.3: IR spectra of 600 nm-thick μ c-Si:H films deposited on single-side-polished c-Si at 0.05 and 0.15 W cm⁻².

A relative increase in bonded hydrogen content of 19% is observed by integrating the wagging mode at $640\,\mathrm{cm^{-1}}$, going from $4.0\,\mathrm{to}\,4.8\%$ in absolute value. The differences observed here may be ascribed to varying hydrogen inclusion within the μc -Si:H layers, either in clustered (Si–H $_x$) or molecular (H $_2$) form [Kroll 96]. Since enhanced hydrogen incorporation and increased instability with increased power density is supported by this FTIR analysis, we suggest that the crystalline grain boundaries are indeed more poorly passivated by hydrogen at higher power density. The fact that we could not see NHSMs in the IR spectra may come simply from insufficient signal from the thin layers analyzed, resulting in insufficient signal-to-noise ratios for this type of characterization.

Total hydrogen content was also evaluated by hydrogen forward scattering (HFS) spectrometry, also known as elastic recoil detection analysis (ERDA). The method relies on the scattering of He²⁺ ions at grazing incidence to the sample; the ions knock off H atoms which are then analyzed to quantitatively profile the hydrogen concentration in the thin film. Since quantification of hydrogen concentration by SIMS can be very difficult, this method is usually favored to evaluate the concentration of both 1H and 2H elements. It has the advantage over FTIR spectroscopy that not only bonded hydrogen is measured, but non-bonded hydrogen is as well. This means that molecular hydrogen trapped in microvoids can also be measured with this technique. With HFS, a relative increase in hydrogen content of 26% is observed between the low- and the high-power regimes, going from 8.7 to 11% in absolute value. However, the regime at 0.10 W cm⁻² with lower $\Phi_{\rm H_2}$, also exhibits a "high" value close to 11% although the stress is lower. Thus, although hydrogen content may influence the intrinsic stress of μc -Si:H layers, we cannot define a clear correlation at this point.

7.3.3 Solar cell performance

Single-junction p-i-n μc -Si:H solar cells with their absorber layer deposited using the regimes described in Section 7.3.1 and detailed in Table 7.1 were prepared. i-layers of 1.0 and 2.5 μ m were evaluated for the newly developed regimes. Solar cell efficiency as a function of absorber layer intrinsic stress is plotted in Figure 7.4.

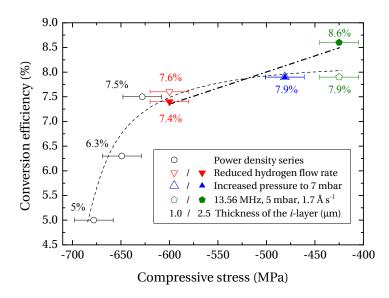


Figure 7.4: Best efficiencies of 1.0- μ m-thick (open symbols) and 2.5- μ m-thick (filled symbols) p-i-n μ c-Si:H solar cells as a function of absorber layer intrinsic stress (detailed in Table 7.1). Both dashed lines are guides to the eye for the thickness series.

Overall, a clear increase in cell performance is observed with reduced intrinsic stress. Looking specifically at the RF power series, we see deterioration of all p-i-n solar cell parameters with increased power density and the associated compressive stress. Going from only 0.05 to 0.10 and 0.15 W cm $^{-2}$, the efficiencies drop from 7.5, to 6.3 and 5.0%, respectively. $V_{\rm oc}$ drops from 510 to 410 mV, FF from 72 to 63% and $J_{\rm sc}$ from 20.4 to 19.4 mA cm $^{-2}$. The silane dissociation increases and the deposition rate increases slightly from 1.4 to 2.5 Å s $^{-1}$, corresponding to low silane depletion fractions between 23 and 34%. Since the pressure already has a relatively quite high value of 3.5 mbar, this deterioration can hardly be explained by increased mean ion energy at such power densities.

On the other hand, the newly developed deposition regimes with increased depletion—*i.e.* with reduced $\Phi_{\rm H_2}$ or increased pressure, which are both associated with a lower stress in the material—lead to higher-efficiency devices. This occurs mainly through improved $V_{\rm oc}$ and FF: for the 0.10 W cm⁻² regime, reduced $\Phi_{\rm H_2}$ lead to an efficiency similar to that obtained using the lowest power density, despite an enhanced growth rate from 1.4 to 2.0 Å s⁻¹. At a higher pressure of 7.0 mbar, higher-quality μc -Si:H is achieved as demonstrated by the high $V_{\rm oc}$ of 535 mV, FF of 74.6%, $J_{\rm sc}$ of 19.7 mA cm⁻² and efficiency of 7.9% for a 1.0- μ m-thick solar cell. Solar cells were also prepared using the low-deposition-rate RF regime detailed in Section 5.2.1

with a 22 mm gap, as it led to the best cell performance at the time of the study. The results shown in Figure 7.4 confirm the observed trend, showing further improvement in the solar cell efficiency with decreased stress in the material. Using the same cell structure, we even pushed the solar cell efficiency to 8.6% by increasing the i-layer thickness to 2.5 μ m.

7.3.4 Conclusion

In this section, we presented various low-deposition-rate conditions for μc -Si:H films used as absorber layers in single-junction solar cells and quantified the films' intrinsic stress. Within the range of our study, increased pressure and reduced hydrogen flow rate during deposition reduced stress, whereas higher power densities tended to increase it. The origin of the stress and the role of hydrogen were discussed, although we could not find a clear relationship between them. Low-stress intrinsic μc -Si:H allowed for the fabrication of better-performing solar cells.

The next sections present stress measurements of μc -Si:H layers deposited at constant and higher growth rates. Such layers were discussed in the previous chapters, and were chosen specifically for this stress study as they were known to lead to increased bulk defect density, or to the formation of significant nanoporous zones once deposited on textured surfaces.

7.4 Relationship to μc -Si:H bulk defect density

In this section, we review the influence of the deposition pressure on the intrinsic stress of the μc -Si:H i-layer, while keeping the growth rate constant at 5 Å s⁻¹ using RF. This pressure

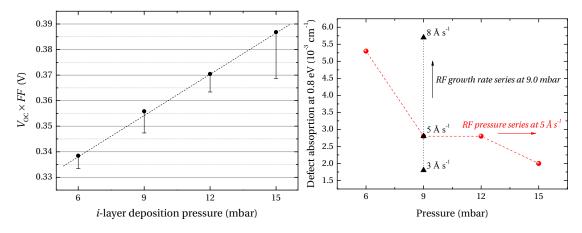


Figure 7.5: $V_{oc} \times FF$ (left) with both the best (symbol) and the mean (bar) value out of the 10 best cells, and the associated FTPS defect absorption value at 0.8 eV (right), for μ c-Si:H solar cells with their i-layers prepared using RF at $5\,\text{Å}\,\text{s}^{-1}$ with increasing pressures or at $3\,\text{Å}\,\text{s}^{-1}$ at a pressure of 9.0 mbar.

series was chosen for the intrinsic stress study as a clear improvement of the bulk material

quality and solar cell performance was observed with increased pressure in Section 5.3.1. Only one new regime at an even lower pressure of 3.0 mbar was developed for this specific study. Figure 7.5 summarizes the defect analysis and cell performance that were presented in Section 5.3.1.

Intrinsic μc -Si:H layers 600 nm in thickness were deposited on top of a thin nucleation layer on $50 \times 10 \times 0.3$ mm³ wafer strips. ϕ_c was adjusted to be constant at 70% throughout the series. Wafer bending and the associated i-layer compressive stress as a function of deposition pressure are plotted in Figure 7.6. A significant drop of the i-layer compressive stress is first

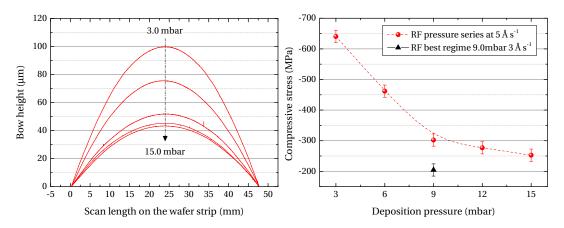


Figure 7.6: Left: Bending of (110) c-Si wafer strips induced by the compressive stress of 600-nm-thick μ c-Si:H i-layers deposited using increasing pressures from 3.0 to 15.0 mbar. Right: Compressive intrinsic stress values derived from the radius of curvature of the samples and the deposited film thicknesses.

observed when the pressure is increased from 3.0 to 9.0 mbar going from -640 to -302 MPa. Above 9.0 mbar, although the stress is still reduced, the slope is less steep and the lowest value of -253 MPa is attained at 15 mbar. Using similar conditions we also evaluated the intrinsic stress of the best μc -Si:H intrinsic material developed during this thesis, deposited at 9.0 mbar using RF (see details in Section 5.4.1). We see that its intrinsic stress is even lower, reaching -204 MPa.

This pressure series at a constant growth rate of 5 $\text{Å}\,\text{s}^{-1}$ demonstrates a clear relationship between the compressive intrinsic stress, the bulk defect density of the μc -Si:H i-layer and the associated solar cell performance.

Changes in the ion bombardment energy and the ion/neutral radical flux ratio are likely responsible for these observations. However it was impossible to measure these quantities in our system during this study. Further work should be done to better understand the relationship between the ion energy flux and the intrinsic stress of the deposited material. Plasma characterization tools such as an impedance sensor probe, $V_{\rm pp}$ probe and rf biased Langmuir probe (e.g. such as the recently released Impedans Ltd. Plato Probe) could help in

this regard. Increased ion bombardment can indeed lead to sputtering or create structural defects with energetic ions that can implant within the deposited material, inducing Si bulk displacement mechanism and increasing the formation of voids [Smets 06].

7.5 Intrinsic stress and μc -Si:H porosity in complete solar cells

Finally, we evaluate the intrinsic stress of μc -Si:H i-layers that are deposited using conditions leading to the growth of dense or porous μc -Si:H once incorporated in solar cells. The hydrogen flow rate series, presented in Chapter 4, was achieved through increased $\Phi_{\rm H_2}$ at a high growth rate of 1.0 nm s $^{-1}$. Very high depletion regimes were used as D was always above 80% here. The power density was adjusted for each regime to get similar ϕ_c . Table 7.2 summarizes the deposition conditions.

Table 7.2: Deposition parameters of the i-layer for the Φ_{H_2} series using VHF, a constant growth rate of $10\,\text{Å}\,\text{s}^{-1}$, using $d_{gap}=12$ mm. D and c_p are obtained from IR laser spectrometer. The associated single-junction μc -Si:H solar cell efficiencies and i-layer intrinsic stress values are also indicated.

Φ _{H2} (sccm)	P_d (W cm ⁻²)	D (%)	<i>c_p</i> (%)	$ au_{ m res.}$ (s)	Best cell efficiency (%)	Intrinsic Stress (MPa)
300	0.34	-	-	1.74	7.9	-
600	0.35	85	2.3	1.01	7.4	-102
800	0.37	84	1.9	0.79	7.2	-112
1200	0.39	83	1.5	0.55	6.8	-108
2000	0.40	80	1.1	0.34	6.4	-117

We recall that for this series no differences in the μc -Si:H material quality were found unless the μc -Si:H was incorporated in the cell on a rough substrate. Indeed, neither FTPS, FTIR, nor XRD can discriminate between the layers, as such characterization techniques are assumed to be sensitive only to the bulk quality of the material. However, once deposited on top of a rough surface such as LPCVD ZnO, high- $\Phi_{\rm H_2}$ deposition regimes lead to the formation of nanoporous regions when the growing fronts encounter each other.

For this study, 600-nm-thick i-layers were deposited on top of a thin and highly crystalline nucleation layer on $50 \times 10 \times 0.3$ mm³ wafer strips. ϕ_c was held constant thorough the series at a high value of around 75–80%. The higher ϕ_c values, obtained in this series of layers, are attributed to the nucleation layer which differs from the previous films (and the actual solar cells) by the absence of trimethylboron—which is known to hinder the crystalline growth—during its deposition. The stress was evaluated again through the wafer bending method and the measurements are presented in Table 7.2. The lowest $\Phi_{\rm H_2}$ conditions could not be evaluated as our new process pumps did not allow us to reach such a high pressure with such

a low gas flow rate.

We observe that the intrinsic stress values of all of these layers lie within -100 to -120 MPa. Considering the margin of error of \pm 20 MPa, no significant trend can be correlated to the formation of the nanoporous regions which reduce the conversion efficiency of μc -Si:H solar cells once in the cell, as depicted again in Figure 7.7.

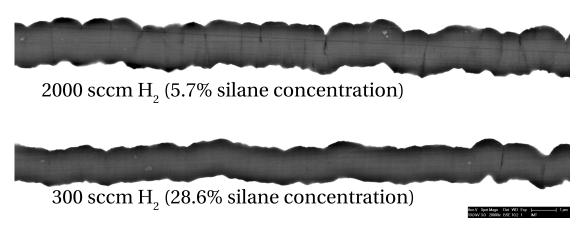


Figure 7.7: SEM images of μ c-Si:H p-i-n solar cells with their i-layers deposited at 10 Å s⁻¹ using a high Φ_{H_2} of 2000 sccm (top) and a low Φ_{H_2} of 300 sccm (bottom) with SiO_x doped layers on the smoothest substrate Z5 60'. The cells have SiO_x doped layers and are on Z5 60'.

The compressive stress values are also much lower than those reported earlier in this chapter, which can be attributed to the enhanced growth rate, but more importantly to the higher crystalline fraction. Residual stress coming from the *a*-Si:H phase is reduced and stress can be released at grain boundaries. This was also observed in other studies [Fu 05, Christova 10].

The results of this $\Phi_{\rm H_2}$ series indicate that intrinsic stress on its own cannot determine μc -Si:H quality once it is embedded in a cell with highly textured interfaces. As with the previous techniques, such as FTIR and FTPS detailed in Section 4.2.2, no difference can be seen in terms of stress unless the bulk material is significantly affected by the deposition regime. This suggests that in this case, the disappearance of nanoporous zones on top of highly textured surfaces with decreased $\Phi_{\rm H_2}$ is not related to a densification process (for which a stress signature would have been expected), but more likely to a reduction of highly reactive radicals (e.g. SiH₂, SiH, Si) contributing to the Si film growth, as discussed in Section 6.3. However, this observation applies only to the limited range of our investigation—relatively high ϕ_c s—and further tests should be conducted to ensure the absence of a correlation between intrinsic stress and μc -Si:H material densification on highly textured morphologies.

7.6 Conclusion

Intrinsic stress of μc -Si:H layers was measured to evaluate its relevance with regard to the performance of single-junction solar cells with μc -Si:H absorber layers. We showed that under moderate silane depletion conditions, decreased $\Phi_{\rm H_2}$ and increased pressure resulted in lower stress in the material and better performing solar cells. Further experiments done at constant growth rate demonstrated that intrinsic stress of the μc -Si:H is strongly correlated to the bulk defect density as measured from FTPS, both of them being symptomatic of increased ion bombardment energy.

Additionally, μc -Si:H i-layers having the same bulk quality signature, but leading to either porous or dense material once deposited onto rough surfaces could not be distinguished by their intrinsic stress values. This suggests that a densification process is not responsible for the improvements observed in the cells, but rather a change in the growing film precursors.

This study highlights the difficulties in assessing the μc -Si:H material quality outside of an actual solar cell device. In devices, the necessary underlying roughness tends to discriminate between the plasma deposition conditions that may or may not favor the formation of nanoporous zones, even if the μc -Si:H bulk electrical properties are similar.

8 Silicon oxide buffer layer at the p-i interface in μc -Si:H and a-Si:H solar cells

In this chapter we present the use of a novel intrinsic silicon oxide buffer layer at the p-i interface of thin-film silicon solar cells and show that its implementation provides significant advantages. For microcrystalline silicon solar cells, with highly crystalline i-layers deposited at high rates, all electrical parameters are improved. Larger efficiency gains are achieved with substrates of increased roughness. For cells with improved i-layer material quality, there is a gain mainly in short-circuit current density. An improvement in carrier collection in the blue region of the spectrum is systematically observed for all the cells. The presence of a silicon oxide buffer layer also promotes the nucleation of the subsequent intrinsic microcrystalline silicon layer. In amorphous silicon solar cells, the silicon oxide buffer layer is proven to act as an efficient barrier to boron cross-contamination, eliminating the need for additional processing steps (e.g. a water vapor flush), while providing a wide-bandgap material at the interface. The implementation of silicon oxide buffer layers thus provides a decisive improvement for both types of cells, as it allows extremely fast deposition of the full p-i-n stack of layers of the cell in a single-chamber configuration while providing a high-quality substrate-resilient p-i interface.

8.1 Introduction

Excellent control of interfaces in thin-film silicon solar cells has been assumed to be of prime importance to achieve high-efficiency devices. For both hydrogenated amorphous (a-Si:H) and microcrystalline (μc -Si:H) silicon solar cells, the open-circuit voltage (V_{oc}) is typically determined by the doped layers, the mobility gap of the intrinsic material and its bulk properties, but also by the relative amount of recombination occurring at the p-i interface region. Moreover, in the p-i-n configuration, this interface may fulfill the additional role of barrier for boron cross-contamination. For an a-Si:H cell, implementation of a wide-bandgap buffer layer at the p-i interface can accommodate for the band offset and reduce the back-diffusion of electrons into the p-layer [Platz 96, Rech 96, Vet 08, Shah 10]. Such a buffer layer also plays a crucial role in the overall light-induced degradation (LID) of an a-Si:H cell. While silicon alloys are often used at this interface, leading to improved initial performance, they tend to

degrade more than regular hydrogen-diluted *a*-Si:H buffers, emphasizing the importance of optimizing this interface for the stabilized state.

In the case of μc -Si:H solar cells, the crystalline fraction of the i-layer is shown to influence the $V_{\rm oc}$ and the overall performance of single-junction cells deposited by plasma-enhanced chemical vapor deposition (PECVD) [Vetterl 00, Johnson 08b, Ellert 12]. More specifically, the p-i interface alone plays a major role with respect to the $V_{\rm oc}$ of the cell [Meier 98, Droz 04, Ito 03, Yue 08]. The use of a thin μc -Si:H buffer layer deposited by hot-wire (HW)-CVD for the first tens of nanometers was shown to significantly improve the $V_{\rm oc}$ in single-junction μc -Si:H solar cells [Klein 04, van den Donker 07, Finger 08]. Although the exact reasons for this improvement have not yet been clearly elucidated, the defect density at the p-i interface was shown not to be the determining factor with regard to V_{oc} [Brammer 03, Finger 08]. More recently, improved electrical performance was achieved through the use of mixed-phase silicon sub-oxide (SiO_x) doped layers in μc -Si:H solar cells [Pingate 06]. Such SiO_x layers were proposed as an effective way to mitigate the negative effects of localized defective regions in a-Si:H or μ c-Si:H cells [Despeisse 10, Cuony 10, Cuony 12, Bugnon 12]. Hence, the concept of controlling interfaces of silicon layers deposited on top of textured surfaces is multifaceted: it has to be revised to take into account film growth dynamics and localized electrical effects arising along the growth plane, as they can drive solar cell performance.

In this chapter we first study the influence of the μc -Si:H i-layer crystalline fraction on solar cell performance. Then, in Section 8.2.1 we present the integration of a thin undoped SiO_x buffer layer at the p-i interface into both μc -Si:H and a-Si:H p-i-n cells. We demonstrate the beneficial effects of such a layer, especially when deposited in a single-chamber configuration, for extremely fast processing of the whole p-i-n stack for both types of solar cells. The relative improvements as a function of intrinsic μc -Si:H material quality and substrate morphology are presented for single- and double-chamber processes. In the case of a-Si:H, we show promising results on how such a SiO_x buffer layer deposited in a single-chamber process can effectively replace time-consuming deposition steps to prevent boron cross-contamination and can provide state-of-the-art solar cells with low relative degradation.

8.2 SiO_x buffer layer in single-junction μc -Si:H solar cells

Single-junction μc -Si:H p-i-n solar cells were prepared in our in-house PECVD reactor with a KAI-M PlasmaBox (49 × 60 cm² powered electrode area) at a deposition temperature of 180 °C. Mixtures of silane and hydrogen were used to prepare intrinsic silicon layers and carbon dioxide was added to obtain SiO_x layers. Trimethylboron and phosphine gases were used for p-type and n-type doping, respectively. The front contact consisted of textured zinc oxide (ZnO) grown by low-pressure chemical vapor deposition (LPCVD) on standard AF45 Schott glass substrates. Under our deposition conditions, ZnO layers naturally develop randomly distributed pyramidal-shaped structures [Faÿ 06, Nicolay 09]. Lowly doped 4.5- μ m-thick (Z5) ZnO layers were subsequently either smoothened through the use of an argon-based

plasma treatment [Bailat 06, Boccard 12a] of 45/60 minutes (Z5 45'/60') in the Oxford system or IPL system, or completely flattened through a mechanical polishing step (Z5 P) [Cuony 11]. Thinner ZnO layers of 1.5 μ m (Z1) with a higher doping concentration, and Asahi U subtrates, were used as front electrodes as well. The μc -Si:H i-layer thickness was 1.2 μ m unless stated otherwise.

Solar cells were patterned to $0.25~\rm cm^2$, and the back contact was LPCVD ZnO covered with a white dielectric reflector. $V_{\rm oc}$ and fill factor (FF) were derived from current-voltage (I-V) measurements of the cells obtained with a dual-lamp solar simulator (Wacom, WXS-220S-L2) in standard test conditions ($25~\rm ^{\circ}C$, AM1.5 global reference spectrum, $100~\rm mW~cm^{-2}$). The short-circuit current densities ($J_{\rm sc}$) reported here, and used to calculate the efficiencies of the best cells, were determined by integrating the product of the external quantum efficiency (EQE) and the incoming photon flux of the AM1.5 global reference spectrum. Total absorption (1-reflection) of the cells was measured using a dual-beam spectrophotometer equipped with an integrating sphere (Perkin Elmer, Lambda 900).

A Raman spectrometer (Renishaw, System 2000) was used to measure the Raman crystallinity factor (ϕ_c) of the μc -Si:H layers using the 514.5 nm emission line of an argon ion laser (see section 2.3 for more details). Measurements were done directly on the solar cells through the glass/front ZnO stack for p-side values and through the back contact for n-side values.

8.2.1 Role of the i-layer crystalline fraction

Before proceeding with the novel p-i interface, we investigate in this section μc -Si:H solar cell performance as a function of the i-layer Raman crystalline fraction. This will prove to be useful when analyzing the impact of the SiO $_x$ buffer.

For this preliminary study, solar cells were prepared based on the RF regime developed at 5 mbar with a deposition rate of around $1.7\,\mathrm{\AA\,s^{-1}}$, using the standard interelectrode distance of 22 mm (see details in section 5.2.1). Only the $1.2\,\mu\mathrm{m}$ -thick i-layer was changed by adjusting the silane input flow rate ($\Phi_{\mathrm{SiH_4}}$), which was increased from 24 to 29 sccm leading to a more amorphous-rich material. The focus of this experiment was not to dissociate the effects of the p-i and i-n interfaces from the bulk, as the Raman crystalline fraction of all of these regions varies concurrently with $\Phi_{\mathrm{SiH_4}}$. Additional tests were done to compensate for the crystallinity gradient that occurs along the growth direction in the cell by increasing $\Phi_{\mathrm{SiH_4}}$ deposition. Figure 8.1 presents solar cell performances on LPCVD ZnO:B treated 60' by plasma (using IPL) and on Asahi U substrates. V_{OC} increases almost linearly increases with increasing $\Phi_{\mathrm{SiH_4}}$. This results from the more amorphous-rich material at the p-i interface [Meier 98] (although at the expense of the FF above a certain threshold), at the i-n interface [Droz 04] and in central part of the i-layer as well [Vetterl 00]. The FF reaches a plateau at around 26–27 sccm and drops abruptly above, while J_{SC} steadily decreases, so that the efficiency has an optimum at $\Phi_{\mathrm{SiH_4}}$ = 26 sccm.

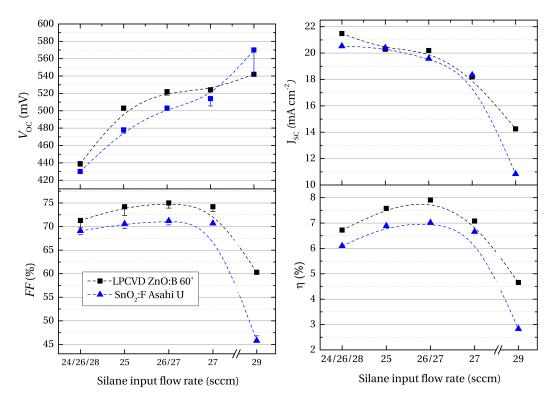


Figure 8.1: Best p-i-n μ c-Si:H solar cells prepared on Z5 60' (IPL) with a 1.2 μ m-thick i-layer grown with increasing silane input flow rate. The bars represent the mean value of the ten best cells on each substrate and the symbols represent the best cell for which J_{sc} and efficiency were calculated.

Looking at the EQEs in Figure 8.2, we observe a significant drop in the blue region of the spectrum with increasing silane input flow rate. This indicates that the amorphous-rich material at the p-i interface does not contribute effectively to the current, which was shown to be due to a reduced electron transport and band offset at the p-i interface [Stiebig 00, Reynolds 09]. While this carrier collection reduction at the p-i interface may not be so important once the μc -Si:H is embedded in a micromorph—since most of the blue region is already absorbed by the top cell—, the associated FF drop would have a significant performance impact on a tandem cell performances when used as a bottom cell. The decrease in crystalline fraction of the overall i-layer also impacts the material bandgap so that a decrease in the infrared EQE is clearly observed as well. This could also limit the performance of a tandem a-Si:H/ μc -Si:H solar cell. However, the use of a μc -Si:H i-layer with a lowered crystalline fraction in the middle cell of an a-Si:H/ μc -Si:H triple-junction solar cell would be beneficial, favoring higher V_{oc} at the expense of infrared absorption, which will occurr anyway in the μc -Si:H bottom cell.

By looking at the differences between EQEs measured at -2 V and 0 V as shown in Figure 8.3a, we observe that the carrier collection efficiency is significantly worse for wavelengths below 600 nm, as well with increasing Φ_{SiH_4} . This behavior was observed on both substrates but

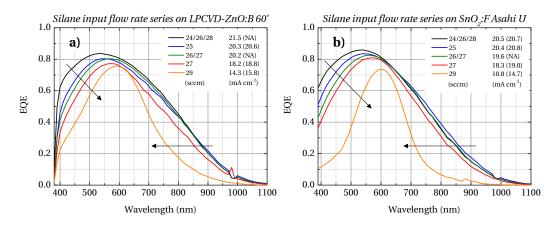


Figure 8.2: EQE of the best p-i-n μ c-Si:H solar cells prepared on Z6 60' (IPL) a the 1.2 μ m-thick i-layer grown with increasing silane input flow rate. When Φ_{SiH_4} gradients were used, all the Φ_{SiH_4} values are reported on the x-axis.

is shown here only on Asahi U for clarity. The boron diffusion coefficient being at least ten

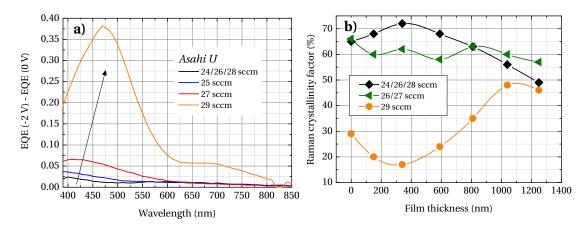


Figure 8.3: (a) Difference between EQE measurements done at -2 V and 0 V for cells with i-layers prepared with increasing silane input flow rate. (b) Raman crystallinity factors measured at various depths within p-i-n cells deposited on Z5 60'.

orders of magnitude higher in a-Si:H than in c-Si [Matsumura 83, Nasuno 02], this additional collection issue may come from enhanced boron-tailing in the device through the increased a-Si:H phase at the p-i interface.

The Raman crystalline fraction profile within the p-i-n cell was also measured by using incremental dry etching of the cell to probe the material at different thicknesses (the penetration depth of our Raman Ar $^+$ laser being around 150 nm in μc -Si:H). The value at 0 nm was measured from the glass side. The profiles for three Φ_{SiH_4} conditions are shown in Figure 8.3b for cells deposited on Z5 60'. With the highest Φ_{SiH_4} of 29 sccm, the crystalline fraction starts

at really low values of around 20% and increases with film thickness. The higher ϕ_c value measured at the bottom of the cell is due to the contribution in the Raman signal of the underlying μc -Si:H p-layer, which has a higher ϕ_c itself. The variations are much smaller for the other two Φ_{SiH_4} values; the crystallinity increase was easily controlled by varying the silane flow rate during the growth to get a constant crystalline fraction along the growth direction.

This section has thus shown that, for a given set of deposition conditions, the i-layer crystalline fraction plays a decisive role in the performance of the solar cells. Although regular μc -Si:H doped layers were used for this study, similar observations were made when SiO_x doped layers were used instead.

8.2.2 Extremely fast and efficient single-chamber deposition process

In this section, we present the electrical performance gains obtained when using a SiO_x buffer layer at the p-i interface of single-junction μc -Si:H solar cells prepared using a single-chamber PECVD process. The newly developed SiO_x buffer layer used in the study was around 6 nm thick and was deposited after the p-layer at a growth rate of about $1\,\text{Å}\,\text{s}^{-1}$ using a high-pressure, high-power regime. The Raman crystallinity factor of this SiO_x buffer layer was evaluated at 64%, by having it thickened to 700 nm within the cell and measured it directly from the p-side. For comparison, the μc -Si:H p-i-n cells were kept strictly similar except for the presence of the buffer layer. Both have SiO_x doped layers, and their 1.2- μ m-thick i-layer was deposited at $1\,\text{nm}\,\text{s}^{-1}$. A schematic of such a cell is presented in Figure 8.4.

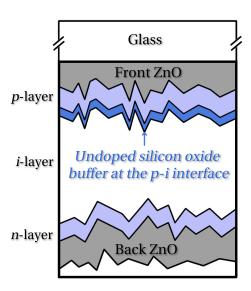


Figure 8.4: Simple schematic of a p-i-n cell with a SiO_x buffer at the p-i interface.

First we present the case with no chamber cleaning between deposition of the p-layer and the i-layer, so that the whole stack of layers was deposited in a row. Table 8.1 summarizes the

solar cell performances on a Z5 45' reference substrate.

Table 8.1: Best p-i-n μ c-Si:H solar cells deposited at 1 nm s $^{-1}$ in a single-chamber process, with and without a SiO_x buffer layer at the p-i interface. The numbers in parentheses are the mean values of the ten best cells on each substrate.

Cleaning between <i>p</i> -and <i>i</i> -layer	SiO _x buffer layer	V _{oc} (mV)	FF (%)	$J_{\rm sc}$ (mA cm ⁻²)	Efficiency (%)
Without		510 (508)	68.7 (68.6)	21.3	7.5
· · · · · · · · · · · · · · · · · · ·	With	519 (519)	70.9 (70.4)	23.1	8.5
With		508 (504)	70.0 (69.4)	22.0	8.0
VVIUI	With	534 (533)	73.2 (72.1)	22.5	8.8

 ϕ_c is very similar in both configurations, although a minor increase is observed for cells incorporating the SiO_x buffer layer, going from 58/60 to 62/64% for the p/n sides, respectively. When the buffer layer is used in this configuration, V_{oc} increases by around 10 mV and FF by 2% absolute. J_{sc} also significantly increases, especially in the blue region of the spectrum as can be seen in Figure 8.5.

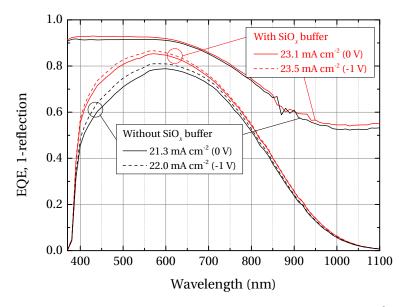


Figure 8.5: EQE of the best p-i-n μ c-Si:H solar cells deposited at 1 nm s^{-1} using a single-chamber process and no cleaning, with (red) and without (black) a SiO_x buffer layer at the p-i interface. Measurements were done at 0 V (solid) and -1 V (dashed). The total absorption of the cells (1–reflection) with and without the SiO_x buffer layer is also shown here.

Carrier collection also improves as can be evaluated from EQE measurements at 0 V and a

Chapter 8. Silicon oxide buffer layer at the p-i interface in μc -Si:H and a-Si:H solar cells

reverse bias voltage of -1 V. Increasing the voltage bias beyond -1 V did not lead to any further increase in current density. Implementation of a SiO_x buffer layer thus results in a 14% relative increase in the solar cell efficiency, going from 7.5 to 8.5%.

Improved collection in the blue region can be related to a reduction in boron cross-contamination from the p- to the i-layer, similar to the a-Si:H case discussed later in Section 8.3. More specifically, in the case of μc -Si:H solar cells, a higher response in the blue region can be directly linked to an improvement of the i-layer nucleation: carriers generated in the a-Si:H-rich phase may not contribute to current because of the reduced electron transport and band offset at the p-i interface [Stiebig 00, Reynolds 09]. Total absorption measurements show that this SiO_x buffer layer on top of the existing p-SiO $_x$ layer provides an additional anti-reflection effect, with a gain exceeding 1% over the full spectrum. Note that just making the p-SiO $_x$ layer thicker resulted in reduced EQE (not shown here). Part of the gain observed in the infrared may be due to the slight crystallinity increase as well. These results also reveal that this SiO_x buffer layer does not induce significant n-type contamination further in the i-layer even though it represents an additional source of oxygen in this single-chamber process.

An additional experiment was done by incorporating a reactor cleaning and pumping step after the p-layer deposition to reduce part of the boron cross-contamination so as to emphasize and isolate the effect of this buffer layer. The loading plate holding the substrates was kept under vacuum at the same temperature during this step. The cells' electrical parameters are presented in Table 8.1. While the cells are better overall, a similar improvement is still observed with the presence of the SiO_x buffer layer: the mean $V_{\rm oc}$ and FF values of the ten best cells increased from 504 to 533 mV and from 69.4 to 72.1% respectively. The $J_{\rm sc}$ of the best cell increased from 22.0 to 22.5 mA cm⁻² and the efficiency from 8.0 to 8.8%.

Secondary ion mass spectrometry (SIMS) measurements were carried out on polished c-Si wafers to evaluate boron content, but no improvement associated with the SiO_x buffer layer was observed. However an effective reduction in contamination in the cells cannot be ruled out completely at this point, since the incorporation of contaminants during deposition is suspected to be facilitated by the defective porous regions [Python 10], which do not form on top of polished c-Si wafer substrates. This is corroborated by an electric-field profile study of μc -Si:H p-i-n solar cells done by cross-sectional scanning Kelvin probe microscopy, in which negative charges observed at the cluster boundaries have been speculated to be related to the presence of activated boron [Dominé 07].

These first experiments demonstrate that efficient control of the p-i interface in μc -Si:H solar cells is achievable in a single-chamber deposition process. These conditions are especially relevant for industry, as they allow one to rapidly process the full p-i-n silicon layer stack in a row. Further tests were done to clarify the origin of the observed gains; they are described hereafter.

8.2.3 Gains as a function of substrate morphology for cells deposited at a high rate

To further understand the origins of the efficiency gain achieved when inserting a SiO_x buffer layer, the roughness of the front ZnO layer was varied. For that purpose, single-junction μc -Si:H p-i-n solar cells with i-layers deposited at 1.5 nm s $^{-1}$ were prepared with and without the SiO_x buffer layer on Z5 P (polished Z5 substrate), on Z1 (σ_{RMS} = 49 nm, high density of sharp little pyramids with 30° average facet inclination, ironed surface increase of 143%), and on Z5 45' (σ_{RMS} = 106 nm, large and smooth pyramids with 18° average facet inclination, ironed surface increase of 115%). The aim of this experiment was to verify whether the efficiency gains were indeed larger on substrates favoring the growth of porous regions in the material as observed in Section 4.4. Here the sharpest substrate was the Z1, the Z5 45' was smoother, and the Z5 P was completely flat, which would in principle eliminate porous regions.

The i-layer was always the same for this series and its deposition conditions were tuned so that ϕ_c was kept > 60%. The combination of a very high deposition rate and a rather high crystalline fraction for the i-layer was chosen so as to grow μc -Si:H material prone to the formation of nanoporous regions. This was done in order to emphasize the electrical quenching effect, if any, of the SiO $_x$ buffer layer for those more challenging conditions. To ensure that observed differences in the cells' performances were related to the presence of the buffer layer inside the device and not to the chamber history and conditions, we took additional precautions: the SiO $_x$ buffer layer was always deposited in the chamber after the post-p-layer-deposition cleaning so that the environment was similar for the subsequent i-layer growth in both cases. For cells without a SiO $_x$ buffer layer, the substrate carrier was just kept under vacuum in another chamber of the system during this step.

Table 8.2 shows ϕ_c measured from both the p- and n-sides of the completed solar cells. ϕ_c is always above 65% when measured from the p-side of the cell. We observe very similar crystalline fractions in both cases, with and without a SiO $_x$ buffer layer.

Table 8.2: Raman crystallinity factor from both the p- and n- sides of p-i-n μ c-Si:H solar cells with the i-layer deposited in the same chamber as the p-layer at a growth rate of 1.5 nm s $^{-1}$ with and without a SiO $_x$ buffer layer.

	ϕ_c (%) - Without	SiO_x buffer layer	ϕ_c (%) - With SiO $_x$ buffer layer		
Substrate type	<i>p</i> -side	<i>n</i> -side	<i>p</i> -side	<i>n</i> -side	
Z5 P	65	70	68	70	
Z1	66	63	65	62	
Z5 45'	70	63	73	65	

The electrical performances of the cells prepared at a high deposition rate on the three different substrates are shown in Figure 8.6.

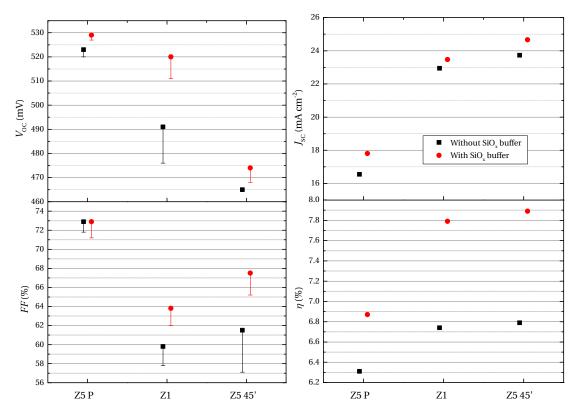


Figure 8.6: Best p-i-n μ c-Si:H solar cell performances for cells deposited at 1.5 nm s⁻¹ in a single-chamber process including a cleaning step after the p-layer, with and without a SiO_x buffer layer at the p-i interface. The bars represent the mean value of the ten best cells on each substrate and the symbols represent the best cell, for which J_{sc} and efficiency were calculated.

A systematic improvement of $V_{\rm oc}$ and FF is observed with the ${\rm SiO}_x$ buffer layer, except for the average FF value on the Z5 P substrate, which is lower by only 0.6%. $J_{\rm sc}$ also improves for all substrates thanks to an enhancement of the EQE in the blue part of the spectrum. As expected, the $V_{\rm oc} \times FF$ product is highest on the flat Z5 P substrate, and decreases with a sharp substrate morphology and increased substrate roughness. Overall, the efficiency significantly increases by 8.9% on Z5 P, 15.9% on Z1 and 16.2% on Z5 45' when the ${\rm SiO}_x$ buffer layer is inserted. A highest efficiency of 7.9% is thus achieved on Z5 45'. The diminished benefit of the ${\rm SiO}_x$ buffer layer with a Z5 P substrate supports the hypothesis of shunt quenching at specific regions, along the p-i interface, where nanoporous defective regions can grow.

8.2.4 Gains with improved *i*-layer material quality and lower ϕ_c

In this section, we review the influence of the buffer layer with an i-layer of better quality both in terms of reduced bulk defect density (as measured with Fourier-transform photocurrent spectroscopy) and nanoporous defective regions (as evaluated through accelerated damp-heat experiments (cf. Section 4.4). This material was deposited at a lower growth rate of 3 Å s^{-1} in

a separate chamber of our KAI-M reactor with no vacuum break in-between. The SiO_x layer was still deposited in the same chamber as the p-layer for the cell without the buffer layer, to ensure similar chamber conditions for the deposition of the n-layer afterwards. Additionally, the i-layer was purposefully deposited with a much lower crystallinity on the p-side of the cell. This was done to favor high $V_{\rm oc}$ of the μc -Si:H cells and observe the influence of the buffer layer in these conditions.

As can be seen in Table 8.3, a large increase in ϕ_c measured from the p-side is observed for cells with a SiO_x buffer layer. Considering the 150 nm Raman collection depth of the 514.5 nm

Table 8.3: Raman crystallinity factor from both the p- and n- sides of p-i-n μ c-Si:H solar cells with the i-layer deposited at a lower growth rate of $3 \, \text{Å} \, \text{s}^{-1}$ in a separate chamber with and without a SiO_x buffer layer.

	ϕ_c (%) - Without	SiO _x buffer layer	ϕ_c (%) - With S	SiO_x buffer layer
Substrate type	<i>p</i> -side	<i>n</i> -side	<i>p</i> -side	<i>n</i> -side
Z5 P	44	60	60	64
Z1	18	61	45	59
Z5 45'	42	57	59	59

argon emission line in standard μc -Si:H, and the very low thickness of the buffer layer, the buffer layer's contribution is considered to be negligible. We conclude that the buffer layer facilitates the nucleation of the subsequent μc -Si:H i-layer. The absolute value of ϕ_c thus increases by 16% on the Z5 P substrate and up to 27% on the Z1 substrate. The presence of a SiO $_x$ layer, obtained either by plasma deposition, controlled oxidizing plasma treatment or simply air exposure, was proven in the past to be indeed very effective for promoting μc -Si:H nucleation and minimizing the a-Si:H incubation layer [Vaucher 97, Pernet 00, Fujiwara 03]. However, while it has been shown that the chemical nature has a preponderant role on the nucleation of μc -Si:H, the substrate topography can also influence ϕ_c as evaluated by a Raman scattering experiment [Vallat-Sauvain 05]. That may explain why we observe lower ϕ_c on the Z1, substrate which consists of small sharp pyramids. As a result, a combination of a high nuclei density together with a favorably oxidized surface is thought to be responsible for the improved nucleation and growth of the μc -Si:H i-layer.

The electrical performances of the cells are reported in Figure 8.7. In spite of significantly higher ϕ_c on all substrates when a buffer layer is used, we observe that similarly high mean $V_{\rm oc}$ values are still retained. The same behavior is observed for the mean FF values which are equal to or above those of the reference cells without ${\rm SiO}_x$ buffer layers.

 $J_{\rm sc}$ also significantly improves for all the cells, mostly thanks to an EQE increase in the blue region of the spectrum. Figure 8.8 presents the EQEs of the solar cells prepared on the Z5 P and Z5 45' substrates with and without a SiO_x buffer layer, and the relative variations of EQE as a function of wavelength for all three substrates. Again a strong increase in the blue part of

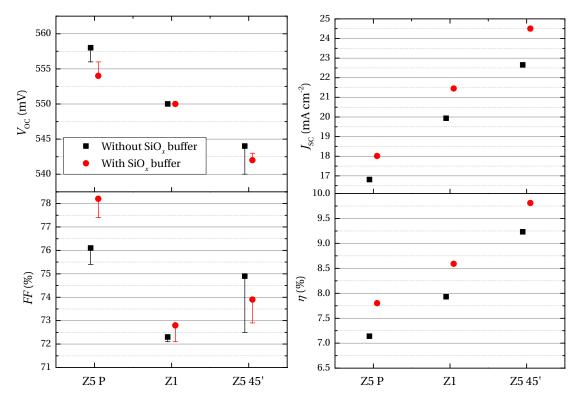


Figure 8.7: Best p-i-n μ c-Si:H solar cell performances for cells deposited at $3 \, \text{Å} \, \text{s}^{-1}$ in a dual-chamber process with and without a SiO_x buffer layer at the p-i interface. The bars represent the mean value of the ten best cells on each substrate and the symbols represent the best cell, for which J_{SC} and efficiency were calculated.

the spectrum is observed, and an increase in the infrared region is also noted on the Z5 45' substrate, which may be due to the enhanced nucleation and crystallinity of the intrinsic material. A relative gain of around 15% is thus observed in the 450 nm region for the three substrates when a SiO_x buffer layer is employed. Poor response in the blue for the reference cells is expected because of the low ϕ_c at the p-i interface, as observed in previous studies. The fact that the buffer layer induces an improvement of ϕ_c can partly explain the gain here.

We do not observe a strong difference in the relative efficiency gain as a function of the substrate morphology, unlike in the previous test in which the absorber layer was deposited at a high rate and had a higher ϕ_c . The presence of the amorphous-rich p-i interface region for the reference cell helped to retain higher performances on rougher substrates.

Overall this experiment with a high-quality bulk absorber layer shows that the use of a thin SiO_x buffer layer provides similar beneficial effects as a high-quality amorphous-rich p-i interface for improved V_{oc} while allowing efficient nucleation of the following i-layer, ensuring good carrier transport. It was confirmed in the past through dark I-V measurements that an amorphous-rich p-i interface significantly reduces saturation current density (J_0) for cells

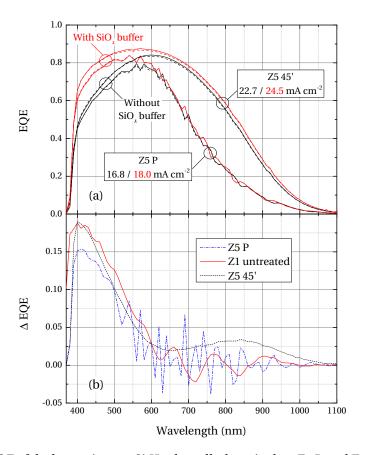


Figure 8.8: (a) EQE of the best p-i-n μ c-Si:H solar cells deposited on Z5 P and Z5 45' substrates at $3 \, \text{Å} \, \text{s}^{-1}$ in a dual-chamber process without the SiO $_x$ buffer layer at the p-i interface (black) and with (red). Measurements were done at 0 V (solid) and -1 V (dashed). (b) Relative variations in EQE for the cells prepared on Z5 P, Z1 and Z5 45' substrates when including the SiO $_x$ buffer layer.

deposited in either the p-i-n [Vetterl 00] or n-i-p sequence [Yue 08, Ito 03]. Here, thanks to the mixed-phase nature of the SiO $_x$ material [Cuony 12], such a buffer layer may allow for a similar reduction of J_0 , but with much reduced thickness because of the lower conductivity of the oxygen-rich phase. It has the added advantage of promoting the nucleation of a high-quality μc -Si:H i-layer on top of it, thanks to the presence of nucleation centers and a surface-oxidized film. Near open-circuit conditions, the free-carrier densities are very high at both interfaces and drift transport weakens as the electric field is reduced, allowing both types of carriers to diffuse more easily and recombine. We think that even larger gains could be obtained with slightly thinner devices for which V_{0c} is even more sensitive to interface quality and band offsets, as recombination in the bulk layer becomes less important.

The electric field at the interface may also be modified because of the slightly *n*-type material, due to oxygen incorporation, which may also help to compensate boron contamination. For instance, Matsui et al.[Matsui 12] recently showed that negatively charged germanium dangling bonds could be compensated by positively charged oxygen donors in the bulk of

 μc -Si_{1-x}Ge $_x$:H solar cells. Similar space-charge compensation phenomena were already observed in the past, such as an improvement in the infrared region of the EQE for boron-compensated μc -Si:H [Meier 94a, Meier 94b]. A reduction in the short-wavelength region has also been associated with the suppression of strong n-type contamination in p-i-n a-Si:H solar cells [Isomura 94, Platz 97] and with boron contents exceeding the compensation values in n-i-p μc -Si:H cells [Yue 12]. Strong boron cross-contamination and reduced collection in the blue region was also observed with increased deposition temperature of the i-layer, resulting in worse cell performance [Nasuno 02], despite a reduction of the bulk defects [Matsui 03a].

Ion bombardment is inherent to conventional PECVD, as opposed to HW-CVD. Within the first seconds of the p-i interface growth, the plasma may thus strongly interact with the underlying p-layer and promote boron release and recycling in the subsequent i-layer deposition. This may be the main reason behind the $V_{\rm oc}$ gains observed even with very thin HW-CVD buffer layers at the p-i interface of p-i-n μc -Si:H solar cells [Klein 04, van den Donker 07, Finger 08]. Such a buffer would effectively bury the p-layer and result in a sharper boron profile at the interface. However, additional experiments should be conducted in the n-i-p configuration to determine the physical origin of the improvements, since the effect of boron back-diffusion, with the p-layer deposited after the i-layer, would be much less severe than the current cross-contamination.

Lastly, similarly to what Klein $et\,al.\,$ [Klein 04] proposed to explain the $V_{\rm oc}$ gains observed with HW-CVD, reduced mobility in the ${\rm SiO}_x$ buffer layer could lead to a reduction of the electron current flowing to the p-layer, hence limiting recombination near or in the p-layer itself. Again, further experiments are required to evaluate this hypothesis by varying the effective mobility in the buffer layer or full i-layer. Although a reduction in boron cross-contamination or in the effective mobility could not be demonstrated here, it is possible that, together with the proposed shunt-quenching mechanism, they all contribute to the observed performance increase.

Implementation of this new SiO_x buffer layer eventually led to the realization of a single-junction p-i-n μc -Si:H record cell efficiency of 10.9% with a 2- μ m-thick i-layer, which is detailed in Chapter 9. The V_{oc} was 535 mV, the FF 74.2% and the J_{sc} 27.5 mA cm⁻² with an anti-reflection layer at the air/glass interface.

8.3 SiO_x buffer layer in single-junction a-Si:H solar cells

Different methods have been proposed to reduce boron cross-contamination in p-i-n a-Si:H solar cells, including various gas flushes such as NF $_3$ [Catalano 88], SF $_6$ [Martins 00], water vapor and ammonia [Kroll 04, Ballutaud 04], and argon combined with chamber evacuation that require significant time [Merdzhanova 12]. High-pressure CO $_2$ plasma treatment was also shown to be effective [Kubon 94] but could never be implemented in a single-chamber process directly on top of the actual substrate. We here report on the first use of such thin SiO $_x$ buffer layer in a standard a-Si:H solar cell developed in our single-chamber KAI-S system

to evaluate how well it performs with regard to boron cross-contamination and stabilized performances.

8.3.1 Improved *a*-Si:H stability

Single-junction a-Si:H p-i-n solar cells were prepared in the KAI-S reactor (see details in Section 2.1) at a higher temperature of 200 °C. They were deposited on 2- μ m-thick ZnO layers with a higher doping concentration (Z2), and the i-layer thickness was kept constant at 250 nm.

Our standard process involves a water vapor flush (WF) and chamber evacuation after deposition of the p-SiO $_x$ layer before proceeding with an a-SiC:H buffer layer deposition. In this experiment we replaced those three time-consuming steps with a single SiO $_x$ buffer layer. In the present study the water flush takes 2 minutes followed by a chamber pumping time extended to 30 minutes. This was done to ensure that we were in the best conditions possible for the purpose of comparison with the SiO $_x$ buffer layer. However, based on our experience, total time involving the water flush can be reduced down to approximately 10 minutes without sacrificing too much efficiency. The SiO $_x$ buffer layer only takes 90 seconds to process and does not require any pumping afterward. Further time reduction is thought to be possible by optimizing the deposition or the treatment at the interface.

Solar cells with different p-i interfaces were prepared and their performances for the initial and degraded states are detailed in Table 8.4.

Table 8.4: Comparison of p-i-n a-Si:H solar cell electrical parameters with different treatments at the p-i interface for the best cell on each substrate in initial and stabilized states. The numbers in parentheses are the mean values of the ten best cells on each substrate.

Buffer layer	WF	State	V _{oc} (mV)	FF (%)	$J_{\rm sc}$ (mA cm ⁻²)	Eff. (%)	LID (%)
None N _	Initial	824 (822)	69.1 (68.7)	14.9	8.5	15.7	
	Stable	830 (829)	60.0 (59.7)	14.1	7.0		
Standard Y a-SiC:H	Initial	897 (896)	76.6 (76.4)	15.6	10.7	23.4	
		Stable	852 (850)	64.4 (64.1)	14.9	8.2	
New SiO_x N	Initial	877 (878)	74.1 (73.4)	16.0	10.4	20.2	
		Stable	870 (868)	64.9 (63.7)	14.7	8.3	
New SiO_x	Y	Initial	882 (878)	75.2 (74.9)	16.0	10.6	18.9
		Stable	877 (872)	66.3 (64.5)	14.7	8.6	

Chapter 8. Silicon oxide buffer layer at the p-i interface in μc -Si:H and a-Si:H solar cells

Without any treatment at the p-i interface, both the initial and stable performances of the cell are very poor with strong collection issues: the $J_{\rm sc}$ of the best cell is 14.9 and 15.4 mA cm $^{-2}$ when measured under 0 V and -1 V, respectively. Standard solar cells prepared with an optimized a-SiC:H buffer layer and a WF at the p-i interface have the highest initial efficiency of 10.7% but degrade significantly to 8.2%.

Using the newly developed SiO_x buffer layer, we studied the influence of the WF: the mean $V_{\rm oc}$ and FF of the ten best cells in this configuration are compared in Figure 8.9 for the initial and degraded states.

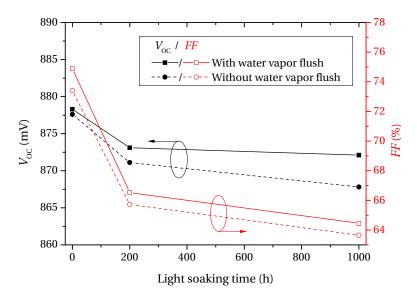


Figure 8.9: Mean values of the $V_{\rm oc}$ (filled symbols) and FF (empty symbols) of the ten best cells using the SiO_x buffer layer with (square symbols, solid line) and without (bullet symbols, dashed line) the WF, before and after light soaking under standard conditions.

Similar $J_{\rm sc}$ of 16.0 mA cm⁻² and collection behavior are observed for cells incorporating a SiO_x buffer layer both with and without the WF. The cells exhibit very high initial performances close to that of the reference cell, with only slightly reduced $V_{\rm oc}$ and FF values, leading to best cell efficiencies of 10.6% and 10.4% with and without the WF, respectively. The corresponding LID decreases compared to the reference cell to 20 and 19%, leading to stabilized efficiencies of 8.6 and 8.3%, respectively. The stabilized $J_{\rm sc}$ is 14.7 and 15.2 mA cm⁻² at 0 V and -1 V bias for both cells. As a result, higher stabilized efficiencies are obtained using this SiO_x buffer layer as compared to the regular a-SiC:H one, even without the WF.

8.3.2 Boron cross-contamination analysis

Boron cross-contamination at the p-i interface was analyzed through SIMS measurements. This analysis was carried out by depositing the stacks "i-layer/p-SiO $_x$ /SiO $_x$ buffer layer/i-layer" and "p-a-SiC:H/a-SiC:H buffer layer/i-layer" on polished wafers, with and without a WF before the buffer layers. The depth profiles are presented in Figure 8.10.

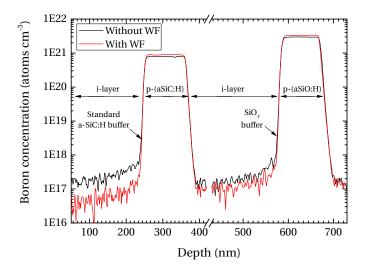


Figure 8.10: SIMS depth profiles of the boron atom concentration of "i-layer/p-SiO_x/SiO_x buffer layer/i-layer" and "p-a-SiC:H/a-SiC:H buffer layer/i-layer" stacks deposited on polished c-Si wafers with and without a WF between the p-layers and the buffer layers.

Using the standard "p-a-SiC:H/a-SiC:H buffer layer" configuration the WF brings a significant advantage, lowering the boron content below 10^{17} atoms cm $^{-3}$ in the i-layer. However, when using the "p-SiO $_x$ layer/SiO $_x$ buffer layer" configuration, we can see that despite a much higher boron content in the p-SiO $_x$ layer, the boron concentration drops sharply to low and comparable values of around 10^{17} atoms cm $^{-3}$ with or without the WF. This demonstrates that the SiO $_x$ buffer layer alone can act as an efficient barrier to boron cross-contamination in a-Si:H solar cells.

Very good control of the p-i interface in a single-chamber process is hence possible through the use of a simple SiO_x buffer layer. State of the art a-Si:H solar cells were efficiently prepared without the need for a time-consuming water vapor flush to reduce boron cross-contamination, using conditions relevant to industry. Further improvement from these preliminary results can also be expected when using this new buffer layer.

8.4 Conclusions

In this chapter, the effects of a thin SiO_x buffer layer inserted at the p-i interface of thin-film a-Si:H and μc -Si:H solar cells deposited on LPCVD ZnO were studied. Significant performance increases were observed for the μc -Si:H solar cells deposited at high deposition rates of 1.0 and 1.5 nm s $^{-1}$ in a single-chamber process. The SiO_x buffer layer seems to limit boron cross-contamination and promote nucleation of the μc -Si:H i-layer. Performance improvements were still observed with an improved i-layer material quality with a lower crystalline fraction, even when processed in a separate chamber. Thanks to this SiO_x buffer layer development, a single-junction p-i-n μc -Si:H record cell efficiency of 10.9% was reached (cf. Chapter 9). Additional optimization and understanding of this buffer layer may help further improve the quality of the interface and enable even higher V_{0c} .

In a-Si:H solar cells, the implementation of such SiO $_x$ buffer layer showed very promising results. High performances and lower light-induced degradation were obtained when the SiO $_x$ buffer layer was used instead of a very time-consuming treatment at the p-i interface with the standard a-SiC:H buffer layer. Based on these a-Si:H and μc -Si:H solar cell results a patent application with TEL Solar is currently pending.

9 Notable solar cell results

This chapter briefly summarizes the best thin-film silicon solar cell efficiencies attained in the laboratory thanks to the μc -Si:H developments presented in this thesis. Results include single-junction and multi-junction for both p-i-n and n-i-p configurations.

9.1 Single-junction μc -Si:H

Superstrate p-i-n configuration

A single-junction μc -Si:H solar cell record efficiency of 10.9% was achieved as a result of the overall work presented in this thesis. This is among the highest efficiencies ever reported in the literature. Figure 9.1 shows both the current-voltage (I-V) curve and EQE measurements of this 0.25 cm² μc -Si:H cell with a 2- μ m-thick intrinsic layer deposited on Z5 45'.

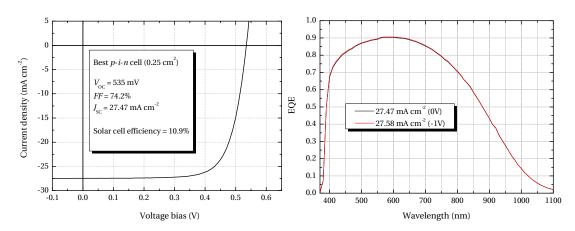


Figure 9.1: I-V (left) EQE under 0 V and -1 V (right) of the best-performing single-junction p-i-n μc -Si:H solar cell (0.25 cm²) with an intrinsic layer thickness of $2 \mu m$.

The $V_{\rm oc}$ is 535 mV, the FF 74.2% and the $J_{\rm sc}$ increases from 26.6 mA cm⁻² to 27.5 mA cm⁻²

with the use of an anti-reflective (AR) coating developed in our laboratory [Escarré 12] (a $J_{\rm sc}$ gain of around 3% over the full spectrum was observed) . The very small difference between EQE measurements under no bias and with a reverse voltage of -1 V demonstrates low recombination and good collection of photo-generated carriers in the intrinsic layer. The μc -Si:H absorber layer exhibits very good bulk material quality as demonstrated by the low FTPS absorption coefficient at 0.8 eV, which is typically between 1.5 and 2.0×10^{-3} cm $^{-1}$. Furthermore, its highly dense structure was confirmed by its high stability during damp-heat tests done on rough substrates for both single-junction and micromorph configurations.

This excellent result was obtained with an absorber layer deposited at 3 Å s^{-1} using RF at 9.0 mbar (cf. Sections 4.2.2, 5.3.1 and 7.4) with dedicated optimization of the SiO_x doped layers (cf. Section 4.2.1) and SiO_x buffer interface (cf. Chapter 8). With this cell design, conversion efficiencies of 10%, without annealing nor AR coating, can be obtained either for thin cells of 1 μ m or thicker ones up to 2.5 μ m. Efficiencies above 11% are thought to be at reach. This p-i-n μ c-Si:H solar cell serves as a baseline for the subcells of multi-junctions thin film silicon solar cells which are presented in this chapter.

Using a narrower gap configuration of 9 mm, the development of high deposition rate regimes using VHF together with further optimized SiO_x doped layers buffer layer led to a 9.8% conversion efficiency devices with the i-layer deposited at 0.7 nm s⁻¹ at a deposition pressure of 12 mbar and 9.3% at 1.5 nm s⁻¹ at 10 mbar, both without AR coating (cf. Section 6.5).

Substrate n-i-p configuration

A n-i-p μc -Si:H cell was also developed based on the superstrate configuration, i.e. using same i-layer and SiO $_x$ doped layers design. It performs similarly well, reaching an efficiency of 10.6% when deposited on hot-silver substrate [Söderström 11], without annealing, as shown in Figure 9.2. The use of SiO $_x$ buffer at the i-p interface is under investigation.

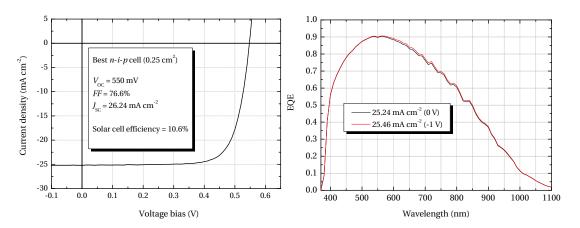


Figure 9.2: I-V (left) EQE under 0 V and -1 V (right) of the best single-junction n-i-p μ c-Si:H solar cell (0.25 cm²) with a 1.75- μ m-thick i-layer deposited on hot silver.

9.2 Micromorph solar cells

Superstrate p-i-n configuration

Significant work has been done by Dr. M. Boccard to improve the electrical and optical performances of tandem a-Si:H/ μc -Si:H, by working on the ZnO front contact morphology and the various trade-offs [Boccard 12b]. Using the μc -Si:H developed in the KAI-M, our current best "thin" micromorph stabilized efficiency is now at 12.2%, with $V_{\rm oc}$ =1.38 V, FF=73.6% and $J_{\rm sc}$ =11.9 mA cm⁻², using less than 1.6 μ m of silicon in total.

Using a thicker configuration (230 nm top cell, 60 nm SiO_x intermediate reflector, 2.2 µm bottom cell), a certified 12.3% efficiency was attained as well, with V_{oc} =1.36 V, FF=71.4% and J_{sc} =12.7 mA cm⁻². The cell exhibits a very low light-induced degradation of only 7%, demonstrating as well the good SiO_x intermediate reflector stability.

Thanks to the work done within the scope of the PEPPER project improved bottom cell quality at higher growth rates could be obtained (cf. Section 6.5). Using VHF and a low gap of 9 mm at 10 mbar to grow the μc -Si:Hi-layer at 7 Å s⁻¹, the best stabilized efficiency attained was 11.9% and is presented in Figure 9.3.

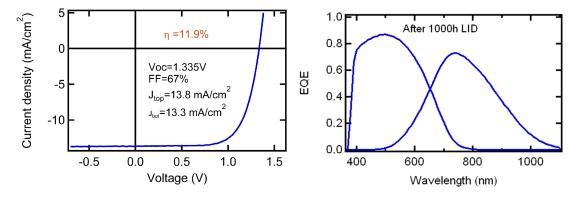


Figure 9.3: I-V (left) and EQE (right) of the best stabilized 1.0 cm² micromorph cell obtained with the bottom cell deposited at $7 \,\mathrm{\AA\,s^{-1}}$.

More recent work led to further improvements, with initial efficiencies as high as 14.0% (V_{oc} =1.36 V, FF=77% and J_{sc} =13.9 mA cm⁻²) with the same growth rate of 7 Å s⁻¹, but the cells are still under LID at the time of writing. At 15 Å s⁻¹, an initial micromorph solar cell efficiency of 13% was also obtained.

Substrate n-i-p configuration

The n-i-p configuration allows the use of an asymmetric intermediate reflector based on LPCVD ZnO [Söderström 09], so that it promotes the top cell $J_{\rm sc}$ significantly. Optimizing this layer and using the μc -Si:H subcell developed along with a well optimized a-Si:H top cell with a SiO $_x$ p-layer, a high stabilized efficiency of 11.6% could be obtained [Biron 13], as shown in Figure 9.4.

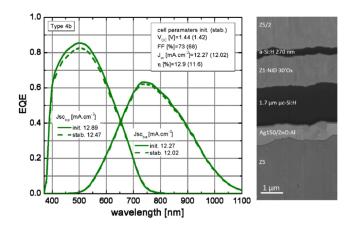


Figure 9.4: Left: EQE of the best stabilized n-i-p micromorph cell. Right: SEM images of focused-ion-beam-prepared cross-sectional views of the solar cell [Biron 13].

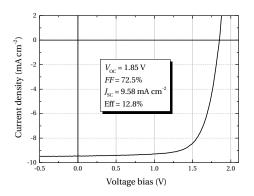
9.3 Triple-junction solar cells

Superstrate p-i-n configuration

Triple-junction a-Si:H/ μc -Si:H/ μc -Si:H solar cells were also prepared based on the μc -Si:H cell developed. While triple-junction are significantly thicker than micromorphs, reaching 3–4 μ m in thickness, they lead to significantly higher stabilized efficiencies, thanks to a reduced top a-Si:H subcell thickness and corresponding light-induced degradation, with relative conversion efficiency degradations as low as 4%.

In the superstrate configuration, using a standard Z2.5 ZnO front electrode treated by plasma and an improved anti-reflective coating, an initial and stabilized cell efficiency of 13.7% ($V_{\rm oc}$ =1.89 V, FF=74.4% and $J_{\rm sc}$ =9.76 mA cm⁻²) and 12.8% ($V_{\rm oc}$ =1.85 V, FF=72.5% and $J_{\rm sc}$ =9.58 mA cm⁻²) were respectively achieved. Stabilized results are presented in Figure 9.5. The subcell thicknesses were 140 nm for the top, 1.5 µm for the middle and 2.6 µm for the bottom.

Combining a highly transparent replicated front structure in UV lacquer and high-mobility thin $\rm In_2O_3$:H TCO ($\mu_e > 100~\rm cm^2~V^{-1}~s^{-1}$), a total current above 30 mA cm⁻² was also obtained. More details can be found in [Schüttauf 13].



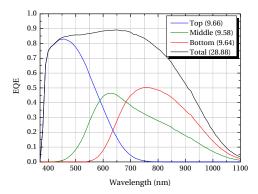
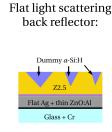


Figure 9.5: I-V (left) EQE (right) of the best-performing triple-junction p-i-n a-Si: $H/\mu c$ -Si: $H/\mu c$ -Si:H solar cell (1 cm²) on Z2.5 treated by plasma.

Substrate n-i-p configuration

Recently, the use of substrates which decouple the growth and scattering interfaces [Sai 11, Söderström 12] was proposed as an alternative to solve the usual trade-off between $V_{\rm oc} \times FF$ and $J_{\rm sc}$ as encountered with conventional TCOs. Indeed, while efficient light scattering requires the front contact to be sufficiently rough, this impacts the solar cell electrical performance. Here the scattering interface is defined by the refractive index contrast between the TCO and a secondary material (a-Si:H here) so that the growth interface can remain perfectly flat and prevent the apparition of nanoporous regions.

In our laboratory, the benefits of such substrate was for the first time demonstrated in n-i-p a-Si:H/ μc -Si:H solar cells [Söderström 12]. The light-scattering interface was made by filling the valleys of a Z2.5 with a-Si:H, which was then mechanically polished and is presented in Figure 9.6, together with the best cell performances. The cell exhibits a very high efficiency of 13.0% stable, which is very close to the recently released world-record efficiency of 13.4% obtained by LG solar [Kim 13].



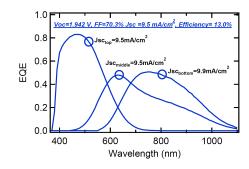


Figure 9.6: Schematic of the innovative flat light-scattering substrate (left) and associated EQE (right) of the best triple-junction n-i-p a-Si: $H/\mu c$ -Si: $H/\mu c$ -Si:H solar cell with a UV nanoimprinted anti-reflective coating [Söderström 13].

10 Conclusion and perspectives

This thesis highlighted crucial aspects of μc -Si:H deposition by PECVD for thin-film silicon PV applications, which will be briefly summarized in Section 10.1. However, further understanding of the μc -Si:H growth mechanisms is still required to go beyond our current limitations and reach even higher growth rates with improved solar cell conversion efficiencies. We discuss future research opportunities in Section 10.2.

10.1 General conclusions

We first investigated in Chapter 3 the roles of both deposition pressure and silane depletion fraction on the growth of μc -Si:H in a large-area VHF PECVD reactor using $d_{\rm gap}=22$ mm. Single-junction μc -Si:H p-i-n solar cells were prepared with i-layers deposited at pressures between 1.2 and 3.5 mbar. We demonstrated that solar cells prepared using higher deposition pressure or increased silane depletion performed significantly better. This improvement in the μc -Si:H quality was further confirmed by the lower defect-related absorption as measured by FTPS on the corresponding solar cells. Amorphization of the μc -Si:H film was observed with increasing power density when using the lowest deposition pressure of 1.2 mbar and was attributed to excessive ion bombardment energy. Indeed, the average ion bombardment energy is expected to decrease with pressure leading to improved material quality and solar cell performance. High silane depletion regimes as simply obtained by reducing the hydrogen flow rate—leading to an increased silane residence time and dissociation efficiency—are associated with a reduction of the time-averaged plasma potential and ultimately the average ion energy as well. Other phenomena associated with plasma chemistry could not be ruled out and may also contribute to the material improvement observed.

Chapter 4 went beyond the simple evaluation of μc -Si:H bulk material quality and highlighted a fundamental aspect of μc -Si:H deposition for PV applications. Thin-film silicon solar cells indeed require highly textured substrates for increased light trapping, and growth on these textures leads to the contribution of two different phases of μc -Si:H material to the overall solar cell efficiency, both of which can drive cell performance. The formation of substrate-

induced defective nanoporous regions was demonstrated to be significantly more dependent on plasma process conditions and to substrate morphology than the bulk phase. More specifically, reduced hydrogen flow rate, using VHF with $d_{\rm gap}$ = 12 mm, was demonstrated to promote the growth of denser material even on a textured surface. FTIR, FTPS and XRD were shown to be insufficient to fully relate device performance to material quality. Damp-heat experiments were demonstrated to be an effective way to evaluate the importance of this nanoporous phase in the solar cells Furthermore, optimized silicon oxide doped layers were confirmed to be effective at reducing the influence of these defective zones on cell performance.

In Chapter 5, we compared the RF and VHF plasma excitation frequencies for the growth of high-quality μc -Si:H using both $d_{\rm gap}$ = 22 mm and 12 mm. We demonstrated that RF provides systematically better-performing μc -Si:H solar cells at moderate growth rates below 5–6 Å s⁻¹. At $d_{\rm gap}$ = 22 mm, better carrier transport properties with increasing i-layer thickness were observed when using RF instead of VHF, allowing for higher $V_{\rm oc}$ and FF together with larger $J_{\rm sc}$. At $d_{\rm gap}$ = 12 mm, a systematic bulk defect density evaluation showed that comparable high-quality bulk material can be obtained using both frequencies. However, μc -Si:H grown on rough substrates using the lower frequency is more dense and leads to better performance overall. A higher density of nanoporous regions in the cells grown using VHF was evidenced through the use of damp-heat experiments, leading to strong $V_{\rm oc}$ instabilities, which are not observed with RF, and contributing to reduced μc -Si:H solar cell performance. However, the advantage of using RF is reduced for higher growth rates since significantly more power density is required at lower excitation frequencies, resulting in increased ion bombardment energy and a poorer μc -Si:H bulk material quality, which dominates solar cell performance.

Chapter 6 investigated in greater depth μc -Si:H material deposited at very high growth rates of around 1 nm s⁻¹. It was shown that reduced hydrogen flow rate and increased pressure using VHF with $d_{gap} = 12$ mm led to better-performing solar cells even though significantly more secondary gas-phase reactions and powder formation are observed. We concluded from this experiment that deposition conditions at the onset of powder formation are beneficial even though excessive powder is of course to be avoided. The strong interplay between μc -Si:H growth rate and the substrate morphology with regard to the formation of nanoporous regions was clearly evidenced: cells deposited at increasing growth rates are much more sensitive to substrate sharpness, showing strong electrical instabilities during the damp-heat tests. Then, the beneficial effect of a reduced d_{gap} for processing μc -Si:H solar cells at high deposition rates was further demonstrated. Going from $d_{\rm gap}$ = 22 to 9 mm, powder formation is reduced so that higher deposition pressures can be used effectively. This results in improved material quality, as assessed by FTPS, and better-performing μc -Si:H solar cells at high growth rates. Finally, this chapter discussed the contributions of the different silicon radicals to the growth of μc -Si:H film. A collaboration with the University of Patras allowed us to perform simulations with detailed sets of conditions. These simulations associated the improvement observed in the μc -Si:H quality with a decrease of the relative contribution of short-lived radicals such as SiH or SiH₂ to the film growth in favor of the monoradicals SiH₃ or Si₂H₅. It appears that high-pressure plasmas are thus interesting because they increase the ratio

 $\Upsilon = (SiH_3 + Si_2H_5)/(SiH + SiH_2)$ by increasing the chances that short-lived radicals will react with hydrogen before they can reach the film.

Chapter 7 focused on relating the intrinsic stress of μc -Si:H i-layers to solar cell performance. Based on a deposition pressure series performed using RF with $d_{\rm gap}$ = 12 mm, we demonstrated that the intrinsic stress of the μc -Si:H is strongly correlated to the bulk defect density as measured from FTPS, probably due to a change in the ion bombardment energy during film growth. However, μc -Si:H i-layers (from the hydrogen flow rate series) with the same bulk quality signature, but different substrate-induced defective nanoporous regions on textured surfaces could not be discriminated by their intrinsic stress values. This suggests that a densification process through increased ion bombardment is not responsible for the reduction of the nanoporous regions in the cells; rather, a change in the film growth precursors is responsible.

Finally, in Chapter 8 we presented a novel intrinsic silicon oxide buffer layer at the p-i interface of thin-film silicon solar cells. Significant performance improvements in all electrical parameters were observed for μc -Si:H solar cells deposited at high deposition rates of 1.0 and 1.5 nm s $^{-1}$ in a single-chamber process. When combined with a more amorphous-rich μc -Si:H i-layer of higher quality, only an improvement in the blue region of the EQE was observed. The origins of the observed improvements are multiple: (i) enhanced i-layer nucleation, (ii) an additional anti-reflection effect, (iii) reduced boron-cross contamination, and (iv) a possible shunt-quenching effect. In a-Si:H solar cells, the implementation of the silicon oxide buffer layer allowed for higher stabilized performances and acted as an efficient barrier to boron cross-contamination, eliminating the need for additional time-consuming processing steps such as a water-vapor flush.

In summary, new insights into the growth of μc -Si:H for PV applications and into solar cell design requirements were highlighted during this thesis. In particular, the clear identification of two separate μc -Si:H phases contributing to overall cell performance allowed us to better understand all our previous observations. It is now clear that deposition regimes leading to a dense material, even on top of highly textured substrates, is of utmost importance for the thin-film silicon PV technology. Indeed, in addition to improved performance, a dense μc -Si:H material also leads to improved solar cell reproducibility as it allows more robustness to front TCO morphology variations and air exposure. Improved cell design, thanks to the implementation of the silicon oxide doped or buffer layers is shown to be a crucial step for achieving high-efficiency and more resilient solar cells. At the beginning of this work, singlejunction μc -Si:H solar cells prepared in our large-area KAI systems had conversion efficiencies of around 7.5% only. Thanks to the significant progress made, we can now produce solar cells with conversion efficiencies significantly above 10%, reaching 10.9% for the best cells with an anti-reflection coating. This work also contributed to the development of very high-efficiency multi-junction thin-film silicon solar cells in the laboratory. A micromorph solar cell with a stabilized efficiency of 12.3% was obtained with its μc -Si:H bottom cell deposited at 7 Å s⁻¹. Triple-junction a-Si:H/ μ c-Si:H/ μ c-Si:H solar cells with high stabilized efficiencies of 12.8%

and 13.0% were also obtained in the p-i-n and n-i-p configurations respectively. Furthermore, a successful collaboration with the University of Patras contributed to the validation of both a fluid plasma simulation code and a Monte Carlo code to simulate the growth kinetics. Both of these are now starting to provide interesting insights into the underlying physics of μc -Si:H growth.

10.2 Perspectives

As discussed already in the introduction, this thin-film silicon PV technology has tremendous potential for future PV electricity generation. It has *almost* everything to establish itself as a major actor in the field: large availability and non-toxicity of the raw materials, excellent scale-up capability, good performance under high temperatures, good shade tolerance, low-temperature processing, homogeneous appearance, tunable color and transparency, compatibility with cheap flexible solutions, etc. But only almost, because, at the moment, conversion efficiency and costs matter the most.

For this reason major efforts need made at a more fundamental level to find new solutions for the technology. Multiple approaches have to be undertaken in order to get a more in-depth understanding of the current limitations and tackle the issues. The growth of high-quality μc -Si:H in particular is a complex phenomenon which requires more attention.

The combined analysis of plasma conditions and μc -Si:H film growth is really important. Dedicated plasma analysis tools are required to observe hidden parameters of rf discharges. More systematic and fundamental investigations of the plasma parameters (even in standard CCP discharges) are necessary to better understand the underlying physics. Such tools would consist for example in $V_{\rm pp}$ probes, post-match impedance probes, or the use of new deposition-tolerant rf-biased Langmuir probes (allowing measurement of $T_{\rm e}$, $n_{\rm e}$, ion flux). The use of an energy-filtered quadrupole mass spectrometer (evaluation of the chemical nature of the neutral, cation and anion radicals and ion energy distribution function) should bring valuable information as well if combined with relevant deposition conditions and material analysis.

The use of plasma sources with greater flexibility with regard to the deposition conditions, offering more control of the ions energies in particular (e.g. additional bias, dual-frequency systems, electrical asymmetry effect), could also provide more knowledge of the plasma requirements for the growth of good-quality μc -Si:H. The evaluation in parallel of alternative high-density plasma sources, as discussed in Section 1.4, is stimulating and should be further promoted. Modified plasma chemistry involving halogenated silane (e.g. fluoride gases for larger grains) for μc -Si:H growth could be interesting as well.

We should strengthen the link between theoretical approaches involving plasma simulation and kinetic Monte Carlo growth kinetics codes and experimental observations. To reach that goal, more rigorous investigations of step coverages of high-quality μc -Si:H should help. Validation of the code results with experiments and ultimately construction of an overall

predictive model is a major goal on the horizon. Such an approach has the advantage of being at the meeting point between all the underlying physics involved (surface physics, plasma physics, molecular dynamics, etc.) and a lot can be learned from it.

Regarding the development of the thin-film silicon technology itself, a better understanding of the current $V_{\rm oc}$ limitations for μc -Si:H solar cell devices should be gained. By achieving denser and better quality μc -Si:H, work on the interfaces and realization of "passivating" contacts with band offsets can be undertaken [Hänni 13]. This should allow the fabrication of devices with $V_{\rm oc}$ well beyond 600 mV. In the medium term, such high-current, high-voltage μc -Si:H devices, could find applications in new state-of-the-art tandem or triple-junction solar cells, with potential conversion efficiencies of over 16%. More fundamental work on a-Si:H material (e.g. Staebler-Wronski effect, reaching higher $V_{\rm oc}$) and silicon-based alloys is also of great interest to develop better multi-junction devices with more effective utilization of the solar spectrum in the near future.

Very encouraging results were obtained within this thesis work, and hopefully they will contribute to this ongoing effort and help further develop the technology.

A Detailed solar cells performances of the comparative study of RF and VHF

This appendix simply lists all the cells electrical performances values that were presented through the form of figures in Section 5.2.1 where only the best values were retained. This decision was taken for the sake of clarity of the Figures 5.3 and 5.4. Here, both the best and mean values out of the ten best cells are shown for cells prepared either using VHF, in Table A.1, or RF, in Table A.2.

Table A.1: Detailed electrical performances of single junction μ c-Si:H solar cells with their i-layer prepared using VHF and the standard 22 mm KAI-M interelectrode gap. The numbers in brackets are the mean values of the ten best cells on each substrate.

Frequency and substrate	Growth Rate (Å s ⁻¹)	Thickness (µm)	V _{oc} (mV)	FF (%)	$J_{\rm sc}$ 0 / -2 V (mA cm ⁻²)	Efficiency (%)
		1.0	503 (497)	71.7 (70.3)	20.0 / 20.3	7.2
	1.6	1.6	510 (507)	69.4 (68.8)	21.0 / 21.3	7.4
VHF		2.9	483 (479)	65.0 (63.9)	23.5 / 23.9	7.4
		1.0	513 (512)	73.3 (72.4)	19.7 / 19.8	7.4
	2.7	1.7	504 (499)	65.3 (64.5)	22.6 / 22.5	7.4
Z5 60'		2.5	500 (493)	64.2 (63.0)	23.7 / 23.7	7.6
		1.2	485 (480)	67.8 (66.2)	20.8 / 21.3	6.8
	3.8	1.9	487 (486)	65.0 (63.4)	20.8 / 21.2	6.6
		2.4	497 (495)	63.0 (62.3)	20.4 / 21.2	6.4

Appendix A. Detailed solar cells performances of the comparative study of RF and VHF

Table A.2: Detailed electrical performances of single junction μ c-Si:H solar cells with their i-layer prepared using RF and the standard 22 mm KAI-M interelectrode gap. The numbers in brackets are the mean values of the ten best cells on each substrate.

Frequency and substrate	Growth Rate (Å s ⁻¹)	Thickness (µm)	V _{oc} (mV)	FF (%)	$J_{\rm sc}$ 0 / -2 V (mA cm ⁻²)	Efficiency (%)
		1.1	524 (518)	74.7 (73.9)	20.2 / NA	7.9
	1.7	2.0	518 (513)	72.6 (71.4)	22.4 / 22.7	8.4
_		2.6	514 (509)	72.1 (70.7)	23.4 / 23.7	8.7
		0.9	517 (512)	72.7 (71.3)	19.9 / NA	7.5
RF Z5 60'	2.8	1.9	508 (501)	71.6 (71.2)	23.0 / 23.4	8.4
23 00		2.7	507 (504)	70.5 (70.4)	24.0 / 24.4	8.6
		1.0	520 (518)	74.1 (73.4)	20.0 / 20.4	7.7
	3.5	2.0	503 (498)	70.1 (69.2)	21.8 / 22.2	7.7
		2.6	492 (493)	69.0 (68.7)	23.7 / 24.0	8.0
		1.1	503 (501)	70.3 (70.4)	19.6 / NA	6.9
	1.7	2.0	508 (505)	69.4 (69.1)	21.1 / 21.6	7.4
RF Asahi U		2.6	511 (509)	69.7 (69.0)	21.2 / 21.8	7.6
		0.9	513 (507)	71.1 (70.7)	19.3 / 19.7	7.0
	2.8	1.9	508 (507)	69.9 (69.2)	21.5 / 21.3	7.6
		2.7	512 (507)	69.9 (69.6)	21.3 / 21.8	7.6

B On the use of the differential pumping for high pressure plasmas

Introduction

Device-grade *a*-Si:H materials grown by low temperature PECVD typically employ low pressure, low depletion deposition regimes. Large scale homogeneity is ensured by using a proper isothermal reactor, with efficient showerhead gas distribution system for controlling both gas pre-heating and gas composition over the whole substrate area before it enters the plasma region. Contamination issues during deposition can be circumvented through the use of a small leak gas conductance between the actual deposition chamber, where the plasma is properly confined, and the outer vacuum chamber: this allows the establishment of a differential pressure during deposition, with a higher pressure inside the deposition chamber.

These characteristics are typically part of the PlasmaBox concept in the KAI systems [Schmitt 89, Bubenzer 90, Perrin 00] developed at TEL Solar (formerly Unaxis Displays division), as shown in Figure B.1.

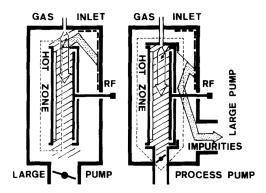


Figure B.1: Conventional capacitive plasma reactor (left) and pressurized plasma box reactor (right). In the first case the degassing impurity flow (gray arrow) mixes with the process gases while in the second case most of this flow is pumped out. Figure and caption taken from [Bubenzer 90].

"The box is slightly leaky but keeps up a pressure gradient of one or two orders of magnitude between the high process gas pressure inside the box and the outer vessel connected permanently to a high rate pump. A completely vacuum-tight plasma box is unpractical since e.g. in a multichamber system substrates have to be transferred in and out".

Similar equipments are typically used for μc -Si:H deposition at growth rate up to about 5 Å s⁻¹, with deposition pressure of around 2.5 mbar or below.

Optimum μc -Si:H deposition conditions greatly differ from a-Si:H

Growing μc -Si:H at higher pressure and/or higher depletion working conditions are typical prerequisites for reaching higher growth rates while keeping device grade quality material. Due to the presence of gas drag forces and much higher diffusivity of hydrogen compared to silane local enrichment of the silane concentration near the leaks of the plasma reactor will take place. This is especially favored at higher pressure differences between the outer chamber and plasma reaction chamber and, hence, enhanced at higher plasma operating pressures. This higher silane concentration combined with high pressure conditions favor the well known undesired powder formation in silane plasmas. The powder itself is then subjected as well to the drag forces present. As a result even localized powder formation sites at the peripheral edges of the inner chamber can generate strong instabilities and significantly affect the entire discharge electrical parameters, which is detrimental for both the overall quality of the deposited material (e.g. thickness and crystallinity variations, creation of defects) and reproducibility.

While inherently leaky reactors are fine for low-pressure regimes such as the ones used for the deposition of a-Si:H or a-SiN $_x$ films, they are not suited to handle significant particulate formation in the plasma. As a result, non-uniformity and instabilities due to powder formation in these regimes are the limiting parameters to the growth of high quality material at high rate or very high pressure regimes in those large area reactors, even with narrow gap configurations.

Improved control of the differential pressure

Retaining the differential pressure concept for PECVD, the establishment of well defined pressure in the zone outside the deposition chamber is advantageous. It allows to precisely control and adjust the immediate pressure drop ratio near the plasma region to avoid the local silane enrichment and limit gas drag forces: this limits aforementioned problems due to powder formation while still keeping a controlled local pressure drop to refrain contamination from the outside if desired.

Outer gas composition can be the same dilution or may also be controlled independently from what is injected in the plasma chamber, and pressure could be independently controlled by different means: for example using butterfly valve on existing system or with properly

defined gas leak conductance between the chambers, so that the pressure ratio can range from as low as possible to equilibrium. This solution allows the use of PlasmaBox reactors at significantly higher working pressures and/or higher depletion regimes, allowing higher growth rates and better material quality over large surfaces without being so much limited with powder formation. Defining the differential pressure $\Delta p = p_{\rm in}$ - $p_{\rm out}$, where $p_{\rm in}$ is the pressure in the volume where the PECVD deposition takes place and $p_{\rm out}$ the pressure in the vacuum chamber, Figure B.2 presents a simple scheme of such solution, when the same pump is used for both volumes. To demonstrate this effect, the set of deposition conditions

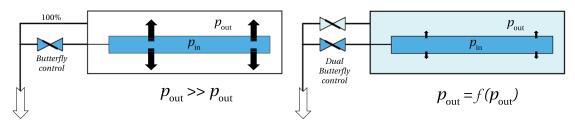


Figure B.2: Left: Standard process using a high differential pressure Δp p_{in} . Right: Improved process with a low differential pressure $\Delta p \leq 0.5-1.0$ mbar or none, at equilibrium.

presented in Section 5.4.1, used to grow a high-quality material at 3 Å s⁻¹with RF, is used here: f=13.56 MHz, $d_{\rm gap}$ =12 mm, P=450 W, p=9.0 mbar and $\Phi_{\rm H_2}$ =2500 sccm. The input silane concentration has to be compensated for the absence of the usual differential pressure to get the same ϕ_c , going from SiH₄=38 sccm to 34 sccm (otherwise the film becomes fully amorphous). The improvement in homogeneity can be seen in Figure B.3. Using the high

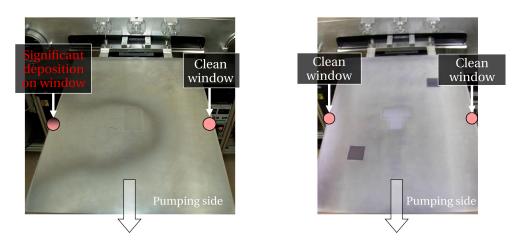


Figure B.3: Deposition of μc -Si:H with a high differential pressure $\Delta p > 8$ mbar (left) and with a low one of $\Delta p = 0.5$ mbar (right).

differential pressure, the *a*-Si:H deposition zone can be clearly identified (ϕ_c < 10%) around the μc -Si:H deposition central region. The presence of the leak near the viewport, is also evidenced by the formation and sticking of powder near the observation window. However,

Appendix B. On the use of the differential pumping for high pressure plasmas

with the low differential pressure (0.5 mbar), the Raman crystallinity factor is kept well within \pm 10% over the area in the a-Si:H/ μc -Si:H transition zone around 50%. Solar cell performances is the same in both cases, indicating that the same material quality is obtained: homogeneity alone is affected.

Small differential pressure values are thus desired for microcrystalline growth and having the ability to freely adjust p_{out} so that it is becomes a function of internal pressure is beneficial for homogeneity and can be defined for a given system and deposition regime: for example $p_{\text{out}} = 0.5 \ p_{\text{in}}$, $p_{\text{out}} = 0.75 \ p_{\text{in}}$ or $p_{\text{out}} = 0.95 \ p_{\text{in}}$ (ideally controlling from maximum differential pressure to equilibrium).

Further Advantages

- In our case this also allowed the use of OES more conveniently as the viewport was always clean even during very dusty regimes.
- Forces applied on the reactor parts from the inside towards the outside can be greatly reduced in high pressure regimes, when the gas pressure difference between the outer vacuum chamber and the inner plasma chamber is reduced, leading to reduced mechanical stress and/or deformation that may also affect leakage rate. A rough estimate of the force exerted on end plates of PlasmaBox in a KAI-1200 with a 10 mbar pressure difference is around 140 kg. Improved lifetime and reduced maintenance times may also result from the reduced mechanical force acting onto the equipment.
- Leakage rate of one PlasmaBox may vary from one to another of the production stack reactor tower leading to discrepancy in deposition regimes used for the growth of microcrystalline silicon, and ultimately increased dispersion in the devices performances from one reactor to another (*e.g.* difference in silane adjustment depending on leak rate, local silane enrichment and powder formation etc.). The solution proposed may as well alleviate this issue by limiting the influence of leakage rate on the plasma conditions.
- Limited powder formation also facilitates reactor cleaning using existent solutions based on either SF_6 , NF_3 or F_2 .

C LPCVD ZnO-based intermediate reflector for micromorph tandem solar cells

This appendix discusses the use of LPCVD ZnO as an intermediate reflector in micromorph solar cells in order to boost the top a-Si:H subcell $J_{\rm sc}$, as presented in the reference [Bugnon 11b]. This work was supported by the Bosch Solar Thin Film GmbH. Didier Dominé is thanked for helpful discussions on the ZnO-based intermediate reflector technology.

The use of zinc oxide (ZnO) based intermediate reflector (ZIR) in micromorph solar cells using low pressure chemical vapor deposition (LPCVD) was investigated. The influences of deposition temperature and dopant gas concentration on grain size and lateral electrical conductivity measurements is presented. Further ZIR deposition conditions were then directly evaluated in micromorph solar cell devices. Their electrical performances were compared to reference cells and cells incorporating silicon oxide based intermediate reflector. It is shown that both reduced ZIR deposition temperature and increased total flow rate allow for better performing devices with increased shunt resistance, as further supported by lock-in thermography shunt imaging. Relative micromorph efficiency increase of above 7% are shown with thin ZnO layers, along with absence of loss or even small increase of total current in the whole structure compared to cells without intermediate reflector.

Introduction

The micromorph tandem cell configuration [Meier 94a], based on monolithic series interconnection of an amorphous silicon (a-Si:H) top cell with a microcrystalline (μc -Si:H) bottom cell, yet represents one of the most effective approach. As a result of the series connection, the tandem short-circuit current density ($J_{\rm sc}$) is limited by the lowest of either the top $J_{\rm sc,Top}$ or bottom $J_{\rm sc,Bot}$ cell current. However, because of the Staebler-Wronski light-induced degradation of a-Si:H based materials [Staebler 77], the top cell should be kept reasonably thin (< 300 nm) in order to mitigate this effect and limit carrier collection losses [Bennett 88]. Thinner cells are also desirable for lower production costs. For these reasons the concept of an intermediate reflector layer (IRL) was first introduced by IMT Neuchâtel [Fischer 96] to increase the top cell current without increasing its thickness. Thanks to the implementation of

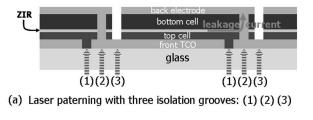
Appendix C. LPCVD ZnO-based intermediate reflector for Micromorph tandem solar cells

such IRL within micromorph solar cells, high stabilized efficiencies laboratory cells could be obtained [Meier 03, Yamamoto 03, Dominé 09, Bailat 10], and high initial module efficiency of 13.5%, and 12% stabilized were also reported [Yamamoto 05].

Intermediate reflector layers (IRL) were first made of a ZnO (ZIR), but more recently the use of doped silicon oxide layer (SOIR) to fulfill this role could also be demonstrated [Buehlmann 07, Lambertz 07]. One of the SOIR advantage is to be deposited directly through conventional plasma enhanced chemical vapor deposition (PECVD) in the same type of reactor as the solar cells. However its main drawback is a low deposition rate in most of the cases below 1 Å/s, while values above 1 nm/s for LPCVD ZIR are fairly typical. With increasing IRL thickness the amount of J_{sc} transferred from the bottom to the top first increases up to around 100 nm then reach a plateau [Fischer 96, Buehlmann 07, Dominé 08]. The difference between the $J_{\text{sc,Top}}$ gain the $J_{\text{sc,Bot}}$ loss in the bottom cell is attributed to increased absorption in the IRL and doped layers but also to increased total reflectance. It has also been demonstrated that the IRL promotes increased light trapping capability of the front transparent conductive oxide (TCO) layer in the 550–700 nm spectral range with enhanced top cell $J_{\text{sc,Top}}$ gains [Dominé 08, Dominé 09].

Apart from providing sufficiently low absorption coefficient and low refractive index compared to silicon, other important characteristics of an IRL for its implementation in a tandem device are its perpendicular and lateral conductivities. While perpendicular conductivity (σ_{\perp}) should remain quite high to prevent a significant increase in series resistance of the device, in-plane conductivity (σ_{\parallel}) should be maintained sufficiently low to limit the series interconnection range of shunts present in either the top or bottom cells, which can decrease both the $V_{\rm oc}$ and the FF [Dominé 09, Vaucher 98]. Another advantage of low σ_{\parallel} values is that leakage current from the ZIR to the back electrode becomes significantly lower, hence allowing to avoid a fourth scribe to insulate the ZIR from the back contact, as proposed by Meier et al. [Meier 02], which main drawback is to increase the dead area of the module as shown in Fig. C.1. The introduction of an IRL also allows the tuning of current balance in the tandem structure, which is known to affect the FF of the device and its overall performance. However, to date, favoring top or bottom limited conditions is still under discussion as it has to take into account the spectral irradiance distribution, the temperature coefficient of the micromorph cell [Repmann 03, Nakajima 04, Yunaz 07a, Dominé 09] along with the intrinsic qualities of each subcell.

In this study we report the development of ZIRs deposited at high rate with LPCVD (between 1 and 3 nm/s) with high lateral resistivity and their implementation in tandem solar cells a-Si:H/ μc -Si:H compared to cells with SOIR and without IRL. Characterization of thin ZnO layers deposited on glass are first presented, then ZIRs are directly evaluated within micromorph solar cells. Cell electrical performances are analyzed under 100% and 0.4% illumination conditions to evaluate shunting issues in the devices along with lock-in thermography imaging. Current repartition in the structure is also examined and absence of total current net loss and even total current gain could be observed for micromorph embedding thin resistive ZIRs.



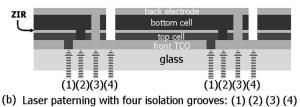


Figure C.1: Top: Conventional tandem cell interconnection with three scribes, in which leakage current from ZIR to back electrode can be detrimental to the module performance. Bottom: Four scribes alternative proposed by Meier et al. [Meier 02] to insulate the ZIR from the back contact. Figure from D.Dominé PhD Thesis [Dominé 09]

Experimental details

ZnO deposition and characterization

The ZnO layers were deposited using a Low Pressure Chemical Vapor Deposition (LPCVD) process, detailed elsewhere [Faÿ 03, Steinhauser 08a]. Precursor gases employed were diethylzinc (DEZ) and water vapors, and doping gas was diborane (B_2H_6) diluted in argon. Optical transmission of the deposited films were obtained using a Perking-Elmer photo-spectrometer with an integrating sphere. The resistivity of the films was measured using a Keithley 617 programmable electrometer in the I/V mode, with 40 nm thick aluminium evaporated coplanar contacts on top of the ZnO layers. The spacing between the contacts was 0.5 mm and the length of the contacts 8 mm. Atomic Force Microscopy (AFM) and Focused Ion Beam/Scanning Electron Microscopy (FIB-SEM) were used to characterize both the morphology of the textured surface and its bulk structure.

Micromorph solar cell devices: fabrication and characterization

Tandem p-i-n a-Si:H/ μc -Si:H tandem cells were prepared to evaluate the influence of the ZIR on their overall performances. SnO₂:F front contact coated glasses (1.5 mm total thickness) from Asahi company in Japan were used as substrates for micromorph solar cells except where stated differently. A thin 15 nm sputtered ZnO layer was deposited on top of these substrates to prevent reduction of the SnO₂ during the standard p-(μc -Si:H) layer process of the a-Si:H top cell [III 83]. For single junction reference cells of top and bottom cells, textured LPCVD ZnO front contact of 2 μ m (Z2) and 5 μ m (Z5, less doped) grown on Schott AF 45 glass were used respectively after surface treatment [Bailat 06]. The patterned cells were 0.25 cm² each

Appendix C. LPCVD ZnO-based intermediate reflector for Micromorph tandem solar cells

for a-Si:H and μc -Si:H single junction devices and 1.2 cm² for micromorph cells. They were defined through a lift-off operation followed by a dry etching of silicon in SF₆+O₂ plasma to access the front contact. For micromorph cells with a ZIR, an additional wet etching step with HNO₃ was employed to complete the patterning. For all the cells the ZnO back contact was covered with a white dielectric reflector.

A medium-sized version of the large area industrial PECVD KAI™systems [Perrin 00] was used to deposit solar cell devices and the SOIR presented in this study. The generator frequency was set to 40.68 MHz and the deposition temperature fixed at 180 °C. Some *a*-Si:H top cells deposited from Bosch Solar Thin Film GmbH (BSTF) on 4 mm glass with Asahi VU front contact were also used to evaluate ZIR performances directly in micromorph devices.

Open circuit voltage ($V_{\rm oc}$) and fill factor (FF) values were derived from current-voltage curves, obtained using a Wacom solar simulator in standard conditions (25 °C, AM1.5g spectrum, 100 mW/cm²). The best cell on every substrate was selected based on its high $V_{\rm oc}$ and FF values under 100% sun illumination and high FF under 0.4% sun illumination conditions. The short circuit current densities ($J_{\rm sc}$) of the best cells were normalized to external quantum efficiency (EQE) measurements at 0 V bias.

Infrared lock-in thermography analysis was performed on the cells, to help identifying the number and nature of the shunts, coming from cell isolation or dust particles.

Results and discussion

ZnO lateral conductivity characterization

ZnO thin film conductivity is known to increase with thickness as the grain size becomes larger and the grain boundary density consequently smaller [Steinhauser 08b]. In order to achieve high lateral resistivity only a few tenth of nanometers were grown: these layers were highly polycrystalline and made of narrow grains with a high boundary density. Also, for a given thickness, decreased temperature or increased precursor flow rates should result in a decrease of adatom surface mobility leading to smaller grain size, providing additional solutions for increasing the layer resistivity [Nicolay 09]. This is shown on AFM images presented in Fig. C.2, where larger grains result from increased thickness or growth temperature. Fig. C.3 shows FIB-SEM images of thick layers grown at low and high temperature. It can be seen that at low temperature, the structure remains granular throughout the growth while at high temperature the grains size increase during the growth.

To investigate the variations of lateral conductivity of the ZnO layers, samples with different thicknesses, dopant and temperature were deposited on glass substrates, with the total pressure kept constant at 0.5 mbar. Results of resistance measurements on these samples are presented in Table C.1.

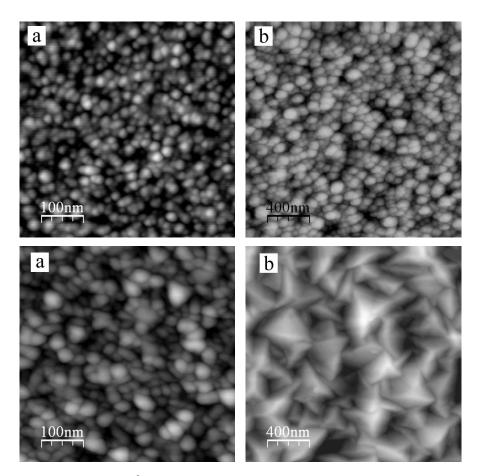


Figure C.2: Left: $0.5\times0.5~\mu m^2$ AFM picture of a 40 nm thick ZnO at 110 °C (top) and 150 °C (bottom). Right: $2.0\times2.0~\mu m^2$ AFM picture of a 1.65 μ m thick ZnO at 110 °C (top) and 150 °C (bottom) (images source from Ref [Nicolay 09]).

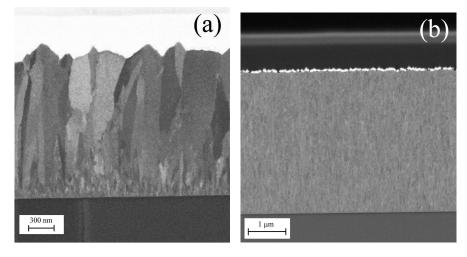


Figure C.3: FIB-SEM picture of a 1.7 μ m thick LPCVD ZnO film deposited at 180 ° C (a) and a 3.5 μ m film at 110 ° C (b).

Appendix C. LPCVD ZnO-based intermediate reflector for Micromorph tandem solar cells

Table C.1: Summary of resistance measurements on thin ZnO layers.

Temperature (°C)	B ₂ H ₆ (sccm)	Thickness (nm)	R_{\parallel} (k Ω)
130	2	20	>×10 ⁶
130	2	40	-
130	2	60	1.9×10^{4}
130	2	75	1.0×10^4
130	2	110	3.6×10^2
130	10	25	5.1×10^4
130	10	125	1.1×10^4
130	20	20	6.3×10^{5}
130	20	120	1.8×10^2
180	2	120	3.8×10^{1}

As expected, the measured resistance of the ZnO layers decreased as the thickness and the temperature increase. In plane conductivities were in the order of 10^{-1} S/cm for the ZIR deposited at $180\,^{\circ}$ C and between 10^{-2} and 10^{-4} S/cm for the deposition at $130\,^{\circ}$ C. Increased dopant flow rate from 2 to 20 sccm led to a decreased resistance, except for the thicker film with 10 sccm. Also, it is worth mentioning here that the SOIR provides a higher lateral resistivity as reported in [Buehlmann 07, Dominé 09] with a value of of 10^{-9} S/cm compared to 10^{-6} S/cm for the ZIR deposited at $130\,^{\circ}$ C and 1 S/cm for the ZIR deposited at $180\,^{\circ}$ C. The influence of deposition pressure was not analyzed in this study but may also be another possibility to further lower the in-plane conductivity.

This study indicates that thin ZnO layers deposited at low temperature should be the preferred solution as ZIR in tandem solar cells. In the next part, ZIR tests done directly within such devices are presented.

ZIR evaluation in micromorph tandem devices

Effect of ZIR thickness and growth temperature

In this section we present micromorph devices with top and bottom cell thicknesses of 270 nm and 1.8 μ m respectively. After the deposition of the top a-Si:H cell, four samples were coated with a ZIR, one sample with 80 nm SOIR and one sample was kept as a reference. Among the ZIRs presented here one is 80 nm thick deposited at 180 °C and the three others were 20, 80 and 120 nm thick deposited at 130 °C. The electrical parameters of the cells are presented in Table C.2.

Table C.2: Electrical parameters of micromorph tandem cells deposited with various intermediate reflectors under 100% and 0.4% sun illumination conditions.

	V _{oc}	FF	J _{sc,Top} (gain)	$J_{ m sc,Bot}$	Sum J _{sc}	$R_{ m sh}$	V _{oc} (0.4%)	R _{sh} (0.4%)	η
IR type	(V)	(%)		$(mA cm^{-2})$		$(\Omega\mathrm{cm}^{-2})$	(V)	$(\Omega\mathrm{cm}^{-2})$	(%)
Without	1.20	68.1	11.4	12.0	23.4	5.4×10^3	0.79	6.8×10^5	9.3
ZIR - 130 °C, 20 nm	1.21	71.1	12.0 (+0.6)	11.2	23.2	4.2×10^3	0.74	2.1×10^5	9.6
ZIR - 130 °C, 80 nm	1.22	73.8	13.1 (+1.7)	10.1	23.2	2.7×10^3	0.64	2.5×10^4	9.0
ZIR - 130 °C, 120 nm	1.22	76.2	13.6 (+2.2)	9.2	22.8	4.8×10^3	0.78	2.3×10 ⁵	8.6
ZIR - 180 °C, 80 nm	1.20	63.2	12.9 (+1.5)	10.1	23.0	4.8×10^2	0.37	8.7×10^3	7.7

The overall $V_{\rm oc}$ of the cells is quite low due to an issue during top a-Si:H cell deposition, but it should not affect the comparison study. The reference a-Si:H cell had a $V_{\rm oc}$ of 717 mV, a FF of 71.2%, a $J_{\rm sc}$ of 15.8 mA cm $^{-2}$ and an initial efficiency of 8.1%. The μc -Si:H bottom cell had a $V_{\rm oc}$ of 510 mV, a FF of 71.4%, a $J_{\rm sc}$ of 21.0 mA cm $^{-2}$ and an efficiency of 7.6%. The reference micromorph cell has an initial efficiency of 9.6% with a top cell current of 11.4 mA cm $^{-2}$.

Fig. C.4 shows the EQE measurements of the micromorph tandem cells with increasing ZIR thickness. With only 20 nm of ZIR a gain of 0.6 mA cm $^{-2}$ is observed in the 500–800 nm region, and with increasing ZIR thickness around 0.16 mA cm $^{-2}$ per 10 nm is further transferred in the top cell, reaching 2.2 mA cm $^{-2}$ gain with the 120 nm ZIR. The total current in the micromorph cells decreased from 23.4 mA cm $^{-2}$ for the reference cell to 23.2 and 22.9 mA cm $^{-2}$ for increasing ZIRs thicknesses of 20 to 120 nm.

Transverse conductivity of the deposited ZIRs is sufficiently high so that it does not impact the series resistance of the micromorphs: only a relative increase of 3% at maximum is observed, which is in fact within the scattering of the micromorph cells references. The advantage of the resistive ZIR deposited at 130 °C is shown here by the strong increase of FF from 63.2% to 71.1% compared to the one deposited at 180 °C, with increased shunt resistance $R_{\rm sh}$. At low illumination it can be seen that the $V_{\rm oc}$ is much lower for the ZIR done at 180 °C, most likely due to increased shunt interconnection range issues. This is the reason why it is advantageous to use the more resistive ZnO layers deposited at lower temperature. However, it should be noted here that the yield was systematically lower for the cells with a ZIR compared to the reference cell, as only the best cells on each substrate are shown here.

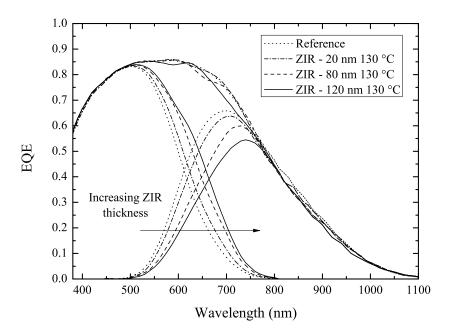


Figure C.4: EQE measurements of micromorph cells with increasing thickness of the ZIR, and without ZIR for reference. The sum of both top and bottom subcells for each micromorph measured is also presented.

Effect of total gas flow for ZIR deposition

In this section micromorph devices with top and bottom cell thicknesses of 210 nm and 1.7 μ m respectively are presented. After the deposition of the top a-Si:H cell, two samples were coated with a ZIR, one sample with 30 nm SOIR and one sample was kept as a reference. The ZIRs deposited at 130 °C only differed by the use of high or low total gas flow (Φ_T). Low flow rate conditions correspond to the conditions of the ZIRs presented in the previous section. The electrical parameters of the cells are presented in Table C.3.

The overall $V_{\rm oc}$ of the cells is again lower than expected which is due to the bottom cell performances. The reference a-Si:H cell had a $V_{\rm oc}$ of 905 mV, a FF of 76.9%, a $J_{\rm sc}$ of 15.0 mA cm $^{-2}$ and an initial efficiency of 10.4%. The μc -Si:H bottom cell had a $V_{\rm oc}$ of 453 mV, a FF of 64.6%, a $J_{\rm sc}$ of 22.4 mA cm $^{-2}$ and an efficiency of 6.6%. The reference cell without intermediate reflector has a relatively low efficiency of 9.0%, due to a poor performing bottom cell, with a top cell current of 10.4 mA/cm2. In the case the 40 nm ZIR deposited with standard total gas flow a significant series resistance increase of 27% is observed (going from 11.3 to 14.3 Ω .cm 2), strongly affecting the fill-factor, although its origin is not clear. All the other cells are very similar in this aspect.

The 30 nm SOIR allows a significant increase of 1.4% in efficiency of the tandem cell thanks to both the mismatch change, going from top to bottom limited conditions, and the increase of the shunt resistance. The best tandem cell with a ZIR was the one deposited with increased total flow rate, which tends to confirm the beneficial effect of this parameter for reducing

Table C.3: Electrical parameters of the second run of micromorph tandem cells deposited with various intermediate reflectors under 100% and 0.4% sun illumination conditions.

	V _{oc}	FF	J _{sc,Top} (gain)	$J_{ m sc,Bot}$	Sum J _{sc}	$R_{\rm sh}$	V _{oc} (0.4%)	R _{sh} (0.4%)	η
IR type	(V)	(%)		(mA cm ⁻²)		$(\Omega\mathrm{cm}^{-2})$	(V)	$(\Omega\mathrm{cm}^{-2})$	(%)
Without	1.28	68.0	10.4	12.3	22.7	1.7×10^3	0.80	6.8×10^5	9.0
SOIR - 30 nm	1.29	75.7	11.6 (+1.2)	10.7	22.3	2.4×10^5	0.70	4.9 × 10 ⁷	10.4
ZIR - 130 °C, 40 nm	1.27	63.8	11.3 (+0.9)	10.7	22.0	2.3×10^3	0.10	3.9×10^3	8.7
ZIR - 130 °C, 40 nm, high Φ_T	1.29	67.4	11.3 (+0.9)	11.6	22.9	3.9×10^3	0.36	1.9×10^4	9.8

lateral conductivity of the ZnO layer. The $J_{\rm sc}$ gain in the top cell was 0.9 mA cm⁻² for each 40 nm thick ZIRs. The total $J_{\rm sc}$ was seen to increase for the 40 nm ZIR deposited with higher total flow rate, going from 22.7 mA cm⁻² to 22.9 mA cm⁻². Raman crystallinity measurements from the n-side of the cells were also carried out but no change could be observed on any of the samples. This gain in current will be discussed more in detail in the next section.

As the ZIR was seen to reduce the yield of the micromorph tandem cells compared to the tandem cell with SOIR or without IR, locking thermography observations were done to check whether the shunts came from the cell isolation or from dust particles. Pictures are shown in Fig. C.5. The shunts were located both on the center and on the edge of the cell. Reference cell and the one with a SOIR exhibited significantly lower shunt density, compared to the micromorphs incorporating a ZIR. However, it can be noted that the ZIR deposited with high fluxes at 130 °C seems to reduce the number of visible shunts compared to the one with standard fluxes, which is also correlated with better performing cells under 1 and 0.4% sun. In addition, the authors think that by working in a cleaner environment, the effect of shunting with the ZIR should also be less prominent as particles would be reduced during this intermediate step.

Tests with top cell from BSTF

The last series presented consisted in trial a-Si:H top cells deposited by BSTF on Asahi Gen 5 (1100 \times 1300 mm²) substrates in ai KAI 1200 sytem, with the bottom cell completed in Neuchâtel in regular KAI-M system. The μc -Si:H absorber layer was 2.0 μ m thick, and the reference single junction cell had a $V_{\rm oc}$ of 513 mV, a FF of 71.4%, a $J_{\rm sc}$ of 21.1 mA cm $^{-2}$ and an efficiency of 7.7%. Micromorph cells details are presented in Table C.4.

The micromorph reference cell had an initial efficiency of 11.0% with a $V_{\rm oc}$ of 1.38 V. Two ZIR

Appendix C. LPCVD ZnO-based intermediate reflector for Micromorph tandem solar cells

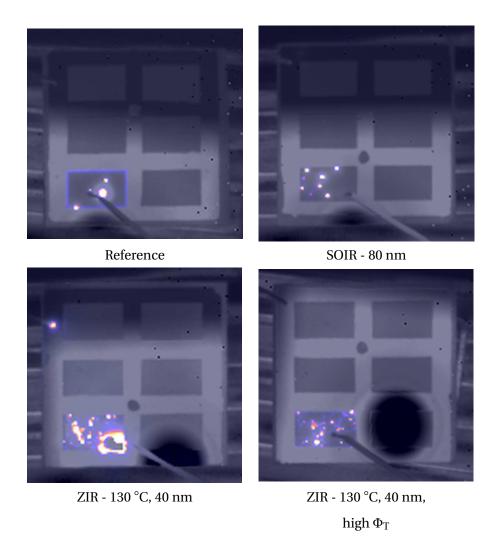


Figure C.5: Lock-in thermography pictures of micromorph cells without intermediate reflector (top left), with a SOIR (top right) and with 40 nm ZIRs deposited at 130 °C using standard total gas flow (bottom left) and high total gas flow (bottom right). Using a forward bias, the shunts positions are represented by the bright regions where localized high leakage current paths are present.

Table C.4: Electrical parameters of micromorph tandem cells deposited with various intermediate reflectors under 100% and 0.4% sun illumination conditions with the top a-Si:H cell deposited at BSTF.

	V _{oc}	FF	J _{sc,Top} (gain)	$J_{\rm sc,Bot}$	Sum J_{sc}	R _{sh}	V _{oc} (0.4%)	R _{sh} (0.4%)	η
IR type	(V)	(%)		$(mA cm^{-2})$		$(\Omega\mathrm{cm}^{-2})$	(V)	$(\Omega\mathrm{cm}^{-2})$	(%)
Without	1.38	72.0	11.1	12.0	23.1	8.6×10^3	0.93	1.3×10^6	11.0
SOIR - 50 nm	1.38	77.2	12.3 (+1.2)	10.6	23.0	8.3×10 ³	0.92	4.3×10^5	11.3
ZIR - 130 °C, 50 nm	1.37	75.1	12.1 (+1.0)	11.2	23.3	7.7×10^3	0.90	2.4×10 ⁵	11.5
ZIR - 130 °C, 280 nm	1.37	75.9	13.0 (+1.8)	9.9	22.9	1.8×10 ³	0.84	7.4×10^4	10.3
ZIR - 110 °C, 40 nm	1.37	73.0	11.6 (+0.5)	11.5	23.1	1.6×10 ³	0.46	1.8×10 ⁴	11.5
ZIR - 110 °C, 120 nm	1.37	73.8	12.2 (+1.0)	10.8	23.0	2.1×10^3	0.86	7.6×10^4	10.9
ZIR - 110 °C, 240 nm	1.38	77.3	12.7 (+1.5)	10.1	22.7	8.7×10^3	0.48	1.2×10 ⁵	10.8
ZIR - 110 °C, 40 nm (more doped)	1.37	75.4	11.9 (+0.7)	11.4	23.3	2.3×10 ⁵	0.82	1.4×10 ⁵	11.8

temperatures, 110 and 130 °C, were tested for different thicknesses. The best cell is obtained with a thin ZIR deposited at 110 °C slightly doped, with an initial efficiency of 11.8% with similar $V_{\rm oc}$ compared to the reference cell. The intentional low doping was done to inhibit the growth of larger grains. All the cells in this series have similar series resistances.

Again, when thin ZIRs of around 40–50 nm were employed the total current was observed to be either unchanged or even improved compared to the reference cell. This can be seen on external quantum efficiency measurements in Fig. C.6 where the reference cell is compared to the cell with a 50 nm ZIR deposited at 130 °C and the cell with a 40 nm thick one at 110 °C more doped, which both exhibit an increase of 0.2 mA/cm² in total current. Most of the gain in total current with these 40–50 nm ZIRs happened in the range of 750–1000 nm. No significant change in Raman crystallinity of the μc -Si:H bottom cell, which could have explained such a gain, could be observed on any of these substrates. This kind of increase in total $J_{\rm SC}$ has already been reported by Yamamoto et al. [Yamamoto 04], even though neither the exact nature of the reflector nor the refractive index and layers thicknesses were specified. One hypothesis is that the gain observed would come from partial reflection of the reflected light from the back electrode at the ZIR providing enhanced light confinement for the bottom cell. It should be noted as well that the a-Si:H top cell thickness can also behave as a half-wavelength plate,

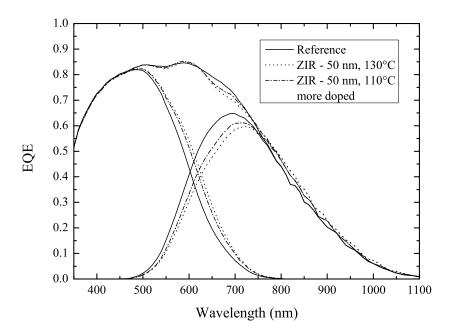


Figure C.6: EQE measurements of micromorph cells without intermediate reflector and with a ZIR of 50 nm deposited at 130 °C. Sum of both top and bottom subcells for each micromorph measured is also presented. Cell details are presented in Table C.4.

such that its thickness also influences the position of minima and maxima which could explain such an effect if well positioned [Vaucher 98, Dominé 09]. Total reflectance measurements were carried out directly on the cells but the use of thick glasses prevented us from having sufficient precision to confirm reduced reflectance. These interference effects may be more pronounced when working with Asahi front TCO, compared to more diffusive as-grown LPCVD ZnO, because of its lower haze parameter (defined as the ratio of diffused over total transmitted light) which translates into increased coherent light through the device.

Finally, from an electrical point of view, it should be noted that EQE measurements of the limiting subcell component in the structure (either top or bottom cell depending on the light bias conditions) were done with the full tandem at short-circuit conditions. This means that the measured subcells were actually operating under slight reverse bias conditions which could have affected carriers collection [Burdick 86, Meusel 03], depending on the significance of its voltage dependency, which can be quite important with shunted cells in particular. For this reason the reference cell and the ones with increased total current were also measured with an additional forward DC bias of 0.45 V and 0.85 V for the top cell and bottom cell respectively. All three cells were exhibiting very similar behavior with a decrease in between 0.20–0.24 mA/cm² for $J_{\rm sc,Top}$, 0.13–0.15 mA/cm² for $J_{\rm sc,Bot}$ and 0.35–0.37 mA/cm² on the overall $J_{\rm sc,Total}$. This confirms that the observed gain in total current with the use of thin ZIRs is mainly an optical effect and not linked to EQE measurement artifacts.

The yield was again slightly lower for the cells implementing a ZIR in this run. However,

increased in plane conductivity may not be the only cause in all those cases. It is possible that because of the additional ex-situ fabrication steps shunting issues may come from dust particles. Working in a cleaner environment may help in this regard. Also the HNO $_3$ wet etching step used to complete the patterning of micromorphs embedding a ZIR may also be an important factor to explain these performances degradation. Even though it is difficult as of now to assess the exact responsibility of this specific step on the shunting issues and reduced yield observed. The authors believe the HNO $_3$ could have effectively etched the ZIR at some places or even accessed the front TCO on the cells borders. A laser-scribing procedure to perform the cells patterning would definitely allow to compare more accurately the ZIR performances with the reference cells and the cells including a SOIR which do not have this additional wet etching step. Further attention is thus required to better evaluate the ZIR solution in this aspect.

Conclusion

Thin ZnO layers exhibiting an anisotropy in conductivity with low in-plane conductivity and high transverse conductivity for use as intermediate reflector in micromorph tandem cells were developed. The use of lower ZnO deposition temperature and lower dopant gas flow showed increased lateral resistivity. The best micromorph cell was done with thin ZIRs of 40–50 nm deposited at low temperature, for which no net loss or even increase in total current were observed. Relative increase of micromorph efficiency above 7% is observed compared to a cell without intermediate reflector. However, shunting issues and lower yield (defined as cells with $V_{\rm oc}$ values above 0.6 V under 0.4% illumination) were identified with micromorph cells incorporating a ZIR compared to reference cells and cells with a SOIR. Better control of the additional steps required for the ZIR fabrication could however limit these problems, and allow for a better evaluation of the ZIR solution.

Bibliography

- [Abelson 93] J.R. Abelson. *Plasma deposition of hydrogenated amorphous silicon: Studies of the growth surface.* Applied Physics A, vol. 56, no. 6, pages 493–512, 1993.
- [Abramov 98] A.S. Abramov, A.Ya. Vinogradov, A.I. Kosarev, M.V. Shutov, A.S. Smirnov & K.E. Orlov. *Ion bombardment of amorphous silicon films during plasma-enhanced chemical vapor deposition in an rf discharge*. Technical Physics, vol. 43, no. 2, pages 180–187, 1998.
- [Amanatides 01] E. Amanatides & D. Mataras. *Frequency variation under constant power conditions in hydrogen radio frequency discharges*. Journal of Applied Physics, vol. 89, no. 3, pages 1556–1566, 2001.
- [Amanatides 02] E. Amanatides, D. Mataras & D. E. Rapakoulias. *Combined effect of electrode gap and radio frequency on power deposition and film growth kinetics in SiH4/H2 discharges*. Journal of Vacuum Science & Technology A: Vacuum, Surfaces, and Films, vol. 20, no. 1, pages 68–75, 2002.
- [Amanatides 11] E. Amanatides, D. Mataras & A. Salabaş. *Simulation of plasma enhanced chemical vapor deposition of microcrystalline silicon thin films in an industrially relevant bench chamber*. In Proceedings of the 26th European Photovoltaic Solar Energy Conference, pages 2695–2698, Hamburg, Germany, 2011.
- [Bailat 02] J. Bailat, E. Vallat-Sauvain, L. Feitknecht, C. Droz & A. Shah. *Influence of substrate on the microstructure of microcrystalline silicon layers and cells*.
 Journal of Non-Crystalline Solids, vol. 299-302, no. Part 2, pages 1219–1223, April 2002.
- [Bailat 04] J. Bailat, E. Vallat-Sauvain, M. Dubey, F. Meillaud, X. Niquille, J. Guillet, A. Shah, A. Poruba, L. Mullerova, J. Springer & M. Vanecek. Active Layer Quality and Open-Circuit Voltage of NIP and PIN Microcrystalline Solar Cells. In Proceedings of the 19th European Photovoltaic Solar Energy Conference, pages 1451–1544, 2004.

[Bailat 06]

J. Bailat, D. Domine, R. Schluchter, J. Steinhauser, S. Fay, F. Freitas, C. Bucher, L. Feitknecht, X. Niquille, T. Tscharner, A. Shah & C. Ballif. *High-Efficiency P-I-N Microcrystalline and Micromorph Thin Film Silicon Solar Cells Deposited on LPCVD ZnO Coated Glass Substrates*. In Photovoltaic Energy Conversion, Conference Record of the 2006 IEEE 4th World Conference on, volume 2, pages 1533–1536, May 2006.

[Bailat 10]

J. Bailat*et al. Recent developments of high-efficiency micromorph tandem solar cells in KAI-M PECVD reactors.* In Proceedings of the 5th World Conference on Photovoltaic Solar Energy Conversion, pages 2720–2723, Valencia, Spain, 2010.

[Ballutaud 04]

J. Ballutaud, C. Bucher, Ch. Hollenstein, A.A. Howling, U. Kroll, S. Benagli, A. Shah & A. Buechel. *Reduction of the boron cross-contamination for plasma deposition of p–i–n devices in a single-chamber large area radio-frequency reactor*. Thin Solid Films, vol. 468, no. 1–2, pages 222–225, 2004.

[Bartlome 09]

R. Bartlome, A. Feltrin & C. Ballif. *Infrared laser-based monitoring of the silane dissociation during deposition of silicon thin films.* Applied Physics Letters, vol. 94, no. 20, page 201501, 2009.

[Bartlome 10]

R. Bartlome, B. Strahm, Y. Sinquin, A. Feltrin & C. Ballif. *Laser applications in thin-film photovoltaics*. Applied Physics B, vol. 100, no. 2, pages 427–436, 2010.

[Bennett 88]

M.S. Bennett & K. Rajan. *The stability of multi-junction a-Si solar cells*. In Photovoltaic Specialists Conference, 1988, Conference Record of the Twentieth IEEE, volume 1, pages 67–72, 1988.

[Berginski 07]

Michael Berginski, Jürgen Hüpkes, Melanie Schulte, Gunnar Schöpe, Helmut Stiebig, Bernd Rech & Matthias Wuttig. *The effect of front ZnO:Al surface texture and optical transparency on efficient light trapping in silicon thin-film solar cells.* Journal of Applied Physics, vol. 101, no. 7, page 074903, 2007.

[Biron 13]

Rémi Biron, Simon Hänni, Mathieu Boccard, Céline Pahud, Karin Söderström, Martial Duchamp, Rafal Dunin-Borkowski, Grégory Bugnon, Laura Ding, Sylvain Nicolay, Gaetano Parascandolo, Fanny Meillaud, Matthieu Despeisse, Franz-Josef Haug & Christophe Ballif. *New progress in the fabrication of n–i–p micromorph solar cells for opaque substrates*. Solar Energy Materials and Solar Cells, vol. 114, no. 0, pages 147–155, 2013.

[Boccard 10]

Mathieu Boccard, Peter Cuony, Corsin Battaglia, Matthieu Despeisse & Christophe Ballif. *Unlinking absorption and haze in thin film silicon solar cells front electrodes.* physica status solidi (RRL) – Rapid Research Letters, vol. 4, no. 11, pages 326–328, 2010.

- [Boccard 11] M. Boccard, P. Cuony, M. Despeisse, D. Dominé, A. Feltrin, N. Wyrsch & C. Ballif. Substrate dependent stability and interplay between optical and electrical properties in [mu]c-Si:H single junction solar cells. Solar Energy Materials and Solar Cells, vol. 95, no. 1, pages 195–198, 2011. 19th International Photovoltaic Science and Engineering Conference and Exhibition (PVSEC-19) Jeju, Korea, 9-13 November 2009.
- [Boccard 12a] M. Boccard, T. Soderstrom, P. Cuony, C. Battaglia, S. Hanni, S. Nicolay, L. Ding, M. Benkhaira, G. Bugnon, A. Billet, M. Charriere, F. Meillaud, M. Despeisse & C. Ballif. Optimization of ZnO Front Electrodes for High-Efficiency Micromorph Thin-Film Si Solar Cells. Photovoltaics, IEEE Journal of, vol. 2, no. 3, pages 229–235, July 2012.
- [Boccard 12b] Mathieu Boccard. Novel Micromorph Solar Cell Structures for Efficient Light Trapping and High-Quality Absorber Layers. PhD thesis, STI, Lausanne, 2012.
- [Bonnet-Eymard 13] M. Bonnet-Eymard, M. Boccard, G. Bugnon, F. Sculati-Meillaud, M. Despeisse & C. Ballif. *Optimized short-circuit current mismatch in multi-junction solar cells*. Solar Energy Materials and Solar Cells, vol. 117, no. 0, pages 120–125, 2013.
- [Bouchoule 91] A. Bouchoule, A. Plain, L. Boufendi, J. Ph. Blondeau & C. Laure. *Particle generation and behavior in a silane-argon low-pressure discharge under continuous or pulsed radio-frequency excitation.* Journal of Applied Physics, vol. 70, no. 4, pages 1991–2000, 1991.
- [Brammer 03] T. Brammer & H. Stiebig. Defect density and recombination lifetime in microcrystalline silicon absorbers of highly efficient thin-film solar cells determined by numerical device simulations. Journal of Applied Physics, vol. 94, no. 2, pages 1035–1042, 2003.
- [Brantley 73] W. A. Brantley. *Calculated elastic constants for stress problems associated with semiconductor devices.* Journal of Applied Physics, vol. 44, no. 1, pages 534–535, 1973.
- [Brenner 49] Abner Brenner & Seymour Senderoff. *Calculation of stress in electrodeposits* from the curvature of a plated strip. Journal of Research of the National Bureau of Standards, vol. 42, no. 2, pages 105–123, February 1949.
- [Bronneberg 11] A.C. Bronneberg, A.H.M. Smets, M. Creatore & M.C.M. van de Sanden. *On the oxidation mechanism of microcrystalline silicon thin films studied by Fourier transform infrared spectroscopy.* Journal of Non-Crystalline Solids, vol. 357, no. 3, pages 884–887, 2011.
- [Bronneberg 12a] A. C. Bronneberg, N. Cankoy, M. C. M. van de Sanden & M. Creatore. *Ion-induced effects on grain boundaries and a-Si:H tissue quality in microcrys-*

- *talline silicon films*. Journal of Vacuum Science & Technology A: Vacuum, Surfaces, and Films, vol. 30, no. 6, page 061512, 2012.
- [Bronneberg 12b] A.C. Bronneberg. *Plasma processing of microcrystalline silicon films : filling in the gaps.* PhD thesis, Technische Universiteit Eindhoven, 2012.
- [Bruno 09] Giovanni Bruno, Pio Capezzuto, Maria M. Giangregorio, Giuseppe V. Bianco & Maria Losurdo. From amorphous to microcrystalline silicon: Moving from one to the other by halogenated silicon plasma chemistry. Philosophical Magazine, vol. 89, no. 28-30, pages 2469–2489, 2009.
- [Bubenzer 90] A. Bubenzer & J.P.M. Schmitt. *Plasma processes under vacuum conditions*. Vacuum, vol. 41, no. 7–9, pages 1957–1961, 1990.
- [Buehlmann 07] P. Buehlmann, J. Bailat, D. Dominé, A. Billet, F. Meillaud, A. Feltrin & C. Ballif.

 In situ silicon oxide based intermediate reflector for thin-film silicon micromorph solar cells. Applied Physics Letters, vol. 91, no. 14, page 143505, 2007.
- [Bugnon 09] G. Bugnon, A. Feltrin, F. Meillaud, J. Bailat & C. Ballif. *Influence of pressure and silane depletion on microcrystalline silicon material quality and solar cell performance*. Journal of Applied Physics, vol. 105, no. 6, page 064507, 2009.
- [Bugnon 10] G. Bugnon, R. Bartlome, G. Parascandolo, M. Despeisse, J. Holovsky, F. Sculati-Meillaud & C. Ballif. *Plasma and Material Characterization Techniques of Microcrystalline Silicon for Solar Cells: The Role of Stress for High Quality Intrinsic Material.* In Proceedings of the 5th World Conference on Photovoltaic Solar Energy Conversion, pages 3009–3012, Valencia, Spain, 2010.
- [Bugnon 11a] G. Bugnon, A. Feltrin, R. Bartlome, B. Strahm, A.C. Bronneberg, G. Parascandolo & C. Ballif. *Microcrystalline and micromorph device improvements through combined plasma and material characterization techniques*. Solar Energy Materials and Solar Cells, vol. 95, no. 1, pages 134–137, 2011. 19th International Photovoltaic Science and Engineering Conference and Exhibition (PVSEC-19) Jeju, Korea, 9-13 November 2009.
- [Bugnon 11b] G. Bugnon, T. Söderström, S. Nicolay, L. Ding, M. Despeisse, A. Hedler, J. Eberhardt, C. Wachtendorf & C. Ballif. *LPCVD ZnO-based intermediate reflector for micromorph tandem solar cells*. Solar Energy Materials and Solar Cells, vol. 95, no. 8, pages 2161–2166, 2011.
- [Bugnon 12] Grégory Bugnon, Gaetano Parascandolo, Thomas Söderström, Peter Cuony, Matthieu Despeisse, Simon Hänni, Jakub Holovský, Fanny Meillaud & Christophe Ballif. A New View of Microcrystalline Silicon: The Role of Plasma Processing in Achieving a Dense and Stable Absorber Material for Photovoltaic Applications. Advanced Functional Materials, vol. 22, no. 17, pages 3665–3671, 2012.

- [Bugnon 13] Grégory Bugnon, Gaetano Parascandolo, Simon Hänni, Michael Stuckelberger, Mathieu Charrière, Matthieu Despeisse, Fanny Meillaud & Christophe Ballif. *Silicon oxide buffer layer at the p–i interface in amorphous and microcrystalline silicon solar cells.* Solar Energy Materials and Solar Cells, no. 0, pages –, 2013.
- [Burdick 86] Joseph Burdick & Troy Glatfelter. *Spectral response and I-V measurements of tandem amorphous-silicon alloy solar cells.* Solar Cells, vol. 18, no. 3-4, pages 301–314, 1986.
- [Catalano 88] A. Catalano & G. Wood. *A method for improved short-wavelength response in hydrogenated amorphous silicon-based solar cells*. Journal of Applied Physics, vol. 63, no. 4, pages 1220–1222, 1988.
- [Chapman 80] B. Chapman. Glow discharge Processes. Wiley-Interscience, 1980.
- [Chittick 69] R. C. Chittick, J. H. Alexander & H. F. Sterling. *The Preparation and Properties of Amorphous Silicon*. Journal of The Electrochemical Society, vol. 116, no. 1, pages 77–81, 1969.
- [Christova 10] K Christova, S Alexandrova, A Abramov, E Valcheva, B Ranguelov, C Longeaud, S Reynolds & P Roca i Cabarrocas. *Structure-related strain and stress in thin hydrogenated microcrystalline silicon films*. Journal of Physics: Conference Series, vol. 253, no. 1, page 012056, 2010.
- [Cicala 98] G. Cicala, G. Bruno & P. Capezzuto. *Plasma deposition chemistry of amorphous silicon–carbon alloys from fluorinated gas.* Journal of Vacuum Science & Technology A: Vacuum, Surfaces, and Films, vol. 16, no. 5, pages 2762–2767, 1998.
- [Cuony 10] P. Cuony, M. Marending, D. T. L. Alexander, M. Boccard, G. Bugnon, M. Despeisse & C. Ballif. *Mixed-phase p-type silicon oxide containing silicon nanocrystals and its role in thin-film silicon solar cells*. Applied Physics Letters, vol. 97, no. 21, page 213502, 2010.
- [Cuony 11] Peter Cuony. *Optical Layers for Thin-film Silicon Solar Cells.* PhD thesis, EPFL-STI, Lausanne, 2011.
- [Cuony 12] Peter Cuony, Duncan T. L. Alexander, Ivan Perez-Wurfl, Matthieu Despeisse, Gregory Bugnon, Mathieu Boccard, Thomas Söderström, Aïcha Hessler-Wyser, Cécile Hébert & Christophe Ballif. Silicon Filaments in Silicon Oxide for Next-Generation Photovoltaics. Advanced Materials, vol. 24, no. 9, pages 1182–1186, 2012.
- [Curtins 87] H. Curtins, N. Wyrsch, M. Favre & A.V. Shah. *Influence of plasma excitation frequency fora-Si:H thin film deposition.* Plasma Chemistry and Plasma Processing, vol. 7, no. 3, pages 267–273, 1987.

- [Dalakos 04] George T. Dalakos, Joel L. Plawsky & Peter D. Persans. *Suppressed surface morphology instabilities in amorphous hydrogenated silicon deposition*. Applied Physics Letters, vol. 85, no. 16, pages 3462–3464, 2004.
- [Dao 07] Thien Hai Dao. *Dépôt de couches minces de silicium à grande vitesse par plasma MDECR*. PhD thesis, Laboratoire de Physique des interfaces et des Couches Minces, 2007.
- [Despeisse 10] M. Despeisse, G. Bugnon, A. Feltrin, M. Stueckelberger, P. Cuony, F. Meillaud, A. Billet & C. Ballif. *Resistive interlayer for improved performance of thin film silicon solar cells on highly textured substrate*. Applied Physics Letters, vol. 96, no. 7, page 073507, 2010.
- [Ding 13] Laura Ding, Sylvain Nicolay, Jérôme Steinhauser, Ulrich Kroll & Christophe Ballif. *Relaxing the Conductivity/Transparency Trade-Off in MOCVD ZnO Thin Films by Hydrogen Plasma*. Advanced Functional Materials, pages n/a-n/a, 2013.
- [Dingemans 08] G. Dingemans, M. N. van den Donker, D. Hrunski, A. Gordijn, W. M. M. Kessels & M. C. M. van de Sanden. *The atomic hydrogen flux to silicon growth flux ratio during microcrystalline silicon solar cell deposition*. Applied Physics Letters, vol. 93, no. 11, page 111914, 2008.
- [Djeridane 08] Yassine Djeridane. Synthèse de nanocristaux par plasma froid et leur rôle dans la croissance de couches minces de silicium microcristallin : Application aux transistors. PhD thesis, LPICM- Laboratoire de Physique des Interfaces et des Couches Minces, Ecole polytechnique, 2008.
- [Dominé 07] D. Dominé, J. Bailat, M. Python, N. Wyrsch, C. Ballif, H. R. Moutinho, C.-S. Jiang & Al-Jassim M. M. *Investigation of the electric-field profile in micro-crystalline silicon p-i-n solar cells by cross-sectional scanning Kelvin probe microscopy*. In Proceedings of the 22nd European Photovoltaic Solar Energy Conference, page 2203–2207, Milan, Italy, 2007.
- [Dominé 08] Didier Dominé, Peter Buehlmann, Julien Bailat, Adrian Billet, Andrea Feltrin & Christophe Ballif. *Optical management in high-efficiency thin-film silicon micromorph solar cells with a silicon oxide based intermediate reflector.* physica status solidi (RRL) Rapid Research Letters, vol. 2, no. 4, pages 163–165, 2008.
- [Dominé 09] D. Dominé. *The role of front electrodes and intermediate reflectors in the optoelectronic properties of high-efficiency micromorph solar cells.* PhD thesis, Université de Neuchâtel, 2009.
- [Dorier 92] J.-L. Dorier, Ch. Hollenstein, A. A. Howling & U. Kroll. *Powder dynamics in very high frequency silane plasmas.* 38th National Symposium of the American Vacuum Society, vol. 10, no. 4, pages 1048–1052, 1992.

- [Drevillon 83] B. Drevillon, J. Perrin, J. M. Siefert, J. Huc, A. Lloret, G. de Rosny & J. P. M. Schmitt. *Growth of hydrogenated amorphous silicon due to controlled ion bombardment from a pure silane plasma*. Applied Physics Letters, vol. 42, no. 9, pages 801–803, 1983.
- [Droz 04] C. Droz, E. Vallat-Sauvain, J. Bailat, L. Feitknecht, J. Meier & A Shah. *Relationship between Raman crystallinity and open-circuit voltage in microcrystalline silicon solar cells*. Solar Energy Materials and Solar Cells, vol. 81, no. 1, pages 61–71, 2004.
- [Dutta 92] Joydeep Dutta, Ulrich Kroll, Patrick Chabloz, Arvind Shah, A. A. Howling, J.-L. Dorier & Ch. Hollenstein. *Dependence of intrinsic stress in hydrogenated amorphous silicon on excitation frequency in a plasma-enhanced chemical vapor deposition process.* Journal of Applied Physics, vol. 72, no. 7, pages 3220–3222, 1992.
- [Ellert 12] Ch. Ellert, C. Wachtendorf, A. Hedler, M. Klindworth & M. Martinek. *Influence of Raman crystallinity on the performance of micromorph thin film silicon solar cells*. Solar Energy Materials and Solar Cells, vol. 96, no. 0, pages 71–76, 2012.
- [Escarré 12] Jordi Escarré, Karin Söderström, Matthieu Despeisse, Sylvain Nicolay, Corsin Battaglia, Gregory Bugnon, Laura Ding, Fanny Meillaud, Franz-Josef Haug & Christophe Ballif. *Geometric light trapping for high efficiency thin film silicon solar cells*. Solar Energy Materials and Solar Cells, vol. 98, no. 0, pages 185–190, 2012.
- [Faÿ 06] S. Faÿ, L. Feitknecht, R. Schlüchter, U. Kroll, E. Vallat-Sauvain & A. Shah. Rough ZnO layers by LP-CVD process and their effect in improving performances of amorphous and microcrystalline silicon solar cells. Solar Energy Materials and Solar Cells, vol. 90, no. 18–19, pages 2960–2967, 2006.
- [Faÿ 10] Sylvie Faÿ, Jérôme Steinhauser, Sylvain Nicolay & Christophe Ballif. *Polycrystalline ZnO: B grown by LPCVD as TCO for thin film silicon solar cells.* Thin Solid Films, vol. 518, no. 11, pages 2961–2966, 2010.
- [Fantz 98] U. Fantz. Spectroscopic diagnostics and modelling of silane microwave plasmas. Plasma Physics and Controlled Fusion, vol. 40, no. 6, pages 1035–1056, 1998.
- [Fantz 06] U. Fantz. *Basics of plasma spectroscopy*. Plasma Sources Science and Technology, vol. 15, no. 4, pages S137–S147, 2006.
- [Faÿ 03] S. Faÿ. L'oxyde de zinc par dépôt chimique en phase vapeur comme contact électrique transparent et diffuseur de lumière pour les cellules solaires. PhD thesis, EPFL, 2003.

- [Feltrin 08] Andrea Feltrin & Alex Freundlich. Material considerations for terawatt level deployment of photovoltaics. Renewable Energy, vol. 33, no. 2, pages 180–185, 2008. E-MRS 2006 Symposium M: Materials, Devices and Prospects for Sustainable Energy.
- [Finger 94] F. Finger, P. Hapke, M. Luysberg, R. Carius, H. Wagner & M. Scheib. *Improvement of grain size and deposition rate of microcrystalline silicon by use of very high frequency glow discharge*. Applied Physics Letters, vol. 65, no. 20, pages 2588–2590, 1994.
- [Finger 03] F. Finger, R. Carius, T. Dylla, S. Klein, S. Okur & M. Gunes. *Stability of microcrystalline silicon for thin film solar cell applications*. Circuits, Devices and Systems, IEE Proceedings -, vol. 150, no. 4, pages 300–8, 2003.
- [Finger 08] F. Finger, Y. Mai, S. Klein & R. Carius. *High efficiency microcrystalline silicon solar cells with Hot-Wire CVD buffer layer*. Thin Solid Films, vol. 516, no. 5, pages 728–732, 2008. Proceedings of the Fourth International Conference on Hot-Wire CVD Cat-CVD Process.
- [Fischer 96]
 D. Fischer, S. Dubail, J. A. Anna Selvan, N. Pellaton Vaucher, R. Platz, Ch. Hof, U. Kroll, J. Meier, P. Torres, H. Keppner, N. Wyrsch, M. Goetz, A. Shah & K.-D.Ufert. *The Micromorph Solar Cell: Extending a-Si:H Technology towards Thin Film Crystalline Silicon*. In Proceedings of the 25th IEEE Photovoltaic Specialists Conference, pages 1053–1056, Washington D.C., USA, 1996.
- [Frammelsberger 10] W. Frammelsberger *et al. Status of the development of micromorph cells and modules at Schott solar thin film Gmbh.* In Proceedings of the 5th World Conference on Photovoltaic Solar Energy Conversion, pages 2788–2792, Valencia, Spain, 2010.
- [Fridman 96] A. A. Fridman, L. Boufendi, T. Hbid, B. V. Potapkin & A. Bouchoule. *Dusty plasma formation: Physics and critical phenomena. Theoretical approach.* Journal of Applied Physics, vol. 79, no. 3, pages 1303–1314, 1996.
- [Fu 05] Y.Q. Fu, J.K. Luo, S.B. Milne, A.J. Flewitt & W.I. Milne. Residual stress in amorphous and nanocrystalline Si films prepared by PECVD with hydrogen dilution. Materials Science and Engineering: B, vol. 124-125, pages 132–137, 2005. EMRS 2005, Symposium D Materials Science and Device Issues for Future Technologies.
- [Fujiwara 02] Hiroyuki Fujiwara, Michio Kondo & Akihisa Matsuda. *Stress-Induced Nucleation of Microcrystalline Silicon from Amorphous Phase*. Japanese Journal of Applied Physics, vol. 41, no. Part 1, No. 5A, pages 2821–2828, 2002.
- [Fujiwara 03] Hiroyuki Fujiwara, Michio Kondo & Akihisa Matsuda. *Interface-layer formation in microcrystalline Si:H growth on ZnO substrates studied by real-time*

spectroscopic ellipsometry and infrared spectroscopy. Journal of Applied Physics, vol. 93, no. 5, pages 2400–2409, 2003.

- [Gordijn 06a] A. Gordijn, L. Hodakova, J.K. Rath & R.E.I. Schropp. *Influence on cell performance of bulk defect density in microcrystalline silicon grown by VHF PECVD*. Journal of Non-Crystalline Solids, vol. 352, no. 9-20, pages 1868–1871, 2006. Proceedings of the 21st International Conference on Amorphous and Nanocrystalline Semiconductors Science and Technology.
- [Gordijn 06b] A. Gordijn, M. Vanecek, W. J. Goedheer, J. K. Rath & R. E. I. Schropp. *Influence of Pressure and Plasma Potential on High Growth Rate Microcrystalline Silicon Grown by Very High Frequency Plasma Enhanced Chemical Vapour Deposition.* Japanese Journal of Applied Physics, vol. 45, no. 8A, pages 6166–6172, 2006.
- [Grabitz 05] P.O. Grabitz, U. Rau & J.H. Werner. *Modeling of spatially inhomogeneous solar cells by a multi-diode approach.* physica status solidi (a), vol. 202, no. 15, pages 2920–2927, 2005.
- [Greenpeace 12] Greenpeace. *Energy* [R]evolution 2012. Rapport technique, Greenpeace, 2012.
- [Guo 98] L. Guo, M. Kondo, M. Fukawa, K. Saitoh & A. Matsuda. High Rate Deposition of Microcrystalline Silicon Using Conventional Plasma-Enhanced Chemical Vapor Deposition. Japanese Journal of Applied Physics, vol. 37, pages 1116– 1118, 1998.
- [Hamers 98] E.A.G Hamers, W.G.J.H.M van Sark, J Bezemer, H Meiling & W.F van der Weg. Structural properties of a-Si:H related to ion energy distributions in {VHF} silane deposition plasmas. Journal of Non-Crystalline Solids, vol. 226, no. 3, pages 205–216, 1998.
- [Hamers 00] E. A. G. Hamers, A. Fontcuberta i Morral, C. Niikura, R. Brenot & P. Roca i Cabarrocas. *Contribution of ions to the growth of amorphous, polymorphous, and microcrystalline silicon thin films.* Journal of Applied Physics, vol. 88, no. 6, pages 3674–3688, 2000.
- [Heintze 93] M Heintze, R Zedlitz & G H Bauer. *Analysis of high-rate a-Si:H deposition in a VHF plasma*. Journal of Physics D: Applied Physics, vol. 26, no. 10, page 1781, 1993.
- [Heintze 96] M. Heintze & R. Zedlitz. *New diagnostic aspects of high rate a-Si:H deposition in a {VHF} plasma.* Journal of Non-Crystalline Solids, vol. 198–200, Part 2, no. 0, pages 1038–1041, 1996. <ce:title>Amorphous Semiconductors-Science and Technology</ce:title>.

- [Hänni 13] Simon Hänni, Grégory Bugnon, Gaetano Parascandolo, Mathieu Boccard, Jordi Escarré, Matthieu Despeisse, Fanny Meillaud & Christophe Ballif. *Highefficiency microcrystalline silicon single-junction solar cells*. Progress in Photovoltaics: Research and Applications, vol. 21, no. 5, pages 821–826, 2013.
- [Hollenstein 00] Ch Hollenstein. *The physics and chemistry of dusty plasmas*. Plasma Physics and Controlled Fusion, vol. 42, no. 10, page R93, 2000.
- [Howling 92] A. A. Howling, J.-L. Dorier, Ch. Hollenstein, U. Kroll & F. Finger. *Frequency effects in silane plasmas for plasma enhanced chemical vapor deposition.*38th National Symposium of the American Vacuum Society, vol. 10, no. 4, pages 1080–1085, 1992.
- [Howling 07] A. A. Howling, B. Strahm, P. Colsters, L. Sansonnens & Ch. Hollenstein. *Fast equilibration of silane/hydrogen plasmas in large area RF capacitive reactors monitored by optical emission spectroscopy.* Plasma Sources Science and Technology, vol. 16, no. 4, pages 679–696, 2007.
- [Howling 10] A. A. Howling, R. Sobbia & Ch. Hollenstein. *Hydrogen-dominated plasma, due to silane depletion, for microcrystalline silicon deposition.* Journal of Vacuum Science & Technology A, vol. 28, no. 4, pages 989–995, 2010.
- [Hrunski 08] D. Hrunski, B. Rech, R. Schmitz, A. Mück, O. Pinçon, U. Breuer & W. Beyer. Influence of contaminations on the performance of thin-film silicon solar cells prepared after in situ reactor plasma cleaning. Thin Solid Films, vol. 516, no. 14, pages 4639–4644, 2008. <ce:title>6th International Conference on Coatings on Glass and Plastics (ICCG6)- Advanced Coatings for Large-Area or High-Volume Products-</ce>
- [Hrunski 13] D. Hrunski, F. Mootz, A. Zeuner, A. Janssen, H. Rost, R. Beckmann, S. Binder, E. Schüngel, S. Mohr, D. Luggenhölscher, U. Czarnetzki & G. Grabosch. *Deposition of microcrystalline intrinsic silicon by the Electrical Asymmetry Effect technique*. Vacuum, vol. 87, no. 0, pages 114–118, 2013. <ce:title>Including rapid communications, original articles and a special section with papers from the Proceedings of the Eleventh International Symposium on Sputtering and Plasma Processes (ISSP 2011) 6–8 July 2011, Kyoto, Japan
- [Hu 91] S. M. Hu. *Stress-related problems in silicon technology.* Journal of Applied Physics, vol. 70, no. 6, pages R53–R80, 1991.
- [IEA 10] International Energy Agency IEA. *Technology Roadmap Solar photovoltaic energy*, 2010.
- [IEA 12] IEA. *Key World Energy Statistics 2012*. Rapport technique, International Energy Agency, 2012.

[III 83] J. H. Thomas III. *X-ray photoelectron spectroscopy study of hydrogen plasma interactions with a tin oxide surface*. Applied Physics Letters, vol. 42, no. 9, pages 794–796, 1983.

[Isomura 94] Masao Isomura, Toshihiro Kinoshita, Yoshihiro Hishikawa & Shinya Tsuda.

Influence of oxygen impurity in the intrinsic layer of amorphous silicon solar cells. Applied Physics Letters, vol. 65, no. 18, pages 2329–2331, 1994.

[Isomura 02] Masao Isomura, Michio Kondo & Akihisa Matsuda. *Device-Grade Amorphous Silicon Prepared by High-Pressure Plasma*. Japanese Journal of Applied Physics, vol. 41, no. Part 1, No. 4A, pages 1947–1951, 2002.

[Ito 03] M. Ito, M. Kondo & A. Matsuda. *The effect of superlattice buffer of microcrystalline silicon solar cells*. In Photovoltaic Energy Conversion, 2003. Proceedings of 3rd World Conference on, volume 3, pages 2726–2729, May 2003.

[Jacobson 11] Mark Z. Jacobson & Mark A. Delucchi. *Providing all global energy with wind, water, and solar power, Part I: Technologies, energy resources, quantities and areas of infrastructure, and materials.* Energy Policy, vol. 39, no. 3, pages 1154–1169, 2011.

[Jaeger-Waldau 13] Arnulf Jaeger-Waldau, Fabio Monforti-Ferrario, Manjola Banja, Hans Bloem, Roberto Lacal Arantegui & Márta Szabó. *Renewable Energy Snapshots* 2012. Rapport technique, Publications Office of the European Union, 2013.

[Jia 07] Haijun Jia, Hajime Shirai & Michio Kondo. *Control of the gas phase and the surface reactions during the high rate synthesis of high quality microcrystalline silicon films: Effects of the source gas supply method and the substrate bias.* Journal of Applied Physics, vol. 101, no. 11, page 114912, 2007.

[Johnson 08a] E V Johnson, Y Djeridane, A Abramov & P Roca i Cabarrocas. *Experiment and modelling of very low frequency oscillations in RF-PECVD: a signature for nanocrystal dynamics*. Plasma Sources Science and Technology, vol. 17, no. 3, page 035029, 2008.

[Johnson 08b] E.V. Johnson, M. Nath, P. Roca i Cabarrocas, A. Abramov & P. Chatterjee. Why does the open-circuit voltage in a micro-crystalline silicon PIN solar cell decrease with increasing crystalline volume fraction? Journal of Non-Crystalline Solids, vol. 354, no. 19–25, pages 2455–2459, 2008. Proceedings of the 22nd International Conference on Amorphous and Nanocrystalline Semiconductors - Science and Technology.

[Jolly 05] J. Jolly & J.-P. Booth. *Atomic hydrogen densities in capacitively coupled very high-frequency plasmas in H[sub 2]: Effect of excitation frequency.* Journal of Applied Physics, vol. 97, no. 10, page 103305, 2005.

- [Kakiuchi 06] Hiroaki Kakiuchi, Hiromasa Ohmi, Yasuhito Kuwahara, Mitsuhiro Matsumoto, Yusuke Ebata, Kiyoshi Yasutake, Kumayasu Yoshii & Yuzo Mori. High-Rate Deposition of Intrinsic Amorphous Silicon Layers for Solar Cells Using Very High Frequency Plasma at Atmospheric Pressure. Japanese Journal of Applied Physics, vol. 45, no. 4B, pages 3587–3591, 2006.
- [Kakiuchi 09] Hiroaki Kakiuchi, Hiromasa Ohmi, Kentaro Ouchi, Keita Tabuchi & Kiyoshi Yasutake. *Microcrystalline Si films grown at low temperatures (90–220 [degree]C) with high rates in atmospheric-pressure VHF plasma.* Journal of Applied Physics, vol. 106, no. 1, page 013521, 2009.
- [Kalache 03] B. Kalache, A. I. Kosarev, R. Vanderhaghen & P. Roca i Cabarrocas. *Ion bombardment effects on microcrystalline silicon growth mechanisms and on the film properties*. Journal of Applied Physics, vol. 93, no. 2, pages 1262–1273, 2003.
- [Kawasaki 97] Hiroharu Kawasaki, Hiroshi Ohkura, Tsuyoshi Fukuzawa, Masaharu Shiratani, Yukio Watanabe, Yasuo Yamamoto, Shinji Suganuma, Masaru Hori & Toshio Goto. *Roles of SiH*₃ *and SiH*₂ *Radicals in Particle Growth in rf Silane Plasmas*. Japanese Journal of Applied Physics, vol. 36, no. Part 1, No. 7B, pages 4985–4988, 1997.
- [Keppner 95] H. Keppner, U. Kroll, J. Meier & A. Shah. *Very High Frequency Glow Discharge: Plasma- and Deposition Aspects.* Solid State Phenomena, vol. 97, pages 97–126, 1995.
- [Kilper 05] T. Kilper, T. Repmann, B. Rech, G. Bräuer & S. Wieder. Development of microcrystalline silicon solar cells using large area capacitively coupled planar electrodes. In Proceedings of the 20th European Photovoltaic Solar Energy Conference, page 1544–1547, Barcelona, Spain, 2005.
- [Kim 13] Soohyun Kim, Jin-Won Chung, Hyun Lee, Jinhee Park, Younho Heo & Heon-Min Lee. *Remarkable progress in thin-film silicon solar cells using high-efficiency triple-junction technology.* Solar Energy Materials and Solar Cells, no. 0, pages –, 2013.
- [Klein 04] S. Klein, T. Repmann & T. Brammer. *Microcrystalline silicon films and solar cells deposited by {PECVD} and {HWCVD}*. Solar Energy, vol. 77, no. 6, pages 893–908, 2004. <ce:title>Thin Film PV</ce:title>.
- [Klein 05] Stefan Klein, Friedhelm Finger, Reinhard Carius & Martin Stutzmann. Deposition of microcrystalline silicon prepared by hot-wire chemical-vapor deposition: The influence of the deposition parameters on the material properties and solar cell performance. Journal of Applied Physics, vol. 98, no. 2, page 024905, 2005.

- [Kluth 09] O. Kluth, P. Losio, S. Bakehe, O. Caglar, H. Goldbach, M. Keller, S. Benagli & J. Meier. *Up-Scaling of High Throughput a-Si Solar Cell Design on ZnO to 1.4m2 Modules*. In Proceedings of the 24th European Photovoltaic Solar Energy Conference, pages 2715–2717, Hamburg, Germany, 2009.
- [Knoesen 95] D. Knoesen, R. E. I. Schropp & W. F. Van Der Weg. Structural Defects in thin Film Amorphous Silicon Films Deposited on Textured TCO Material. MRS Proceedings, vol. 377, page 597, 1995. Symposium A.
- [Köhler 85] K. Köhler, D. E. Horne & J. W. Coburn. Frequency dependence of ion bombardment of grounded surfaces in rf argon glow discharges in a planar system. Journal of Applied Physics, vol. 58, no. 9, pages 3350–3355, 1985.
- [Konagai 11] Makoto Konagai. *Present Status and Future Prospects of Silicon Thin-Film Solar Cells.* Japanese Journal of Applied Physics, vol. 50, page 030001, 2011.
- [Kondo 00] M. Kondo, M. Fukawa, L. Guo & A. Matsuda. High rate growth of microcrystalline silicon at low temperatures. Journal of Non-Crystalline Solids, vol. 266-269, pages 84–89, May 2000.
- [Kondo 03a] M. Kondo. *Microcrystalline materials and cells deposited by RF glow discharge.* Solar Energy Materials and Solar Cells, vol. 78, no. 1-4, pages 543–566, July 2003.
- [Kondo 03b] Michio Kondo. *Microcrystalline materials and cells deposited by {RF} glow discharge.* Solar Energy Materials and Solar Cells, vol. 78, no. 1–4, pages 543–566, 2003. <ce:title>Critical review of amorphous and microcrystalline silicon materials and solar cells</ce:title>.
- [Kondo 05] M. Kondo, T. Matsui, Y. Nasuno, C. Niikura, T. Fujibayashi, A. Sato, A. Matsuda & H. Fujiwara. Crucial processing steps for microcrystalline silicon bottom cells. In Proceedings of the 31st IEEE Photovoltaic Specialists Conference, pages 1377–1382, Lake Buena Vista, Fla, USA, 2005.
- [Kroely 10] Laurent Kroely. Process and material challenges in the high rate deposition of microcrystalline silicon thin lms and solar cells by Matrix Distributed Electron Cyclotron Resonance plasma. PhD thesis, Laboratoire de Physique des interfaces et des Couches Minces, 2010.
- [Kroll 94] U. Kroll, Y. Ziegler, J. Meier, H. Keppner & A. Shah. *More Insight into the VHF-Glow-Discharge by Plasma Impedance Measurements*. MRS Proceedings, vol. 336, page 115, January 1994.
- [Kroll 96] U. Kroll, J. Meier, A. Shah, S. Mikhailov & J. Weber. Hydrogen in amorphous and microcrystalline silicon films prepared by hydrogen dilution. Journal of Applied Physics, vol. 80, no. 9, pages 4971–4975, 1996.

[Kroll 04]

U. Kroll, C. Bucher, S. Benagli, I. Schönbächler, J. Meier, A. Shah, J. Ballutaud, A. Howling, Ch. Hollenstein, A. Büchel & M. Poppeller. *High-efficiency p-i-n a-Si:H solar cells with low boron cross-contamination prepared in a large-area single-chamber PECVD reactor*. Thin Solid Films, vol. 451–452, no. 0, pages 525–530, 2004. <ce:title>Proceedings of Symposium D on Thin Film and Nano-Structured Materials for Photovoltaics, of the E-MRS 2003 Spring Conference</ce:title>.

[Kubon 94]

M. Kubon, N. Schultz, M. Kolter, C. Beneking & H. Wagner. *Modification of TCO-p interface in a-Si:H solar cells by intermediate layers and plasma treatments*. In Proceedings of the 12th European Photovoltaic Solar Energy Conference, page 1268–1270, Amsterdam, Netherlands, 1994.

[Kunii 08]

T. Kunii, K. Murata, M. Matsumoto*et al. Efficient Production Technology for Microcrystalline Silicon Solar Cells Using a Localized Plasma Confinement (LPC) CVD Method.* In Proceedings of the 33rd IEEE Photovoltaic Specialists Conference, San Diego, CA, USA, 2008.

[Lambertz 07]

A. Lambertz, A. Dasgupta, W. Reetz, A. Gordijn, R. Carius & F.Finger. *Microcrystalline Silicon Oxide as Intermediate Reflector for Thin Film Silicon Solar Cells.* In Proceedings of the 22th EU-PVSEC, pages 1839–1842, Milan, Italy, 2007.

[Lebib 05]

S. Lebib & P. Roca i Cabarrocas. *Effects of ion energy on the crystal size and hydrogen bonding in plasma-deposited nanocrystalline silicon thin films.* Journal of Applied Physics, vol. 97, no. 10, page 104334, 2005.

[Li 09]

Hongbo B.T. Li, Ronald H. Franken, Jatindra K. Rath & Ruud E.I. Schropp. Structural defects caused by a rough substrate and their influence on the performance of hydrogenated nano-crystalline silicon n–i–p solar cells. Solar Energy Materials and Solar Cells, vol. 93, no. 3, pages 338–349, 2009.

[Lieberman 89] M. A. Lieberman. *Spherical shell model of an asymmetric rf discharge*. Journal of Applied Physics, vol. 65, no. 11, pages 4186–4191, 1989.

[Lieberman 02] M A Lieberman, J P Booth, P Chabert, J M Rax & M M Turner. *Standing wave and skin effects in large-area, high-frequency capacitive discharges.* Plasma Sources Science and Technology, vol. 11, no. 3, page 283, 2002.

[Liebermann 05] M. A. Liebermann & A. J. Lichtenberg. Principles of Plasma Discharges and Materials Processing, 2nd Edition. Wiley-Interscience, 2005.

[Lyka 06] B. Lyka, E. Amanatides & D. Mataras. Simulation of the Electrical Properties of SiH_4/H_2 RF Discharges. Japanese Journal of Applied Physics, vol. 45, no. 10B, pages 8172–8176, 2006.

- [Mai 05] Y. Mai, S. Klein, R. Carius, J. Wolff, A. Lambertz, F. Finger & X. Geng. Microcrystalline silicon solar cells deposited at high rates. Journal of Applied Physics, vol. 97, no. 11, page 114913, 2005.
- [Marques 07] L. Marques, J. Jolly & L. L. Alves. *Capacitively coupled radio-frequency hydro-gen discharges: The role of kinetics.* Journal of Applied Physics, vol. 102, no. 6, page 063305, 2007.
- [Martins 00] R. Martins, I. Ferreira, A. Cabrita & E. Fortunato. *Improvement of a-Si:H device stability and performances by proper design of the interfaces.* Journal of Non-Crystalline Solids, vol. 266–269, Part 2, no. 0, pages 1094–1098, 2000.
- [Matsuda 80] Akihisa Matsuda, Satoshi Yamasaki, Katsumi Nakagawa, Hideyo Okushi, Kazunobu Tanaka, Sigeru Iizima, Mitsuo Matsumura & Hideo Yamamoto. Electrical and Structural Properties of Phosphorous-Doped Glow-Discharge Si:F:H and Si:H Films. Japanese Journal of Applied Physics, vol. 19, no. 6, pages L305–L308, 1980.
- [Matsuda 04] Akihisa Matsuda. *Thin-Film Silicon —Growth Process and Solar Cell Application*—. Japanese Journal of Applied Physics, vol. 43, no. 12, pages 7909–7920, 2004.
- [Matsui 02] Takuya Matsui, Masaharu Tsukiji, Hiroyuki Saika, Toshihiko Toyama & Hiroaki Okamoto. *Correlation between Microstructure and Photovoltaic Performance*of Polycrystalline Silicon Thin Film Solar Cells. Japanese Journal of Applied Physics, vol. 41, no. Part 1, No. 1, pages 20–27, 2002.
- [Matsui 03a] T. Matsui, T. Fujibayashi, Y. Nasuno, H. Fukuhori, Y. Kanemitsu, M. Kondo & A. Matsuda. Impurity diffusion effect on p/i interface properties of p-i-n junction microcrystalline silicon solar cells. In Photovoltaic Energy Conversion, 2003. Proceedings of 3rd World Conference on, volume 2, pages 1831–1834, May 2003.
- [Matsui 03b] T. Matsui, M. Kondo & A. Matsuda. *Origin of the Improved Performance of High-Deposition-Rate Microcrystalline Silicon Solar Cells by High-Pressure Glow Discharge*. Japanese Journal of Applied Physics, vol. 42, no. 8, pages 901–903, 2003.
- [Matsui 04] T. Matsui*et al. High efficiency and high deposition-rate microcrystalline silicon p-i-n solar cells.* In Proceedings of the 19th European Photovoltaic Solar Energy Conference, pages 1407–1410, Paris, France, 2004.
- [Matsui 10] Takuya Matsui, Haijun Jia & Michio Kondo. *Thin film solar cells incorporating microcrystalline* $Si_{1-x}Ge_x$ *as efficient infrared absorber: an application to double junction tandem solar cells.* Progress in Photovoltaics: Research and Applications, vol. 18, no. 1, pages 48–53, 2010.

- [Matsui 12] Takuya Matsui, Chia-Wen Chang, Kouichi Mizuno, Yoshiaki Takeuchi & Michio Kondo. Compensation of Native Defect Acceptors in Microcrystalline Ge and $Si_{1-x}Ge_x$ Thin Films by Oxygen Incorporation: Electrical Properties and Solar Cell Performance. Japanese Journal of Applied Physics, vol. 51, page 091302, 2012.
- [Matsumura 83] Hideki Matsumura, Masaaki Maeda & Seijiro Furukawa. *Study on Impurity Diffusion in Glow-Discharged Amorphous Silicon*. Japanese Journal of Applied Physics, vol. 22, no. Part 1, No. 5, pages 771–774, 1983.
- [McCaughey 89] Michael J. McCaughey & Mark J. Kushner. *Electron transport coefficients in dusty argon plasmas*. Applied Physics Letters, vol. 55, no. 10, pages 951–953, 1989.
- [McCaughey 91] Michael J. McCaughey & Mark J. Kushner. *A model for particulate contam*inated glow discharges. Journal of Applied Physics, vol. 69, no. 10, pages 6952–6961, 1991.
- [Meier 94a] J. Meier, S. Dubail, R. Flückiger, D. Fischer, H. Keppner & A. Shah. *Intrinsic microcrystalline silicon A promising new thin film solar cell material.* In Conference Records of the 24th IEEE PVSC, page 409, Hawaii, USA, 1994.
- [Meier 94b] J. Meier, R. Flückiger, H. Keppner & A. Shah. *Complete microcrystalline p-i-n solar cell Crystalline or amorphous cell behavior?* Applied Physics Letters, vol. 65, no. 7, pages 860–862, 1994.
- [Meier 96] J. Meier, P. Torres, R. Platz, S. Dubail, U. Kroll, J. A. Anna Selvan, N. Pellaton Vaucher, Ch. Hof, D. Fischer, H. Keppner, A. Shah, K. D. Ufert, P. Giannoulès & J Koehler. On the Way Towards High Efficiency Thin Film Silicon Solar Cells by the "Micromorph" Concept. MRS Proceedings, vol. 420, page 3, 1996.
- [Meier 98] J Meier, S Dubail, J Cuperus, U Kroll, R Platz, P Torres, J.A Anna Selvan, P Pernet, N Beck, N Pellaton Vaucher, Ch Hof, D Fischer, H Keppner & A Shah. Recent progress in micromorph solar cells. Journal of Non-Crystalline Solids, vol. 227–230, Part 2, no. 0, pages 1250–1256, 1998.
- [Meier 02] J. Meier, J. Spitznagel, S. Faÿ, C. Bucher, U. Graf, U. Kroll, S. Dubail & A. Shah. Enhanced Light-Trapping for Micromorph Tandem Solar Cells by LP-CVD ZnO. In Proceedings of the 29th IEEE Photovoltaic Specialists Conference, pages 1118–1121, New Orleans, Louisiana, USA, 2002.
- [Meier 03] J. Meier, J. Spitznagel, U. Kroll, C. Bucher, S. Faÿ, T. Moriarty & A. Shah. *High-Efficiency Amorphous and Micromorph Silicon Solar Cells*. In Proceedings of the 3rd World Conference on Photovoltaic Solar Energy Conversion, pages 2801–2805, Osaka, Japan, 2003.

- [Meillaud 06] F. Meillaud, A. Shah, C. Droz, E. Vallat-Sauvain & C. Miazza. Efficiency limits for single-junction and tandem solar cells. Solar Energy Materials and Solar Cells, vol. 90, no. 18-19, pages 2952–2959, 2006. 14th International Photovoltaic Science and Engineering Conference.
- [Meillaud 08] F. Meillaud, E. Vallat-Sauvain, Arvind Shah & C. Ballif. *Kinetics of creation and of thermal annealing of light-induced defects in microcrystalline silicon solar cells.* Journal of Applied Physics, vol. 103, no. 5, page 054504, 2008.
- [Meillaud 09] F. Meillaud, A. Feltrin, D. Dominé, P. Buehlmann, M. Python, G. Bugnon, A. Billet, G. Parascandolo, J. Bailat, S. Fay, N. Wyrsch, C. Ballif & A. Shah. Limiting factors in the fabrication of microcrystalline silicon solar cells and microcrystalline/amorphous (micromorph) tandems. Philosophical Magazine, vol. 89, no. 28-30, pages 2599–2621, 2009.
- [Merdzhanova 12] T. Merdzhanova, J. Woerdenweber, T. Zimmermann, U. Zastrow, A.J. Flikweert, H. Stiebig, W. Beyer & A. Gordijn. *Single-chamber processes for a-Si:H solar cell deposition*. Solar Energy Materials and Solar Cells, vol. 98, no. 0, pages 146–153, 2012.
- [Meusel 03] M. Meusel, C. Baur, G. Létay, A. Bett, W. Warta & E. Fernandez. Spectral response measurements of monolithic GaInP/Ga(In)As/Ge triple-junction solar cells: Measurement artifacts and their explanation. Progress in Photovoltaics: Research and Applications, vol. 8, no. 11, pages 499–514, 2003.
- [Müller 04] Joachim Müller, Bernd Rech, Jiri Springer & Milan Vanecek. *TCO and light trapping in silicon thin film solar cells*. Solar Energy, vol. 77, no. 6, pages 917–930, 2004. <ce:title>Thin Film PV</ce:title>.
- [Nakajima 04] Akihiko Nakajima, Mitsuru Ichikawa, Toru Sawada, Masashi Yoshimi & Kenji Yamamoto. *Spectral Characteristics of Thin-Film Stacked-Tandem Solar Modules*. Japanese Journal of Applied Physics, vol. 43, no. 10, pages 7296–7302, 2004.
- [Nakano 06] Y. Nakano, S. Goya, T. Watanabe, N. Yamashita & Y. Yonekura. High-deposition-rate of microcrystalline silicon solar cell by using VHF PECVD. Thin Solid Films, vol. 506-507, pages 33–37, 2006. The Joint Meeting of 7th APCPST (Asia Pacific Conference on Plasma Science and Technology) and 17th SPSM (Symposium on Plasma Science for Materials) 7th APCPST/17th SPSM.
- [Naruse 12] Y. Naruse, M. Matsumoto, T. Sekimoto, M. Hishida, Y. Aya, W. Shinohara, A. Fukushima, S. Yata, A. Terakawa, M. Iseki & M. Tanaka. *Identification of defective regions in thin-film Si solar cells for new-generation energy devices*. In Photovoltaic Specialists Conference (PVSC), 2012 38th IEEE, pages 003118–003123, 2012.

- [Nasuno 01] Yoshiyuki Nasuno, Michio Kondo & Akihisa Matsuda. *Effects of Substrate Surface Morphology on Microcrystalline Silicon Solar Cells.* Japanese Journal of Applied Physics, vol. 40, no. Part 2, No. 4A, pages L303–L305, 2001.
- [Nasuno 02] Yoshiyuki Nasuno, Michio Kondo, Akihisa Matsuda, Hitoshi Fukuhori & Yoshihiko Kanemitsu. *Formation of interface defects by enhanced impurity diffusion in microcrystalline silicon solar cells*. Applied Physics Letters, vol. 81, no. 17, pages 3155–3157, 2002.
- [Nicolay 09] S. Nicolay, S. Faÿ & C. Ballif. *Growth Model of MOCVD Polycrystalline ZnO*. Crystal Growth & Design, vol. 9, no. 11, pages 4957–4962, 2009.
- [Niikura 04] C. Niikura, M. Kondo & A. Matsuda. *Preparation of microcrystalline silicon films at ultra high-rate of 10 nm/s using high-density plasma.* Journal of Non-Crystalline Solids, vol. 338-340, pages 42–46, June 2004.
- [Niikura 07] C. Niikura, N. Itagaki & A. Matsuda. *Guiding principles for obtaining high-quality microcrystalline silicon at high growth rates using SiH4/H2 glow-discharge plasma*. Japanese Journal of Applied Physics, vol. 46, no. 5, pages 3052–3058, 2007.
- [Noda 03] M. Noda, T. Nishimiya, K. Yamaguchiet al. Large area thin film Si tandem module production using VHF plasma with a ladder-shaped electrode. In Proceedings of 3rd World Conference on Photovoltaic Energy Conversion, pages 1849–1851, Osaka, Japan, 2003.
- [Nunomura 07] S. Nunomura & M. Kondo. *Characterization of high-pressure capacitively coupled hydrogen plasmas*. Journal of Applied Physics, vol. 102, no. 9, page 093306, 2007.
- [Nunomura 08] S. Nunomura & M. Kondo. *Positive ion polymerization in hydrogen diluted silane plasmas.* Applied Physics Letters, vol. 93, no. 23, page 231502, 2008.
- [Nunomura 09] S Nunomura & M Kondo. *Precursor flux-dependent microstructure of thin-film silicon prepared by hydrogen diluted silane discharge plasmas*. Journal of Physics D: Applied Physics, vol. 42, no. 18, page 185210, 2009.
- [Oda 88] Shunri Oda, Jun'Ichirou Noda & Masakiyo Matsumura. *Preparation of a-Si:H Films by VHF Plasma CVD*. MRS Proceedings, vol. 118, page 117, January 1988.
- [Oerlikon Solar 12] Oerlikon Solar. *Press release from 16 Jan. 2012*. More information available at http://www.oerlikon.com/ecomaXL/index.php?site=SOLAR_EN_press_releases_detail&udtx_id=9082, 2012.
- [Ovshinsky 78] Stanford R. Ovshinsky. *A new amorphous silicon-based alloy for electronic applications*. Nature, vol. 276, pages 482–484, November 1978.

- [Parascandolo 10a] G. Parascandolo, R. Bartlome, G. Bugnon, T. Söderström, B. Strahm, A. Feltrin & C. Ballif. *Impact of secondary gas-phase reactions on microcrystalline silicon solar cells deposited at high rate.* Applied Physics Letters, vol. 96, no. 23, page 233508, 2010.
- [Parascandolo 10b] Gaetano Parascandolo, Grégory Bugnon, Andrea Feltrin & Christophe Ballif. *High-rate deposition of microcrystalline silicon in a large-area PECVD reactor and integration in tandem solar cells.* Progress in Photovoltaics: Research and Applications, vol. 18, no. 4, pages 257–264, 2010.
- [PEPPER 10] FP7 EU PEPPER. FP7 European project PEPPER. More information available at http://pepper.epfl.ch, 2010.
- [Pernet 00] P. Pernet, M. Hengsberger, C. Hof, M. Goetz & A. Shah. *Growth of thin p-\mu c-Si:H layers for n-i-p solar cells: Effects of the H*₂- *or CO*₂-*plasma treatments*. In Proceedings of the 16th European Photovoltaic Solar Energy Conference, page 498–501, Glasgow, UK, 2000.
- [Perrin 89] Jérôme Perrin, Yoshihiko Takeda, Naoto Hirano, Hideharu Matsuura & Akihisa Matsuda. Effect of Ion Bombardment on the Growth and Properties of Hydrogenated Amorphous Silicon-Germanium Alloys. Japanese Journal of Applied Physics, vol. 28, no. Part 1, No. 1, pages 5–11, 1989.
- [Perrin 90] J. Perrin. *Deposition of amorphous silicon alloys*. Pure and Applied Chemistry, vol. 62, no. 9, pages 1681–1688, 1990.
- [Perrin 96] J. Perrin, O. Leroy & M. C. Bordage. *Cross-Sections, Rate Constants and Transport Coefficients in Silane Plasma Chemistry*. Contributions to Plasma Physics, vol. 36, no. 1, pages 3–49, 1996.
- [Perrin 98] Jérôme Perrin, Masaharu Shiratani, Patrick Kae-Nune, Hervé Videlot, Jacques Jolly & Jean Guillon. Surface reaction probabilities and kinetics of H, SiH_3 , Si_2H_5 , CH_3 , and C_2H_5 during deposition of a-Si:H and a-C:H from H_2 , SiH_4 , and CH_4 discharges. Journal of Vacuum Science & Technology A: Vacuum, Surfaces, and Films, vol. 16, no. 1, pages 278–289, 1998. International workshop on basic aspects of nonequilibrium plasmas interacting with surfaces (BANPIS"97).
- [Perrin 00] J. Perrin, J. Schmitt, Ch. Hollenstein, A. A. Howling & L. Sansonnens. *The physics of plasma-enhanced chemical vapour deposition for large-area coating: industrial application to flat panel displays and solar cells.* Plasma Physics and Controlled Fusion, vol. 42, no. 12B, pages B353–B363, 2000.
- [Pingate 06] N. Pingate, D. Yotsaksri & P. Sichanugrist. *Microcrystalline SiO and its Application to Solar Cell.* In Photovoltaic Energy Conversion, Conference Record of the 2006 IEEE 4th World Conference on, volume 2, pages 1507–1508, May 2006.

- [Platz 96] R. Platz, D. Fischer, C. Hof, S. Dubail, J. Meier, U. Kroll & A. Shah. *H2-Dilution* vs. *Buffer Layers for Increased Voc.* MRS Proceedings, vol. 420, page 51, 1996.
- [Platz 97] R. Platz, D. Fischer, S. Dubail & A. Shah. *a-Si:H/a-Si:H stacked cell from VHF-deposition in a single chamber reactor with 9% stabilized efficiency.* Solar Energy Materials and Solar Cells, vol. 46, no. 2, pages 157–172, 1997.
- [Powell 02] M. J. Powell, S. C. Deane & R. B. Wehrspohn. *Microscopic mechanisms for creation and removal of metastable dangling bonds in hydrogenated amorphous silicon*. Phys. Rev. B, vol. 66, page 155212, October 2002.
- [Prasad 89] Kshem Prasad, F. Finger, H. Curtins, A. Shah & J. Bauman. *Preparation and Characterization of Highly Conductive (100 S/cm) Phosphorus Doped mu c-Si:H Films Deposited Using the VHF-GD Technique*. MRS Proceedings, vol. 164, page 27, January 1989.
- [Python 08] Martin Python, Evelyne Vallat-Sauvain, Julien Bailat, Didier Dominé, Luc Fesquet, Arvind Shah & Christophe Ballif. *Relation between substrate surface morphology and microcrystalline silicon solar cell performance*. Journal of Non-Crystalline Solids, vol. 354, no. 19–25, pages 2258–2262, 2008. Proceedings of the 22nd International Conference on Amorphous and Nanocrystalline Semiconductors.
- [Python 09] M. Python, O. Madani, D. Dominé, F. Meillaud, E. Vallat-Sauvain & C. Ballif. Influence of the substrate geometrical parameters on microcrystalline silicon growth for thin-film solar cells. Solar Energy Materials and Solar Cells, vol. 93, no. 10, pages 1714–1720, 2009.
- [Python 10] M. Python, D. Dominé, T. Söderström, F. Meillaud & C. Ballif. *Microcrystalline silicon solar cells: effect of substrate temperature on cracks and their role in post-oxidation.* Progress in Photovoltaics: Research and Applications, vol. 18, no. 7, pages 491–499, 2010.
- [Rath 03] J.K Rath. Low temperature polycrystalline silicon: a review on deposition, physical properties and solar cell applications. Solar Energy Materials and Solar Cells, vol. 76, no. 4, pages 431–487, 2003. <ce:title>Photovoltaics and photoactive materials properties, technology and applications</ce:title>.
- [Rech 96] B. Rech, C. Beneking & H. Wagner. *Improvement in stabilized efficiency of a-Si:H solar cells through optimized p/i-interface layers*. Solar Energy Materials and Solar Cells, vol. 41-42, no. 0, pages 475–483, 1996.
- [Rech 06] B. Rech, T. Repmann, M.N. van den Donker, M. Berginski, T. Kilper, J. Hüpkes,
 S. Calnan, H. Stiebig & S. Wieder. *Challenges in microcrystalline silicon based solar cell technology*. Thin Solid Films, vol. 511-512, pages 548–555, 2006.
 EMSR 2005 Proceedings of Symposium F on Thin Film and Nanostructured Materials for Photovoltaics EMRS 2005 Symposium F.

- [Repmann 03] T. Repmann, J. Kirchhoff, W. Reetz, F. Birmans, J. Muller & B. Rech. *Investigations on the current matching of highly efficient tandem solar cells based on amorphous and microcrystalline silicon*. In Photovoltaic Energy Conversion, 2003. Proceedings of 3rd World Conference on, volume 2, pages 1843–1846, 12-16 2003.
- [Reynolds 09] Steve Reynolds, Reinhard Carius, Friedhelm Finger & Vladimir Smirnov. Correlation of structural and optoelectronic properties of thin film silicon prepared at the transition from microcrystalline to amorphous growth. Thin Solid Films, vol. 517, no. 23, pages 6392–6395, 2009. <ce:title>Proceedings on the Sixth Symposium on Thin Films for Large Area Electronics</ce:title>.
- [Roschek 03] T. Roschek. *Microcrystalline Silicon Solar Cells Prepared by 13.56 MHz PECVD*. PhD thesis, Forschungszentrum Jülich GmbH, 2003.
- [Sai 10] Hitoshi Sai, Haijun Jia & Michio Kondo. Impact of front and rear texture of thin-film microcrystalline silicon solar cells on their light trapping properties.
 Journal of Applied Physics, vol. 108, no. 4, page 044505, 2010.
- [Sai 11] Hitoshi Sai, Yoshiaki Kanamori & Michio Kondo. *Flattened light-scattering substrate in thin film silicon solar cells for improved infrared response.* Applied Physics Letters, vol. 98, no. 11, page 113502, 2011.
- [Saito 05] Keishi Saito, Masafumi Sano, Shotaro Okabe, Shuichiro Sugiyama & Kyousuke Ogawa. *Microcrystalline silicon solar cells fabricated by VHF plasma CVD method.* Solar Energy Materials and Solar Cells, vol. 86, no. 4, pages 565–575, 2005.
- [Saito 11] Kimihiko Saito & Michio Kondo. *Control of preferential orientation of microcrystalline silicon and its impact on solar cell performance.* Progress in Photovoltaics: Research and Applications, vol. 19, no. 7, pages 858–864, 2011.
- [Sakai 90] Hiroshi Sakai, Takasi Yoshida, Toshio Hama & Yukimi Ichikawa. *Effects of Surface Morphology of Transparent Electrode on the Open-Circuit Voltage in a-Si:H Solar Cells.* Japanese Journal of Applied Physics, vol. 29, no. Part 1, No. 4, pages 630–635, 1990.
- [Sansonnens 98] L. Sansonnens, A. A. Howling & Ch. Hollenstein. *Degree of dissociation measured by FTIR absorption spectroscopy applied to VHF silane plasmas*. Plasma Sources Science and Technology, vol. 7, no. 2, pages 114–118, 1998.
- [Sansonnens 00] L. Sansonnens, A. A. Howling & Ch. Hollenstein. *A gas flow uniformity study in large-area showerhead reactors for RF plasma deposition.* Plasma Sources Science and Technology, vol. 9, no. 2, pages 205–209, 2000.
- [Sansonnens 06] L Sansonnens, A A Howling & Ch Hollenstein. *Electromagnetic field nonuni*formities in large area, high-frequency capacitive plasma reactors, including

electrode asymmetry effects. Plasma Sources Science and Technology, vol. 15, no. 3, page 302, 2006.

- [Sato 93] K. Sato, Y. Matsui, K. Adachi, Y. Gotoh, Yasuo Hayashi & H. Nishimura. *Hydro-gen plasma treatment of ZnO-coated TCO films*. In Photovoltaic Specialists Conference, 1993., Conference Record of the Twenty Third IEEE, pages 855–859, 1993.
- [Schade 84] H. Schade, Z E. Smith, J.H. Thomas III & A. Catalano. *Hydrogen plasma interactions with tin oxide surfaces*. Thin Solid Films, vol. 117, no. 2, pages 149–155, 1984.
- [Schicho 12] S. Schicho, F. Köhler, R. Carius & A. Gordijn. *The relationship of structural properties of microcrystalline silicon to solar cell performance*. Solar Energy Materials and Solar Cells, vol. 98, no. 0, pages 391–397, 2012.
- [Schmitt 89] J.P.M. Schmitt. *Amorphous silicon deposition: Industrial and technical challenges.* Thin Solid Films, vol. 174, Part 1, no. 0, pages 193–202, 1989.
- [Schüttauf 13] Schüttauf. -. To be published, 2013.
- [Schwarzenbach 96] W. Schwarzenbach, A. A. Howling, M. Fivaz, S. Brunner & Ch. Hollenstein. Sheath impedance effects in very high frequency plasma experiments. Journal of Vacuum Science & Technology A: Vacuum, Surfaces, and Films, vol. 14, no. 1, pages 132–138, 1996.
- [Söderström 09] T. Söderström, F.-J. Haug, X. Niquille, V. Terrazzoni & C. Ballif. *Asymmetric intermediate reflector for tandem micromorph thin film silicon solar cells*. Applied Physics Letters, vol. 94, no. 6, page 063501, 2009.
- [Söderström 11] K. Söderström, F.-J. Haug, J. Escarré, C. Pahud, R. Biron & C. Ballif. *Highly reflective nanotextured sputtered silver back reflector for flexible high-efficiency n–i–p thin-film silicon solar cells*. Solar Energy Materials and Solar Cells, vol. 95, no. 12, pages 3585–3591, 2011.
- [Söderström 13] Karin Söderström. *Coupling light into thin silicon layers for high-efficiency solar cells.* PhD thesis, STI, Lausanne, 2013.
- [Shah 04] A. V. Shah, H. Schade, M. Vanecek, J. Meier, E. Vallat-Sauvain, N. Wyrsch, U. Kroll, C. Droz & J. Bailat. *Thin-film silicon solar cell technology*. Progress in Photovoltaics: Research and Applications, vol. 12, no. 2-3, pages 113–142, 2004.
- [Shah 10] Arvind Shah. Thin-film silicon solar cells. EPFL Press, first edition edition, 2010.

- [Smets 06] A. H. M. Smets & M. Kondo. *The role of ion-bulk interactions during high rate deposition of microcrystalline silicon by means of the multi-hole-cathode VHF plasma*. Journal of Non-Crystalline Solids, vol. 352, no. 9-20, pages 937–940, June 2006.
- [Smets 07] A. H. M. Smets, W. M. M. Kessels & M. C. M. van de Sanden. *The effect of ion-surface and ion-bulk interactions during hydrogenated amorphous silicon deposition.* Journal of Applied Physics, vol. 102, no. 7, page 073523, 2007.
- [Smets 08] A. H. M. Smets, T. Matsui & M. Kondo. *High-rate deposition of microcrystalline silicon p-i-n solar cells in the high pressure depletion regime*. Journal of Applied Physics, vol. 104, no. 3, page 034508, 2008.
- [Sobajima 08] Y. Sobajima, S. Nakano, M. Nishino, Y. Tanaka, T. Toyama & H. Okamoto. Microstructures of high-growth-rate (up to 8.3 nm/s) microcrystalline silicon photovoltaic layers and their influence on the photovoltaic performance of thin-film solar cells. Journal of Non-Crystalline Solids, vol. 354, no. 19–25, pages 2407–2410, 2008. Proceedings of the 22nd International Conference on Amorphous and Nanocrystalline Semiconductors - Science and Technology.
- [Söderström 12] Karin Söderström, Grégory Bugnon, Rémi Biron, Céline Pahud, Fanny Meillaud, Franz-Josef Haug & Christophe Ballif. *Thin-film silicon triple-junction solar cell with 12.5efficiency on innovative flat light-scattering substrate.* Journal of Applied Physics, vol. 112, no. 11, page 114503, 2012.
- [Soppe 03] W.J. Soppe, A.C.W. Biebericher, C. Devilee, H. Donker & H. Schlemm. High rate growth of micro-crystalline silicon by microwave-PECVD. In Photovoltaic Energy Conversion, 2003. Proceedings of 3rd World Conference on, volume 2, pages 1655–1658Vol.2, 2003.
- [Staebler 77] D. L. Staebler & C. R. Wronski. *Reversible conductivity changes in discharge-produced amorphous Si.* Applied Physics Letters, vol. 31, no. 4, pages 292–294, 1977.
- [Steinhauser 08a] J. Steinhauser. Low Pressure Chemical Vapor Deposited Zinc Oxide for Silicon Thin Film Solar Cells Optical and Electrical Properties. PhD thesis, Université de Neuchâtel, 2008.
- [Steinhauser 08b] J. Steinhauser, S. Faÿ, N. Oliveira, E. Vallat-Sauvain, D. Zimin, U. Kroll & C. Ballif. *Electrical transport in boron-doped polycrystalline zinc oxide thin films.* physica status solidi (a), vol. 205, no. 8, pages 1983–1987, 2008.
- [Steinhauser 11] Jérôme Steinhauser, Stefan Meyer, Marlène Schwab, Sylvie Faÿ, Christophe Ballif, U. Kroll & D. Borrello. *Humid environment stability of low pressure chemical vapor deposited boron doped zinc oxide used as transparent electrodes in thin film silicon solar cells.* Thin Solid Films, vol. 520, no. 1, pages 558–562, 2011.

- [Sterling 65] H.F. Sterling & R.C.G. Swann. *Chemical vapour deposition promoted by r.f. discharge.* Solid-State Electronics, vol. 8, no. 8, pages 653–654, 1965.
- [Stiebig 00] H Stiebig, T Brammer, J Zimmer, O Vetterl & H Wagner. *Investigation of the optoelectronic properties of \mu c-Si:H pin solar cells.* Journal of Non-Crystalline Solids, vol. 266–269, Part 2, no. 0, pages 1104–1108, 2000.
- [Stoffels 95] W. W. Stoffels, E. Stoffels, G. M. W. Kroesen & F. J. de Hoog. *Electron density fluctuations in a dusty Ar/SiH[sub 4] rf discharge*. Journal of Applied Physics, vol. 78, no. 8, pages 4867–4872, 1995.
- [Strahm 07a] B. Strahm. *Investigations of radio-frequency, capacitively-coupled large area industrial reactor : cost-effective production of thin film microcrystalline silicon for solar cells.* PhD thesis, EPFL, 2007.
- [Strahm 07b] B. Strahm, A. A. Howling, L. Sansonnens & Ch. Hollenstein. *Plasma silane concentration as a determining factor for the transition from amorphous to microcrystalline silicon in SiH4/H2 discharges.* Plasma Sources Science and Technology, vol. 16, no. 1, pages 80–89, 2007.
- [Strahm 07c] B. Strahm, A. A. Howling, L. Sansonnens, Ch. Hollenstein, U. Kroll, J. Meier, Ch. Ellert, L. Feitknecht & C. Ballif. *Microcrystalline silicon deposited at high rate on large areas from pure silane with efficient gas utilization*. Solar Energy Materials and Solar Cells, vol. 91, no. 6, pages 495–502, March 2007.
- [Strahm 09] B Strahm, A. Feltrin, R. Bartlome & C. Ballif. *Optical emission spectroscopy to diagnose powder formation in SiH4-H2 discharges*. In Proceedings of SPIE conference on Thin Film Solar Technology, San Diego, 2009.
- [Strahm 10] B. Strahm & Ch. Hollenstein. *Powder formation in SiH4-H2 discharge in large area capacitively coupled reactors: A study of the combined effect of interelectrode distance and pressure.* Journal of Applied Physics, vol. 107, no. 2, page 023302, 2010.
- [Stutzmann 85] Martin Stutzmann. *Role of mechanical stress in the light-induced degradation of hydrogenated amorphous silicon.* Applied Physics Letters, vol. 47, no. 1, pages 21–23, 1985.
- [Taira 03] S. Taira, M. Shima, K. Murata & M. Tanaka. *A role of a-Si:H buffer layer for controlling the impurity profiles near p/i interface of microcrystalline silicon solar cell.* In Proceedings of 3rd World Conference on Photovoltaic Energy Conversion, 2003., volume 2, pages 1816–1819Vol.2, May 2003.
- [Takahashi 07] Eiji Takahashi, Yasuaki Nishigami, Atsushi Tomyo, Masaki Fujiwara, Hirokazu Kaki, Kiyoshi Kubota, Tsukasa Hayashi, Kiyoshi Ogata, Akinori Ebe & Yuichi Setsuhara. Large-Area and High-Speed Deposition of Microcrystalline Silicon

Film by Inductive Coupled Plasma using Internal Low-Inductance Antenna. Japanese Journal of Applied Physics, vol. 46, no. 3B, pages 1280–1285, 2007.

- [Takai 00] Madoka Takai, Tomonori Nishimoto, Michio Kondo & Akihisa Matsuda. *Effect of higher-silane formation on electron temperature in a silane glow-discharge plasma*. Applied Physics Letters, vol. 77, no. 18, pages 2828–2830, 2000.
- [Takai 01] M. Takai, T. Nishimoto, M. Kondo & A. Matsuda. *Anomalous behavior of electron temperature in silane glow discharge plasmas*. Thin Solid Films, vol. 390, no. 1-2, pages 83–87, 2001.
- [Takeuchi 01] Yoshiaki Takeuchi, Hiroshi Mashima, Masayoshi Murata, Satoshi Uchino & Yoshinobu Kawai. *Characteristics of Very-High-Frequency-Excited SiH*₄ *Plasmas using a Ladder-Shaped Electrode.* Japanese Journal of Applied Physics, vol. 40, no. Part 1, No. 5A, pages 3405–3408, 2001.
- [Terakawa 13] A. Terakawa. *Review of thin-film silicon deposition techniques for high-efficiency solar cells developed at Panasonic/Sanyo*. Solar Energy Materials and Solar Cells, no. 0, pages –, 2013.
- [Torres 96] P. Torres, J. Meier, R. Flückiger, U. Kroll, J. A. Anna Selvan, H. Keppner, A. Shah, S. D. Littelwood, I. E. Kelly & P. Giannoulès. *Device grade microcrystalline silicon owing to reduced oxygen contamination*. Applied Physics Letters, vol. 69, no. 10, pages 1373–1375, 1996.
- [Tsai 86] C. C. Tsai, J. C. Knights, G. Chang & B. Wacker. *Film formation mechanisms in the plasma deposition of hydrogenated amorphous silicon.* Journal of Applied Physics, vol. 59, no. 8, pages 2998–3001, 1986.
- [Tzolov 97] M. Tzolov, F. Finger, R. Carius & P. Hapke. *Optical and transport studies on thin microcrystalline silicon films prepared by very high frequency glow discharge for solar cell applications.* Journal of Applied Physics, vol. 81, no. 11, pages 7376–7385, 1997.
- [ur Rehman 11] Aman ur Rehman, H. C. Kwon, W. T. Park & J. K. Lee. *A study of the role of various reactions on the density distribution of hydrogen, silylene, and silyl in SiH*₄/*H*₂ *plasma discharges.* Physics of Plasmas, vol. 18, no. 9, page 093502, 2011.
- [Usui 79] S. Usui & M. Kikuchi. *Properties of heavily doped GD-Si with low resistivity.* Journal of Non-Crystalline Solids, vol. 34, no. 1, pages 1–11, 1979.
- [Vallat-Sauvain 05] E. Vallat-Sauvain, J. Bailat, J. Meier, X. Niquille, U. Kroll & A. Shah. *Influence of the substrate's surface morphology and chemical nature on the nucleation and growth of microcrystalline silicon*. Thin Solid Films, vol. 485, no. 1–2, pages 77–81, 2005.

- [Vallat-Sauvain 06] E. Vallat-Sauvain, C. Droz, F. Meillaud, J. Bailat, A. Shah & C. Ballif. *Determination of Raman emission cross-section ratio in hydrogenated microcrystalline silicon.* Journal of Non-Crystalline Solids, vol. 352, no. 9-20, pages 1200–1203, June 2006.
- [van den Donker 05] M. N. van den Donker, B. Rech, F. Finger, W. M. M. Kessels & M. C. M. van de Sanden. *Highly efficient microcrystalline silicon solar cells deposited from a pure SiH[sub 4] flow.* Applied Physics Letters, vol. 87, no. 26, page 263503, 2005.
- [van den Donker 06] M. N. van den Donker. *Microcrystalline Silicon Solar Cells: Looking Beyond the Glass.* PhD thesis, Forschungszentrum Jülich GmbH, 2006.
- [van den Donker 07] M. N. van den Donker, S. Klein, B. Rech, F. Finger, W. M. M. Kessels & M. C. M. van de Sanden. *Microcrystalline silicon solar cells with an open-circuit voltage above 600 mV*. Applied Physics Letters, vol. 90, no. 18, page 183504, 2007.
- [van Oort 87] R.C. van Oort, M.J. Geerts, J.C. van den Heuvel & J.W. Metselaar. *Hydro-gen plasma etching of amorphous and microcrystalline silicon*. Electronics Letters, vol. 23, no. 18, pages 967–968, 1987.
- [Vanecek 02] M. Vanecek & A. Poruba. Fourier-transform photocurrent spectroscopy of microcrystalline silicon for solar cells. Applied Physics Letters, vol. 80, no. 5, pages 719–721, 2002.
- [Vaucher 97] N. Pellaton Vaucher, B. Rech, D. Fischer, S. Dubail, M. Goetz, H. Keppner, N. Wyrsch, C. Beneking, O. Hadjadj, V. Shklover & A. Shah. Controlled nucleation of thin microcrystalline layers for the recombination junction in a-Si stacked cells. Solar Energy Materials and Solar Cells, vol. 49, no. 1–4, pages 27–33, 1997.
- [Vaucher 98] N. Pellaton Vaucher. *Cellules solaires en silicium amorphe et microcristallin: Optimalisation électrique et optique de la structure tandem.* PhD thesis, Université de Neuchâtel, 1998.
- [Veprek 68] S. Veprek & V. Marecek. *The preparation of thin layers of Ge and Si by chemical hydrogen plasma transport.* Solid-State Electronics, vol. 11, no. 7, pages 683–684, 1968.
- [Veprek 83] S Veprek, Z Iqbal, R O Kuhne, P Capezzuto, F A Sarott & J K Gimzewski. Properties of microcrystalline silicon. IV. Electrical conductivity, electron spin resonance and the effect of gas adsorption. Journal of Physics C: Solid State Physics, vol. 16, no. 32, page 6241, 1983.
- [Vet 08] B. Vet & M. Zeman. Relation between the open-circuit voltage and the band gap of absorber and buffer layers in a-Si:H solar cells. Thin Solid Films,

vol. 516, no. 20, pages 6873–6876, 2008. <ce:title>Proceedings on Advanced Materials and Concepts for Photovoltaics EMRS 2007 Conference, Strasbourg, France</ce:title>.

- [Vetterl 00] O. Vetterl, F. Finger, R. Carius, P. Hapke, L. Houben, O. Kluth, A. Lambertz, A. Mück, B. Rech & H. Wagner. *Intrinsic microcrystalline silicon: A new material for photovoltaics*. Solar Energy Materials and Solar Cells, vol. 62, no. 1-2, pages 97–108, 2000.
- [Vetterl 01] O Vetterl, A Lambertz, A Dasgupta, F Finger, B Rech, O Kluth & H Wagner. Thickness dependence of microcrystalline silicon solar cell properties. Solar Energy Materials and Solar Cells, vol. 66, no. 1–4, pages 345–351, 2001. <ce:title>PVSEC 11 - Part II</ce:title>.
- [Wang 97] De-Zhen Wang & J. Q. Dong. *Kinetics of low pressure rf discharges with dust particles.* Journal of Applied Physics, vol. 81, no. 1, pages 38–42, 1997.
- [Willeke 83] Gerhard Philipp Willeke. *The Structural and Electronic Properties of Microcrystalline Silicon Produced in a Glow Discharge Plasma*. PhD thesis, University of Dundee, 1983.
- [Windischmann 91] H. Windischmann. *Intrinsic stress in sputtered thin films*. Journal of Vacuum Science & Technology A: Vacuum, Surfaces, and Films, vol. 9, no. 4, pages 2431–2436, 1991.
- [Yamamoto 03] K. Yamamoto*et al. Novel HYBRID thin film silicon solar cell and module.* In Proceedings of the 3rd World Conference on Photovoltaic Solar Energy Conversion, pages 2801–2805, Osaka, Japan, 2003.
- [Yamamoto 04] Kenji Yamamoto, Akihiko Nakajima, Masashi Yoshimi, Toru Sawada, Susumu Fukuda, Takashi Suezaki, Mitsuru Ichikawa, Yohei Koi, Masahiro Goto, Tomomi Meguro, Takahiro Matsuda, Masataka Kondo, Toshiaki Sasaki & Yuko Tawada. *A high efficiency thin film silicon solar cell and module*. Solar Energy, vol. 77, no. 6, pages 939–949, 2004. Thin Film PV.
- [Yamamoto 05] Kenji Yamamoto, Akihiko Nakajima, Masashi Yoshimi, Toru Sawada, Susumu Fukuda, Takashi Suezaki, Mitsuru Ichikawa, Yohei Koi, Masahiro Goto, Tomomi Meguro, Takahiro Matsuda, Masataka Kondo, Toshiaki Sasaki & Yuko Tawada. *A thin-film silicon solar cell and module*. Progress in Photovoltaics: Research and Applications, vol. 13, no. 6, pages 489–494, 2005.
- [Yan 11] Baojie Yan, Guozhen Yue, Laura Sivec, Jeffrey Yang, Subhendu Guha & Chun-Sheng Jiang. *Innovative dual function nc-SiO[sub x]:H layer leading to a* > 16% efficient multi-junction thin-film silicon solar cell. Applied Physics Letters, vol. 99, no. 11, page 113512, 2011.

[Yue 08] Guozhen Yue, Baojie Yan, Charles Teplin, Jeffrey Yang & Subhendu Guha. *Optimization and characterization of i/p buffer layer in hydrogenated nanocrystalline silicon solar cells*. Journal of Non-Crystalline Solids, vol. 354, no. 19–25, pages 2440–2444, 2008. Proceedings of the 22nd International Conference on Amorphous and Nanocrystalline Semiconductors - Science and Technology.

[Yue 12] Guozhen Yue, Baojie Yan, Laura Sivec, Yanhua Zhou, Jeffrey Yang & Subhendu Guha. *Effect of impurities on performance of hydrogenated nanocrystalline silicon solar cells*. Solar Energy Materials and Solar Cells, vol. 104, pages 109–112, 2012.

[Yunaz 07a] Ihsanul Afdi Yunaz, Kobsak Sriprapha, Shuichi Hiza, Akira Yamada & Makoto Konagai. Effects of Temperature and Spectral Irradiance on Performance of Silicon-Based Thin Film Multijunction Solar Cells. Japanese Journal of Applied Physics, vol. 46, no. 4A, pages 1398–1403, 2007.

[Yunaz 07b] Ihsanul Afdi Yunaz, Akira Yamada & Makoto Konagai. *Theoretical Analysis of Amorphous Silicon Alloy Based Triple Junction Solar Cells.* Japanese Journal of Applied Physics, vol. 46, no. 47, pages L1152–L1154, 2007.

CURRICULUM VITÆ

Grégory BUGNON

Rue de la Maladière, 8 2000 Neuchâtel

Nationality: Swiss and French

E-mails: <u>gregory.bugnon@epfl.ch</u>

gb.pvlab@gmail.com



Education

Switzerland

- 2007 Master 2 Professionnel Techniques et Applications des Plasmas UJF, Grenoble.
- 2005 Master 2 Recherche Astrophysique et Milieux Dilués UJF, LAOG, Grenoble.
- 2004 Master 1 Physique et ingénieries UJF, Grenoble.
- 2003 Licence de Physique UJF, Grenoble.
- 2001 DEUG de Sciences de la Matière Université Joseph Fourier, Grenoble.
- 1999 Baccalauréat Général, série Scientifique Lycée de La Versoie, Thonon-les-Bains.

Experience

- 2007 *PhD candidate at the Institut de Microtechnique de Neuchâtel PV-Lab EPFL* 6 months internship / 2 years engineer / 3.5 years PhD candidate.
- 2005 Internship on stellar evolution at the observatory of Geneva

Simulations with STAREVOL code to study the role of internal gravity waves in low mass stars in the transport of angular momentum and the mixing of chemicals in stellar interiors (Resp. Dr. Corinne Charbonnel).

2004 - Internship at the Côte d'Azure observatory in the Cassiopée laboratory of Nice

Working 4 months on a simulation code to study the fluid description for Landau damping of dispersive MHD (magnetosonic and Alfvén) waves in warm collisionless plasmas (Resp. Dr. Thierry, Passot).

2000–2003 summer breaks: Wireless network technician for Spacecom-CSF

- Deployment of wireless network stations in Geneva and Lausanne areas for public services and private sector: on-site surveys for feasibility study, installations, measurements, settings and optimization of these links.
- Installation and set-up of a real-time network performance monitoring system, using Cacti on a Linux server, to analyze the overall network activity and load on each node.
- Creation of the internet website http://www.spacecom-csf.com.

2003 - Internship at the INTEGRAL Science Data Centre (ISDC)

INTEGRAL is a gamma-ray mission of the European Space Agency devoted to observing the gamma-ray sky. Introduction to the satellite data analysis system at the scientific centre. Participation to a study on the Galactic Plane Scan (GPS) using SPI and ISGRI data. Writing of a final report on this data analysis.

2001 - Network technician at the International Electrotechnical Commission (IEC)

- Helped upgrading the network from the 100VG-AnyLAN to the 100BaseT technology,
- Various maintenance operations.

1998 - Database operator for Hewlett-Packard

Building of a database under Access, statistical processing and writing of a final report.

Scientific Contribution

- Participation to 7 international conferences (5 orals & 2 posters), with 3 follow up proceedings.
- Best Student Presentation Award at the 33th PVSC, San Diego (2008).
- More than 50 co-authored peer-reviewed articles, including 5 as first author.
- 3 patents filled.

Remerciements

J'exprime en premier lieu ma profonde gratitude envers le professeur Christophe Ballif qui dirige le laboratoire photovoltaïque et couches minces électroniques de Neuchâtel, qui m'a accordé sa confiance pour accomplir mon travail au sein de son équipe. J'ai particulièrement apprécié son énergie, sa force de travail et son engagement pour défendre la technologie du photovoltaïque et lui assurer la place qu'elle mérite dans notre société.

Je pense souvent avoir eu beaucoup de chance d'être monté à bord de ce navire du PV-Lab, d'y travailler pour toujours apprendre davantage et rencontrer des gens de tous les horizons dans ce domaine passionnant du photovoltaïque. Ce fut un réel plaisir. J'adresse ici ma reconnaissance à toutes les personnes du laboratoire qui m'ont permis de mener à bien mon projet, et surtout pour le temps qu'elles m'ont toujours accordé lorsque j'en avais besoin. Je remercie tout spécialement Andrea Feltrin qui m'a accueilli spontanément dans l'équipe, guidé lors de mes premiers pas avec cette technologie et qui m'a offert sa constante disponibilité. Je tiens aussi à remercier Fanny Sculati-Meillaud pour ses conseils avisés, son franc-parler et son entrain pendant toutes ces années de projets et de thèse.

Je voudrais également remercier toutes les personnes qui m'ont énormément apporté et aidé tout au long de cette expérience. Je ne peux pas toutes les mentionner ici mais je pense notamment à Julien, Didier, Thomas, Xavier, Gaetano, Matthieu, Oscar, Jakub, Richard, Sylvain, Karin, Rémi, Linus, Mustapha, Michael, Simon, Max et Bénédicte. Un grand merci à Laura et Mathieu pour leur gentillesse et leur aide (et nos vacances partagées!). Merci aussi à Mary-Claude pour sa grande disponibilité, son précieux support dans les méandres administratifs et sa bonne humeur. Je pense aussi à Hassan toujours présent pour assurer la bonne santé informatique du PV-Lab. En dehors du laboratoire j'aimerais encore remercier Uli Kroll, Alan Howling, Benjamin Strahm et Lefteris Amanatides, qui ont pris le temps de répondre à mes nombreuses questions et m'aider au cours de certaines de mes expériences.

J'ai eu aussi la possibilité de travailler dans les meilleures conditions grâce à toute l'équipe technique qui fait un travail fantastique pour que cette grande machine du PV-Lab soit toujours bien huilée et en parfait état de marche! Je suis donc spécialement reconnaissant envers Reto, Cédric, Jérémie, Lionel et Joël. J'ai une pensée particulière pour Jean-Luc qui, grâce à son travail, nous a permis au PV-Lab de profiter d'outils remarquables au quotidien.

Remerciements

Ce manuscrit a été entièrement relu et corrigé par Lara Sands et Zachary Holman, et j'aimerais les remercier ici pour leurs efforts assidus et toutes ces heures consenties!

Je tiens aussi à remercier les membres de mon jury de thèse, Prof. Paul Muralt, Dr. Julian Cashmore, Dr. Ivo Furno, et Dr. Takuya Matsui, de m'avoir honoré de leur présence et d'avoir bien voulu porter leur attention à mon travail.

Enfin c'est naturellement ma famille, mes proches et tous ceux que j'aime que je remercie du fond du cœur pour tout ce qu'ils m'ont apporté. Et je dédie spécialement cette thèse à mon père, homme d'exception trop tôt disparu qui par la pensée est toujours resté à mes côtés.

Neuchâtel, le 22 Octobre 2013

Grégory Bugnon